

**Strain-Induced Microstructural and Ordering Behaviors of
Epitaxial Fe_{38.5}Pd_{61.5} Films
Grown by Pulsed Laser Deposition**

A Dissertation

Presented to
the faculty of the School of Engineering and Applied Science
University of Virginia

In partial fulfillment
of the requirements for the degree

Doctor of Philosophy

by

Matthew A. Steiner

May 2014

Approval Sheet

**The dissertation
is submitted in partial fulfillment of the requirements
for the degree of
Doctor of Philosophy**

Matthew A. Steiner

The dissertation has been read and approved by the examining committee:

James M. Fitz-Gerald

Advisor

William A. Soffa

Chairperson

Leonid V. Zhigilei

Jerrold A. Floro

Cass. A Sackett

Accepted for the School of Engineering and Applied Science:



Dean, School of Engineering and Applied Science

May 2014

Table of Contents

| | |
|--|----|
| 1 - Motivation & Background | 1 |
| 1.1 - FCC Based Ordered Phases | 3 |
| 1.1.1 - The L1 ₀ Crystal Structure | 4 |
| 1.1.2 - The L1 ₂ Crystal Structure | 6 |
| 1.2 - The Fe-Pd Binary System | 8 |
| 1.2.1 - Overview | 8 |
| 1.2.2 - The Fe _{38.5} Pd _{61.5} Eutectoid Region | 10 |
| 1.2.3 - Studies Approaching the Eutectoid Composition | 13 |
| 1.2.4 - Effects at Fe-rich Compositions | 15 |
| 1.3 - Related Material Systems | 18 |
| 1.3.1 - The Au-Cu System | 18 |
| 1.3.2 - The Fe-Pt System | 19 |
| 1.3.3 - The Co-Pt System | 21 |
| 1.4 - Pulsed Laser Deposition | 25 |
| 1.5 - Fe-Pd Thin Films in Literature | 26 |
| 2 - Experimental Procedures | 41 |
| 2.1 - Fe _{38.5} Pd _{61.5} Target | 41 |
| 2.2 - Deposition Setup and Conditions | 41 |
| 2.3 - Characterization Techniques | 44 |
| 2.3.1 - Scanning Electron Microscopy (SEM) | 44 |
| 2.3.2 - Energy Dispersive X-ray Spectroscopy (EDXS) | 46 |
| 2.3.3 - Atomic and Magnetic Force Microscopy (AFM-MFM) | 48 |
| 2.3.4 - Vibrating Sample Magnetometry (VSM) | 49 |
| 2.3.5 - Auger Electron Spectroscopy (AES) | 49 |
| 2.3.6 - High Resolution Transmission Electron Microscopy (HRTEM) | 50 |
| 2.3.7 - X-ray Diffractometry (XRD) | 52 |
| 2.4 - Quantitative X-ray Diffraction | 53 |
| 3 - Deposition Temperature Series | 65 |
| 3.1 - Introduction | 65 |
| 3.2 - Film Growth and Morphology | 66 |
| 3.2.1 - Film Thickness and Growth Rate | 66 |
| 3.2.2 - Surface Morphology and Growth Modes | 68 |
| 3.3 - Magnetic Properties | 71 |
| 3.4 - Crystallographic Properties | 73 |
| 3.4.1 - Orientation and Epitaxy | 73 |
| 3.4.2 - Phase Assignment | 74 |

| | |
|---|------------|
| 3.5 - Strain Behavior | 77 |
| 3.5.1 - Heteroepitaxial Strain Dynamics | 77 |
| 3.5.2 - Thermal Mismatch | 80 |
| 3.5.3 - Epitaxial Strain Energetics | 82 |
| 3.6 - Ordering Behavior | 88 |
| 3.7 - Major Findings | 91 |
| 4 - L1' Ordering : Evidence of L1₀-L1₂ Hybridization | 93 |
| 4.1 - Introduction | 93 |
| 4.2 - History of L1' Ordering | 94 |
| 4.3 - Formal Treatment of the Ordered Phases | 98 |
| 4.3.1 - Structure Factor and Allowed Reflections | 98 |
| 4.3.2 - L1 ₀ and L1 ₂ Formal Notations | 100 |
| 4.3.3 - Expansion to the L1' phase | 104 |
| 4.4 - Observation of the L1' Phase | 109 |
| 4.4.1 - XRD Methodology and Analysis of Error | 110 |
| 4.4.2 - L1' Confirmation through XRD Results | 112 |
| 4.4.3 - Feasibility of an L1 ₀ -L1 ₂ Microstructure | 115 |
| 4.5 - Origination of L1' Behavior | 119 |
| 4.5.1 - The Case for L1 ₂ Perturbation : Snoek/Zener Type Effects | 119 |
| 4.5.2 - The Case for Native L1': Simultaneous Continuous Ordering | 120 |
| 4.5.3 - First Principles Calculation of Instability Temperatures | 122 |
| 4.6 - Major Findings | 129 |
| 5 - Two-phase Films Grown at 550°C | 131 |
| 5.1 - Introduction | 131 |
| 5.2 - Characterization of the Two-Phase Microstructure | 132 |
| 5.2.1 - Backscattered Electron Microscopy | 132 |
| 5.2.2 - X-Ray Diffraction | 135 |
| 5.2.3 - Magnetic Properties | 137 |
| 5.2.4 - Composition: Auger Electron Microscopy | 140 |
| 5.3 - Origins of the Two-Phase Decomposition | 145 |
| 5.3.1 - Argument for a Strain-Induced Transition | 145 |
| 5.3.2 - Metastable Phase Diagram | 150 |
| 5.3.3 - Formation and Diffusion | 152 |
| 5.4 - Major Findings | 154 |
| 6 – Contributions and Suggested Work | 156 |
| 6.1 - Contributions to the Field | 156 |
| 6.2 - Suggested Future Work | 158 |

*"For every complex problem there is an answer
that is clear, simple, and wrong."*

~ H.L. Mencken

Foremost I would like to acknowledge Kirsten Andersen, who had to suffer through countless late dinners and grouchy weekends while I undertook this endeavor. I would like to thank my parents for bringing me into this world and supporting my education, and my adviser Jim Fitz-Gerald for not prematurely sending me back out of it no matter how much I may have tempted him. I would also like to thank the countless undergraduate and graduate students who have played contributing roles over the years to the work presented.

1 – Motivation and Background

Magnetic thin films of 3d-4d/5d transition metal alloys such as Fe-Pt, Co-Pt, and Fe-Pd are of technological interest due to their ordered $L1_0$ tetragonal intermetallic phases, which exhibit high magnetocrystalline anisotropies of $K \sim 10^7$ to 10^8 ergs/cm³ that are comparable to rare earth magnets [1-6]. Rare earth permanent magnets, based on 3d transition metals alloyed with the 4f lanthanide series, have become ubiquitous since their development in the 1970s [7, 8]. Despite their prevalent use in modern technology, they are limited by a tendency to be vulnerable to corrosion, as well as brittle due to a lack of available slips systems in their complex crystal structure [7, 8]. Both of these issues can cause intractable problems for nanoscale applications. The strong hard-magnet properties of 3d-4d/5d magnetic alloys, combined with the ductility and chemical inertness of their ennobled metallic nature, allow these material systems to remain above the thermally induced $KV/k_B T$ superparamagnetic limit at the nanometer scale, making them ideal for applications in ultra-high-density magnetic storage or micro-electro-mechanical systems [9]. Within this class of materials, Fe-Pd alloys possess comparatively moderate magnetocrystalline anisotropies relative to Co-Pt and Fe-Pt. The Fe-Pd system, however, exhibits a considerably lower range of order-disorder transition temperatures that renders the material well-suited for nanostructured magnetic applications by enabling lower processing temperatures [10, 11]. In addition, the high economic demand for Pt makes Pd based alternatives of considerable technological interest.

Experimental work to date near the $Fe_{38.5}Pd_{61.5}$ eutectoid composition between the $L1_0$ and $L1_2$ phases of the Fe-Pd system, bounding one side of the technologically relevant $L1_0$ phase region, is limited and has left large uncertainties in the experimental phase diagram (Fig. 1) [10].

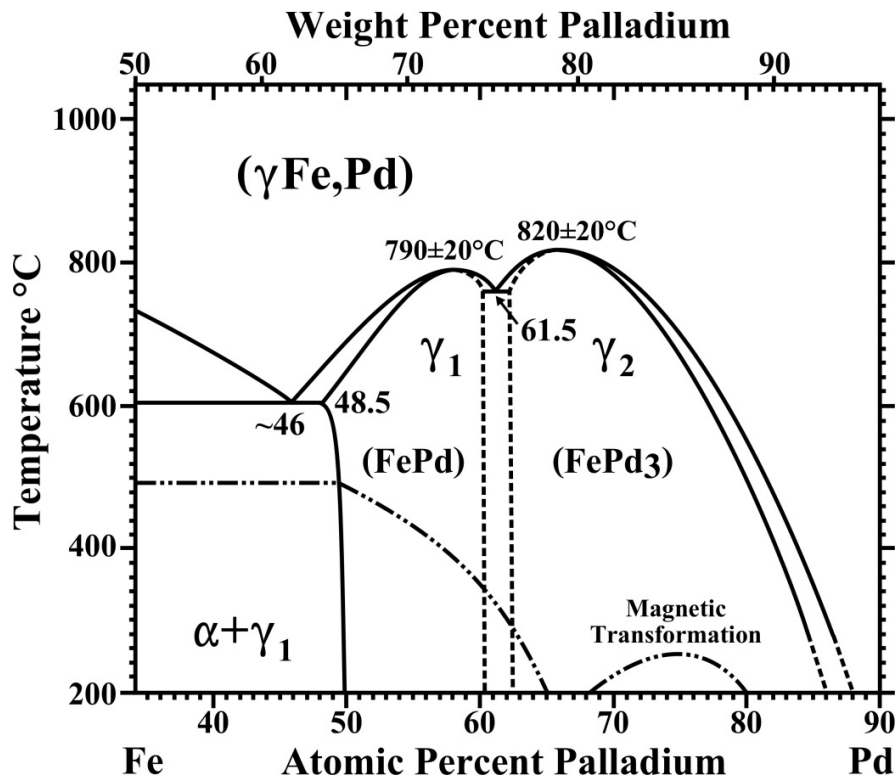


Fig. 1 – Partial experimental phase diagram of the Fe-Pd material system [10]. Of special note is the eutectoid decomposition located at $Fe_{38.5}Pd_{61.5}$ from the disordered FCC γ phase to the γ_1 - $L1_0$ (FePd) and γ_2 - $L1_2$ (FePd₃) ordered phases. The uniformly dashed lines in the diagram represent uncertain boundaries in the experimental phase diagram; the broken lines represent the magnetic transformation temperature.

The work included in this thesis began as an attempt to better understand the complicated phase behavior of this unexplored region of the binary diagram and solidify a gap in the experimental record. The related Co-Pt system has been shown to decompose into a novel, strain-induced chessboard microstructure at the eutectoid composition between its ordered $L1_0$ and $L1_2$ intermetallic phases [12, 13], and it is thought that producing similar strain-induced microstructures in related 3d-4d/5d material systems may be possible [14]. Strain-induced effects are observed for the $Fe_{38.5}Pd_{61.5}$ thin films presented within this thesis, but they are of a considerably different nature than the microstructural behavior produced at the Co-Pt eutectoid.

1.1 – FCC Based Ordered Phases

This thesis will focus largely on the Pd-rich phases of the Fe-Pd system, which consist of a Face Centered Cubic (FCC) phase and the $L1_0$ and $L1_2$ ordered structures derived from this parent lattice. The conventional cell for the FCC lattice is a cube with an atom at each corner and situated in the middle of each face, containing a total of four atomic sites (Fig. 2). Each of these atomic sites in the disordered binary alloy is a statistical entity that has some probability of being either an Fe or Pd atom, and can be treated as a compositional superposition of the two.

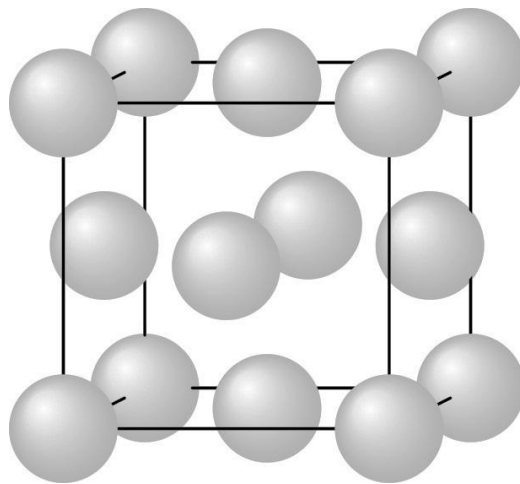


Fig. 2 – *The conventional cell of an FCC structure, with statistical atoms at the corners and face centers. This structure will serve as a parent cell to all ordered phases of the Fe-Pd system.*

This FCC configuration results in a close-packed structure, with $\{111\}$ close-packed planes and $\langle 110 \rangle$ close-packed directions, and each atom having a coordination of twelve nearest neighbors. The FCC structure is given the Strukturbericht designation A1 [15], and Pearson symbol cF4, which can be broken down as cubic Face centered with a 4 atom cell [16]. This places the structure in space group $Fm\bar{3}m$, no. 225, with a statistical atom residing in the Wyckoff 4(a) positions at $(0, 0, 0)$, $(\frac{1}{2}, 0, \frac{1}{2})$, $(\frac{1}{2}, \frac{1}{2}, 0)$, and $(0, \frac{1}{2}, \frac{1}{2})$. The symmetry operators of this space group are displayed in Fig. 3.

Face Centered Cubic: $Fm\bar{3}m$ No. 225

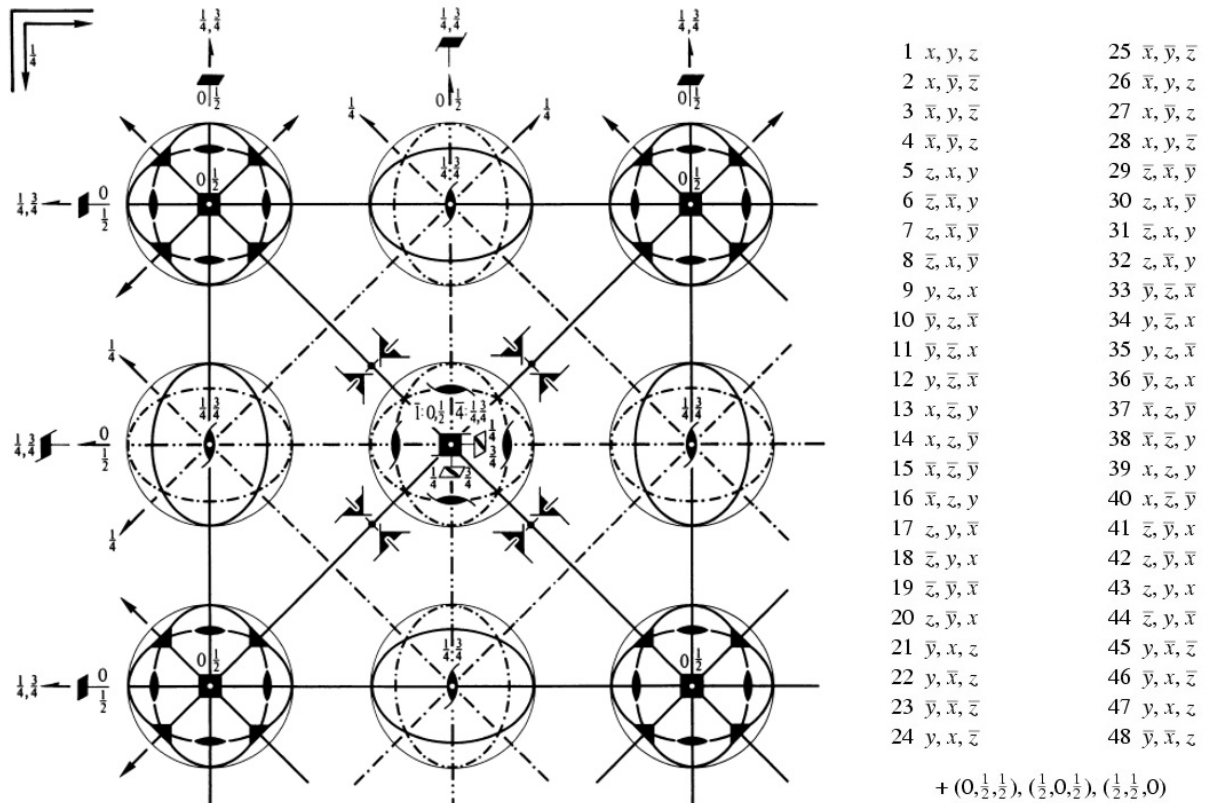


Fig. 3 – The space group symmetry for the FCC structure represented graphically with all appropriate symmetry operators, along with a list of all symmetric points [17]. The three-fold axis running through the body diagonal is indicative of cubic symmetry.

1.1.1 - The $L1_0$ Crystal Structure

The $L1_0$ (Stukturbericht designation) structure is a crystallographic derivative of the FCC parent lattice. The ordered structure has less symmetry than its parent and can be envisioned as alternating monolayers of two constituent elements on an FCC scaffold. These alternating monolayers result in the large magnetocrystalline anisotropies of magnetic $L1_0$ alloys, giving the

phase its desirable magnetic properties [18]. The conventional unit cell for $L1_0$ has a Pearson symbol of tP4 (tetragonal Primitive 4-atom) and is related closely to a compositionally modified FCC conventional cell, as the tetragonal c/a ratio is generally close to unity. The $L1_0$ primitive cell is reduced to a tP2 two atom basis and is related to the $L1_0$ conventional cell in a manner superficially similar to the Bain correspondence between FCC and BCC structures (Fig. 4).

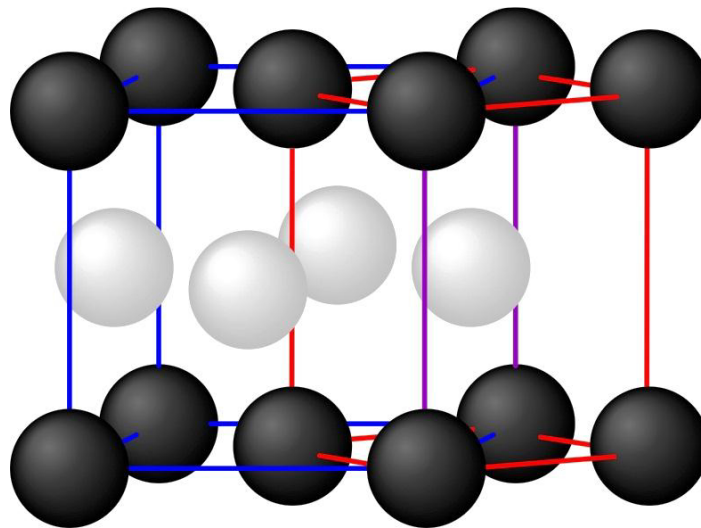


Fig. 4 – The $L1_0$ conventional cell (Blue) and primitive cell (Red). The conventional cell can be seen to correlate to an FCC parent lattice with atomic sites occupied by alternating layers.

This places the structure in space group $P4/mmm$, no. 123, with one element residing in the Wyckoff 1(a) position at $(0,0,0)$ and 1(c) position at $(\frac{1}{2}, \frac{1}{2}, 0)$, while the other element is found at positions 2(e) at $(\frac{1}{2}, 0, \frac{1}{2})$ and $(0, \frac{1}{2}, \frac{1}{2})$. Observing the symmetry operators of the $L1_0$ space group (Fig. 5), there is a notable absence of a three-fold symmetry axis along the body diagonal, representing a shift from cubic to tetragonal symmetry.

L1₀ : P4/mmm no. 123

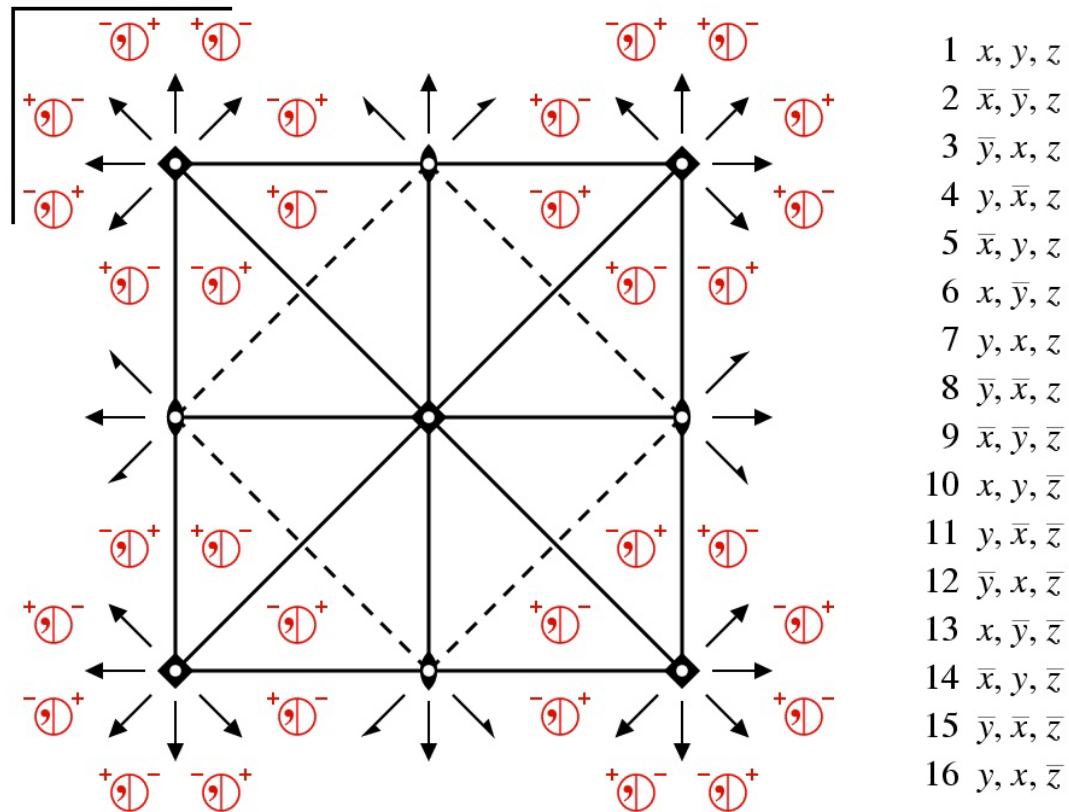


Fig. 5 – The space group symmetry for the L1₀ structure represented graphically with all appropriate symmetry operators, along with a list of all symmetric points [17]. Tetragonality has eliminated the three-fold axis running through the body diagonal of the FCC parent.

1.1.2 - The L1₂ Crystal Structure

The L1₂ (Stukturbericht designation) structure is also a crystallographic derivative of the FCC parent lattice. The face centered atoms found at Wyckoff positions 3(c) at $(\frac{1}{2}, 0, \frac{1}{2})$, $(\frac{1}{2}, \frac{1}{2}, 0)$, and $(0, \frac{1}{2}, \frac{1}{2})$ are now a different species than the minor constituent element at position 1(a) $(0, 0, 0)$. The conventional cell for L1₂ is its primitive cell, which corresponds closely to the conventional cell of FCC (Fig. 6). L1₂ is in space group $Pm\bar{3}m$, no. 221, and as it maintains cubic symmetry it has a threefold symmetry along the body diagonal (Fig. 7).

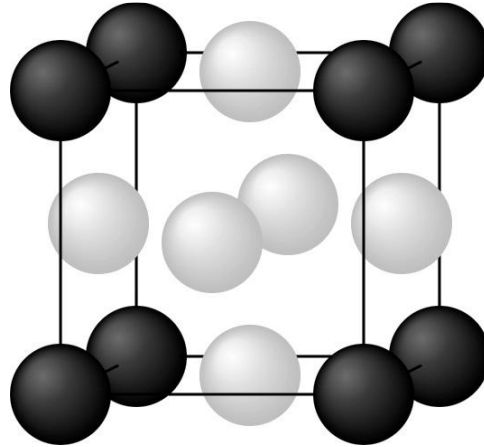


Fig. 6 – The $L1_2$ structure conventional cell, which is also a simple cubic primitive cell.

$L1_2$: $Pm\bar{3}m$ no. 221

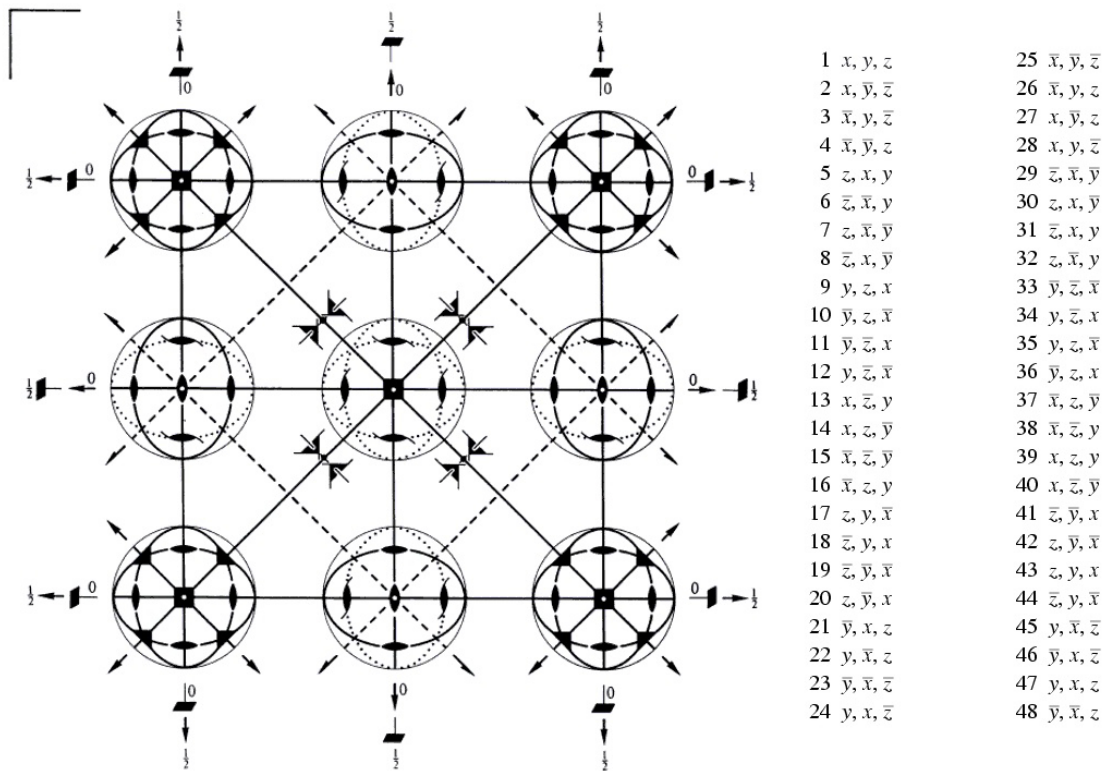


Fig. 7 – The space group symmetry for the $L1_2$ structure represented graphically with all appropriate symmetry operators, along with a list of all symmetric points [17]. The three-fold axis running through the body diagonal shows that the FCC cubic symmetry is preserved.

1.2 - The Fe-Pd Binary System

1.2.1 - Overview

The experimental phase diagram commonly cited for the Fe-Pd system is given by Massalski (Fig. 8) [10]. At high temperatures and Pd-rich compositions the diagram is dominated by the FCC γ -phase. The L_{10} and L_{12} ordered phases can both be found at lower temperatures on the Pd-rich half of the phase diagram, a region that will be discussed later in greater detail. The Fe-rich side of the diagram is dominated at low temperatures by a two-phase α -Fe + L_{10} region, giving way to Body Centered Cubic (BCC) α -Fe for low Pd at % alloys. With rising temperatures the Fe-rich side of the diagram transitions to an α + γ two-phase region, and eventually to solely γ -(Fe-Pd) after a possible miscibility gap. Near the Fe-rich liquidus a small region of BCC δ -Fe can be found, similar to the phase diagram of steel.

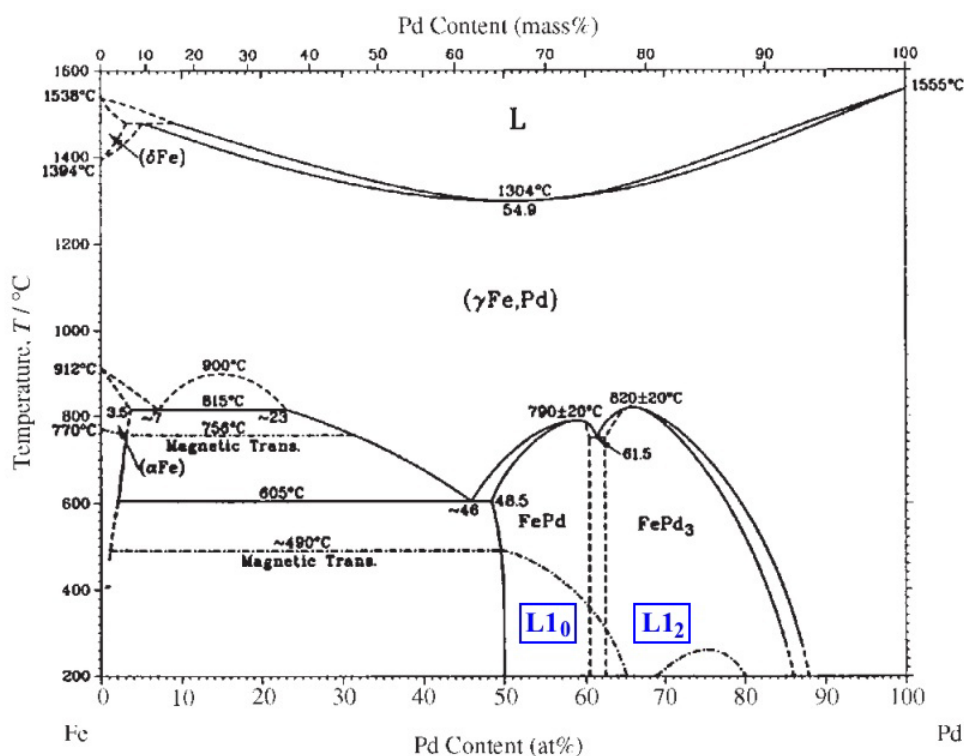


Fig. 8 – The classically cited experimental Fe-Pd binary phase diagram given by Massalski [10]. The work in this thesis will focus on the FCC $\rightarrow L_{10} + L_{12}$ eutectoid at 61.5 at % Pd.

Thorough reviews are available concerning the accuracy of the Fe-Pd experimental diagram [19-21]. Ghosh *et al.* [19] in particular perform an excellent line-by-line analysis of the entire diagram, which is reproduced partially in Fig. 9 along with their own computational work. The studies determining the solidus-liquidus of the diagram [22-24] and the Fe-rich features [21, 25-28] are not of great concern for the solid state Pd-rich work presented in this thesis. It is worth noting ambiguities, however, in the region containing the ordered FePd and FePd₃ phases. The ordered phase boundaries in the experimental diagram have been determined by thermal analysis [23, 26, 29], magnetic measurements [30, 31], diffraction [32, 33], dilatometry [30], and electrical resistivity [34]. The experimental diagram given by Massalski relies heavily on the data provided by Kußman and Jessen [30] and Takezawa *et al.* [34]. It can be seen from Fig. 9 this data is not fully corroborated by all other studies, but both studies are in close agreement with each other and large portions of the other available data points.

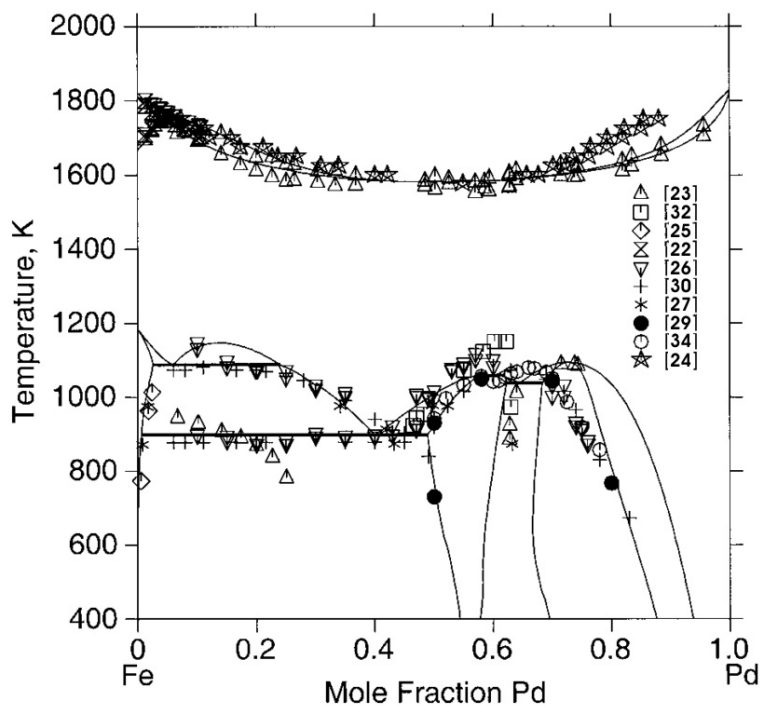


Fig. 9 – A compilation of experimental work on the Fe-Pd phase diagram presented by Ghosh *et al.* [19], along with the results from their own computational model (added lines).

Studies spanning the Fe-Pd diagram are available documenting both the lattice constants and magnetic properties of the BCC, FCC, $L1_0$ and $L1_2$ phases of the alloy as a function of composition [35, 36]. A comprehensive study of the diffusion behavior of both the Fe and Pd species across all alloy compositions has also been published [37].

1.2.2 – The $Fe_{38.5}Pd_{61.5}$ Eutectoid Region

The experimental phase diagram presented in previous section (Figs. 8 and 9) shows a great deal of uncertainty in the region below the FCC $\rightarrow L1_0 + L1_2$ eutectoid at 61.5 at % Pd. A closer look at the experimental diagram can be made, centering on the eutectoid region (Fig. 1).

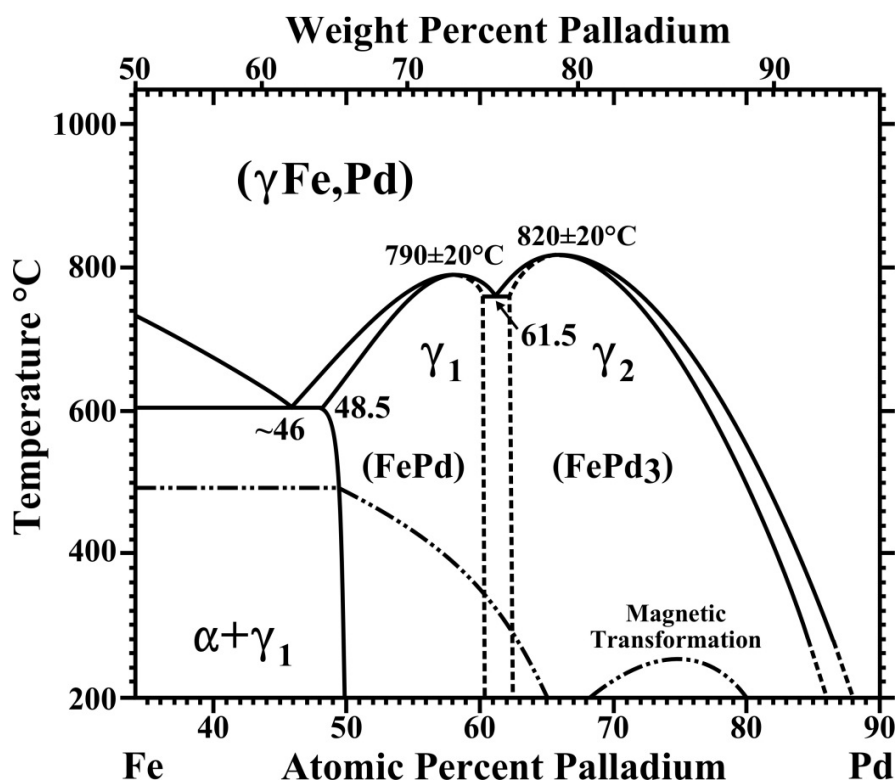


Fig. 1 (Repeated) – Partial experimental phase diagram of the Fe-Pd material system [10]. Of special note is the eutectoid decomposition located at $Fe_{38.5}Pd_{61.5}$ from the disordered FCC γ phase to the $\gamma_1 - L1_0 (FePd)$ and $\gamma_2 - L1_2 (FePd_3)$ ordered phases. The uniformly dashed lines in the diagram represent uncertain boundaries in the experimental phase diagram; the broken lines represent the magnetic transformation temperature.

One of the most distinctive features of the Fe-Pd eutectoid region is that the congruent temperatures for both $L1_0$ and $L1_2$ types of ordering do not fall, as would be normally expected, on the stoichiometric FePd and FePd₃ compositions. This shift in the congruent ordering temperatures is attributed to multi-body or magnetic interactions, as the magnetic contribution to the free energy of the system is expected to be relatively large [38]. The Curie temperature, above which the material changes from a ferromagnetic to paramagnetic state, is established for the alloy from a number of studies [28, 30, 34, 39, 40] and has a maximum value at 50 at % Pd. $L1_0$ type ordering is suggested to lead to a decrease in the magnetic transformation temperature compared to disordered FCC, starting small and diverging toward the eutectoid composition [28, 30, 34]. The magnetic transformation temperature of $L1_2$ reaches a maximum at 75 at % Pd, which is stoichiometric FePd₃.

Enthalpies of formation for the FCC based phases of the system have been calculated, with the prediction that both $L1_0$ and $L1_2$ have enthalpies of formation in the territory of -0.004 Ry/atom. The enthalpy of ordering (ΔH_f : disorder \rightarrow order), however, is much greater for $L1_0$ than $L1_2$, as the enthalpy of formation for FCC drops from 0.004 Ry/atom to -0.001 Ry/atom between the Fe₅₀Pd₅₀ and Fe₂₅Pd₇₅ compositions [41]. Several studies concerning phonon dispersion curves, lattice constant modeling as a function of temperature, and calculated migration enthalpies are also available for stoichiometric FePd and FePd₃ [42-47]. Of particular interest are two papers that present computational phase diagrams for the Fe-Pd system modeled from select experimental thermodynamic data, which may yield further insights into the alloy's behavior [19, 48]. Both of these models predict an inflection of the $L1_0 + L1_2 \rightarrow L1_2$ phase boundary back to 70-71 at % Pd at 300°C. This type of phase boundary inflection is a known feature of all phase diagrams with ordered constituents, as thermodynamics at 0 K dictate that all

ordered phases must be present as stoichiometric line compounds to minimize entropy; however it will generally occur only at cryogenic temperatures. Both diagrams also experience a shift in their eutectoid composition closer to 65 at % Pd and a broadening of their $L1_0 + L1_2$ two phase region. While both diagrams differ significantly from the experimental phase diagram presented in Fig. 8, namely in behavior below the ordering transition, they are remarkably similar to each other (Fig. 10).

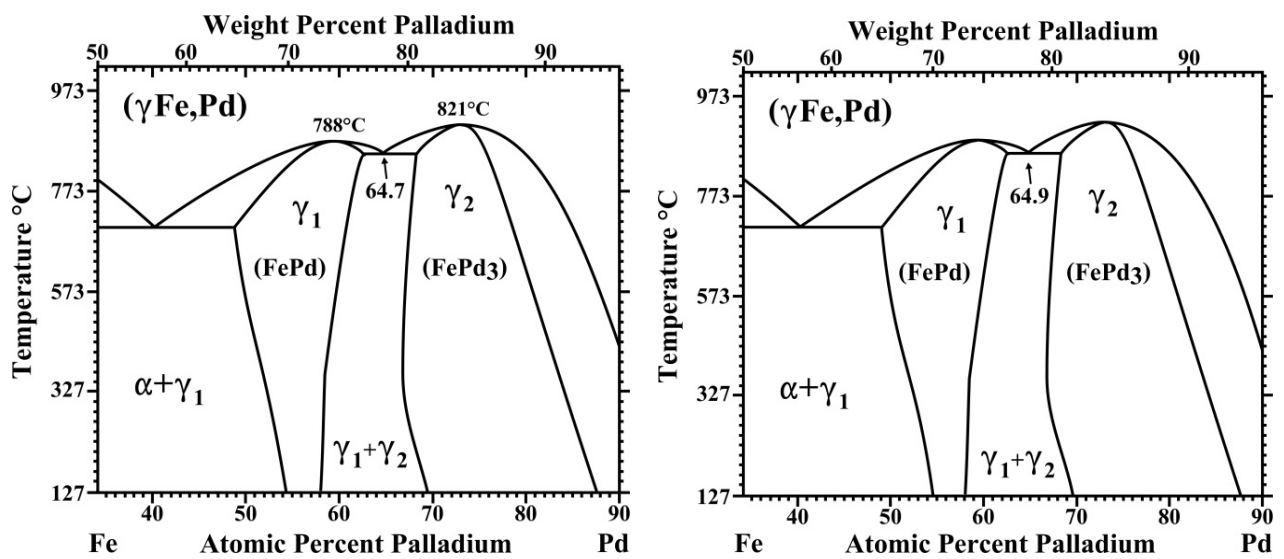


Fig. 10 – Computational phase diagrams (Left) [19] and (Right) [48] created by fitting select experimental thermodynamic data. Notable changes from the experimental diagram include a shift in the eutectoid composition and a broadening of the $L1_0 + L1_2$ two-phase region.

Extensive modeling of the technologically relevant FePd phase has been performed from first principles by two academic groups using cluster variation methods. Mehaddene *et al.* [42, 43, 49-51] focused their work primarily on pair potentials and migration energies within the system. Mohri *et al.* [41, 52-55], in contrast, closely address the ordering dynamics of the system and analyze the contribution made by the tetragonal distortion, presenting a modeled diagram of the $L1_0$ ordering transition. In this model, non-optimal tetragonality of the FePd

phase is shown to require an exponentially increasing contribution to the configurational energy [41]. The group was able to reproduce the order transition temperature from first principles using both cluster variation methods and separately with Lennard-Jones pair potentials [38]. Despite this success, in both cases the composition of congruent ordering was at 50 at % Pd instead of the non-stoichiometric experimental value. This shift was attributed to the unaccounted magnetic energy contribution to the system. The magnetic anisotropy of 3d-4d/5d $L1_0$ alloys have been modeled, including FePd, from spin orbit interactions using local spin density approximations [56]. Vacancy movement in FePd has also been reconstructed using molecular dynamics, showing that diffusion should not disrupt long range order in the alloy [57].

Additional sources concerning the Pd-rich side of the eutectoid, including the ordered FePd₃ phase, are limited. Phonon dispersion curves and modeled pair potentials are available for both FePd₃ [58] and Pd-rich (> 90 at %) FCC [59], as well as data on the electronic structure of FePd₃ [60]. The magnetic behavior of both the ordered $L1_2$ and disordered FCC across the 70 to 100 at % Pd region has been directly measured [61], as well as modeled for FePd₃ [62]. $L1_2$ type ordering is not expected to significantly impact the lattice parameters of the system.

1.2.3 – Studies Approaching the Eutectoid Composition

There are a handful of studies of $L1_0$ Fe-Pd in the 57 to 60 at % Pd range that provide the closest data points published to date near the eutectoid two-phase field. One of these is the only known study to show a coexisting mixture of the $L1_0$ and $L1_2$ phases for Fe-Pd [63]. This mixture was created by depositing Pd followed by Fe onto NaCl substrates, creating 10 nm nanoparticles of approximately 58 at % Pd on average. The resulting nanoparticles were two-phase in nature and consisted of a Pd-rich $L1_2$ core and Fe-rich $L1_0$ outer shell. The core-shell structure of the particles was attributed to the order of elemental deposition and the limited

annealing time of the particular study (10 min), rather than resulting from an equilibrium two-phase field. Similar nanoparticle depositions by the same authors with longer annealing times, also centered about 58 at % Pd averages, have yielded particles of only the $L1_0$ phase [64-67]. These studies provide a picture of how the Pd saturated $L1_0$ phase will behave magnetically at the nanoscale. The nanoparticles in these studies were deposited at low temperatures, forming in the disordered FCC phase, and subsequently annealed; the increased kinetics available at higher temperatures allowing for transition into the ordered $L1_0$. For $\sim\text{Fe}_{42}\text{Pd}_{58}$ particles undergoing annealing, ordering was found to begin around 500°C (1 hr) and to fully complete at 600°C (1 hr). Of great importance to the findings later in this thesis, the 10 nm $\text{Fe}_{42}\text{Pd}_{58}$ nanoparticles reach a coercivity of 3000 Oersted upon fully ordering to $L1_0$. Another study reports $\text{Fe}_{43}\text{Pd}_{57}$ 3 nm nanoparticles (likely aggregated into larger clusters) grown by wet chemistry exhibiting a similar ordering transition temperature range and coercivities above 1200 Oersted [68]. The closest study to the $\text{Fe}_{38.5}\text{Pd}_{61.5}$ eutectoid is based on the *in situ* neutron diffraction of heated nanocrystalline powders, including the $\text{Fe}_{40}\text{Pd}_{60}$ composition [69].

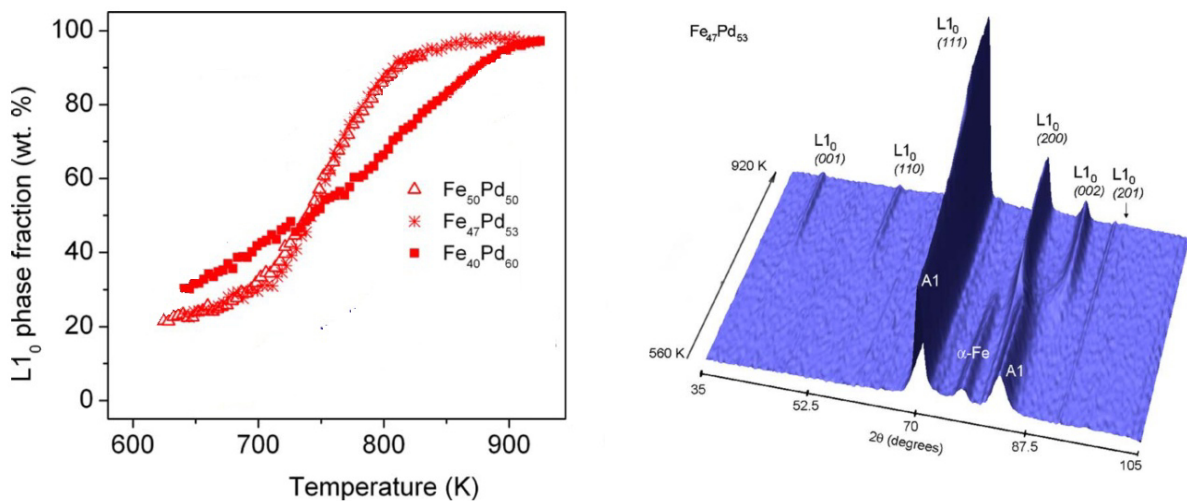


Fig. 11 – Select data from Ref. 69. Ordering to the $L1_0$ phase at several Fe-Pd compositions is shown as a function of temperature (Left) as determined by neutron diffraction (Right).

This study shows that the Fe₄₀Pd₆₀ has a notably slower ordering transition than compositions nearer to the stoichiometric FePd; completing closer to 625°C than 525°C and lacking a distinct onset (Fig. 11). Neutron diffraction can also provide additional information on the magnetic moment of Fe atoms in a sample and confirms that at Fe₄₀Pd₆₀ the alloy undergoes a magnetic transformation beginning at 250°C and completing at 325°C [69], agreeing well with the experimental phase diagram.

1.2.4 – Effects at Fe-rich Compositions

Much of the literature on Fe-Pd concerns the Fe-rich $\alpha + L1_0$ region of the diagram and it would be negligent to review the system without briefly addressing some of the phenomena found at these compositions. One cluster of active study centers on formation of exchange spring magnets of the magnetically soft α -Fe and hard L1₀ phases [70-74]. This requires a fine microstructure of the two phases, allowing for magnetic coupling of the Fe-rich α phase, which has a high saturation magnetization, with the high coercivity of the anisotropic L1₀ to produce a large magnetic energy product.

Near the FePd composition, ordering has been found to result in a very distinct polytwinned microstructure [1, 5, 75-79]. In this morphology macrotwins are themselves comprised of a series of {110} microtwins, with the alternation of the L1₀ tetragonal c-axis serving to relieve strain that would otherwise build during ordering (Figs. 12 & 13). The coercivity of the polytwinned FePd microstructure is relatively low despite its fine structure, for while it contains a high density of anti-phase and twin boundaries, neither of these features provides a strong retarding force on magnetic domain wall motion [1]. Heavily cold working and subsequently annealing the alloy below the critical ordering temperature results in concomitant recrystallization and L1₀ ordering, avoiding the polytwinned morphology. This fine, essentially equiaxed, microstructure of L1₀ crystallites provides a higher density of domain pinning sites and has an accompanying eightfold increase in coercivity [75].



Fig. 12 – Select data showing both the micro and macrotwins of the polytwinned microstructure of FePd [76]. A) Scanning electron backscattered electron micrograph, B) Multibeam bright field transmission electron micrograph, C) Illustration of the alternating tetragonal c-axes for the microtwins of the structure.

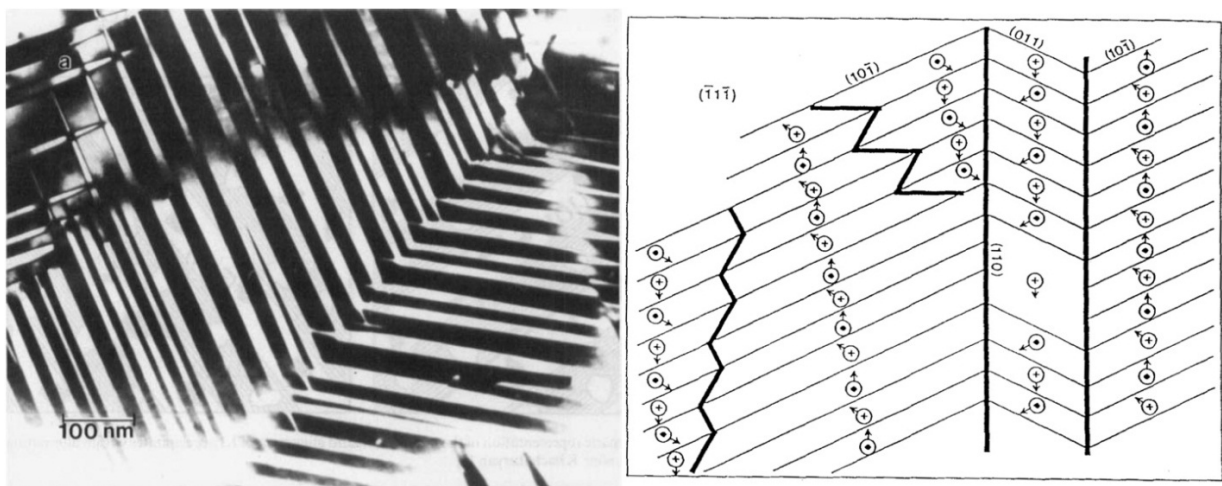


Fig. 13 – A closer look at the microtwins of a polytwinned microstructure of FePd by transmission electron micrograph (left) [77], along with a schematic of the magnetic domain configuration where arrows represent the magnetization vectors (right).

The last major grouping of studies concerns the Fe₇₀Pd₃₀ composition, which has been shown to exhibit phenomena ranging from vanishing thermal expansion to shape memory alloy behavior [80-89]. The INVAR effect that leads to negligible thermal expansions across a certain temperature range, classically observed in the Fe-Ni system, originates from strong magneto-

volumetric coupling in the material; resulting in a sizable negative magnetic contribution to the thermal expansion that is large enough to offset the positive phonon contribution for relatively low temperatures [87]. The shape-memory effect of the $\text{Fe}_{70}\text{Pd}_{30}$ alloy results from a diffusionless structural transformation from the high temperature FCC phase to a lower temperature, lower symmetry martensitic phase, which importantly has multiple variants with their own specific shape changes [88]. As the alloy is ferromagnetic, it is possible to affect its microstructure by applying an external magnetic field. For low-anisotropy ferromagnetic shape-memory alloys, applied fields result in conventional magnetostriction, i.e. rotating the magnetization direction with respect to the magnetic easy axis of the lattice, which does not force a phase change and requires relatively little energy [90]. In the case of $\text{Fe}_{70}\text{Pd}_{30}$, a magnetic field can physically rearrange the variants of martensite, known as the Ferromagnetic Shape-Memory Effect (FSME), resulting in large strains [89, 91]. This requires a high mobility of twin interfaces between the variants and large anisotropies to constrain the magnetization to an easy axis. The difference between these two mechanisms is illustrated in Fig. 14.

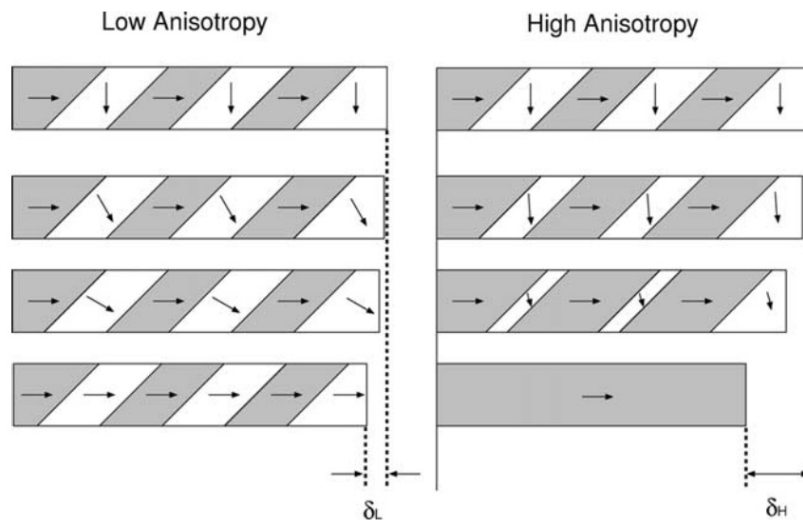


Fig. 14 – Schematic drawing of magnetostriction (left) and FSME (right) as the magnetic field increases from top to bottom [88]. Arrows represent the magnetic easy axis of each region. $\text{Fe}_{70}\text{Pd}_{30}$ composition will follow the FSME behavior, which requires more energy for transformation but results in larger physical changes ($\Delta l \approx 0.6\%$) [88].

1.3 – Related Material Systems

Given the sparse literature available for the Fe-Pd alloy near the eutectoid composition it is worth conducting a brief review of several related systems. This will be limited for conciseness to an analysis of their phase diagrams and special observations on the microstructure of eutectoid Co-Pt. Further references to these systems, however, will appear in greater detail throughout each chapter in relation to specific discussions.

1.3.1 – The Au-Cu System

The Au-Cu system serves as the archetypal FCC-based ordered system, exhibiting both the $L1_0$ (AuCu) and two $L1_2$ ($AuCu_3$, Au_3Cu) ordered phases. Review literature for Au-Cu is available covering experimental and computational approaches [92, 93], which are both in close agreement. Only the $AuCu_3$ phase of the system is considered to be prototypical of $L1_2$ behavior, due to uncertainties concerning portions of the Au_3Cu region, therefore AuCu- $AuCu_3$ is the relevant eutectoid for study in relation to $Fe_{38.5}Pd_{61.5}$ (Fig. 15). Studies on this eutectoid [94, 95] place it at 64 at % Cu and, while establishing the likelihood of a eutectoid based on the convergence of the FCC + $L1_0$ and FCC + $L1_2$ lines, they make no distinct reference to the microstructure underneath it or direct confirmation of the two-phase field. One older study makes some attempt at phase identification at lower temperatures but, unable to detect the co-existence of the $L1_0$ and $L1_2$ phases, concluded that if a two-phase field existed beneath the eutectoid it must be very narrow [96]. Some of this may be attributed to the relatively low ordering transition temperatures for the Au-Cu system compared to Fe-Pd, Fe-Pt, or Co-Pt. In combination with what may be a low driving force near the eutectoid composition for a transition between the two ordered phases, the temperature range of the order-disorder transition dramatically limits the available rates of diffusion for the ordered phases of Au-Cu [94]. If one

of the ordered phases is nucleated first it may therefore come to dominate the system metastably, even if the alloy exists in a two-phase equilibrium field. Both AuCu and AuCu₃ experience congruent ordering at their stoichiometric compositions.

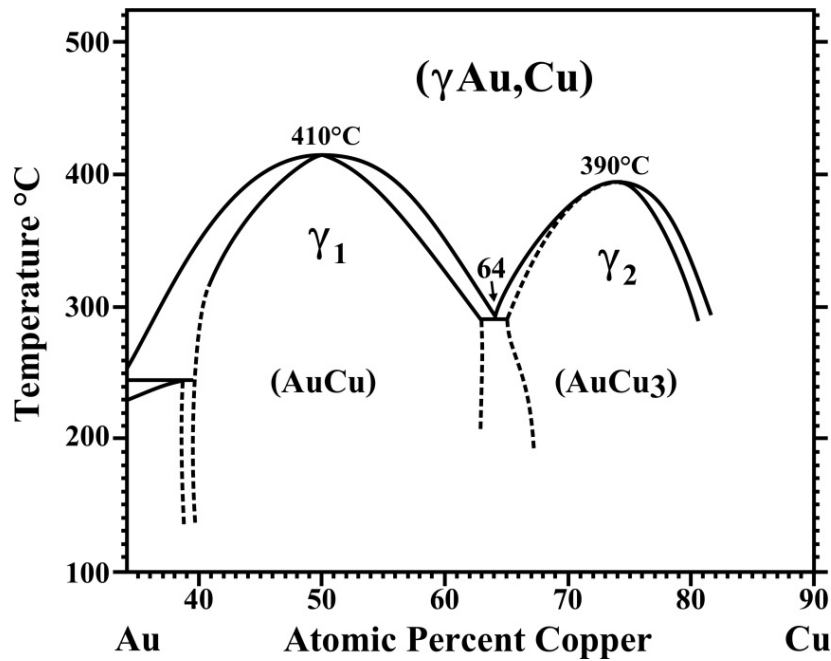


Fig. 15 – Partial experimental phase diagram of the Au-Cu material system near the relevant eutectoid [92]. The uniformly dashed lines in the diagram represent uncertain boundaries in the experimental phase diagram, notably bounding the two-phase $L1_0 + L1_2$ region of concern.

1.3.2 – The Fe-Pt System

The Fe-Pt system is the most studied of the three ordered systems with strong magnetic properties, due to its high magnetocrystalline anisotropies, and exhibits an $L1_0$ FePt, $L1_2$ FePt₃, and at least a metastable $L1_2$ Fe₃Pt phase. The phase diagram of Fe-Pt, however, is highly tentative as there are large disagreements between studies. One of the most widely cited Fe-Pt diagrams is presented at its $L1_0$ - $L1_2$ eutectoid in Fig. 16 [10]. The two-phase field below the eutectoid presented in this particular diagram experiences a notable strong linear shift with temperature toward Pt-rich compositions.

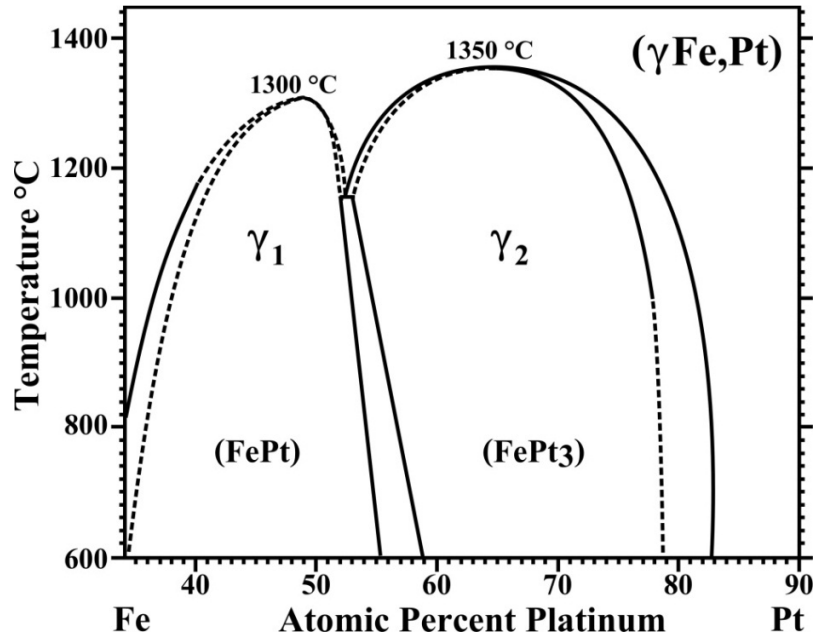


Fig. 16 – Partial experimental phase diagram of the Fe-Pt material system near the relevant eutectoid, from the source most widely cited in literature [10]. The uniformly dashed lines in the diagram represent the large number of uncertain boundaries.

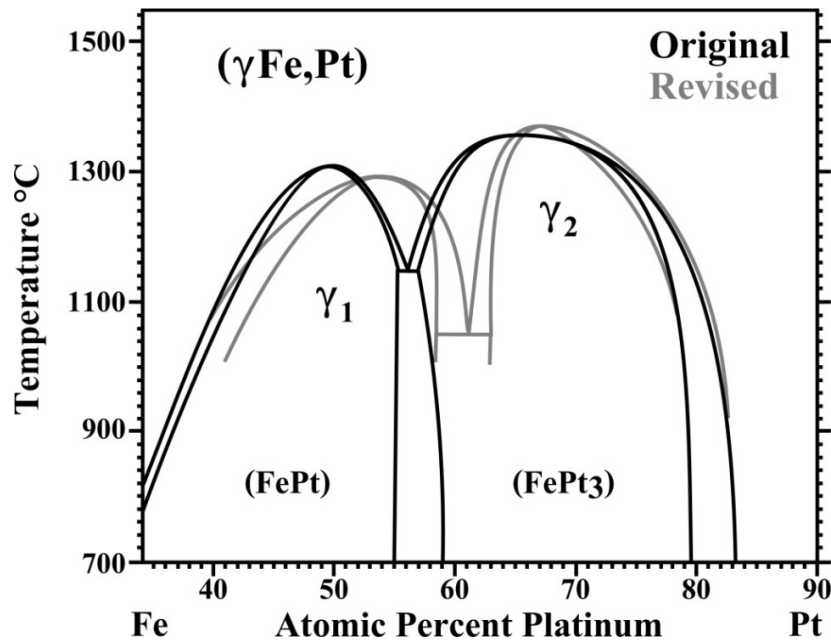


Fig. 17 – Partial experimental phase diagrams of the Fe-Pt material system near the relevant eutectoid from more recent sources. Okamoto's original [97] diagram is close to Fig. 16 in form excluding directly beneath the eutectoid. The revised diagram [98] becomes more similar to the Fe-Pd diagram seen in Fig. 1, especially in the location of the eutectoid.

A more recent phase diagram, presented by Okamoto in 1993 [97] and revised in 2004 [98], is closer in character to the other related systems (Fig. 17). The most recent revision shifts the congruent temperature of $L1_0$ away from the stoichiometric FePt and the diagram starts to resemble that presented for the Fe-Pd system (Fig. 1). Review papers are available covering the contradictory experimental results and history of the diagram in further detail [97-100]. No report or direct observation of an FePt-FePt₃ bulk microstructure has been made.

1.3.3 – The Co-Pt System

The Co-Pt system shares the same desirable $L1_0$ magnetic properties of Fe-Pd and Fe-Pt alloys and has the distinction of having published microstructural results for the $L1_0 + L1_2$ phase region below its eutectoid. The exact form of the Co-Pt phase diagram is a matter of open debate. Many older diagrams confirm the presence of an $L1_0$ phase, and a possible $L1_2$ region is only penciled in [10, 101]. Some newer studies have suggested diagrams that include a eutectoid, but agree on little other than the general form of the diagram; demonstrated by the competing diagrams in Fig. 18 [42, 102, 103].

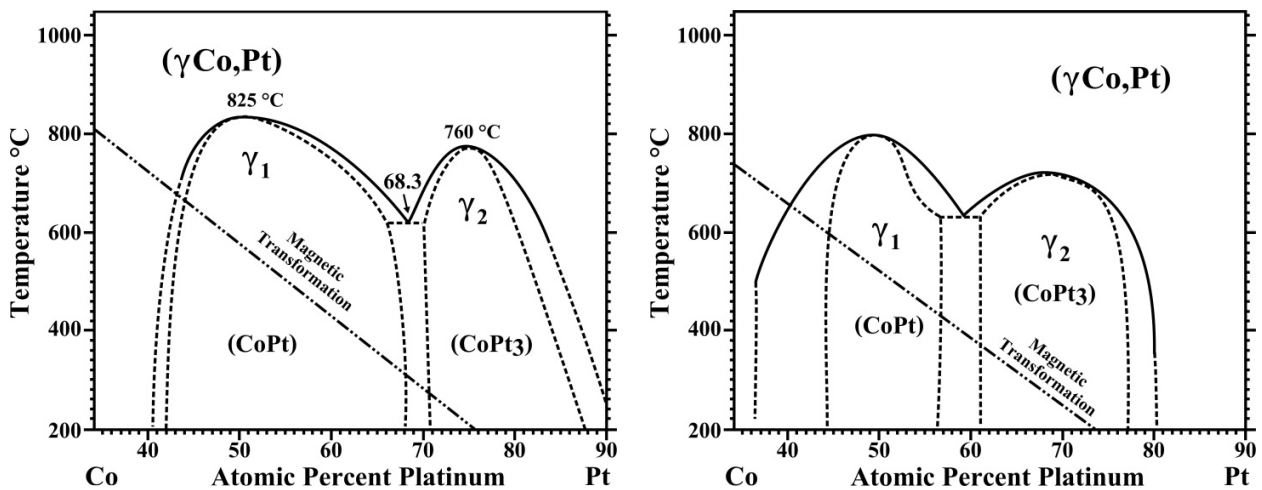


Fig. 18 – Partial experimental phase diagrams (Left) [102] and (Right) [42] of the Co-Pt material system near the relevant eutectoid, showing disagreements in all but the general form.

One particular study presents a partial phase diagram of the Co-Pt eutectoid that can be taken as particularly reliable, having been verified by high resolution transmission electron microscopy and directly observing a two-phase $L1_0 + L1_2$ structure (Fig. 19) [104]. The authors of this study take care, however, to note the diagram's approximate nature as chemical inhomogeneity and damage from ion milling could not be fully avoided.

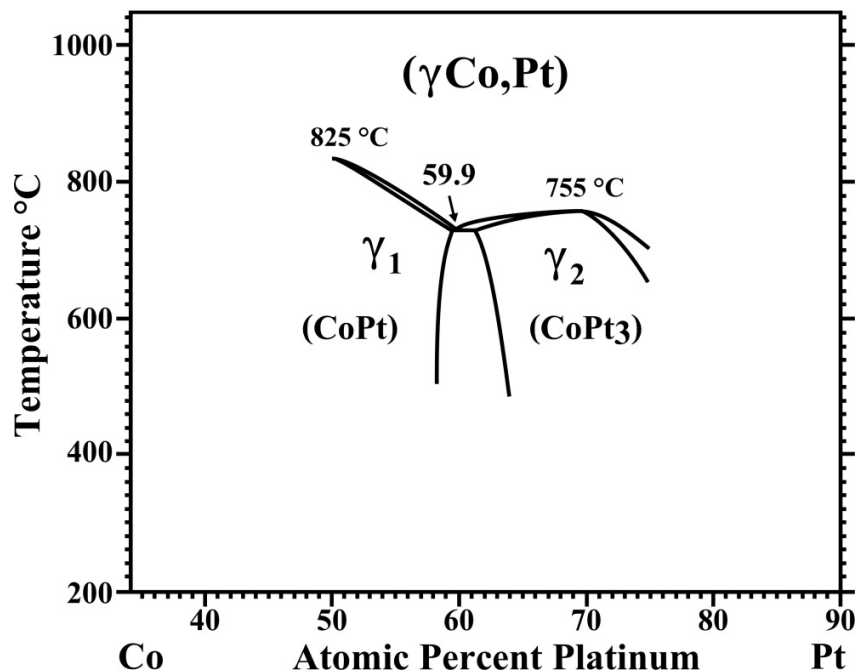


Fig. 19 – Partial experimental phase diagram of the Co-Pt material system near the relevant eutectoid, verified by high resolution transmission electron microscopy [104].

The Co-Pt microstructure produced in the $L1_0 + L1_2$ region is novel and consists of a chessboard like pattern of $L1_2$ and alternating variants of $L1_0$ oriented along the $\langle 100 \rangle$ directions of the $L1_2$ phase (Fig. 20) [12, 13, 104]. This microstructure is reached as the alloy attempts to optimally relieve coherency strain caused by the tetragonal $L1_0$ phase forming within a cubic matrix, and this mechanism has been successfully modeled for the system (Fig. 21) [12]. The original high resolution transmission electron microscopy work on this structure is particularly convincing and, though not reproduced here, deserves special mention [104].

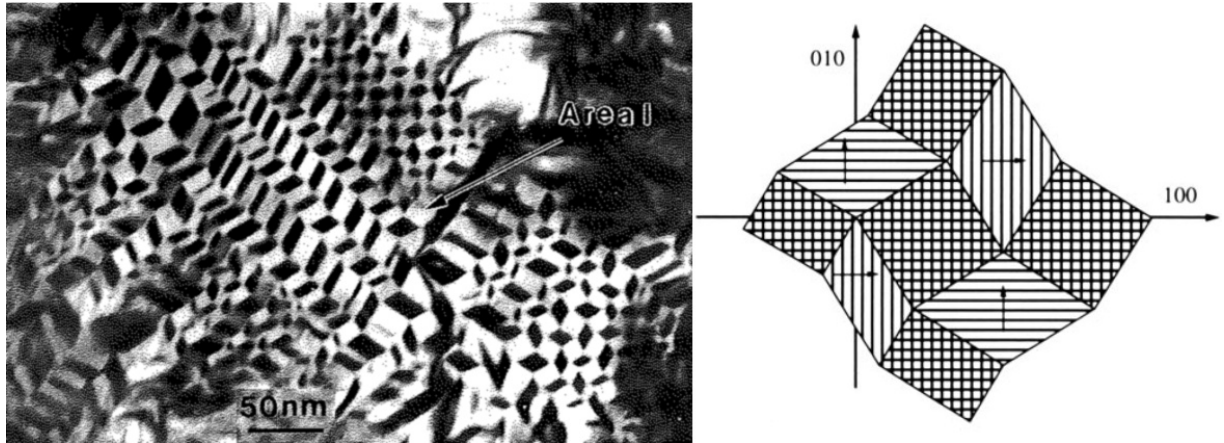


Fig. 20 – Dark field transmission electron micrograph highlighting the $L1_2$ phase ($L1_0$ dark) of the Co-Pt chessboard microstructure, along with a schematic of the phase orientations [104].

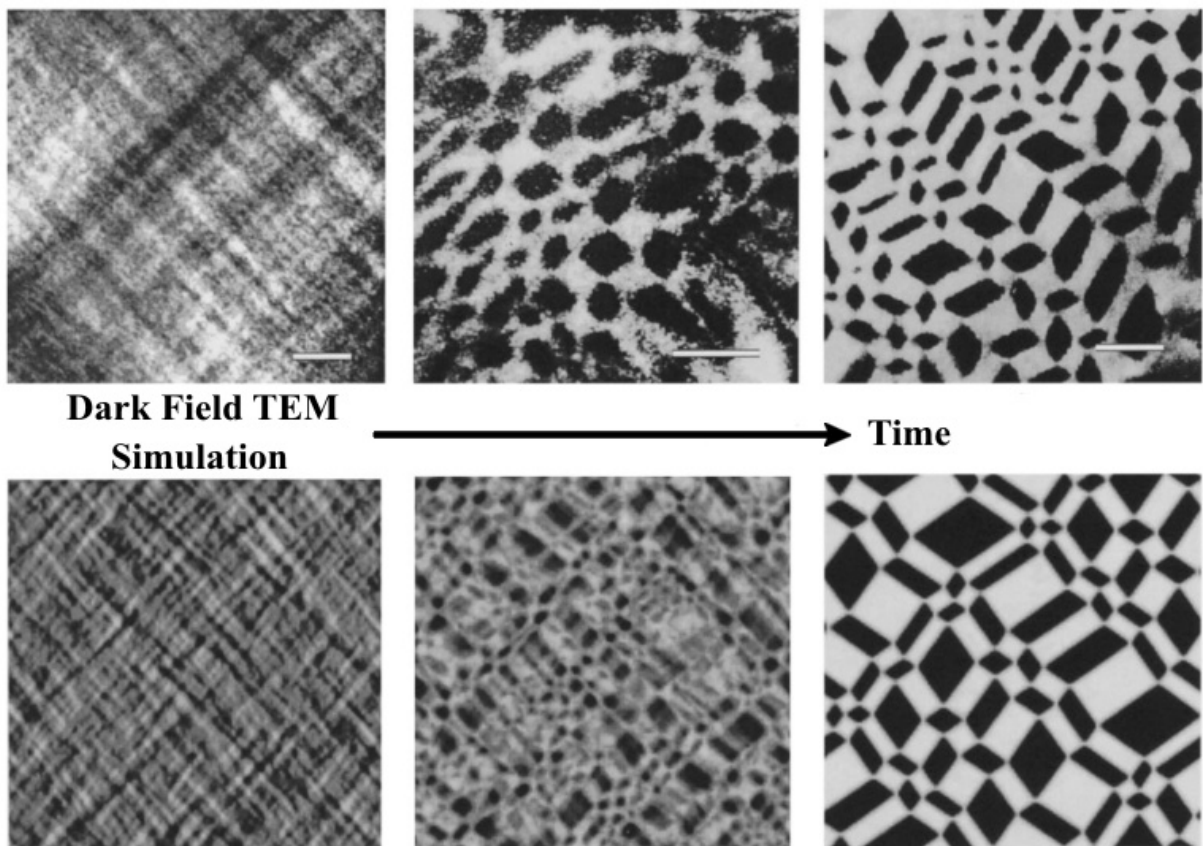


Fig. 21 – Dark field transmission electron micrographs highlighting the $L1_2$ phase ($L1_0$ dark) of the Co-Pt chessboard microstructure as series of annealing time, along with a simulated dark field contrast pattern [12]. The “tweed” contrast in the images on the left is indicative of coherency strain in the micrograph.

Chessboard microstructures induced by coherency strain have been found in several other metallic alloys that experience a two-phase decomposition into cubic and tetragonal/hexagonal phases; including AuCu-Pt/Ag [105], $(\text{Ti,Nb})_3\text{Al}$ [106] and NiFe [107]. Consequentially there is a distinct possibility that chessboards could be produced as the eutectoid microstructure of the Fe-Pd system. Columnar chessboard structures have been observed to form via the same coherency mechanism in ceramic oxide films (Fig. 22), raising the possibility that metallic systems that exhibit chessboards in the bulk could also be grown in a similar manner [14].

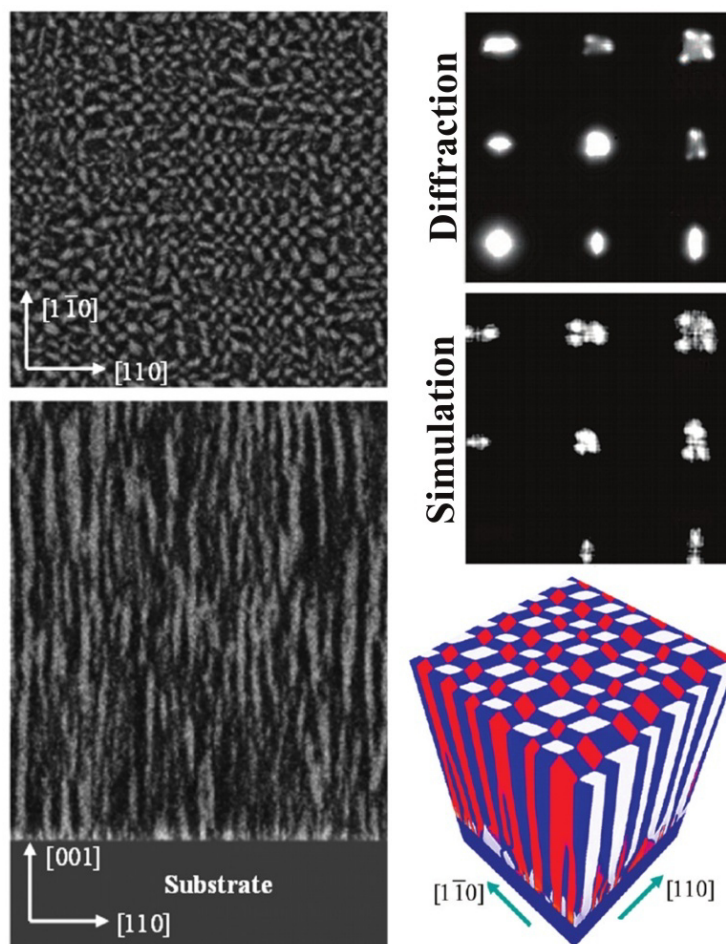


Fig. 22 – Simulated columnar chessboard microstructure matching the diffraction spectra of a ZnMnGaO_4 thin film [14]. It may be possible to grow similar films from metallic systems that exhibit the chessboard microstructure in the bulk.

1.4 – Pulsed Laser Deposition

The Pulsed Laser Deposition (PLD) technique was first used to deposit films in 1965 [108] but came into being as a field of study in the early 1980s [109, 110] and was popularized later in the later in the decade after it was used to successfully deposit some of the first viable Type II superconducting thin films [111]. At its core the technique consists of a pulsed, generally ultraviolet, laser that is focused onto a solid target inside a vacuum chamber, resulting in ablation from the target's surface and the transfer of energetic species to a substrate (Fig. 23). Two broad books have been written concerning the process and applications of PLD [112, 113].

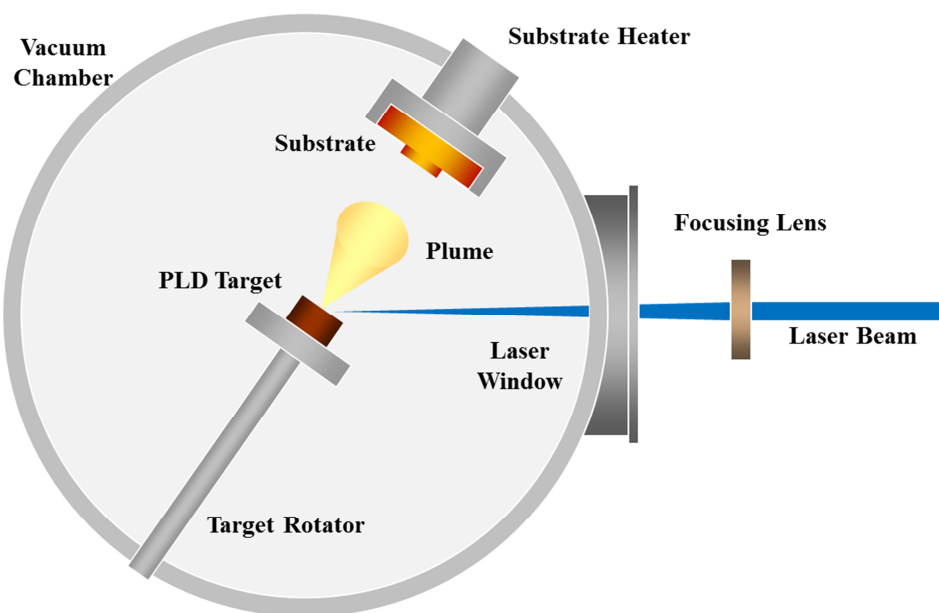


Fig. 23 – Illustration of a typical PLD experimental setup. An ultraviolet laser is focused onto a rotating target inside a vacuum chamber, leading to heating/ablation and formation of a forward directed plasma plume with sufficient momentum for material to reach a heated substrate.

The choice of ultraviolet wavelengths comes from the high absorption coefficients of most materials in the ultraviolet region, stemming from the photon energy (~ 5 eV) being on the order of typical bond energies. Pulses are generally chosen to be of nanosecond length scale so that

energy from the laser is thermally confined to the near surface region, leading to the explosive vaporization of a small material volume rather than bulk evaporation. The target is usually rotated between pulses to avoid compounding topographical changes to the target surface, which are known to alter both the effective fluence (energy per area) and the types of ejected species.

The ablated material results in the formation of a forward distributed plasma plume which consists of a mixture of excited ions, nanoclusters, nanoparticles, and micro-scale particles that result from ejected topographic features or melted drops from the target surface. The density and shape of this plume, and the nanoparticles that form within the plume during flight, can be controlled through the use of background gases of different molecules and pressures. Typically inert gases such as Ar, Ne, He are used for depositions, but reactive gases such as O₂ allow for the ready creation of oxide films. Material in the plume eventually arrives at a substrate, which is usually heated to enable faster diffusion kinetics. Much of the material arriving to the substrate is still in an ionic or kinetically excited state, and arrives suddenly as a wave rather than as a continuous flux, resulting in films grown from PLD often possessing different properties than similar films grown through other deposition techniques.

One of the strengths of PLD is that the stoichiometry of material deposited is often preserved from the target material, largely responsible for its success with complex superconducting oxides such as YBa₂Cu₃O_{7-x}. This makes PLD a well suited choice for studies involving single, exact compositions as many films can be created from one bulk target; without deposition parameters introducing variability in film stoichiometry.

1.5 – Fe-Pd Thin Films in Literature

Much of the technological interest in Fe-Pd as a system comes in the form of nanoscale magnetic applications. These require large magnetocrystalline anisotropies (K) to overcome the

superparamagnetic limit at small volumes (V), where thermal fluctuations in the sample can randomly change the magnetic state over the Néel relaxation time

$$\tau(ns) = \exp\left(\frac{KV}{k_bT}\right) \quad (1)$$

A magnetic data storage device with a lifetime of ten years will require a factor of at least 35 inside the exponential of Eq. 1. This allows for a minimum theoretical device grain diameter of 5 nm for FePd [114], which is the approximate minimum onset size for ordering behavior found in FePd nanoparticles [115]. The corrosion resistance of Fe-Pd alloys is especially desirable in conjunction with these small scales [116].

Fe-Pd thin films have been grown using a number of deposition techniques, including Molecular Beam Epitaxy (MBE) [116-139], PLD [140-143], sputtering [118-120, 144-154] and electrochemistry [155-157]. During deposition onto Si/SiO₂ substrates [116-120, 140, 144-148] films tend to grow with random crystallographic orientation, favoring low energy {111} planes, though strain induced by thermal mismatch during cooling can be used strategically to impart a (001) preferential texture of the L1₀ c-axis out of the plane [146, 147], as can the deposition and annealing of multilayer structures [148]. Epitaxial films of Fe-Pd have been grown using MgO substrates directly [118-126, 141, 142, 149-152], or on top of Cr [127-136], Au [137], Pd [134-136, 137, 158], and Pt [139, 154] seed layers; all of which help mitigate mismatch in lattice parameters between the film and substrate. Fe-Pd in FCC-based phases has been shown to align Fe-Pd(001)[010] || MgO(001)[010] on MgO (001) substrates [123, 124, 149-151], while the body centered α phase of the alloy aligns with a 45° rotation BCC(001)[110] || MgO(001)[010] [142]. The FCC-based phases of the system have also been found to grow epitaxial on other orientations of MgO so that Fe-Pd(110)[001] || MgO(110)[001] and Fe-Pd(111)[$\bar{1}\bar{1}0$] || MgO(111)[$\bar{1}\bar{1}0$] [150, 151]. The light tetragonality of L1₀ FePd introduces only a small wrinkle

into these orientation relationships, aligning the *c*-axis preferentially out of the plane for MgO (001) but aligning randomly on MgO (110) and MgO (111) so that they produce four and eight possible $L1_0$ variants respectively. It is also expected that Fe-Pd will grow epitaxially on NaCl substrates, though this has only been confirmed by the growth of cube-on-cube nanoparticles and not films [63-67, 159]. Most films in the literature are being grown explicitly for their $L1_0$ magnetic properties, but there is pursuit to achieve shape-memory properties at the $Fe_{70}Pd_{30}$ composition [117, 122, 141, 142, 145, 153, 155].

The literature on Fe-Pd thin film growth via PLD is light on deposition specific details. The group able to achieve the highest quality films [141, 142] did so by depositing at room temperature under ultra-high vacuum conditions onto MgO (001), but they did not publish the fluence, number of pulses, deposition time or rate. Additionally, these studies were focused on shape-memory properties so they did not include any data on ordering behavior. In another study, films were deposited at a fluence of 3 J/cm^2 onto Si, though the characterization provided is rudimentary in concern to growth properties [140]. The remaining PLD study produced room temperature films of an aggregated nanoparticulate nature at 9 J/cm^2 , consistent with the very high deposition rates they report. Fluences on the order of 9 J/cm^2 tend to result in non-plasma ejection of material from the target, and the growth of poorer quality films; the optimal PLD fluence for most transition metals being in the range of 2 to 3 J/cm^2 [112, 113].

Thin films generally deposit in the disordered phase of an ordered system and subsequently order, either by depositing at elevated temperatures or post-deposition annealing, with the increased kinetics available approaching the ordering temperature of the material. Nanoscale films are expected to order at lower temperatures than the bulk [160] and FePd nanoparticles are known to be fully ordered by 600°C after an onset of ordering behavior around 400°C [69, 161]. This same 400°C onset / 600°C completion ordering behavior has also been

observed in FePd thin film studies [126, 148]. Ordering behavior is based on kinetics, so it is possible to induce higher degrees of ordering at lower temperatures by using longer annealing times or impacting the rate of diffusion through properties such as microstructure. The choice of MBE onto MgO (001) over sputtering onto Si (001) for the room temperature deposition of FePd films has been shown to result in an earlier onset of ordering during post-deposition annealing, which is suggested to complete closer to 500°C [118-120]. Metallic seed layers on MgO (001) have also been shown to promote *c*-axis L₁₀ ordering [154], and ion bombardment can bring the order temperature as low as 200°C by introducing additional vacancies for diffusion [137].

Several thin film studies include the characterization of epitaxial film morphology as a function of deposition temperature and provide useful background for the films that will be presented as results during this thesis. The most detailed of these tracks the morphology of sputtered FePd on MgO (001), deposited between 25°C and 600°C (Fig. 24) [152].

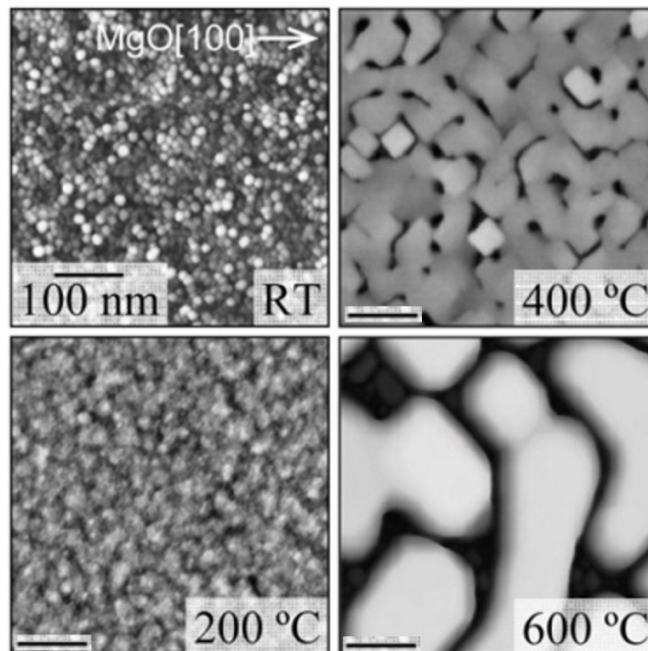


Fig. 24 – Atomic force micrographs of FePd on MgO (001) grown at four different temperatures [152]. Of particular note is the formation of facets along the $\langle 110 \rangle$ directions with the onset of coalescence and island growth modes.

With increasing deposition temperature the film can be seen to transition from a nanoparticulate state limited by diffusion, to a coalesced network or separated islands with clear faceting along the $\langle 110 \rangle$ directions. This results from largely $\{110\}$ facets for the networked film and lower-energy $\{111\}$ facets for the islands, as confirmed by atomic force microscopy.

Another study compares films deposited by MBE at both 400°C and 100°C , the latter of which was annealed post-deposition at 400°C for comparison (Fig. 25) [125]. The films deposited at 400°C grew as faceted islands, while those annealed after deposition formed voids aligned with preferential orientation along two orthogonal axes. The authors claim these directions to be of type $\langle 100 \rangle$ but this is inconsistent their own markings in Fig. 25, and it is unclear from the paper how the direction was determined.

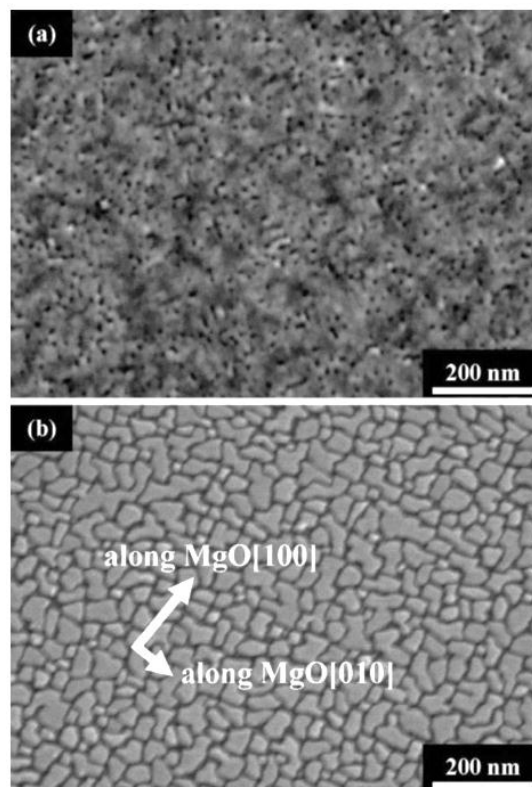


Fig. 25 – Scanning electron micrographs of FePd on MgO (001) (A) grown at 100°C and annealed at 400°C and (B) grown at 400°C [125]. Both show a clear trend for the film to facet along two (somewhat ambiguous) orthogonal directions, possibly $\langle 100 \rangle$ or $\langle 110 \rangle$.

A third study also presents a film morphology with distinct rectangular voids faceted along two orthogonal directions, in this case an $\text{Fe}_{70}\text{Pd}_{30}$ film grown at 630°C by MBE on MgO (001) (Fig. 26) [122]. This film is claimed to be a mixture of the FCC, BCC and L1_0 phases of the system but no diffraction results are presented. It does, however, continue the strong trend of orthogonal faceting behavior of voids and islands of the Fe-Pd system on MgO (001) surfaces.

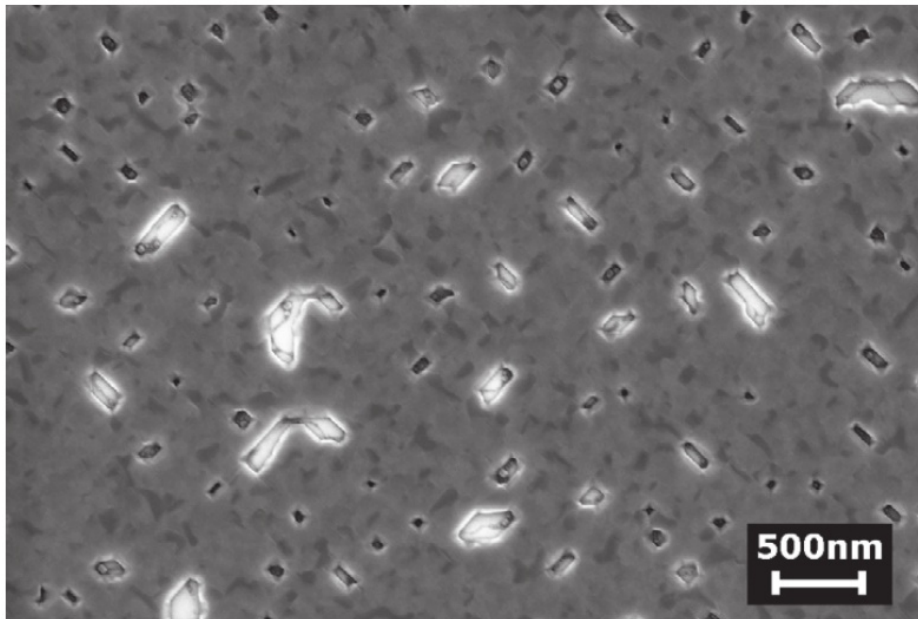


Fig. 26 – Scanning electron micrograph of an $\text{Fe}_{70}\text{Pd}_{30}$ film grown at 630°C by MBE [122] exhibiting strong orthogonal faceting behavior of rectangular voids. The darker rectangles are claimed to be voids that have begun to fill with depositing material, as opposed to the brighter voids which show charging effects from the insulating MgO surface.

These morphologies are specific to the native MgO (001) surface and not epitaxy in general, as 50 nm FePd films grown by MBE at 347°C on 60 nm Pd (001) thin films, themselves grown on MgO (001), exhibit an alternate trend [134-136]. These films form a pattern of 2 nm tall cross-hatched steps on the surface, determined to be the result of $\{111\}$ microtwins extending from the surface all the way into the Pd substrate (Fig. 27). Substrate conditions will be shown in this thesis to play a crucial role in the final morphology of Fe-Pd thin films.

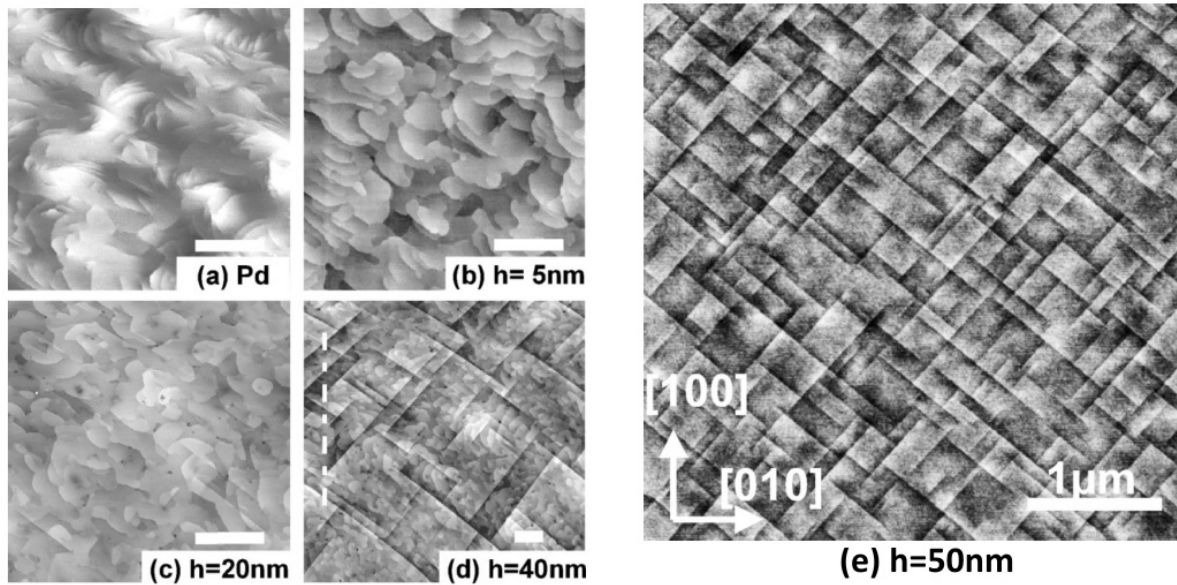


Fig. 27 – Scanning tunneling micrographs (a-d), with 100 nm scale bars, of the Pd surface and 5 to 40 nm FePd thin films, along with an atomic force micrograph of a 50 nm FePd film (e); as presented in Refs. 134-136. Cross-hatching from {111} microtwins is visible on the surface.

The magnetic domain behavior of c-axis oriented FePd films during magnetization has been studied extensively using both magnetic force microscopy [162] and Lorentz transmission electron microscopy [163]. FePd films with weak anisotropy and small film thicknesses prefer to align with a magnetic axis residing in-plane, which transitions out of the plane as the balance between the magnetostatic energy and the energy contributed from the uniaxial anisotropy changes with film thickness [129-132]. The magnetic saturation behavior of low deposition temperature Fe-Pd thin films, presumably BCC/FCC, has been observed across almost the entire compositional range of alloys and is presented in Fig. 28 [30, 116]. $L1_0$ type ordering may lead to saturations up to 30% higher [35, 164], though the strain present in thin films is known to alter the magnetic moments residing on both Fe and Pd atoms in FePd [165]. Magnetic coercivity is more dependent upon the microstructural, ordering, and crystalline properties of each film.

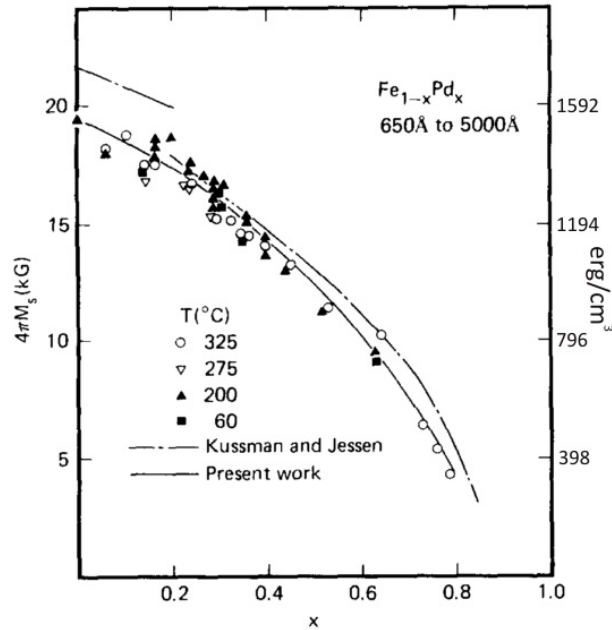


Fig. 28 – Saturation magnetizations of Fe-Pd alloy thin films grown at different compositions as a function of composition [116], superimposed on Kussman’s (sic) bulk data [30]. The magnetization falls with lower Fe concentrations as Fe carries most of the magnetic moment.

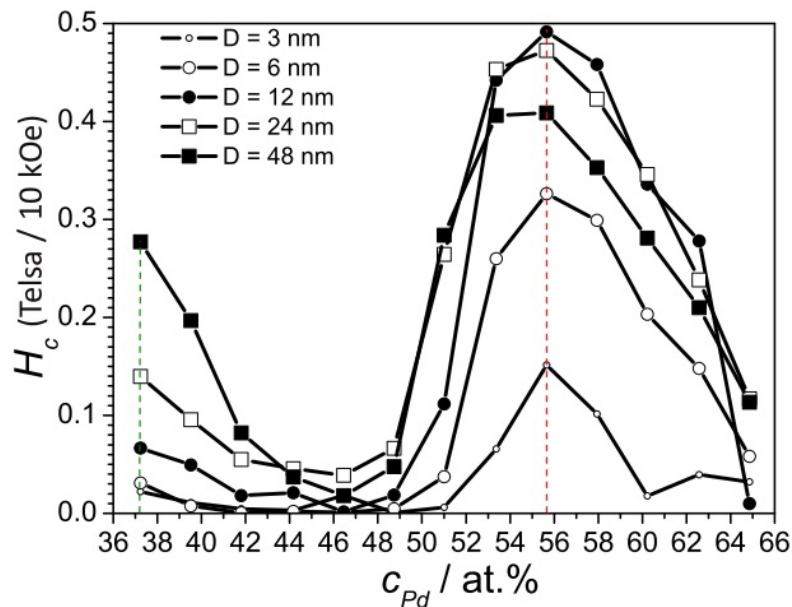


Fig. 29 – Coercivity of Fe-Pd alloy islands of varying diameter (D) as a function of composition [144]. The highest coercivities are found at 56 at % Pd near the congruent ordering composition. Islands approaching the superparamagnetic limit experience a decrease in coercivity, but still maintain hard magnetic properties across the $L1_0$ compositional range.

For FePd films coercivities routinely range between 1 kOe and 5 kOe [118, 120, 121, 125, 144, 146-148, 156]. Coercivity studies as a function of island diameter and composition, of single domain Fe-Pd island forming films annealed at 510°C on Si, provides a reasonable expectation for thin film coercivity behavior (Fig. 29) [144]. Coercivity of L1₀ Fe-Pd can be seen to reach a maximum at about 56 at % Pd, which is much closer to the congruent ordering composition of 58 at % Pd than stoichiometric FePd. Films below 50 at % Pd are two-phase in nature as predicted by the phase diagram, explaining the lower coercivities in the Fe-rich range. Disappointingly, crystallographic analysis was conducted in intervals stopping at 59 at % Pd and was is not presented for the eutectoid region. The island size has a large influence on coercivity for diameters below 12 nm. 3 nm nanoparticles, which may have trouble maintaining long range order, can still register coercivities above 1 kOe. These findings are important in relation to the results presented later in this thesis, where a conspicuous lack of coercivity will be used as supporting evidence.

References

- [1] T. Klemmer, D. Hoydick, H. Okumura, B. Zhang, and W. Soffa, *Scripta Metall. Mater.* **33**, 1793 (1995)
- [2] M. Vlasova, G. Kandaurova, and N. Shchegoleva, *J. Mag. Mag. Mater.* **22**, 138 (2000)
- [3] R. Skomski, A. Kashyap, and J. Zhou, *Scripta Mater.* **53**, 389 (2005)
- [4] D. Laughlin, K. Srinivasan, M. Tanese, and L. Wang, *Scripta Mater.* **53**, 383 (2005)
- [5] B. Zhang, M. Lelovic, and W. Soffa, *Scripta Metall. Mater.* **25**, 1577 (1991)
- [6] M. Rao and W.A. Soffa, *Scripta Mater.* **36**, 735 (1997)
- [7] R. Strnat, *J. Magn. Magn. Mater.* **100**, 38 (1991)
- [8] J. Herbst and J. Croat, *J. Magn. Magn. Mater.* **100**, 57 (1991)
- [9] J. Wang, *Proc. IEEE* **98**, 1847 (2008)
- [10] T. Massalski, H. Okamoto, P. Subramanian, and L. Kacprzak, *Binary Alloy Phase Diagram 2nd ed.* (ASM International, Materials Park, 1990)
- [11] C. Issro, W. Püschl, W. Pfeiler, P. Rogl, W. Soffa, M. Acosta, G. Schmerber, R. Kozubski, and V. Pierron-Bohnes, *Scripta Mater.* **53**, 447 (2005)
- [12] Y. Bouar, A. Loiseau, and A. Khachatryan, *Acta Mater.* **46**, 2777 (1998)
- [13] Y. Bouar and A. Loiseau, *Acta Mater.* **49**, 2679 (2001)
- [14] Y. Ni, W. Rao, and A. Khachatryan, *Nano Letters* **9**, 3275 (2009)
- [15] Strukturbericht, *Zeitschrift für Kristallographie, Kristallgeometrie, Kristallphysik, Kristallchemie*. Utrecht : A. Oosthoek; 1913ff
- [16] W. Pearson, *A handbook of lattice spacings and structures of metals and alloys, vol. 2* (Pergamon Press, Oxford, 1967)
- [17] T. Hahn, *International Tables for Crystallography Volume A: Space-group symmetry*, (International Union of Crystallography, 2006)
- [18] D. Laughlin, K. Srinivasan, M. Tanese, and L. Wang, *Scripta Materialia* **53**, 383 (2005).
- [19] G. Ghosh, C. Kantner, and G.B. Olson, *J. Phase Equilib.* **20**, 295 (1999)
- [20] O. Kubaschewski, *Iron-Binary Phase Diagrams* (Springer-Verlag, Berlin, 1982) p. 88–91
- [21] H. Okamoto, *Phase Diagrams of Binary Iron Alloys* (ASM International, 1993) p 319–325
- [22] W. Gibson and W. Hume-Rothery, *J. Iron Steel Inst.* **189**, 243 (1958)
- [23] A. Grigorjew, *Z. Anorg. Chem.* **209**, 295 (1932)
- [24] J. Tomiska, *Z. Metallkd.* **80**, 888 (1989)
- [25] R. Hultgren and C. Zapffe, *AIME* **133**, 58 (1939)
- [26] V. Kuprina and A. Grigor'ev, *Russ. J. Inorganic Chem.* **4**, 297 (1959)
- [27] E. Raub, H. Beeskow, and O. Loebich, Jr., *Z. Metallkd.* **54**, 549 (1963)
- [28] M. Fallot, *Ann. Phys.* **10**, 291 (1938)
- [29] T. Takezawa and T. Yokoyama, *J. Jpn. Inst. Met.* **45**, 1112 (1981)

- [30] A. Kußman and K. Jessen, *Z. Metallkd.* **54**, 504 (1963)
- [31] R. Hocart and M. Fallot, *Compt. Rend.* **204**, 1465 (1937)
- [32] G. Alaverdov and S. Shavlo, *Zh. Tekh. Fiz.* **9**, 211 (1939)
- [33] E.N. Babnov et al., *Fiz. Met. Soedin.* **6**, 3 (1978)
- [34] T. Takezawa, T. Miwa, and T. Yokoyama, *J. Jpn. Inst. Met.* **51**, 285 (1987)
- [35] E. Burzo and P. Vlais, *J. Optoelectronics Adv. Mater.* **12**, 1869 (2010)
- [36] S. Zhang, K. Sumiyama, and Y. Nakamura, *J. Magn. Magn. Mater.* **73**, 58 (1988)
- [37] J. Fillon and D. Calais, *J. Phys. Chem. Solids* **38**, 81 (1977)
- [38] T. Horiuchi, H. Uzawa M. Igarashi, F. Abe, and T. Mohri, *Calphad* **26**, 3 (2002)
- [39] J. Crangle, *Philos. Mag.* **5**, 335 (1960)
- [40] E. Wollan, J. Cable, W. Kohler, and M. Wilkinson, *J. Phys. Soc. Jpn.* **17**, 38 (1962)
- [41] Y. Chen, T. Atago, and T. Mohri, *J. Phys. Cond. Mat.* **14**, 1903 (2002)
- [42] T. Mehaddene, E. Kentzinger, B. Hennion, K. Tanaka, H. Numakura, A. Marty, V. Parasote, M. Cadeville, M. Zemirli, and V. Pierron-Bohnes, *Phys. Rev. B*, **69**, 024304 (2004)
- [43] T. Mehaddene, M. Zemirli, V. Pierron-Bohnes, M. Cadeville, B. Hennion, A. Marty, I. Schuster, K. Tanaka, and H. Numakura, *Catalysis Today* **89**, 313 (2004)
- [44] A. Al-Ghaferi, P. Müllner, H. Heinrich, G. Kostorz, and J. Wiezorek, *Acta Materialia* **54**, 881 (2006)
- [45] S. Ghosh, *Intermetallics*, **17**, 708 (2009)
- [46] S. Ghosh, *J. Phys. Cond. Mat.* **20**, 275208 (2008)
- [47] T. Ichitsubo and K. Tanaka, *J. Applied Phys.* **96**, 6220 (2004)
- [48] R. Davies, R. Dinsdale, A. Gisby, J. Robinson, and J. Martin, *Calphad* **26**, 229 (2002)
- [49] T. Mehaddene, O. Adjaoud, R. Kozubski, K. Tanaka, H. Numakura, J. M. Sanchez, C. Issro, W. Pfeiler, and V. Pierron-Bohnes, *Scripta Materialia* **53**, 435 (2005)
- [50] T. Mehaddene, *Condensed Matter* **17**, 485 (2005)
- [51] T. Mehaddene, J. M. Sanchez, R. Caudron, M. Zemirli, and V. Pierron-Bohnes, *Eur. Phys. J. B* **41**, 207 (2004)
- [52] T. Mohri, Y. Chen, and M. Ohno, *Materials Science Forum* **479**, 3075 (2005)
- [53] T. Mohri, T. Horiuchi, H. Uzawa, M. Ibaragi, M. Igarashi, and F. Abe, *J. Alloys and Compounds* **318**, 13 (2001)
- [54] T. Mohri and Y. Chen, *Materials Transactions* **45**, 1478 (2004)
- [55] T. Mohri, M. Ohno, and Y. Chen, *J. Phase Equil. Diff.* **27**, 47 (2006)
- [56] I. Solovyev, P. Dederichs, and I. Mertigs, *Phys. Rev. B* **52**, 419 (1995)
- [57] C. Goyhenex, R. V. P. Montsouka, M. Kozlowski, and V. Pierron-Bohnes, *Solid State Phenomena* **129**, 59 (2007)
- [58] W. Stirling, R. Cowley, and M. Stringfellow, *J. Phys. F: Metal Phys.* **2**, 421, (1972)
- [59] B. Dutta and S. Ghosh, *J. Phys. Cond. Mat.* **21**, 395401 (2009)

- [60] C. Kuhnen and E. Silva, *J. Magn. Magn. Mater.* **67**, 260 (1987)
- [61] N. Miyata, K. Tomotsune, H. Nakada, M. Hagiwara, H. Kadomatsu, and H. Fujiwara, *J. Phys. Soc. Jpn.* **55**, 946 (1986)
- [62] B. Dutta, S. Bhandary, S. Ghosh, and B. Sanyal, *Phys. Rev. B* **86**, 024419 (2012)
- [63] K. Sato, J. G. Wen, and J. M. Zuo, *J. Appl. Phys.* **105**, 093509 (2009)
- [64] K. Sato and Y. Hirotsu, *Materials Transactions* **47**, 59 (2006)
- [65] K. Sato, B. Bian, and Y. Hirotsu, *Jpn. J. Appl. Phys.* **39**, 1121 (2000)
- [66] K. Sato, B. Bian, and Y. Hirotsu, *J. Appl. Phys.* **91**, 8516 (2002)
- [67] K. Sato and Y. Hirotsu, *J. Appl. Phys.* **93**, 6291 (2003)
- [68] S. Sharma, N. Gajbhiye, and R. Ningthoujam, *AIP Conf. Proceedings* **1313**, 125 (2010)
- [69] J. Lyubina, O. Gutfleisch, and O. Isnard, *J. Appl. Phys.* **105**, 07A717 (2009)
- [70] N. Sakuma, T. Ohshima, T. Shoji, Y. Suzuki, R. Sato, A. Wachi, A. Kato, Y. Kawai, A. Manabe, and T. Teranishi, *ACS Nano*, **5**, 2806 (2011)
- [71] J. Kawamura, K. Sato, and Y. Hirotsu, *J. Appl. Phys.* **96**, 3906 (2004)
- [72] T. Ichitsubo, S. Takashima, E. Matsubara, Y. Tamada, and T. Ono, *Appl. Phys. Letters* **97**, 182508 (2010)
- [73] T. Schied, a. Lotnyk, C. Zamponi, L. Kienle, J. Buschbeck, M. Weisheit, B. Holzapfel, L. Schultz, and S. Fähler, *J. Appl. Phys.* **108**, 033902 (2010)
- [74] J. Lin, L. Loh, P. Lee, T. Tan, S. Springham, and R. Rawat, *Appl. Surf. Sci.* **255**, 4372 (2009)
- [75] J. Wiezorek, *Materials Science Forum* **543**, 1487 (2007)
- [76] H. Xu and J. Wiezorek, *Acta Materialia* **52**, 395 (2004)
- [77] B. Zhang and W. Soffa, *Physica Status Solidi* **131**, 707 (1992)
- [78] B. Zhang, T. Klemmer, D. Hoydick, and W. Soffa, *IEEE Trans. Magn.* **30**, 589 (1994)
- [79] B. Zhang and W. Soffa, *IEEE Trans. Magn.* **27**, 5328 (1991)
- [80] P. Hong and G. Olson, *J. Magn. Magn. Mater.* **129**, 191 (1994)
- [81] J. Felten, T. Kinkus, A. Reid, J. Cohen, and G. Olson, *Metall. Mater. Trans. A* **28**, 527 (1997)
- [82] M. Sato, B. Grier, S. Shapiro, and H. Miyajima, *J. Phys. F: Met. Phys.* **12**, 2117 (1982)
- [83] H. Seto, Y. Noda, and Y. Yamada, *J. Phys. Soc. Jpn.* **59**, 978 (1990)
- [84] F. Liot and C. Hooley, *arXiv preprint arXiv:1208.2850* (2012)
- [85] R. Stern, S. Willoughby, A. Ramirez, J. MacLaren, J. Cui, Q. Pan, and R. James, *J. Appl. Phys.* **91**, 7818 (2002)
- [86] M. Winterrose, M. Lucas, A. Yue, I. Halevy, L. Mauger, J. Muñoz, J. Hu, M. Lerche, and B. Fultz, *Phys. Rev. Letters* **102**, 237202 (2009)
- [87] P. Mohn, E. Supanetz, and K. Schwarz, *Aus. J. Phys.* **46**, 651 (1993)
- [88] J. Cui, T. Shield, and R. James, *Acta Materialia*, **52**, 35 (2004)

- [89] R. James and M. Wuttig, *Philos. Mag. A* **77**, 1273 (1998)
- [90] A. Clark, *Ferromagnetic materials* (North-Holland, Amsterdam, 1980)
- [91] R. Tickle and R. James, *J. Magn. Magn. Mater.* **195**, 627 (1999)
- [92] H. Okamoto, D. Chakrabarti, D. Laughlin, and T. Massalski, *Bulletin of Alloy Phase Diagrams* **8**, 454 (1987)
- [93] B. Sundman, S. Fries, and W. Oates, *Calphad* **22**, 335 (1998)
- [94] F. Rhines, W. Bonds and R. Rummel, *Trans. Amer. Soc. Met.* **47**, 578 (1955)
- [95] G. Grube, G. Schoenmann, F. Vaupel and W. Weber, *Z. Anorg. Chem.* **201**, 41 (1931)
- [96] G. Preston, *J. Inst. Metals* **46**, 477 (1931)
- [97] H. Okamoto, *Phase Diagrams of Binary Iron Alloys* (ASM International, Materials Park, OH, 1993), pp. 330-36.
- [98] H. Okamoto, *J. Phase Equilib. Diffus.* **25**, 395 (2004)
- [99] P. Fredriksson and B. Sundman, *Calphad* **25**, 535 (2002)
- [100] Y. Nosé, A. Kushida, T. Ikeda, H. Nakajima, K. Tanaka, and H. Numakura *Materials Transactions* **44**, 2723 (2003)
- [101] H. Okamoto, *J. Phase Equilibria* **22**, 591 (2001)
- [102] N. Nagasaki, M. Hirabayashi, *Thermal Equilibrium Phase Diagrams of Alloys* (Agune Technology Center, Tokyo, 2001)
- [103] D. Kim, J. E. Saal, L. Zhou, S. Shang, Y. Du, and Z.-K. Liu, *Calphad* **35**, 323 (2011)
- [104] C. Leroux, A. Loiseau, D. Broddin, and G. Van Tendeloo, *Phil. Mag. B* **64**, 57 (1991)
- [105] K. Udoh, A. El Araby, Y. Tanaka, K. Hisatsune, K. Yasuda, G. Tendeloo, and J. Landuyt, *Mater. Sci. Eng.* **203**, 154 (1995)
- [106] L. Bendersky and W. Boettinger, *Acta Metall. Mater.* **42**, 2337 (1994)
- [107] A. Suzuki and M. Takeyama, *J. Mater. Res.* **21**, 21 (2006)
- [108] H. Smith and A. Tuner, *Appl. Opt.* **4**, 147 (1965)
- [109] J. Cheung and T. Magee, *J. Vac. Sci. Technol. A* **1**, 1604 (1983)
- [110] H. Sankur, *Materials Research Symposium*, Boston (Nov. 1983)
- [111] T. Venkatesan and S. Green, *Industrial Physicist* **2**, 22 (1996)
- [112] R. Eason, *Pulsed Laser Deposition of Thin Films* (John Wiley and Sons, New York, 2007)
- [113] D. B. Chrisey and G. K. Hubler, *Pulsed Laser Deposition* (John Wiley and Sons, New York, 1994)
- [114] K. Sato, T. Konno and Y. Hirotsu, *J. Appl. Phys.* **105**, 034308 (2009)
- [115] D. Weller and A. Moser, *IEEE Trans. Magn.* **35**, 4423 (1999)
- [116] M. Lee and W. Lee, *J. Appl. Phys.* **50**, 444 (1979)
- [117] I. Kock, T. Edler, and S. Mayr, *J. Appl. Phys.* **103**, 046108 (2008)
- [118] C. Issro, M. Abes, W. Püschl, B. Sepiol, W. Pfeiler, P. Rogl, G. Schmerber, W. Soffa, R. Kozubski, and V. Pierron-Bohnes, *Metall. Mater. Trans. A* **37**, 3415 (2006)

- [119] C. Issro and V. Pierron-Bohnes, MRS Proceedings **980**, 3 (2006)
- [120] C. Issro, W. Puschl, W. Pfeiler, P. Rogl, W. Soffa, M. Acosta, G. Schmerber, R. Kozubski, and V. Pierronbohnes, Scripta Materialia **53**, 447 (2005)
- [121] M. Carbucicchio and R. Ciprian, J. Phys: Conf. Series **217**, 012111 (2010)
- [122] L. Kühnemund, T. Edler, I. Kock, M. Seibt, and S. Mayr, New J. Phys. **11**, 113054 (2009)
- [123] V. Myagkov, V. Zhigalov, L. Bykova, L. Solov'ev, and G. Bondarenko, JETP Letters **91**, 481 (2010).
- [124] V. Myagkov, V. Zhigalov, B. Belyaev, L. Bykova, L. Solovyov, and G. Bondarenko, J. Magn. Magn. Mater. **324**, 1571 (2012)
- [125] D. Wei and Y. Yao, Appl. Phys. Let. **95**, 172503 (2009)
- [126] A. Kovács, K. Sato, and Y. Hirotsu, J. Appl. Phys. **102**, 123512 (2007)
- [127] J. BenYoussef, H. Le Gall, N. Vukadinovic, V. Gehanno, A. Marty, Y. Samson, and B. Gilles, J. Magn. Magn. Mater. **202**, 277 (1999)
- [128] D. Halley, P. Auric, P. Bayle-Guillemaud, B. Gilles, A. Marty, and D. Jalabert, J. Appl. Phys. **91**, 9757 (2002)
- [129] V. Gehanno, R. Hoffmann, Y. Samson, A. Marty, and S. Auffret, Eur. Phys. J. B **10**, 457 (1999)
- [130] V. Gehanno, C. Revenant-Brizard, A. Marty, and B. Gilles, J. Appl. Phys. **84**, 2316 (1998)
- [131] V. Gehanno, A. Marty, B. Gilles, and Y. Samson, Phys. Rev. B **55**, 552 (1997)
- [132] V. Gehanno, Y. Samson, A. Marty, B. Gilles, and A. Chamberod, J. Magn. Magn. Mater. **172**, 26 (1997)
- [133] D. Halley, B. Gilles, P. Bayle-Guillemaud, R. Arenal, A. Marty, G. Patrat, and Y. Samson, Phys. Rev. B **70**, 1 (2004)
- [134] D. Halley, A. Marty, P. Bayle-Guillemaud, B. Gilles, J. Attane, and Y. Samson, Phys. Rev. B **70**, 174438 (2004)
- [135] D. Halley, Y. Samson, A. Marty, P. Bayle-Guillemaud, C. Beigné, B. Gilles, and J. Mazille, Phys. Rev. B **65**, 1 (2002)
- [136] D. Halley, Y. Samson, A. Marty, C. Beigné, and B. Gilles, Surface Science **481**, 25 (2001)
- [137] D. Ravelosona, C. Chappert, H. Bernas, D. Halley, Y. Samson, and a. Marty, Journal of Applied Physics **91**, 8082 (2002)
- [138] X. Sun, X. Xu, Z. Tang, G. Dong, and X. Jin, Phys. Let. A **372**, 1687 (2008)
- [139] H. Xu, H. Heinrich, and J. Wiezorek, Intermetallics **11**, 963 (2003)
- [140] M. Sorescu, L. Diamandescu, and A. Grabias, Intermetallics **14**, 780 (2006)
- [141] T. Edler, J. Buschbeck, C. Mickel, S. Fähler, and S. Mayr, New J. Phys. **10**, 063007 (2008)
- [142] J. Buschbeck, I. Lindemann, L. Schultz, and S. Fähler, Phys. Rev. B **76**, 1 (2007)
- [143] A. Kulovits, J. Leonard, and J. Wiezorek, Intermetallics **15**, 1606 (2007)

- [144] T. Schied, A. Lotnyk, C. Zamponi, L. Kienle, J. Buschbeck, M. Weisheit, B. Holzapfel, L. Schultz, and S. Fähler, *J. Appl. Phys.* **108**, 033902 (2010)
- [145] D. Vokoun, J. Shih, T. Chin, and C. Hu, *J. Magn. Magn. Mater.* **281**, 105 (2004)
- [146] T. Ichitsubo, S. Takashima, E. Matsubara, S. Tsukimoto, Y. Tamada, and T. Ono, *J. Appl. Phys.* **109**, 033513 (2011)
- [147] T. Ichitsubo, S. Takashima, E. Matsubara, Y. Tamada, and T. Ono, *Appl. Phys. Lett.* **97**, 182508 (2010)
- [148] Y. Endo, Y. Yamanaka, Y. Kawamura, and M. Yamamoto, *Jap. J. Appl. Phys.* **44**, 3009 (2005)
- [149] A. Itabashi, M. Ohtake, S. Ouchi, F. Kirino, and M. Futamoto, *EPJ Web of Conf.* **40**, 07001 (2013)
- [150] M. Ohtake, O. Yabuhara, K. Tobar, F. Kirino, and M. Futamoto, *J. Appl. Phys.* **109**, 07B757 (2011)
- [151] O. Yabuhara, M. Ohtake, K. Tobar, T. Nishiyama, F. Kirino, and M. Futamoto, *Thin Solid Films* **519**, 8359 (2011)
- [152] M. Ohtake, S. Ouchi, F. Kirino, and M. Futamoto, *J. Appl. Phys.* **111**, 07A708 (2012)
- [153] Z. Wang, T. Iijima, G. He, T. Takahashi, and Y. Furuya, *Int. J. Appl. Electromagn. Mech.* **12**, 61 (2000)
- [154] P. Caro, A. Cebollada, D. Ravelosona, F. Briones, D. García, M. Vázquez, and A. Hernando, *J. Appl. Phys.* **81**, 5050 (1997)
- [155] F. Wang, S. Doi, K. Hosoiri, H. Yoshida, T. Kuzushima, M. Sasadaira, and T. Watanabe, *Electrochimica Acta* **51**, 4250 (2006)
- [156] F. Takata, G. Pattanaik, W. Soffa, P. Sumodjo, and G. Zangari, *Electrochem. Communications* **10**, 568 (2008)
- [157] G. Strukova, G. Strukov, S. Bozhko, Y. Kabanov, I. Shmytko, A. Mazilkin, N. Sobolev, E. Zhiteytshev, A. Sukhanov, V. Voronkova, and L. Tagirov, *J. Nanosci. and Nanotech.* **11**, 8907 (2011)
- [158] L. Szunyogh, J. Zabloudil, A. Vernes, P. Weinberger, B. Újfalussy, and C. Sommers, *Phys. Rev. B* **63**, 1 (2001)
- [159] K. Sato, K. Aoyagi, and T. Konno, *J. Appl. Phys.* **107**, 024304 (2010)
- [160] M. Allalen, T. Mehaddene and H. Bouar, *J. Phys.: Cond. Mat.* **19**, 036218 (2007)
- [161] K. Watanabe, H. Kura, and T. Sato, *Sci. Tech. Adv. Mater.* **7**, 145 (2006)
- [162] O. Klein, Y. Samson, A. Marty, S. Guillous, M. Viret, C. Fermon, and H. Alloul, *J. Appl. Phys.* **89**, 6781 (2001)
- [163] A. Masseur, C. Gatel, P. Bayle-Guillemaud, A. Marty, and J. Toussaint, *Ultramicroscopy* **110**, 20 (2009)
- [164] X. Sun, X. Xu, G. Dong, and X. Jin, *Phys. Lett. A* **372**, 1687 (2008)
- [165] I. Galanakis, S. Ostanin, M. Alouani, H. Dreyss, and H. Edert, *Comp. Mater. Sci.* **17**, 455 (2000)

2 - Experimental Procedures

2.1 - Fe_{38.5}Pd_{61.5} Target

An Fe_{38.5}Pd_{61.5} target for PLD was prepared by vacuum arc-melting high purity metals (> 99.95 at %) in an Ar atmosphere, followed by homogenization at temperatures above 900°C. The ingot was subsequently worked into a suitable target by repeated cold-rolling and then annealed to induce recrystallization; this created a flat sample wide enough to be used in a standard 1" diameter PLD target holder (Fig. 1). Each deposition would start on a polished portion of the surface. When areal overlap with the ablation tracks left by previous depositions could not be avoided, the target would be polished back to a 1200 grit finish with SiC paper, sonicated to remove debris, and rinsed with ethanol.



Fig. 1 - The Fe_{38.5}Pd_{61.5} PLD target seen post-deposition. Two ring shaped deposition tracks show differences to the target surface resulting from ablation of material as the target is rotated.

2.2 - Deposition Setup and Conditions

All film samples in this thesis were prepared by PLD from a single Fe_{38.5}Pd_{61.5} target using a KrF excimer laser (Lambda Physik COMPex 205, $\lambda = 248$ nm; 25 ns FWHM) at a repetition rate of 10 Hz for 12-30 minutes, running at a fluence of 3.0 J/cm². The optical pathway (Fig. 2) started at the laser window and was reflected off an adjustable 45° ultraviolet

mirror, allowing the beam to be centered onto the target inside the PLD chamber. The beam was then passed through an aperture and focused onto the target with a 25.4 cm focal length lens, passing into the PLD chamber through an ultraviolet transparent vacuum window. An adjustable iris diaphragm aperture was used, set to remove stray scattering from the mirror and control collimation, rather than removing a significant portion of the high intensity beam. The intensity of the beam was measured inside the chamber with a pyroelectric energy meter averaging twice over 125 pulses, and the spot size at the target was determined with ultraviolet sensitive laser burn paper (Laser Alignment Products Zap-It™).

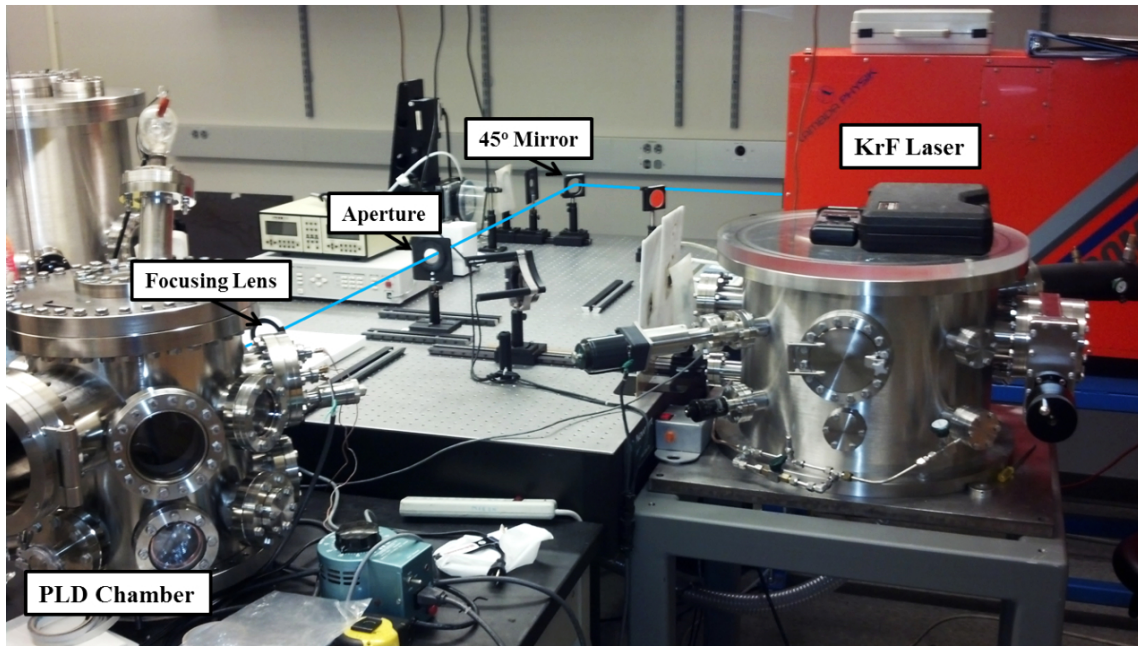


Fig. 2 - The laser beam optical path used for the deposition of all samples in this thesis. The adjustable 45° mirror allows for position control within the PLD chamber, while the aperture serves to remove diffuse scatter and collimate the beam.

MgO (001) oriented substrates (CrysTec GmbH, Sigma Aldrich or MTI Corp.) were mounted using colloidal Ag paint (Ted Pella) to a MeiVac resistive heater located 5.5 cm from the target (Fig. 3). The temperature was monitored by two k-type thermocouples, one located

inside the heater element and the second placed on the surface. Substrates were held at a temperature within two degrees of 500°C, 550°C, 600°C, or 650°C during deposition, which was started once both thermocouples were in agreement and a steady state was reached. Prior to each deposition, the chamber was evacuated to high vacuum (10^{-4} Pa) with a turbomolecular pump while the heater reached deposition temperatures, removing volatile elements as the colloidal Ag paint annealed. The chamber was then backfilled to a deposition pressure of 100 mTorr (13.3 Pa) with Ar, and the polished PLD target was conditioned at 10 Hz for one minute with the substrate shuttered. Conditioning helps to removed possible surface contaminants from the target, as well as oxidation, without depositing them onto the substrate. Immediately following deposition the samples were cooled to room temperature by venting the chamber with Ar, falling from 600°C to 300°C within approximately 20 minutes. The films when then removed once the heater reached 50°C and was safe to handle, then stored within a desiccator until analysis.

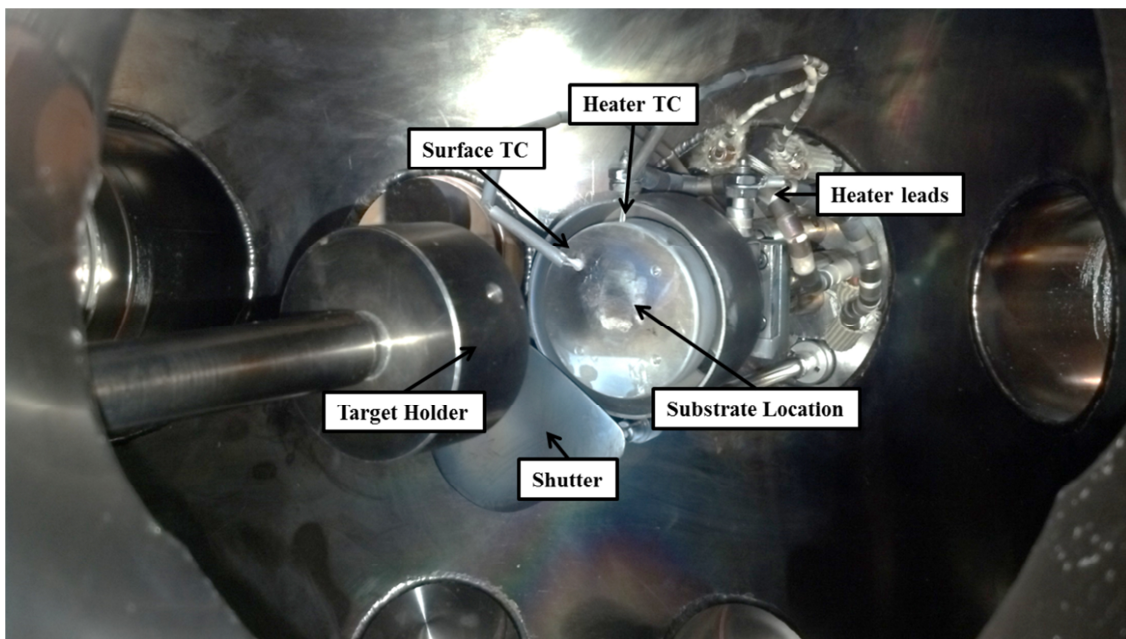


Fig. 3 - Configuration inside the vacuum chamber (target holder retracted slightly for view). The shutter allows for deposition to be paused while the laser conditions the target, while the two thermocouples (TC) monitor the temperature of the resistive heater.

2.3 – Characterization Techniques

2.3.1 - Scanning Electron Microscopy (SEM)

One of the primary characterization techniques used on all samples in this thesis was a JEOL JSM-6700F cold cathode field-emission scanning electron microscope equipped with an annular backscattered electron detector. At first principle SEM employs an accelerated electron source (order keV) which, controlled by a series of apertures and magnetic lenses, is focused to a probe and rastered across the surface of a sample held under vacuum. This results in a number of different elastic and inelastic interactions, and the emission of electron (secondary, Auger, backscattered) or photon (cathodoluminescence, X-rays) signals which are subsequently picked up by various detectors located around the SEM chamber [1].

Secondary electrons are produced by the inelastic excitation of valence electrons in the sample by the electron beam, leading to their release (< 50 eV). These free electrons are then pulled from the sample by an Everhart-Thornley detector held at a small positive bias inside the vacuum chamber. Due to their low energy, only secondary electrons created at the surface of the sample are able to reach the detector, providing the best resolution of all the SEM signals and limited predominantly by the focusing power of the magnetic lenses. With good alignment, proper conditions, and appropriate samples the resolution will approach ~ 1 nm in scale. This high resolution, combined with good signal production, makes secondary electrons the normal imaging mode for most SEM work, and a common tool for the analysis of microscale or nanostructures. The samples in this study were imaged without the addition of a conductive coating, at an operating voltage of 5 kV and beam current of 20 pA to avoid surface charging.

Backscattered electrons come from elastic Rutherford scattering in the material, leading high-energy incident electrons to change direction and leave the sample. Backscattered electron

signal is therefore more sensitive to surface topology (escape path) and atomic number density (protons for scattering) of the sample, making it useful in the compositional analysis of flat samples. The resolution of backscattered electron microscopy is broader than that of secondary electrons, as electrons now travel deeper into the sample and spread with scattering over a larger interaction volume. For bulk materials this forces the use of lower voltages (lower penetration depths) to increase resolution, but is made difficult by a corresponding drop in backscattered signal. For thin films it is desirable to place the backscattered interaction volume solely within the film. The MgO substrate is considerably less dense than the Fe & Pd in the films, and without loss of generality backscattered electrons reaching the substrate can be taken either to be lost out the back of the film and do not reach the detector, or are scattered so broadly by the substrate before return to the film that they provide only diffuse signal. Monte Carlo simulations can be used to approximate the interaction volume and electron paths, and thus resolution and yield, for Fe-Pd thin films [2, 3]. Fig. 4 shows four Monte Carlo simulations for Fe and Pd (approximated as Ag, $\Delta Z = 1$) at beam energies of 5 keV and 20 keV, performed for 100 nm thick films [3]. It can be seen that at 20 keV for both elements most electrons travel into the substrate before they could be deflected back to the surface, resulting in both poor signal and a very broad resolution. Lowering the accelerating voltage to 5 keV, many electrons now escape through the surface as backscattered electrons, and most do not reach the substrate at all. The majority of escaping electrons occur within a 50 nm diameter spread with a roughly Gaussian distribution, and the highest intensity is focused within ± 10 nm of the incident beam. This is qualitatively confirmed later by samples in this thesis, which are able to resolve features with a backscattered resolution in the territory of 10 nm at 5 keV.

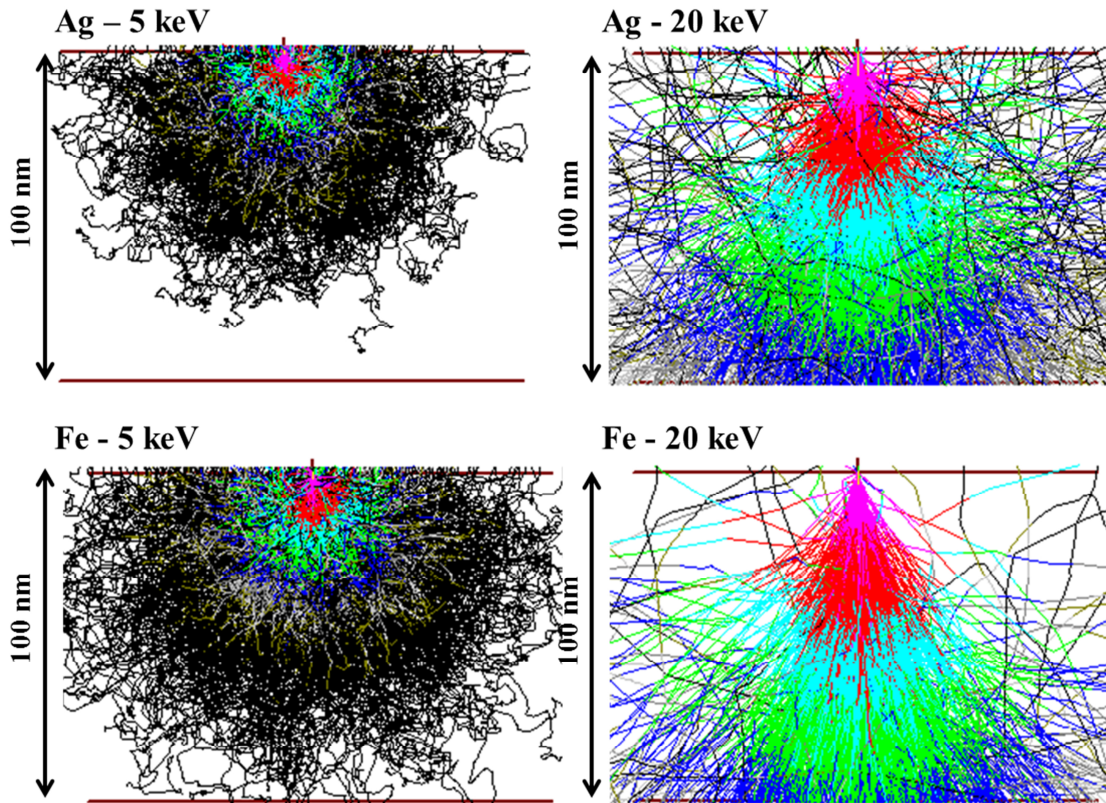


Fig. 4 - Monte Carlo simulations for 100 nm thin films of Fe and Ag (~Pd) at 5 keV and 20 keV beam energies [3]. Both elements have a higher resolution and signal of backscattered electrons at 5 keV, as most incident electrons exit the back of the film at 20 keV and are effectively lost.

2.3.2 – Energy Dispersive X-ray Spectroscopy (EDXS)

When an energetic (keV) electronic beam interacts with material, tightly bound core-shell electrons can be removed from individual atoms, leaving behind vacancies and an excited electronic state. Through a limited set of transitions allowed by quantum physics, outer-shell electrons relax to fill this vacancy on the picosecond time scale and emit photons in the X-ray intensity range characteristic to the element involved. The spatial resolution of EDXS is on the order of micrometers and follows the approximation

$$R(\mu\text{m}) = \frac{0.064 (E_0(\text{keV})^{1.7} - E_x(\text{keV})^{1.7})}{\rho_{\text{mass}}} \quad (1)$$

where E_0 is the beam energy, E_x is the energy of the characteristic X-ray being observed, and ρ_{mass} is the mass density of the material [1]. This poor spatial resolution will require the inclusion of additional compositional analysis techniques for the quantitative analysis of nanoscale structures.

EDXS is generally a qualitative method when employed in conjunction with SEM, as it is heavily dependent on spread and absorption of the incident electron beam and internal absorption of the characteristic X-rays. Software packages tuned to the specific machine and detector being used, and modeling the background radiation present, can be utilized to reduce some of this error and produce “semi-quantitative” results. Through the rigorous application of constant beam parameters, long acquisitions and multiple standards, the technique can also be used to produce close quantitative results for a specific sample [4].

EDXS for this thesis was performed on a Princeton Gamma Tech (PGT) Prism 2000 Spectrometer with a resolution of 135 eV (FWHM) equipped to the SEM. Running at an accelerating voltage of 20 keV, working distance of 15 mm, current of 0.04 nA, and take-off angle of 31° , bulk samples of pure Fe and Pd were calibrated into the PGT Spirit microanalysis software. Acquisitions were performed until the major characteristic lines of the elements reached 10,000 counts (approx. 20 min), and the dead time of the detector was held under 15% to reduce artifacts. Maintaining the same conditions, a bulk sample with a known $\text{Fe}_{50}\text{Pd}_{50}$ composition was then analyzed to account for changes due to inter-elemental mixing, exhibiting a relative increase in the predicted Fe value at 56.48 at % Fe. This second standardization accounts for hard to model interactions involving cross-species absorption and fluorescence. In

the compositional vicinity of Fe₅₀Pd₅₀ this mixing interaction should remain approximately constant and the Fe₅₀Pd₅₀ sample can be used as a reliable standard using the following equation

$$\frac{I_{Fe}}{I_{Pd}} = K_{mix} \frac{Fe \text{ At}\%}{Pd \text{ At}\%} \quad (2)$$

with $K_{mix} = 1.298$, which can be applied generally to the range of Fe_{38.5}Pd_{61.5}. The Fe_{38.5}Pd_{61.5} bulk target is measured pre-standardization by the software to be 54.91 at % Pd, and standardizing off Fe₅₀Pd₅₀ this results in a predicted composition of 61.25 at % Pd. The error commonly associated with this methodology is $\pm 2\%$, so this result agrees well with the expected Fe_{38.5}Pd_{61.5} composition of the target.

Limited EDXS was also performed during transmission electron microscopy on an EDAX Titan 300ST detector with an ultra-thin window and a resolution of 134 eV (FWHM). EDXS is naturally quantitative in transmission electron microscopy as the thin samples and higher beam energies needed for transmission limit spread of the electron beam and eliminate many of the more complicated effects present in scanning microscopy.

2.3.3 – Atomic and Magnetic Force Microscopy (AFM-MFM)

AFM is a type of scanning probe microscopy, where a finely controlled mechanical cantilever makes physical contact with a surface while rastering across it, producing a direct 3-D map of the sample's surface topography [5]. MFM utilizes a thin film magnetic coating on a standard AFM tip. Running just above the surface of the sample without making contact, the pull on the cantilever due to magnetic forces can be used to observe and map the magnetic domain structure of the sample [5, 6]. Specific samples were characterized by both AFM and MFM using an Asylum Research Cypher Scanning Probe Microscope with a Si AFM tip (9 nm diameter) and a CoCr coated Si MFM tip (47 nm diameter).

2.3.4 – Vibrating Sample Magnetometry (VSM)

VSM is a technique used to measure the magnetic hysteresis loops of small samples by monitoring the flux change in a solenoid coil when a sample is mechanically vibrated in close proximity [7, 8]. In practice the sample is secured on a vibrating rod located across a 2 cm gap separating two solenoid coils that together generate a variable magnetic field. This allows for the measurement for the magnetic moment (and thus magnetization) of a sample for a given applied external magnetic field, which in turn can be used to calculate useful magnetic properties such as coercivity and saturation magnetization. For thin film samples the measurement can be made either with the magnetic field running perpendicular or parallel to the film's surface. All hysteresis measurements in this thesis were conducted on a 7400 Series LakeShore VSM.

2.3.5 – Auger Electron Spectroscopy (AES)

Auger electrons are emitted as one of the many types of signals during SEM in a process similar to the creation of characteristic X-rays. After a core-shell electron is excited out of an atom by the incident electron beam, an outer-shell electron relaxes to fill the vacancy. Instead of emitting energy in the form of a characteristic X-ray photon, the process transfers energy to a third electron in the form of kinetic motion, leading to its ejection from the atom. These Auger electrons have characteristic energies on the scale of hundreds eV that are dictated by the allowed quantum transitions within the excited atom. This relatively low energy range makes Auger electron detection surface sensitive, with resolution falling between secondary and backscattered signals, and much more localized than characteristic X-rays. As the sampling depth of AES is only a few nanometers, and the incident electron beam can be focused to less than 10 nm laterally, high resolution Auger microscopy is critical to quantitative compositional analysis at the nanoscale [9].

Auger electron microscopy for compositional analysis was performed on a Physical Electronics PHI 710 Scanning Auger Nanoprobe Microscope in collaboration with Dennis Paul & Dr. John Hammond of Physical Electronics. The surface sensitivity of Auger spectroscopy requires in-situ cleaning of the surface, and an in-situ Ar ion sputtering source (2kV, 1uA) was utilized to remove surface contaminants originating from sample exposure to ambient air between deposition and analysis. Zalar rotation [10-12] was employed during sputter cleaning to minimize topographical effects [13] and a cylindrical mirror analyzer was utilized to reduce analyzer induced shadowing.

2.3.6 – High Resolution Transmission Electron Microscopy (HRTEM)

Samples deposited via PLD onto TEM grids (20 nm continuous carbon, type-a, Ted Pella 1821) were characterized via bright-field high resolution transmission electron microscopy on an FEI Titan STEM equipped with a Schottky field-emission gun, operating at 300 kV with a point resolution of 0.2 nm (information limit 0.09 nm).

In contrast to SEM, the electron beam in HRTEM passes through a thin sample (1 to 50 nm) and a micrograph of the image plane, diffraction plane, or additional signals or spectrographic results are collected on the other side. Phase-contrast of the electrons passing through the sample allows for the atomic resolution analysis of crystal structures [14]. This is often done by using a Fast Fourier Transform (FFT) to view the reciprocal space of a micrograph, which can be interpreted in a manner similar to an electron diffraction pattern. An example is presented in Fig. 5, showing two Fe-Pd nanoparticles grown by the author using Matrix Assisted Pulsed Laser Evaporation (MAPLE) from metal-acetate precursors. It can be seen through FFT analysis of the phase-contrast image plane micrographs that the particles can be determined to be of two different, $L1_0$ and $L1_2$, ordered structures.

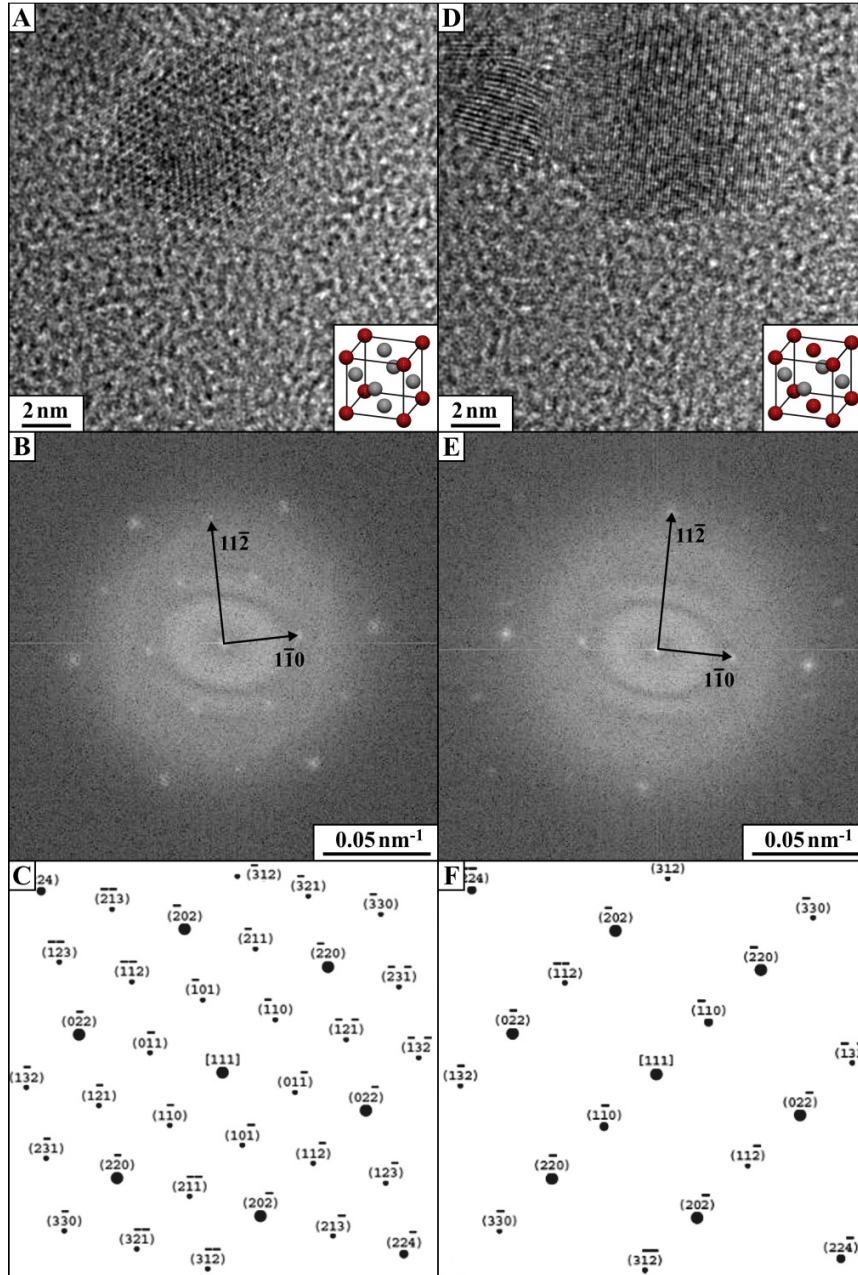


Fig. 5 - (A) HRTEM micrograph of an $L1_2$ Fe-Pd particle deposited by MAPLE as seen down a $\langle 111 \rangle$ direction (B) Fast Fourier transform (FFT) reciprocal space of the micrograph, showing $L1_2$ superlattice peaks and three-fold symmetry (C) Modeled $L1_2$ electron diffraction pattern (D) HRTEM micrograph of an $L1_0$ Fe-Pd particle deposited by MAPLE as seen down a $\langle 111 \rangle$ direction (E) FFT of the micrograph, showing only $L1_0$ superlattice peaks with a characteristic c -axis stretch and a breaking of the three fold cubic symmetry. (F) Modeled $L1_0$ electron diffraction pattern.

2.3.7 – X-ray Diffractometry (XRD)

The label of XRD covers a large range of techniques that involve the interaction of X-rays with a sample and the subsequent measurement of their distribution with a detector. These all involve scattering following Bragg's Law, or diffraction, off of the crystallographic planes of the material, supplying information about orientation and crystallographic properties. A number of geometries can be utilized for diffraction, with each providing a different subset of information. Data presented in this thesis was collected under θ - 2θ , ϕ -rotation, or Reciprocal Space Mapping (RSM) conditions. From this data, properties such as lattice parameters, crystallinity, strain, epitaxy, orientation, and ordering can be deduced. X-ray Reflectivity (XRR), utilizing Fresnel's equations for reflectivity, can additionally be used to predict the roughness and thickness of thin film layers. All crystallographic analysis was performed on a Rigaku SmartLab X-Ray Diffractometer using a Ge (220) 2-bounce incident beam monochromator, parallel beam setup, and Cu-K α 1 radiation. The standard XRD geometry for an epitaxial film is shown in Fig. 6, highlighting common terms that will be used in this thesis.

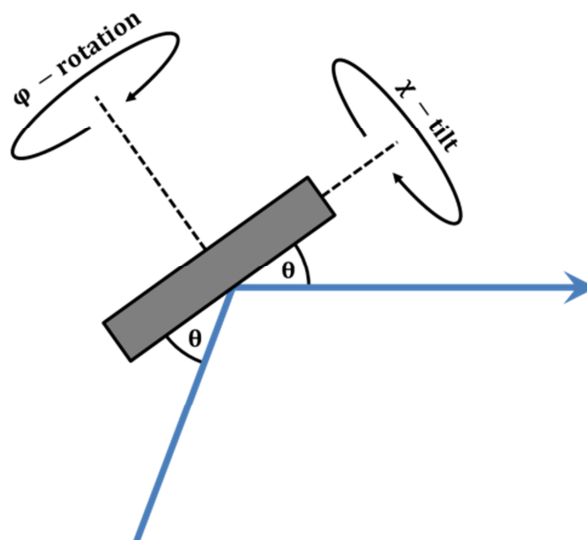


Fig. 6 - Illustration of different parameters in an XRD epitaxial film geometry, including the Bragg angle θ , as well as the definitions of ϕ -rotation and χ -tilt.

2.4 – Quantitative X-ray Diffraction

Through the use of quantitative XRD analysis, the extent and nature of crystallographic ordering can be determined by comparison of diffraction peaks associated with fundamental and superlattice reflections of a crystal structure. Such analysis can be quite complicated and requires a firm understanding of the many interactions and detector geometry effects that occur during the diffraction process [15-19]. These correction terms are derived in detail in this section.

Bragg diffraction occurs when electromagnetic waves with wavelength (λ), comparable to crystallographic plane spacing, are scattered by the sample and undergo constructive interference. For many materials this requires X-Rays, often generated in the laboratory setting from characteristic electronic transitions in 3d transition metals. These X-rays are scattered elastically by electrons in the material, known as Thomson scattering (the quasi-nonrelativistic case of Compton scattering in the lower energy range $Ry \ll E \ll m_e c^2$), a process that causes the electrons to oscillate as Hertz dipoles and become a source of re-emitted radiation. A free electron at position R_0 will be impinged by an incoming X-ray plane wave $E_0 \exp(iK_0 R_0 - i\omega t)$, where E_0 is the electric field, K_0 is the wave vector, and ω is the angular frequency. As time dependence is not of concern the $i\omega t$ term can be discarded for simplicity. The oscillating single electron will then emit radiation with outgoing wave vector K , with an amplitude at position R of

$$E(R) \propto \frac{E_0}{R} \sin\angle(E_0, R) \exp(-iKR) \quad (3)$$

As the scattering is elastic, K and K_0 share the same magnitude of $2\pi/\lambda$. For the many atoms in a crystal, each located at a lattice vector $r_n = n_1 a + n_2 b + n_3 c$ where a , b , and c are the lattice parameters, the scattering at position R from an electron at position r_n can be written as

$$E_n(R) \propto \exp(-iK_0 r_n) \frac{E_0}{|R-r_n|} \sin\angle(E_0, R - r_n) \exp(-iK(R - r_n)) \quad (4)$$

Supplying that interatomic distances are small compared to the area being measured, $R - r_n \approx R$, the sum over all the scattering atoms in the crystal will be

$$E_{All}(R) \propto \exp(-iKR) \frac{E_0}{R} \sin \angle(E_0, R) \sum_n \exp(-i(K - K_0)r_n) \quad (5)$$

The vector $K - K_0$ can be collected as the vector Q , known as the scattering vector, which has a magnitude of $4\pi \sin(\theta)/\lambda$ (Fig. 7).

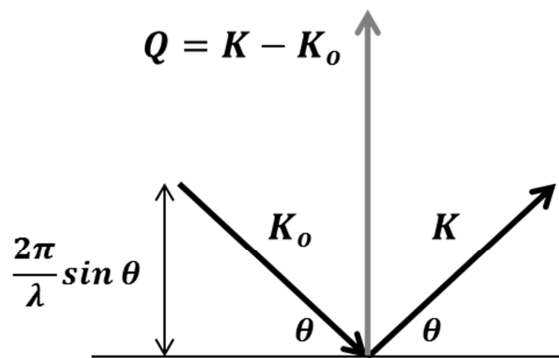


Fig. 7 - Illustration of the scattering vector Q geometry, which is constructed by subtracting the initial wave vector K_0 from the outgoing wave vector K .

In order to determine the conditions for constructive interference we must look at the difference in the phase of the scattered radiation caused by translating r_n , which follows

$$\Delta\phi = (r_n \cdot Q) \quad (6)$$

For constructive interference $\Delta\phi$ must equal $2\pi N$, where N is an integer, so that radiation coming from all points in the structure remains in phase. To find the solution satisfying this condition a reciprocal lattice $r_{hkl}^* = ha^* + kb^* + lc^*$ is introduced, where a^* , b^* , and c^* are reciprocal space unit vectors of a primitive lattice, related to the real lattice by

$$a^* = 2\pi \frac{b \times c}{a \cdot (b \times c)}; \quad b^* = 2\pi \frac{c \times a}{b \cdot (c \times a)}; \quad c^* = 2\pi \frac{a \times b}{c \cdot (a \times b)} \quad (7)$$

With this reciprocal lattice defined, it is easy to find values of the scattering vector, Q , which force Eq. 6 to take values of $2\pi N$, utilizing the relation

$$r_{hkl}^* \cdot r_n = 2\pi(hn_1 + kn_2 + ln_3) = 2\pi(N_1 + N_2 + N_3) = 2\pi N \quad (8)$$

Solutions for constructive interference will therefore follow $Q = r_{hkl}^*$, where r_{hkl}^* is the inverse of the interplanar d -spacing of reflection (h, k, l) , which for an orthogonal system can be written

$$Q = r_{hkl}^* = \frac{2\pi}{d_{hkl}} = 2\pi \sqrt{\left(\frac{h}{a}\right)^2 + \left(\frac{k}{b}\right)^2 + \left(\frac{l}{c}\right)^2} \quad (9)$$

Knowing the magnitude of Q , found in Fig. 7, this simplifies into the form of the well-known Bragg's Law, with the geometric derivation illustrated in Fig. 8.

$$\lambda = 2 \frac{1}{\sqrt{\left(\frac{h}{a}\right)^2 + \left(\frac{k}{b}\right)^2 + \left(\frac{l}{c}\right)^2}} \sin(\theta) \quad (10)$$

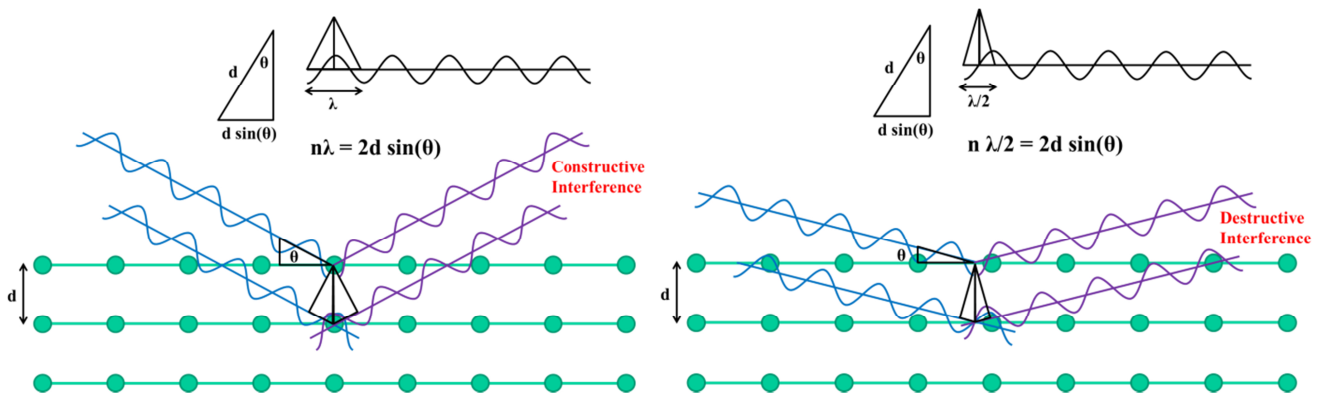


Fig. 8 – The classic geometric derivation of Bragg's law illustrated for both perfectly constructive and perfectly destructive interference scenarios.

In order to arrive at quantifiable intensities the terms in Eq. 5 must be analyzed further, as reflection intensity will follow $I \propto (E)(E^*)$, or $I \propto E^2$, for most crystals under the kinematical theory limit, where the sample can be viewed as a mosaic of small perfect crystals (i.e. “ideally

imperfect”) and multi-scattering effects can be ignored. The last term in Eq. 5 can be re-written as Eq. 11 by applying a continuous limit and defining an electronic charge distribution ρ_e .

$$\sum_n \exp(-i(K - K_0)r_n) = \int \rho_e(r) \exp(-iQr) dr \quad (11)$$

As the structure is composed of repeating unit cells, the intensity scattered will be proportional to this base repeating unit; which itself can be divided into a summation of the atoms within it.

$$\int_{Cell} \rho_e(r) \exp(-iQr) dr = \sum_{Cell} \int_{Atom} \rho_e(r) \exp(-iQ(r - r_n)) dr \quad (12)$$

The term being integrated in Eq. 12 (Eq. 13) is known as the atomic form factor, f_x , and represents the integrated scattering caused by the electrons in an atom of species x.

$$f_x = \int_{Atom} \rho_e(r) \exp(-iQr) dr \quad (13)$$

The atomic form factor determines the strength of scattering from a given position of the unit cell and will depend on the element located there, its electronic state, and the scattering vector Q. Experimentally it can be computed from numerical Hartree-Fock wave functions, fitted with nine coefficients to the following equation

$$f_x(\theta) = \sum_{i=1}^4 a_i \exp\left(-b_i \left(\frac{\sin(\theta)}{\lambda}\right)^2\right) + C \quad (14)$$

Solutions to these wave functions are available, determined from experimental data (Fig. 9) [20].

Iron

| i = | 1 | 2 | 3 | 4 |
|----------------|---------|--------|---------|---------|
| a _i | 11.9185 | 7.0485 | 3.3434 | 2.2723 |
| b _i | 4.8739 | 0.3402 | 15.9330 | 79.0339 |
| c _i | 1.4082 | | | |

Palladium

| i = | 1 | 2 | 3 | 4 |
|----------------|---------|---------|---------|---------|
| a _i | 19.5123 | 15.3800 | 5.3833 | 0.8101 |
| b _i | 0.6858 | 7.9571 | 23.1808 | 65.9295 |
| c _i | 4.9143 | | | |

Fig. 9 - Solutions for Hartree-Fock wave functions in Eq. 14, determined empirically and satisfying the atomic form factor of Fe and Pd [20].

Having satisfied the integral, Eq. 12 can be reduced to a simple summation that is known as the structure factor, F , of the material.

$$F = \sum_{Cell} f_n \exp(-iQr_n) \quad (15)$$

From the derivation of Bragg diffraction we know that constructive interference can only occur at certain lattice plane conditions, moving from general lattice coordinates (n_1, n_2, n_3) to unit cell positions (x, y, z) in Eq. 8, we can express the structure factor in its most classic form

$$F_{hkl} = \sum_{Cell} f_n \exp(-i2\pi(hx + ky + lz)) \quad (16)$$

The structure factor, F_{hkl} , accounts for the contribution of each atom in the unit cell to a lattice reflection (h, k, l) of the crystal. As Euler's equation $e^{ix} = \cos(x) + i \sin(x)$ can take both positive and negative values, atoms are able to destructively interfere and modify the intensity of reflections. Summed over the n atoms of position (x, y, z) in the crystal structure, this term determines the classification of extinct, fundamental, and superlattice peaks. The structure factor will affect the final intensity as $I \propto F_{hkl}^2$.

The term $\sin\angle(E_0, R)$ remaining in Eq. 5 accounts for the polarizing effect of reflection off a sample. Incoming X-rays have E-fields vibrating in directions perpendicular to their propagation. For an unpolarized source, polarization is randomly distributed but can be sorted by projection into σ -polarized photons with an E-field vibrating in the plane perpendicular to the diffraction plane, and π -polarized photons that vibrate in the diffraction plane. For σ -polarized photons $\sin\angle(E_0, R) = 1$, while for π -polarized photons $\sin\angle(E_0, R) = |\cos 2\theta|$. As the intensity follows the square of the electric field, and both polarizations are equally likely, a polarization correction for an unpolarized source can be reached

$$P_{unpolarized} = \frac{1 + \cos^2(2\theta)}{2} \quad (17)$$

For diffraction employing a monochromatic source, X-rays arrive to the sample already partially polarized. Correcting for this is not simple and will depend on the heavily on the monochromator being used. For source monochromators functioning in the plane of diffraction, this will further affect the intensity of the π -polarization component by a polarization factor p_0 :

$$P_{monochromated} = \frac{1+p_0 \cos^2(2\theta)}{1+p_0(2\theta_m)} \quad (18)$$

The polarization factor p_0 for the Ge (220) single crystal double bounce monochromator ($\theta_m = 22.69^\circ$) used in this thesis can be found by adding a multiplicative term dependent on the Bragg angle of the monochromator for each reflection. With single crystals the kinematical approximation used to arrive at the π -polarization from a mosaic crystal, $\cos^2(2\theta_m)$, is no longer appropriate and the dynamical approach modifies the term to $|\cos(2\theta_m)|$ [19, 21, 22]. Consequently, for the monochromator used in this study $p_0 \approx |\cos(2\theta_m)|^2$. In real systems the actual polarization will reside imperfectly between these two extremes, so it is important to address it as a possible source of error. Analysis of complex superlattice structures, discussed in Chapter 4, will be performed with the relative intensities of two pairs of peaks. Errors associated with this term are completely canceled for the more critical of the peak pairs, which is used to determine the type of ordering present, as the peaks share a common Bragg angle at different χ -tilts. The second peak pair has two different θ s, and is used to determine the degree, as opposed to type, of ordering; which is less critical to the major findings of this thesis. Reasonable deviations of p_0 , for example $p_0 = |\cos(2\theta_m)|^{2.5}$, lead to a < 2 % error in the relative intensities of this pair when applied to the actual data, and a maximum of 6 % for the extreme limit $p_0 = |\cos(2\theta_m)|^4$. Any errors introduced here further support major findings, which are conservative. The choice of $p_0 = |\cos(2\theta_m)|^2$ results in some films reaching but not exceeding 100% ordering, which circumstantially supports the appropriateness of the approximation.

Having already arrived at two terms that affect the diffracted intensity, this is a convenient point to collect these and any additional corrections to be made into a single expression, which can be written as

$$I \propto (F_{hkl})^2 * M * L * G * P * A * T * D. \quad (19)$$

The multiplicity term M accounts for the number planes in a crystallographic family, for example M = 8 for the {111} planes of a cubic structure. This term can be ignored for epitaxial samples as each peak represents a single variant of the reflection family.

The Lorentz (L) and geometry (G) factors are often collected into one term with the polarization factor (P), and collectively referred to as the Lorentz-Polarization factor. This simplification is only appropriate for polycrystalline, randomly oriented samples and an unpolarized source. The Lorentz factor accounts for diffraction occurring at angles neighboring the Bragg condition, resulting in an angular dependence to the integrated intensity. In a θ -2 θ geometry this contribution follows $I \propto \sin(2\theta)^{-1}$. The derivation for this term sources back to diffraction conditions within the crystal. As incident planar waves move through the crystal, their scattering and reconstruction leads to a change in transmitted amplitude, as well as a phase shift of q_0 per plane. As the wave passes through p planes, this leads to a phase-lag of pq_0 over the traveled distance distance $x = pd/\sin(\theta)$, where d is the interplanar spacing. This results in a total phase shift of $(2\pi/\lambda) x + pq_0$. Alternatively this shift can be written as $(2\pi/\lambda)(1 - \delta)x$, which makes $(1 - \delta)$ the refractive index and

$$\delta = -\left(\frac{\lambda}{2\pi}\right) \frac{\sin(\theta)}{d} q_0 \quad (20)$$

For an angle θ_1 near the Bragg angle θ_0 , Bragg's law can be rewritten as

$$2d\sin(\theta_1) + \left(\frac{\lambda}{2\pi}\right) 2q_0 = m\lambda \quad (21)$$

$$2d\sin(\theta_1) = m\lambda + \left(\frac{2d}{\sin(\theta_1)}\right) \delta \quad (22)$$

And as $2d\sin(\theta_1)$ is very close to $m\lambda$

$$2d\sin(\theta_1) = m\lambda \left(1 + \frac{\delta}{\sin^2\theta_1}\right) \quad (23)$$

This expansion to the classical Bragg equation allows for some constructive scattering at small deviations from the Bragg condition. As we would like a relation between the span of this alteration, $\Delta\theta_0 = \theta_1 - \theta_0$, as a function of θ , we solve for θ_1 and make a substitution into Eq. 22

$$2d\sin(\Delta\theta_0 + \theta_0) = m\lambda + \left(\frac{2d}{\sin(\theta_1)}\right) \delta \quad (24)$$

$$2d\sin(\Delta\theta_0)\cos(\theta_0) + 2d\cos(\Delta\theta_0)\sin(\theta_0) = m\lambda + \left(\frac{2d}{\sin(\theta_1)}\right) \delta \quad (25)$$

$$2d\Delta\theta_0\cos(\theta_0) + 2d\sin(\theta_0) = m\lambda + \left(\frac{2d}{\sin(\theta_1)}\right) \delta \quad (26)$$

Having made good use of trigonometry and the small angle approximation, the two inner terms of Eq. 26 satisfy Bragg's law and can be removed, allowing a solution for $\Delta\theta_0$

$$\Delta\theta_0 = \frac{\delta}{\cos(\theta_0)\sin(\theta_1)} \quad (27)$$

$$\Delta\theta_0 = \frac{2\delta}{\sin(2\theta_0)} \quad (28)$$

As peak shape remains Gaussian in nature $I \propto \Delta\theta_0$, and the Lorentz correction has been arrived at

$$L \propto \frac{1}{\sin(2\theta)} \quad (29)$$

The geometry factor adds two terms related to polycrystalline diffraction geometries. The first concerns the number of crystallites in a polycrystalline sample that are oriented to satisfy Bragg's law. A collection of randomly oriented crystals will have their normal vectors spread evenly about a sphere surrounding the sample. However only those that meet the Bragg condition will diffract, which translates to those with a normal vector oriented at angle $90 - \theta$.

These diffracting crystals have normal vectors that form a ring on the sphere, of circumference $2\pi(r \cdot \sin(90-\theta))$. With an infinitely small change in angle, $\Delta\theta$, this ring has width $r \cdot \sin(\Delta\theta) = r\Delta\theta$ via the small angle approximation. The fractional area on the sphere's surface that the ring represents is the angular density of randomly oriented crystals able to diffract for a given θ :

$$\rho_{planes} = \frac{r\Delta\theta \cdot 2\pi r \sin(90-\theta)}{4\pi r^2} = \frac{\Delta\theta \cos(\theta)}{2} \quad (30)$$

The crystals that do diffract lead to a diffraction cone originating from the sample, which intersects a surrounding sphere along a circle with a circumference of $2\pi r \cdot \sin(2\theta)$. As the detector is of fixed width it will only pick up a slice of this cone, leading to an intensity $I \propto 1/\sin(2\theta)$. These two combined terms are referred to as the geometry factor (Eq. 31) and are important for non-textured polycrystalline films, must be modified for textured samples, and can be ignored for single crystals and epitaxy.

$$G_{poly} \propto \frac{\cos(\theta)}{\sin(2\theta)} \quad (31)$$

The absorption factor (A) accounts for Beer-Lambert absorption of X-rays as they travel through the sample (Fig. 10). It depends on the Bragg angle θ , tilt χ of the sample about the beam axis, the linear attenuation coefficient μ of the sample, and sample thickness t .

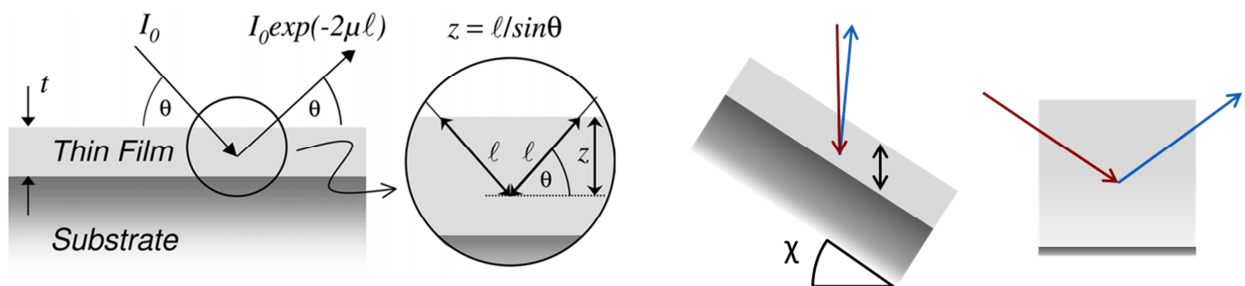


Fig. 10 - Illustration of the pathway in a thin film the absorption correction is integrated over in Eqs. 32-34, using the Beer-Lambert law of form $I = I_0 \exp(-\mu x)$.

For thin films the absorption factor follows

$$A \propto \int_0^{\ell_{max}} I_o \exp(-2\mu\ell) d\ell \quad (32)$$

$$A \propto 1 - \exp(-2\mu\ell_{max}); \ell_{max} = \frac{t}{\sin(\theta)\cos(\chi)} \quad (33)$$

$$A \propto 1 - \exp\left(\frac{-2\mu t}{\sin(\theta)\cos(\chi)}\right) \quad (34)$$

With thick samples, A can be seen to approach unity and is often ignored. The mass density of Fe_{38.5}Pd_{61.5} is calculated to be

$$\rho_{mass} = \frac{4 \text{ atoms} (At_{Fe} 55.85 \frac{g}{mol} + At_{Pd} 106.4 \frac{g}{mol})}{6.022 \times 10^{23} \frac{\text{atoms}}{mol} * (3.83 \text{ \AA})^3} = 1.017 \times 10^7 \frac{g}{m^3} \text{ at } 61.5\% Pd \quad (35)$$

This can be used to convert from mass attenuation coefficients [23] to linear attenuation

$$\frac{\mu}{\rho} = At_{Fe} 0.03056 \frac{m^2}{g} + At_{Pd} 0.02017 \frac{m^2}{g} = 0.02417 \frac{m^2}{g} \text{ at } 61.5\% Pd \quad (36)$$

$$\mu = 244583 \frac{1}{m} \quad (37)$$

The Debye-Waller temperature factor (T) involves an angle dependent dampening effect due to thermally driven vibrational displacements of atoms from lattice sites, and is given by

$$T = \exp\left(-B \left(\frac{\sin(\theta)}{\lambda}\right)^2\right) \quad (38)$$

where B is the isotropic temperature factor for the sample (or $8\pi^2 u^2$ where u^2 is the mean square displacement from the atom's average position). At room temperature the Debye-Waller factor rarely contributes more than a couple percentage points of change but remains important for quantitative analysis. At 300 K migration energies are similar between FePd & FePd₃ and the isotropic temperature factor can be taken as $B = 0.442 \text{ \AA}^2$ for Fe_{38.5}Pd_{61.5} [24].

When employing a tilt along χ , part of the sample is moved out of the ideal diffraction condition for the detector, leading to a defocusing correction (D). This factor must be determined empirically for a given diffractometer geometry, which can be done with a bulk polycrystalline sample by tracking the intensity change of a reflection while tilting in χ [25]. The $\text{Fe}_{38.5}\text{Pd}_{61.5}$ target was found to have mild crystallographic texture left over from processing, making assignment of a correction factor only tentative. The $\{112\}$ and $\{121\}$ χ -tilted peaks relevant to this paper have a Bragg angle of approximately 29.5° , consequently a high purity W sintered target (which did not exhibit texture) $\{200\}$ peak of 29.16° was used to confirm the defocusing factor for the diffractometer at $D(\{112\}/\{121\}) = 2.86$ [26].

The methodology for X-ray analysis outlined in this section is able to predict the relative intensities of published Fe-Pd bulk standards for the disordered, $L1_0$ and $L1_2$ phases for major peaks generally within 2-3 % despite a number of variable factors such as texture, degree of crystallinity, ordering and grain size effects known to cause variations in the bulk references [27]. In the case of epitaxial thin films the predictive power of such quantitative methods will be more accurate, with the elimination of indeterminate texture and more control over the diffraction geometry.

References

- [1] J. Goldstein, D. Newbury, D. Joy, C. Lyman, P. Echlin, E. Lifshin, L. Sawyer and J. Michael, *Scanning Electron Microscopy and X-ray Microanalysis: Third Edition* (Springer, 2003)
- [2] D. Joy, *Monte Carlo Modeling for Electron Microscopy and Microanalysis* (Oxford University Press, 1995)
- [3] D. Joy, *MC_Demo - Monte Carlo Modeling for WIN98 – Software*
- [4] ASTM Standard E1508 - 12a *Standard Guide for Quantitative Analysis by Energy-Dispersive Spectroscopy* (ASTM International, West Conshohocken, PA, 2003)
- [5] V. Bellito (editor) *Atomic Force Microscopy - Imaging, Measuring and Manipulating Surfaces at the Atomic Scale* (InTech, 2012)
- [6] U. Hartmann, *Annu. Rev. Mater. Sci.* **29**, 53 (1999)
- [7] S. Foner, *Rev. Sci. Instrum.* **27**, 548 (1956)
- [8] B. Cullity, *Introduction to Magnetic Materials* (Addison-Wesley, Reading, MA, 1972)
- [9] C. Powell and M. Seah, *J. Vac. Sci. Technol. A* **8**, 735 (1990)
- [10] S. Hofmann and A. Zalar, *Surf. Interface Anal.* **10**, 7 (1987)
- [11] A. Zalar, *Thin Solid Films* **124**, 223 (1985)
- [12] A. Zalar, *Surf. Interface Anal.* **9**, 41 (1986)
- [13] V. Smentkowski, *Prog. Surf. Sci.* **64**, 1 (2000)
- [14] B. Fultz and J. Howe, *Transmission Electron Microscopy and Diffraction of Materials*, 3rd ed. (Springer, Berlin, 2008)
- [15] B. Cullity, *Elements of X-ray Diffraction* (Addison-Wesley, Reading, MA, 1956)
- [16] M. Birkholz, *Thin Film Analysis by X-Ray Scattering* (John Wiley & Sons, Weinheim, 2006)
- [17] B. Warren, *X-Ray Diffraction* (Addison-Wesley, Reading, MA, 1969)
- [18] R. James *The Optical Principles Of The Diffraction Of X Rays Vol II* (G. Bell and Sons, London, 1962)
- [19] J. Als-Nielsen and D. McMorrow, *Elements of Modern X-ray Physics 2nd ed.* (John Wiley & Sons, Singapore, 2011)
- [20] D. Cromer and J. Mann, *Acta Crystallogr.* **A24**, 321 (1968)
- [21] W. Parrish and J. I. Langford, *International Tables for Crystallography. Vol. C Chapter 2.3* (Springer Online, 2006)
- [22] Y. Suortti and T. Paakkari, *J. Appl. Cryst.* **1**, 121 (1968)
- [23] J. Hubbell and S. Seltzer, *Tables of X-Ray Mass Attenuation Coefficients and Mass Energy-Absorption Coefficients* (NIST, Gaithersburg, MD, 2004)
- [24] T. Mehaddenea *et al.*, *Catal. Today* **89**, 313 (2004)
- [25] Y. Liu *et al.*, *Textures and Microstructures.* **35**, 283 (2003)
- [26] W. Davey, *Phys. Rev.* **26**, 736 (1925)
- [27] PDF 03-065-3253, PDF 04-002-1994, PDF 04-003-5067, PDF 03-065-9971, and PDF 04-004-8630 (ICDD, 2011)

3 – Deposition Temperature Series

3.1 - Introduction

Study began with the PLD of $\text{Fe}_{38.5}\text{Pd}_{61.5}$ thin films onto MgO (001) substrates constituting a deposition temperature series. This series was intended to establish the feasibility and temperature range required for growing smooth, continuous and possibly epitaxial films by PLD on MgO (001) at the $\text{Fe}_{38.5}\text{Pd}_{61.5}$ composition. At high temperatures these films would be expected to order, though which ordered phases and microstructures would appear was an open question. The approximate temperature range of the ordering transition under non-equilibrium conditions could be established for any ordered phases that did appear, as the transition is expected to be lower for nanoscale films grown by PLD than in bulk equilibrium. The study presents clear answers concerning the morphological behavior of $\text{Fe}_{38.5}\text{Pd}_{61.5}$ films on MgO (001) and shows that at high temperatures films come to preference an $L1_2$ phase, tetragonally distorted by strain, rather than a two-phase $L1_0$ - $L1_2$ microstructure. In this chapter the results of the initial temperature series are analyzed and several important observations are made, two of which have been expanded into the studies constituting the remainder of this thesis.

Based on the publication history for epitaxial Fe-Pd growth on MgO substrates, in addition to knowledge of physical vapor deposition thin film growth regimes [1-3], four deposition temperatures were chosen for the temperature series: 500°C, 550°C, 600°C, and 650°C. These temperatures are illustrated on the equilibrium phase diagram in Fig. 1 and color coded throughout the figures in this chapter for convenience. The deposition temperatures are 100 to 250 K lower than the expected bulk equilibrium ordering transition, ranging from 0.75 to 0.90 T_0 . They are also well above the magnetic transformation temperature, so the magnetic

properties of the film will be negligible during the growth process. The films in this study were grown at identical deposition conditions on Crystec GmbH substrates over a 48 hour period to reduce any sources of experimental variance.

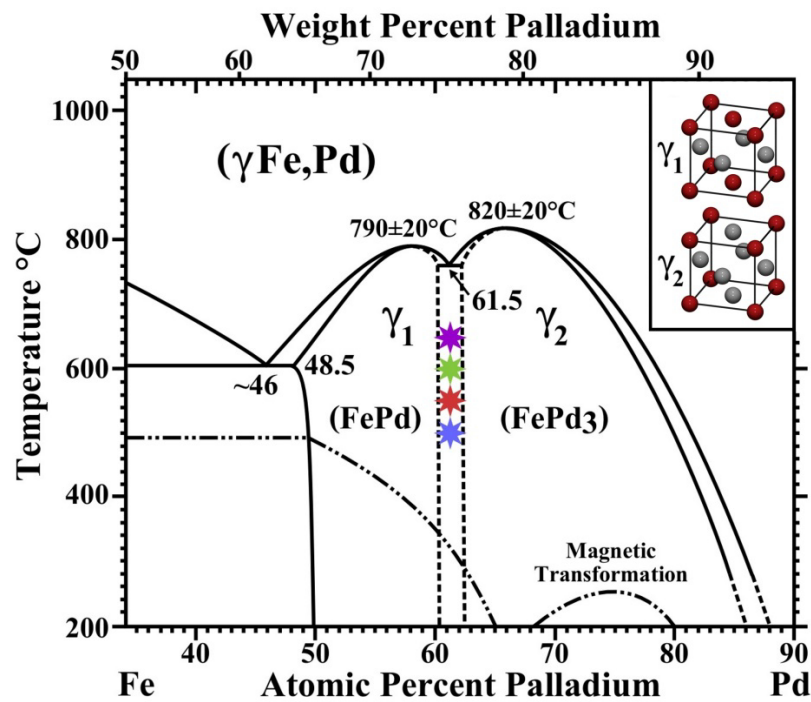


Fig. 1 - Partial phase diagram of the Fe-Pd material system, marked with the parameters of the films deposited in this study. Of special note is the eutectoid decomposition located at $\text{Fe}_{38.5}\text{Pd}_{61.5}$ from the disordered FCC γ phase to the $L1_0$ (FePd) and $L1_2$ (FePd₃) ordered phases. The uniformly dashed lines in the diagram represent uncertain boundaries in the experimental phase diagram; the broken lines represent the expected magnetic transformation.

3.2 - Film Growth and Morphology

3.2.1 – Film Thickness and Growth Rate

Thickness and deposition rate can play a critical role in many of a film's final properties. One method for determining film thickness is cross-sectional SEM. This method is destructive in nature, requiring cleavage of the substrate, and was performed after other characterization

methods were exhausted. As the MgO substrates are insulating, the low voltage and current conditions needed to avoid charge buildup are at odds with optimal resolution and signal production, respectively. From Fig. 2 it can be seen that the $\text{Fe}_{38.5}\text{Pd}_{61.5}$ films deposited are approximately 50 nm thick.

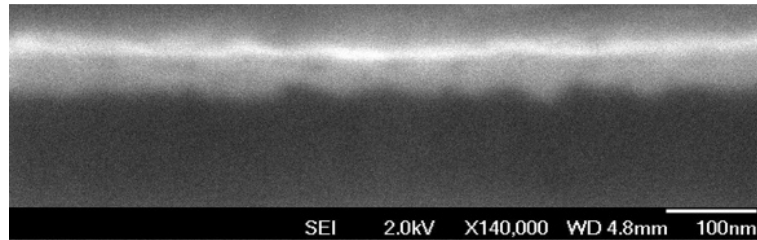


Fig. 2 - Cross-sectional SEM micrograph of a cleaved $\text{Fe}_{38.5}\text{Pd}_{61.5}$ film grown at 600°C.

X-ray reflectivity is an accurate and non-destructive technique for determining the thickness of thin films, but requires films with very low surface roughness. For the films in this study only those grown at 600°C were amenable to XRR measurements. The XRR method fits observed reflection data to simulated data utilizing film roughness, density and thickness. For the 600°C films, modeling suggests a density of approximately 10 g/cm^3 (calculated to be 10.017 g/cm^3 in Chapter 2) and a thickness on the order of 45 nm (Fig. 3). The final fit is a good qualitative match but has a relatively low correlation $R = 0.08$, which likely arises from film roughness. The model suggests a roughness of $\sim 1 \text{ nm}$, which holds true over regions of the film, but the actual surface will be seen to have additional topographical features of a larger scale. As both Fe and Pd have similar and approximately negligible vapor pressures in the temperature range being studied ($< 10^{-10} \text{ atm}$) [4], the sticking coefficient for incoming material flux to the substrate will be constant across all four deposition temperatures. Consequently, all films in the study should have the same amount of deposited material, equal in mass to a 45-50 nm

smooth film as observed at 600°C. This mass translates to 260 atomic monolayers of an FCC based Fe-Pd crystal structure, deposited 0.4 monolayers per second (7200 pulses, 10 Hz).

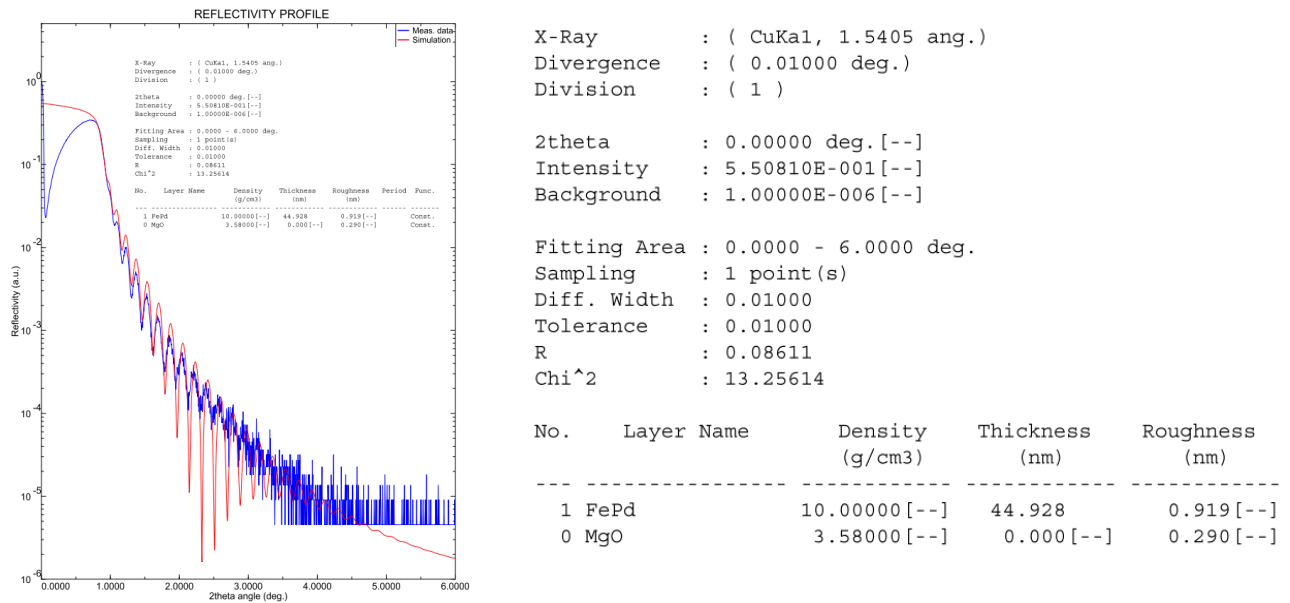


Fig. 3 - XRR data from an Fe_{38.5}Pd_{61.5} film grown at 600°C, with a qualitatively accurate model yielding a more definitive film thickness in the same 45 to 50 nm range as cross-sectional SEM.

3.2.2 – Surface Morphology and Growth Modes

Scanning electron microscopy shows a clear dependence of the films’ morphology on deposition temperature. This is best explained under the Structure Zone Model (SZM) [1] for film growth, which relates microstructural dependence in the films to the onset of different growth kinetic regimes expressed in units T/T_m, where T_m is the melting temperature of the alloy (Fig. 4). In zone I (T/T_m < 0.3) low mobility of incoming atoms leads to films with poor density and a large number of dislocations and voids. Approaching zone II (0.3 < T/T_m < 0.5), surface and grain boundary diffusion enable the formation of columnar grains resulting the beginning of epitaxy and smooth films, with dislocations located primarily at the grain boundaries. In zone III

($0.5 > T/T_m$) temperatures are high enough for the onset of bulk diffusion and coalescence of the film results in larger grain sizes. For $\text{Fe}_{38.5}\text{Pd}_{61.5}$ with $T_m \approx 1573$ K, the region for zone II growth is expected to be between the temperatures of 200 to 515°C.

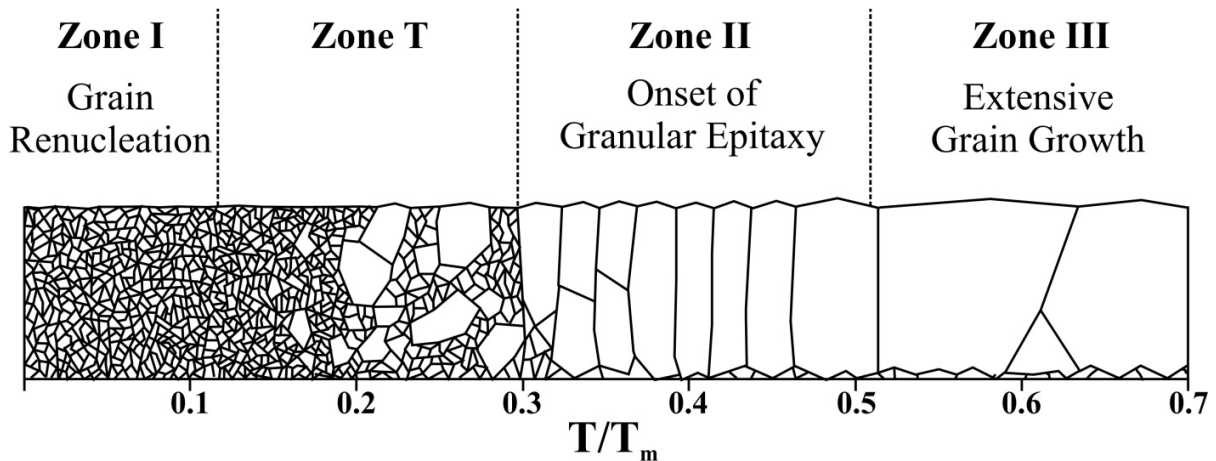


Fig. 4 - Illustration of the SZM, starting at low temperatures limited diffusion leads to low density films with high void densities. The onset of surface diffusion with increasing temperature leads to columnar grain growth, and above $T/T_m = 0.5$ bulk diffusion results in coalescence and larger grain sizes [1].

Films grown at 500°C have a nanoscale granular structure following zone II columnar grain growth and forming a continuous coverage of the MgO substrate (Fig. 5). Characteristic domed caps of the columnar grains can be seen on the surface and place their diameter at approximately 50 nm. Depositions at 550°C, in theory, have begun to transition away from zone II growth and should result in a larger grain structure; however, many unexpected regular geometric surface features with a 10 to 20 nm topology above the matrix are observed. This will be shown to be the result of a unique two-phase decomposition at this temperature. Films grown at 600°C are nearly continuous and show clear coalescence (zone III growth). Films grown at 650°C consist of nucleated islands that have not coalesced, suggesting that surface diffusion is able to act faster than the arrival of new material to the substrate.

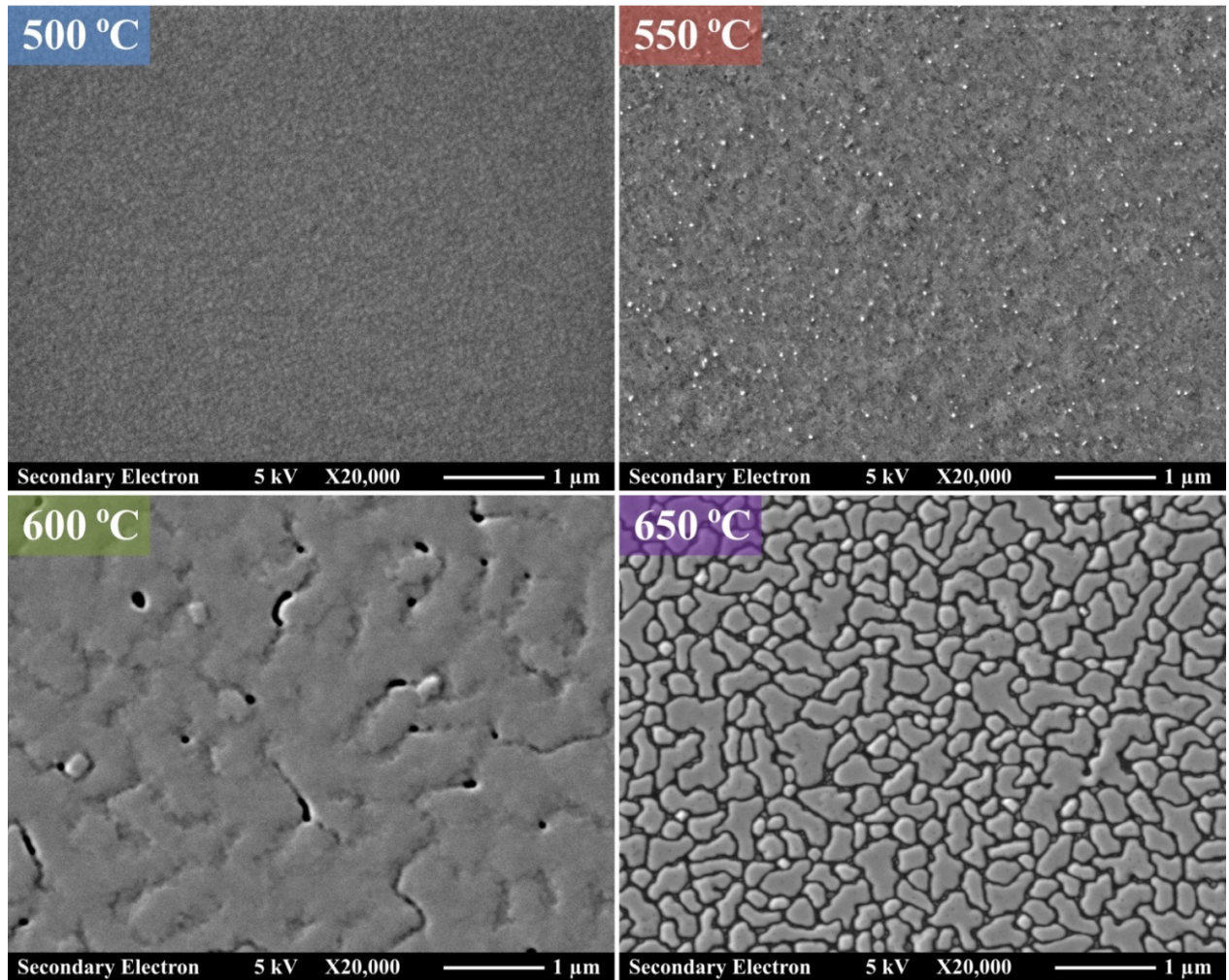


Fig. 5 - SEM micrographs of $Fe_{38.5}Pd_{61.5}$ films grown at four different temperatures showing respectively: **500°C** continuous film composed of fine columnar grains, **550°C** continuous film with distinctive rectangular features rising from the surface, resulting from a two-phase nature, **600°C** continuous film in the final stages of coalescing, **650°C** film in island growth mode.

The overall dependence of structure and morphology on deposition temperature is characteristic of thermally-activated surface diffusion during Volmer-Weber film growth, and is consistent with the literature for equiatomic FePd alloys grown on MgO (001) substrates [2, 3]. The distinctive morphology found in the films grown at 550°C is unique to the films in this study at the $Fe_{38.5}Pd_{61.5}$ composition. All films were analyzed by standardized EDXS and have no observable deviations from the target stoichiometry. Backscattered electron microscopy

suggests films grown at 500°C, 600°C, and 650°C are single-phase in nature and have no observable concentration gradients, in contrast to the films grown at 550°C (Fig. 6).

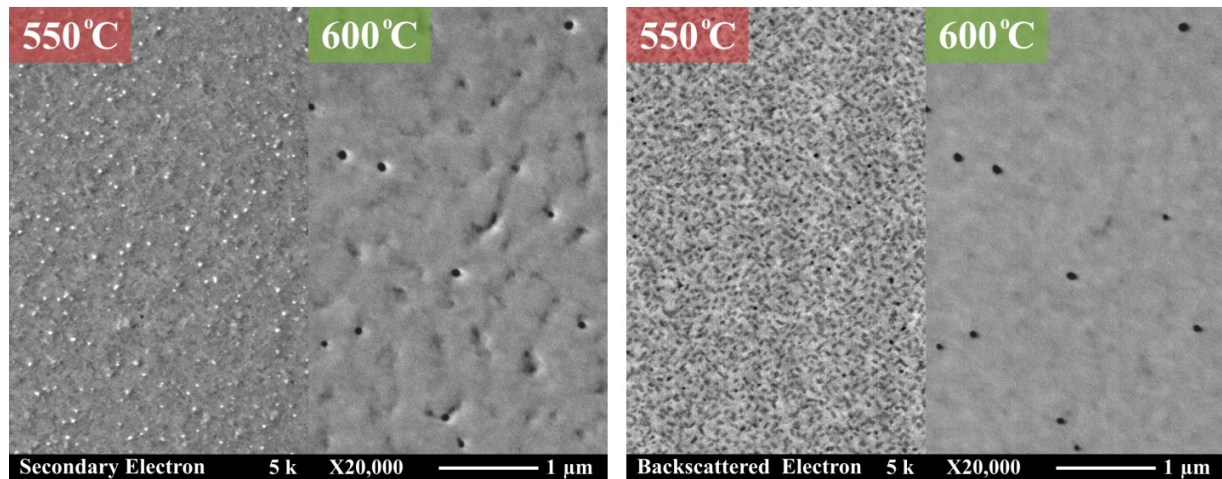


Fig. 6 – Secondary and backscattered electron micrographs contrasting films grown at 550°C and 600°C. The films at 550°C have a clear two-phase composition, while all contrast at 600°C can be explained by variations in thickness.

3.3 – Magnetic Properties

Hysteresis loops performed by VSM with an applied field perpendicular to the surface (Fig. 7) show that films grown at all four of the deposition temperatures are ferromagnetic, as evidenced by their non-zero saturation remanence [5]. The $\text{Fe}_{38.5}\text{Pd}_{61.5}$ films grown at temperatures of 500°C, 600°C and 650°C exhibit similar magnetic properties to each other; possessing saturation magnetizations on the order of 600 to 700 emu/cm^3 . The magnetic moments of these films were calculated to be 1.066 μ_{B} , 0.952 μ_{B} , and 0.980 μ_{B} per atomic site, respectively. These values are closer in magnitude to the 1.2 μ_{B} per atomic site expected in the bulk material for both the disordered FCC and ordered L_{12} phases at this composition, than the 1.6 μ_{B} per site expected for the magnetically hard L_{10} phase at $\text{Fe}_{38.5}\text{Pd}_{61.5}$ [6, 7]. A loss of saturation magnetization on the order of 20 % from the bulk (FCC / L_{12}) value is consistent with other nanoscale systems of similar length scales, as disorder at the films' interfaces can reduce

the mean magnetic moment per atom [8]. The coercivities of the 500°C, 600°C and 650°C films, between 333 and 405 Oersted, place them well outside the expected range of values for L₁₀ ordering. L₁₀ ordered Fe₄₂Pd₅₈ 10 nm particles grown on MgO substrates, near the Fe_{38.5}Pd_{61.5} composition and considerably smaller than the films, still exhibit coercivities above 3000 Oersted [9]. Consequently, the existence of anything but very weakly ordered L₁₀ is inconsistent with the magnetic properties of the films, while the FCC and L₁₂ phases could be expected to result in hysteresis loops similar to the observed behavior.

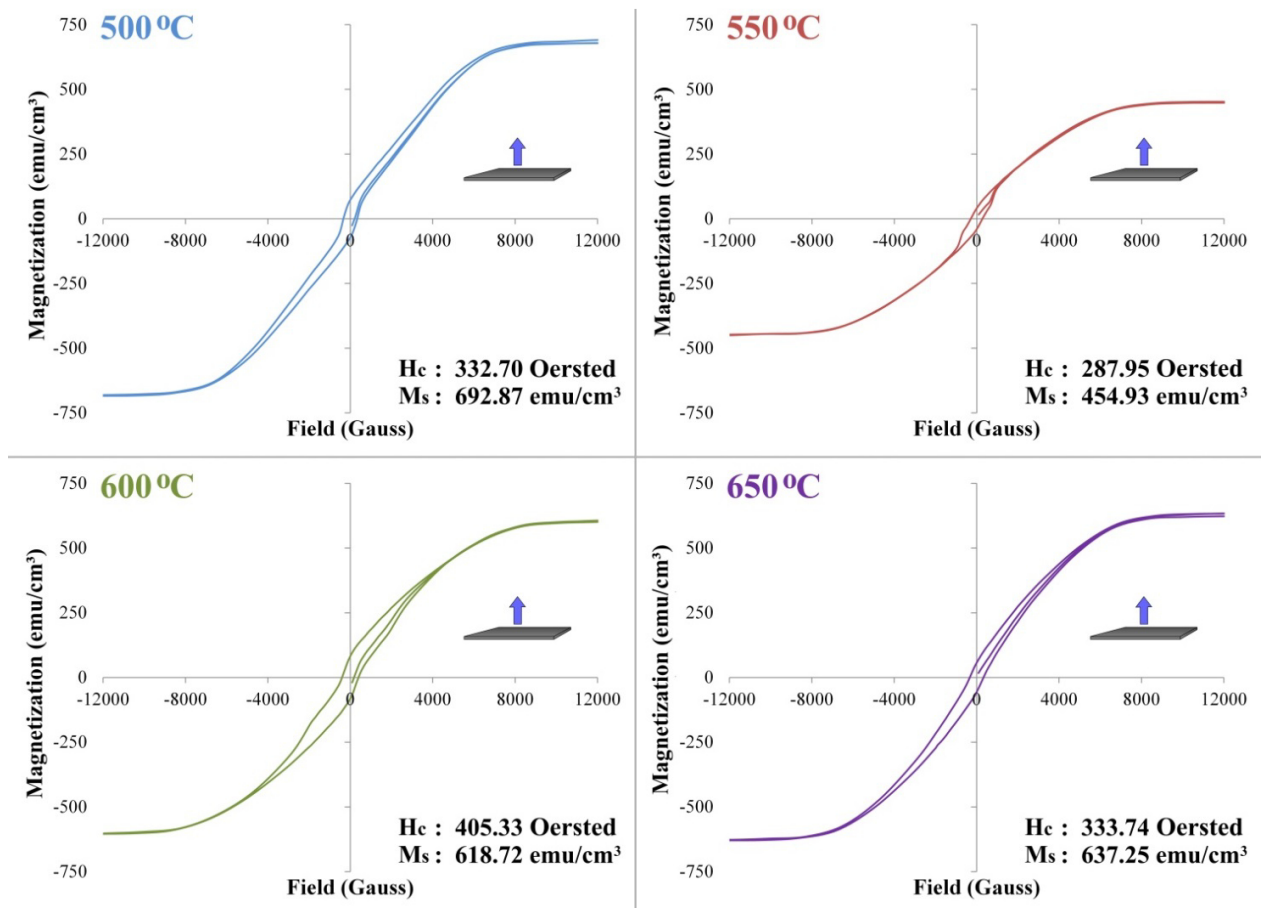


Fig. 7 - VSM hysteresis loops taken perpendicular to films grown at the four different deposition temperatures, all showing some degree of ferromagnetic behavior. Deviations to the hysteresis loops of the 500°C and 600°C films from the simple ferromagnetic behavior seen at 650°C are attributed to domain wall pinning on inhomogeneities, while those of the 550°C film result from what will be shown to be a two-phase microstructure.

Curvature deviations in the hysteresis loops of both the 500°C and 600°C films, compared to the simpler ferromagnetic behavior exhibited by the 650°C film, are attributed to domain wall pinning on inhomogeneities such as grain boundaries and other defects. The hysteresis curve of the 550°C film has both a lower coercivity and saturation magnetization, and the width of the hysteresis loop collapses for magnetizations above 120 emu/cm³. This suggests that the 550°C films have a more complicated magnetic nature than those found in the films deposited at other temperatures. These films will be addressed separately after further characterization (Chapter 5).

3.4 - Crystallographic Properties

3.4.1 - Orientation and Epitaxy

Rotational XRD ϕ -scans, where the film is placed into a suitable θ - 2θ condition for diffraction from a given family of planes and rotated about the ϕ -axis, show films at deposition temperatures between 500°C and 650°C are grown with cube-on-cube epitaxy to the MgO (001) substrates. If the film is randomly oriented no ϕ dependence would be expected, and with increasing texture the films should start to exhibit clear peaks. For cube-on-cube epitaxy, peaks of the same crystallographic family for the MgO substrate and Fe-Pd film will align, as seen in Fig. 8. The {111} family of peaks, being a fundamental reflection for both the cubic and tetragonal Fe-Pd structures, is an optimal choice for these scans. The variation in height for both the MgO and Fe-Pd peaks observed in Fig. 8 is an artifact of the alignment, step size and fast scan speeds, disappearing with closer attention to each peak.

A detailed look at a pair of {111} peaks, as seen in Fig. 9, can be used to more finely assess the degree of epitaxy in the films. For the 500°C films, the {111} Fe-Pd peaks are broad in comparison to the substrate, with a full width half maximum (FWHM) of 0.97°. This is consistent with the presence of low-angle tilt boundaries in the epitaxial film, necessary for the

columnar structure. Films grown at higher temperatures, possessing larger-grained microstructures, consistently have FWHMs on the order of half those of the 500°C films.

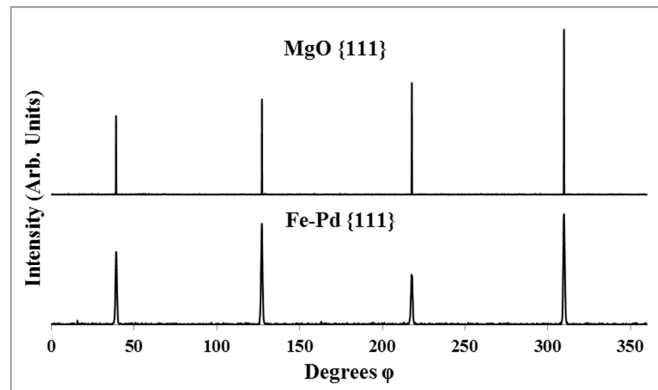


Fig. 8 - XRD ϕ -scans about the Fe-Pd {111} and MgO {111} peaks of an $Fe_{38.5}Pd_{61.5}$ film grown at 500°C confirm cube-on-cube epitaxy of the film.

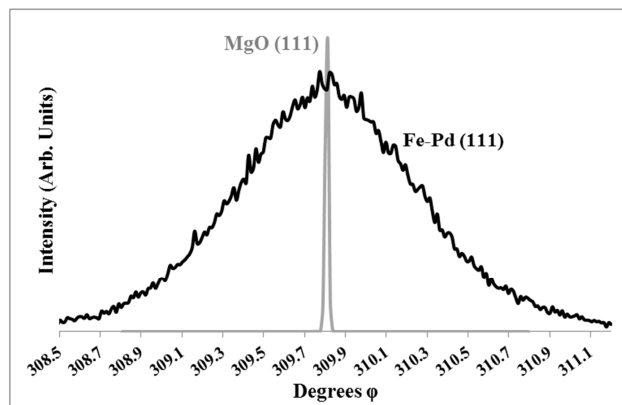


Fig. 9 - High resolution XRD ϕ -scan about the Fe-Pd (111) and MgO (111) peaks of an $Fe_{38.5}Pd_{61.5}$ film grown at 500°C, highlighting broadening of the film peak.

3.4.2 - Phase Assignment

Cube-on-cube epitaxy of the films results in conventional θ -2 θ XRD spectra ($\chi = 0$) that exhibit film peaks only for crystallographic planes normal to the substrate surface (Fig. 10). All of the $Fe_{38.5}Pd_{61.5}$ films in this study have a (001) diffraction peak present, which is an extinct reflection for the disordered FCC phase and confirms that the films are at least partially ordered. The degree of ordering, related to the size of the ordered (001) superlattice peak, can be seen to increase as the peak quadruples in integrated intensity with escalating deposition temperatures.

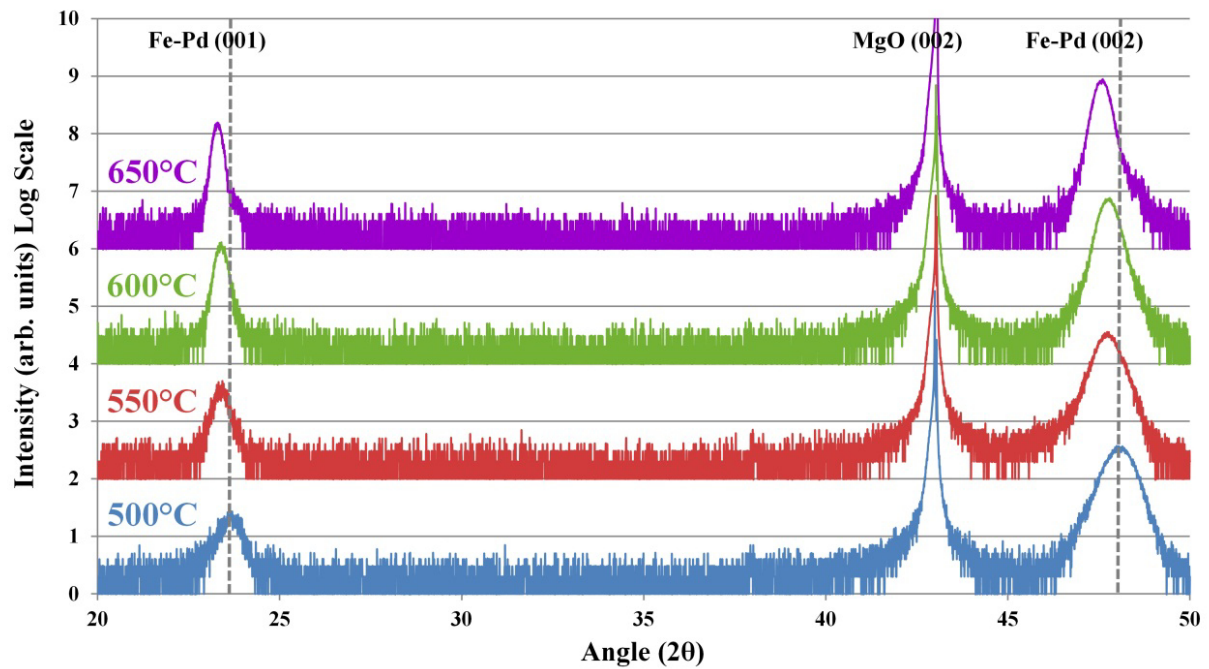


Fig. 10 - θ - 2θ X-Ray Diffraction patterns of the $Fe_{38.5}Pd_{61.5}$ film temperature series showing only epitaxial film peaks. Increased ordering, as evidenced by the intensification of the (001) film peaks, is observed with elevating temperatures. Higher temperatures are also accompanied by a shift of film peaks to lower angular values, signifying larger c -axis lattice constants.

| Film | $2\theta_{001}$ | $2\theta_{002}$ | I_{001}/I_{002} | C_{001} | C_{002} | A_{Poisson} | Strain | Strain _⊥ |
|----------|-----------------|-----------------|-------------------|-----------|-----------|----------------------|----------------------|---------------------|
| 500°C #1 | 23.50 θ | 47.74 θ | 0.033 | 3.782 Å | 3.807 Å | 3.852 Å | 0.396 % | -1.100 % |
| 500°C #2 | 23.57 θ | 48.88 θ | 0.051 | 3.771 Å | 3.796 Å | 3.856 Å | 0.499 % | -1.387 % |
| 550°C #1 | 23.40 θ | 47.74 θ | 0.081 | 3.799 Å | 3.807 Å | 3.849 Å | 0.316 % | -0.878 % |
| 550°C #2 | 23.42 θ | 47.82 θ | 0.092 | 3.795 Å | 3.801 Å | 3.851 Å | 0.363 % | -1.009 % |
| 600°C #1 | 23.36 θ | 47.71 θ | 0.096 | 3.805 Å | 3.809 Å | 3.847 Å | 0.279 % | -0.774 % |
| 600°C #2 | 23.39 θ | 47.76 θ | 0.098 | 3.799 Å | 3.806 Å | 3.849 Å | 0.321 % | -0.891 % |
| 650°C #1 | 23.30 θ | 47.58 θ | 0.114 | 3.815 Å | 3.819 Å | 3.844 Å | 0.185 % | -0.513 % |
| 650°C #2 | 23.25 θ | 47.49 θ | 0.128 | 3.823 Å | 3.826 Å | 3.841 Å | 0.114 % | -0.318 % |

Table 1 - The peak locations, out-of-plane lattice parameters, and calculated strains of the films studied. A relaxation of strain towards the expected cubic bulk parameter of 3.836 Å can be seen with elevating temperatures. The ratio of the (001) and (002) integrated peak intensities rises with increasing temperature, and allows for the determination of the ordering parameter.

The c-axis lattice parameter of the films expands with increasing deposition temperatures, as evidenced by a shift of the diffraction peaks to lower angular values, representing a relaxation of the tetragonal distortion caused by epitaxial strain. The two Fe-Pd film peaks present acuminate with increasing temperature, with the increased sharpness representing a rise in lattice periodicity as defects are annealed out of the depositing film.

The presence of all four {101} Fe-Pd peaks in XRD ϕ -scans of the deposited films yields great insight into the phases that may be present. Reflections of type {101} are extinguished for the disordered FCC phase due to destructive interference. The tetragonal $L1_0$ phase possesses {110} superlattice reflections but not {101}, making them orientation specific. The $L1_2$ phase has allowed {101} reflections regardless of its orientation as it is a cubic system. The four {101} peaks found in ϕ scans can therefore only be formed by the $L1_2$ ordered phase, or by two simultaneous variants of the tetragonal $L1_0$ existing with c-axes along perpendicular in-plane directions (in addition to a variant normal to the film accounting for the (001) peak).

Although non-trivial, the presence of the $L1_0$ phase is eliminated by a combination of XRD analysis of high-order diffraction peaks, which clearly show the films have a singular set of lattice parameters with no sign of tetragonal peak splitting, and magnetic hysteresis loops with coercivities no larger than 300-400 Oersted, much smaller than expected for $L1_0$ ordering in thin films. It is also telling that the lattice parameters of the system move with increasing temperature toward those expected for $L1_2$ at this composition, and would put the films into compression for $L1_0$ when they should be in tension. This leads to the conclusion that the films grown at 500°C, 600°C, and 650°C are all of a primarily $L1_2$ nature and the $L1_0$ ordered phase is either absent or represents a very small volume fraction. The films grown at 550°C possess a more complicated microstructure and are discussed at length in Chapter 5. These findings are

unexpected, as the c-axis oriented $L1_0$ phase has a more accommodating lattice parameter for epitaxial growth on the MgO (001) substrate. If epitaxial growth were to deter the formation of a phase, educated guesswork leads to the exclusion of $L1_2$ and not $L1_0$.

3.5 – Strain Behavior

3.5.1 - Heteroepitaxial Strain Dynamics

The absence of the $L1_0$ phase from the system at its eutectoid composition suggests that the phase diagram originally presented is subject to some level of skepticism, although conditions in thin films can diverge dramatically from the bulk equilibrium state due to strain. MgO has a cubic rock salt structure with a lattice parameter of 4.212 Å [10]. The bulk lattice constants for the FCC and $L1_2$ phases at the specific $Fe_{38.5}Pd_{61.5}$ composition used here are approximately 3.83 Å, while $L1_0$ at this composition has $a = 3.88$ Å and $c = 3.73$ Å ($\{2a+c\}/3 = 3.83$ Å) [11]. XRD analysis, combined with the alloy's Poisson ratio of 0.36 [12], yields an equilibrium (i.e. relaxed) lattice parameter of 3.836 Å for the films deposited. This closely matches the values predicted for FCC or $L1_2$ and shows that it is reasonable to treat the system as a strained film starting from the bulk equilibrium. The $Fe_{38.5}Pd_{61.5}$ alloy, therefore, has a lattice mismatch approaching 9% as it tries to conform epitaxially to the MgO substrate. However, it is unlikely that the film remains coherent to the substrate for more than a few monolayers and the actual instantaneous strain the system faces will be much smaller, due to partial relaxation from misfit dislocations along the interface (Fig. 11).

For the Fe-Pd system, ordinary dislocations will have a Burgers vector of $a/2\langle 110 \rangle$ (disordered) or $a\langle 110 \rangle$ (ordered $L1_0$ or $L1_2$) types and glide along the $\{111\}$ set of planes [13]. It is worth noting $a/2\langle 110 \rangle$ dislocations are still possible in the ordered phases but leave behind an anti-phase boundary [13]. At the (001) substrate maximal interfacial relaxation will occur when

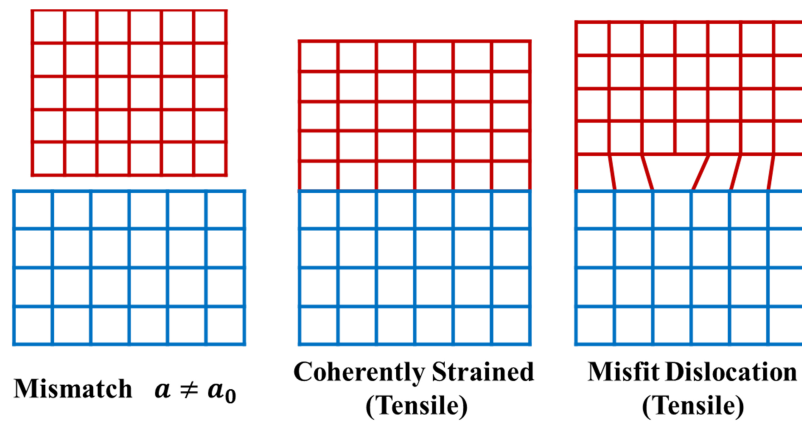


Fig. 11 – Illustration of the role of misfit dislocations at the interface relieving strain in the film.

the dislocations are of full edge character, with Burgers vectors of either $a[110]$ or $a[1\bar{1}0]$. As neither of these edge dislocations can have both their Burgers vector (b) and line direction (L) in the same $\{111\}$ glide plane ($b \cdot L = 0$ for edge), their movement is dominated by slow climb processes. Consequently, dislocations of a mixed screw/edge character, e.g. $a[101]$, known as 60° dislocations and well known to be glissile in cubic heteroepitaxial thin films, are expected to play a large role in relieving stress at the interface (Fig. 12) [14-16].

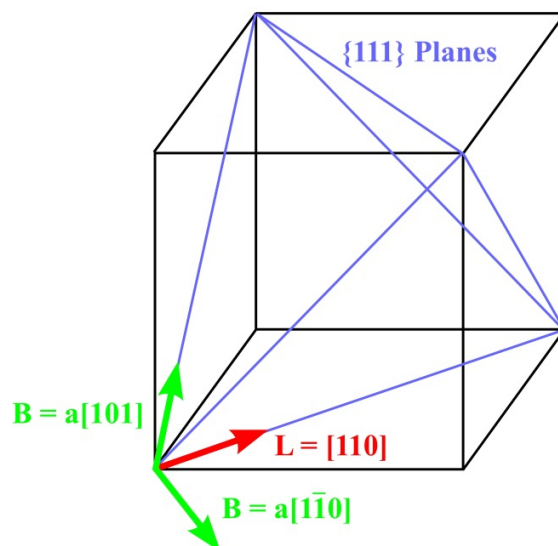


Fig. 12 – Illustration of the line direction, burgers vectors, and $\{111\}$ slip planes available for misfit dislocations. $b = a[101]$ “ 60° ” dislocations are able to glide in the system.

Once formed at the free surface, these 60° dislocations form a dislocation half loop which is able to glide to the interface and relieve strain (Fig. 13). It can be shown that the misfit portion of the loop, with $L = [1\bar{1}0]$ and $b \propto [10\bar{1}]$, once formed is indeed pulled to the surface by the tensile stress in the film, and that the remaining “threading” portions $L = [\bar{1}\bar{1}2]$ and $L = [11\bar{2}]$ are pulled by a resolved force through the crystal, extending the misfit. The force per unit length of a dislocation follows the equation

$$\frac{F}{length} = [b \cdot \sigma] \times [L] \quad (1)$$

In this case σ is the tensile stress in the film

$$\sigma = \begin{bmatrix} \sigma_0 & 0 & 0 \\ 0 & \sigma_0 & 0 \\ 0 & 0 & 0 \end{bmatrix} \quad (2)$$

For the misfit portion of the dislocation loop this leads in a resolved force in toward the interface

$$\frac{F}{l} = \begin{bmatrix} \sigma_0 & 0 & 0 \\ 0 & \sigma_0 & 0 \\ 0 & 0 & 0 \end{bmatrix} \begin{bmatrix} 1 \\ 0 \\ -1 \end{bmatrix} \times \begin{bmatrix} 1 \\ -1 \\ 0 \end{bmatrix} \propto -\sigma_0 \hat{z} \quad (3)$$

And for the two threading portions force resolves along opposite in-plane directions

$$\frac{F}{l} = \begin{bmatrix} \sigma_0 & 0 & 0 \\ 0 & \sigma_0 & 0 \\ 0 & 0 & 0 \end{bmatrix} \begin{bmatrix} 1 \\ 0 \\ -1 \end{bmatrix} \times \pm \begin{bmatrix} 1 \\ 1 \\ -2 \end{bmatrix} \propto \sigma_0 (\pm \hat{z} \pm 2\hat{y}) \quad (4)$$

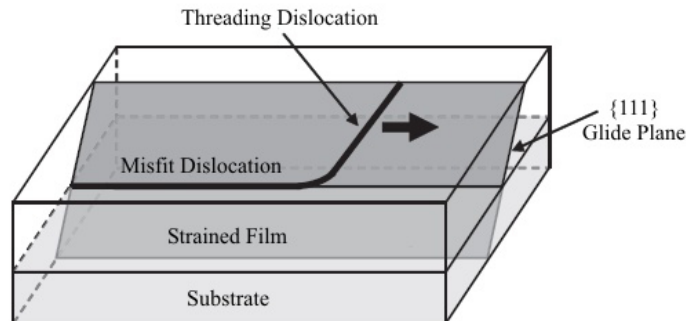


Fig. 13 – Illustration of a threading 60° misfit dislocation propagating along the interface.

Strain can arise both from lattice and thermal mismatch between the film and substrate. All the Fe-Pd films are found to be in tension along the in-plane directions and experience a Poisson compression perpendicular to the film (Table 1). The decrease of film strain with rising deposition temperature is consistent with the thermally activated formation and glide of misfit dislocations.

3.5.2 – Thermal Mismatch

Strain from thermal mismatch arises from differences in thermal expansion between the film and substrate. Both strain components of the films decrease in magnitude with increasing deposition temperature, inconsistent with significant thermal mismatch strain. Thermal expansion is often quoted in terms of an average linear thermal expansion coefficient α , and for MgO this is $1.34 \times 10^{-5} \text{ K}^{-1}$ above 0°C [10]. Thermal expansion however is not always constant and can be better formulated when it is of importance. Plotting the linear expansion coefficients of MgO, determined by three different experimental methods, it can be seen that α rises steadily over the range of temperatures used for deposition (Fig. 14) [17-19].

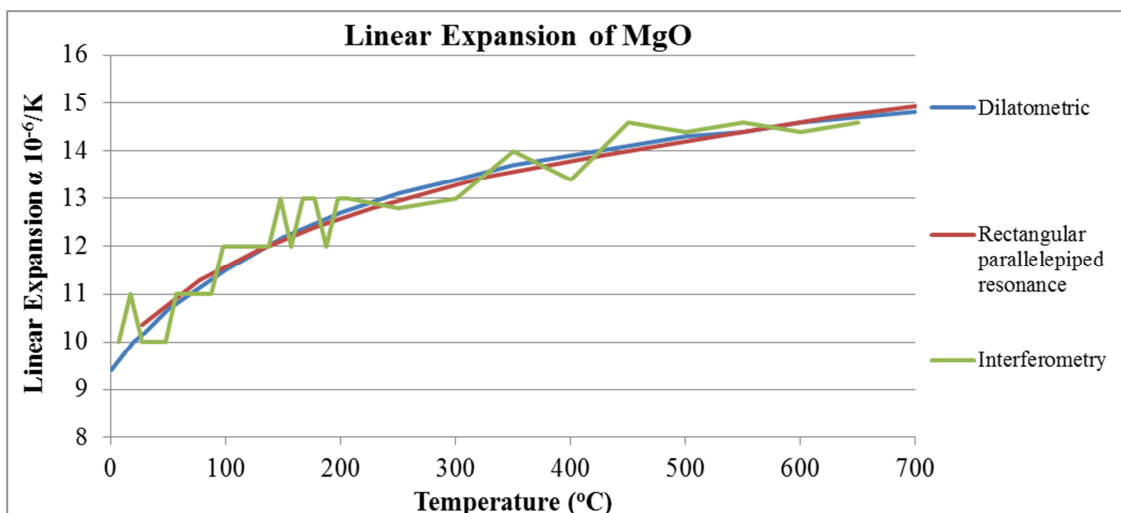


Fig. 14 – Linear expansion coefficients for MgO measured over the study’s temperature range from three different measurement techniques [17-19].

This data can in turn be used to find a more accurate effective average linear expansion coefficient for the deposition temperatures of the study (Fig. 15). For the 500°C films this is slightly lower at $1.29 \times 10^{-5} \text{ K}^{-1}$ than the original constant, while for films at 650°C it approaches the original constant at $1.33 \times 10^{-5} \text{ K}^{-1}$. $\text{Fe}_{38.5}\text{Pd}_{61.5}$ has coefficient of $1.35 \times 10^{-5} \text{ K}^{-1}$ at 20°C [20], and the data suggests that it remains approximately constant below 650°C, with the possibility of a small increase at elevated temperatures (e.g. to $1.40 \times 10^{-5} \text{ K}^{-1}$ by 700°C) [11, 20, 21]. As a consequence, the largest expected difference in the average linear expansion is on the order of $0.10 \times 10^{-5} \text{ K}^{-1}$, resulting thermal strains below 0.065%, and it's possible the contribution to tensile strain from thermal expansion could be as low as 0.001% for some films deposited between 500°C and 650°C. The scale of thermal strain is therefore negligible compared to the strains observed in Table 1.

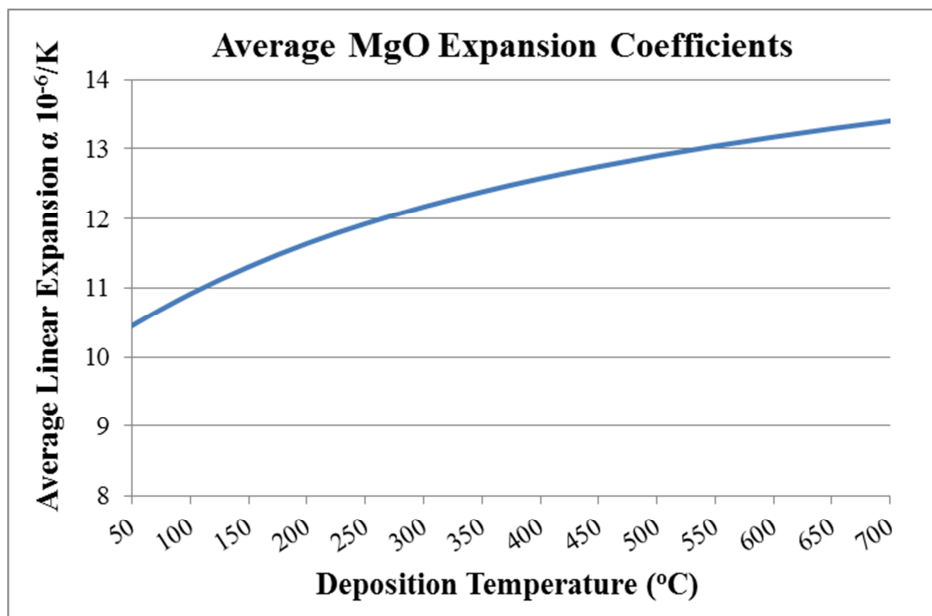


Fig. 15 – Average linear expansion coefficients for the MgO substrates, taken from room temperature to a given deposition temperature. i.e. $(\bar{\alpha})(Dep.T) = \Delta l/l_{RT}$.

3.5.3 – Epitaxial Strain Energetics

Having ruled out a significant contribution from thermal mismatch, the primary contribution to strain is expected to source from epitaxial conformance to the substrate. In order to discuss elasticity in thin films, the anisotropic version of Hooke's law must be invoked:

$$[\sigma_{ij}] = [c_{ijkl}][\varepsilon_{kl}] \quad (5)$$

$$\begin{bmatrix} \sigma_{xx} \\ \sigma_{yy} \\ \sigma_{zz} \\ \sigma_{yz} \\ \sigma_{zx} \\ \sigma_{xy} \end{bmatrix} = \begin{bmatrix} c_{11} & c_{12} & c_{13} & c_{14} & c_{15} & c_{16} \\ c_{21} & c_{22} & c_{23} & c_{24} & c_{25} & c_{26} \\ c_{31} & c_{32} & c_{33} & c_{34} & c_{35} & c_{36} \\ c_{41} & c_{42} & c_{43} & c_{44} & c_{45} & c_{46} \\ c_{51} & c_{52} & c_{53} & c_{54} & c_{55} & c_{56} \\ c_{61} & c_{62} & c_{63} & c_{64} & c_{65} & c_{66} \end{bmatrix} \begin{bmatrix} \varepsilon_{xx} \\ \varepsilon_{yy} \\ \varepsilon_{zz} \\ 2\varepsilon_{yz} \\ 2\varepsilon_{zx} \\ 2\varepsilon_{xy} \end{bmatrix} \quad (6)$$

In this Voigt notation σ_{xx} represents a stress along the x-direction of a crystal, while σ_{xz} is a shear force in the x-z plane, similarly for strains ε_{xx} and ε_{xz} . The top left quadrant of the stiffness tensor c_{ij} accounts for extension-extension coupling, the bottom right quadrant accounts for shear-shear coupling, and the remaining quadrants are extension-shear coupling between stress and strain.

For a cubic crystal, such as FCC or L1₂, symmetry reduces the stiffness tensor to

$$[c_{ij}]_{cubic} = \begin{bmatrix} c_{11} & c_{12} & c_{12} & & & \\ c_{12} & c_{11} & c_{12} & & & \\ c_{12} & c_{12} & c_{11} & & & \\ & & & c_{44} & & \\ & & & & c_{44} & \\ & & & & & c_{44} \end{bmatrix} \quad (7)$$

While tetragonal crystals of type P4/mmm, such as L1₀, reduce to the form

$$[c_{ij}]_{tetra} = \begin{bmatrix} c_{11} & c_{12} & c_{23} & & & \\ c_{12} & c_{11} & c_{23} & & & \\ c_{23} & c_{23} & c_{33} & & & \\ & & & c_{44} & & \\ & & & & c_{44} & \\ & & & & & c_{66} \end{bmatrix} \quad (8)$$

As cubic systems can be treated as a special case of the tetragonal, derivations need to be made only once. For a tetragonal film in biaxial tension from cube-on-cube epitaxy

$$\begin{bmatrix} \sigma_0 \\ \sigma_0 \\ 0 \\ 0 \\ 0 \\ 0 \end{bmatrix} = \begin{bmatrix} c_{11} & c_{12} & c_{23} & & & \\ c_{12} & c_{11} & c_{23} & & 0 & \\ c_{23} & c_{23} & c_{33} & & & \\ & & & c_{44} & & \\ & 0 & & & c_{44} & \\ & & & & & c_{66} \end{bmatrix} \begin{bmatrix} \varepsilon_{xx} \\ \varepsilon_{yy} \\ \varepsilon_{zz} \\ 2\varepsilon_{yz} \\ 2\varepsilon_{zx} \\ 2\varepsilon_{xy} \end{bmatrix} \quad (9)$$

Using linear algebra, the bottom three lines of Eq. 9 reduce to $\varepsilon_{yz} = \varepsilon_{zx} = \varepsilon_{xy} = 0$, leaving

$$\begin{bmatrix} \sigma_0 \\ \sigma_0 \\ 0 \end{bmatrix} = \begin{bmatrix} c_{11} & c_{12} & c_{23} \\ c_{12} & c_{11} & c_{23} \\ c_{23} & c_{23} & c_{33} \end{bmatrix} \begin{bmatrix} \varepsilon_{xx} \\ \varepsilon_{yy} \\ \varepsilon_{zz} \end{bmatrix} \quad (10)$$

$$\sigma_0 = c_{11}\varepsilon_{xx} + c_{12}\varepsilon_{yy} + c_{23}\varepsilon_{zz} \quad (11)$$

$$\sigma_0 = c_{12}\varepsilon_{xx} + c_{11}\varepsilon_{yy} + c_{23}\varepsilon_{zz} \quad (12)$$

$$0 = c_{23}\varepsilon_{xx} + c_{23}\varepsilon_{yy} + c_{33}\varepsilon_{zz} \quad (13)$$

By the symmetry of Eqs. 11 and 12, it is clear that $\varepsilon_{xx} = \varepsilon_{yy}$, and it follows that

$$\varepsilon_{zz} = -2 \left(\frac{c_{23}}{c_{33}} \right) \varepsilon_{xx} \quad (14)$$

$$\sigma_0 = (c_{11} + c_{12})\varepsilon_{xx} + c_{23}\varepsilon_{zz} \quad (15)$$

This allows for the calculation of the biaxial modulus M , a term which relates the in-plane film strain with an associated stress

$$\sigma_0 = \left(c_{11} + c_{12} - 2 \frac{c_{23}^2}{c_{33}} \right) \varepsilon_{xx} = M \varepsilon_{xx} \quad (16)$$

$$M = \left(c_{11} + c_{12} - 2 \frac{c_{23}^2}{c_{33}} \right) \quad (17)$$

The biaxial modulus can be used to find the elastic energy density for a biaxially strained film, which will follow $W_{el} = M\epsilon^2$. The in-plane strain contribution, ϵ , will in turn be heavily dependent on the availability of misfit dislocations to relieve strain at the interface. As the $L1_2$ and $L1_0$ phases share a common Burgers vector, $b = a\langle 101 \rangle$, the relative ease of creating misfit dislocations will correspond to the dislocation energy $E \propto Gb^2$ where G can be taken as the Voigt average of the shear modulus. The Voigt average approximates the moduli by averaging across all possible tensor rotations. For a tetragonal system this is given by the equations [22] :

$$G_{voigt} = \frac{A-B+3C}{5} \quad (18)$$

$$A = \frac{2c_{11}+c_{33}}{3} \quad B = \frac{2c_{23}+c_{12}}{3} \quad C = \frac{2c_{44}+c_{66}}{3}$$

The Poisson ratio can also be approximated in this manner, and yields results of approximately $\gamma = 0.35$, slightly shy of the experimentally determined value of $\gamma = 0.36$ [12].

$$\gamma_{voigt} = \frac{A+4B-2C}{4A+6B+2C} \quad (19)$$

Ideally, the components of the alloy's stiffness tensor would be known for all three phases at the non-stoichiometric composition. Given limited study of the eutectoid region of the Fe-Pd phase diagram, these values can only be interpolated from the available data. Table 2 compiles all available experimental measurements of the stiffness constants for the relevant phases of the Fe-Pd system. The disordered FCC phase has been characterized at both equiatomic $Fe_{50}Pd_{50}$ and Pd-rich $Fe_{10}Pd_{90}$ compositional extrema [23, 24], and experiences a slight stiffening in transverse components of the tensor with increasing Pd content. The $L1_0$ phase at the equiatomic FePd composition has been analyzed across a series of processing conditions [23, 25, 26] and varies considerably from the FCC values. The $FePd_3 L1_2$ phase has only one experimental value which was taken at liquid nitrogen temperature (80 K) and therefore

cannot be compared directly with the other measurements, which were made at ambient temperature conditions [26]. Additionally, values at elevated temperature are available for equiatomic L1₀ and disordered Fe₅₀Pd₅₀ [26].

| Type | Temp. | C ₁₁ | C ₁₂ | C ₂₃ | C ₃₃ | C ₄₄ | C ₆₆ | M (GPa) | G (GPa) | Ref. |
|---------------------------------------|--------|-----------------|-----------------|-----------------|-----------------|-----------------|-----------------|---------|---------|------|
| γ - Fe ₁₀ Pd ₉₀ | RT | 229 | 165 | | | 86 | | 156 | 64 | 24 |
| γ - Fe ₅₀ Pd ₅₀ | RT | 215 | 161 | | | 83 | | 135 | 61 | 23 |
| L1 ₀ -FePd | RT | 226 | 154 | 154 | 238 | 92 | 96 | 181 | 71 | 23 |
| L1 ₀ -FePd | RT | 218 | 148 | 151 | 227 | 92 | 94 | 165 | 70 | 23 |
| L1 ₀ -FePd | RT | 214 | 143 | 143 | 227 | 92 | 93 | 177 | 70 | 25 |
| L1 ₀ -FePd | RT | 213 | 142 | 146 | 225 | 92 | 99 | 166 | 71 | 25 |
| L1 ₀ -FePd | RT | 248 | 159 | 159 | 239 | 95 | 86 | 195 | 72 | 26 |
| L1 ₂ -FePd ₃ | 80 K | 206 | 122 | | | 90 | | 183 | 71 | 26 |
| L1 ₀ -FePd | 860 K | 202 | 122 | 122 | 200 | 76 | 48 | 175 | 56 | 26 |
| γ - Fe ₅₀ Pd ₅₀ | 1020 K | 178 | 125 | | | 64 | | 127 | 49 | 26 |

Table 2 – Experimental values of the stiffness tensor, biaxial and shear moduli for FCC, L1₂ and L1₀ phases at different temperatures and compositions.

For the Fe_{38.5}Pd_{61.5} composition, the known stiffness values for the FCC phase are close enough that they can be linearly interpolated without any substantial loss of accuracy. As the L1₂ phase maintains the cubic nature of the disordered FCC, it is expected that its elastic properties will be similar. Study of the FCC → L1₂ ordered transition on the elasticity of AuCu₃, a closely related material system, demonstrates that this is a reasonable assumption. Theoretical work suggests that ordering results in a correlated 4% maximum rise in C₁₁ and C₁₂ for AuCu₃ [27], and experimental data shows no change in the elastic constants within the margin of error [28]. Similar theoretical work on FePd₃ predicts a model-dependent 2.4 to 8.4% rise in the bulk modulus, B, going from disordered to fully ordered L1₂ [29]. The Voigt average of the bulk modulus for cubic system [30] is given by

$$B_{cubic} = \frac{c_{11} + 2c_{12}}{3} \quad (20)$$

If, with ordering, the C_{11} and C_{12} components follow a comparable correlated increase as expected for AuCu_3 , the behavior of $L1_2$ at $\text{Fe}_{38.5}\text{Pd}_{61.5}$ can also be approximated as about 4 % stiffer than the disordered phase (maximum ordering possible at non-stoichiometric $\text{Fe}_{38.5}\text{Pd}_{61.5}$ being $S_{\max} = 0.82$). For the $L1_0$ phase at $\text{Fe}_{38.5}\text{Pd}_{61.5}$, values of the stiffness constants can be found by first-order interpolation; observing the percentage differences between FCC and the average of the data $L1_0$ at $\text{Fe}_{50}\text{Pd}_{50}$, translating this percentage to $\text{Fe}_{38.5}\text{Pd}_{61.5}$, and accounting linearly for the loss of order due to non-stoichiometry ($S_{\max} = .77$). The approximated values for all three phases of $\text{Fe}_{38.5}\text{Pd}_{61.5}$ can be found in Table 3. If we accept these values as accurate, it is clear that the $L1_0$ phase has a larger biaxial and shear moduli than the two cubic phases at this composition. While these are room temperature values, data taken closer to the deposition temperatures (Table 2) suggests that the biaxial modulus for $L1_0$ remains considerably larger than the cubic phases across the entire temperature range.

| Type | Temp. | C_{11} | C_{12} | C_{23} | C_{33} | C_{44} | C_{66} | M (GPa) | G (GPa) |
|---|-------|----------|----------|----------|----------|----------|----------|---------|---------|
| $\gamma - \text{Fe}_{38.5}\text{Pd}_{61.5}$ | RT | 219 | 162 | | | 86 | | 141 | 63 |
| $L1_2 - \text{Fe}_{38.5}\text{Pd}_{61.5}$ | RT | 228 | 169 | | | 89 | | 147 | 65 |
| $L1_0 - \text{Fe}_{38.5}\text{Pd}_{61.5}$ | RT | 226 | 153 | 153 | 232 | 94 | 94 | 177 | 71 |

Table 3– Approximate values of the stiffness tensor, biaxial and shear moduli for FCC, $L1_2$ and $L1_0$ phases based on interpolation from known data.

The higher biaxial moduli of the $L1_0$ phase could explain in part why it is not strongly favored by the 4.212 Å MgO substrate, despite having a lattice parameter of 3.88 Å compared to the 3.83 Å of the cubic phases. Misfit dislocations relieving strain have a linear energy density of $E_1 \approx Gb^2/2\pi$, though their strain field is complicated by introduction of the MgO interface. As the dislocation energy density will prove to be negligible, the strain field can be approximated as being half in the film and half in the substrate ($G= 124$ GPa [31]). Each of these misfit dislocations results in a relaxation on the interface that is a projection of their edge character along one direction, i.e. $a[101] \cdot [100] = a$ and $a[101] \cdot [010] = 0$.

Two perpendicular dislocations over a square meter of material will relieve (a/m) worth of biaxial tensile strain, using a total dislocation length 2 m. The areal energy density of dislocations required to relieve $\Delta\varepsilon$ strain is thus

$$\frac{E_{dislocation}}{m^2} = (2m) \left(\frac{Gb^2}{2\pi} \right) \left(\frac{\Delta\varepsilon}{a/m} \right) \left(\frac{1}{m^2} \right) = \frac{2aG\Delta\varepsilon}{\pi} \quad (21)$$

Using this convention, W_{el} can be written accounting for a thickness t and coherent strain ε_0 as

$$\frac{E_{elastic}}{m^2} = M(\varepsilon_0 - \Delta\varepsilon)^2 t \quad (22)$$

This allows for the total energy related to elastic strain and misfit dislocations to be calculated for the $L1_0$ and $L1_2$ phases as a function of the strain relieved from coherence for a 50 nm thick film (Fig. 16). The strain energetics of the system suggests that $L1_0$ is still favored, but, after significant relaxation has occurred ($> 80\%$), the difference in strain energy between $L1_0$ and $L1_2$ will play only a negligible role. As evidenced by the strain energy at full relaxation, which is the maximum contribution of $E_{dislocation}$, the elastic term dominates the dislocation energy for most strains, placing emphasis on the larger biaxial modulus M of $L1_0$. Consequentially, the trend in strain related energy would still hold if $a/2[110]$ happens to be the dominant dislocation instead of $a[110]$. It can be inferred from the strain energies that the preference for $L1_2$ must come from strain-induced effects in another contribution to the system, such as the large magnetic energy. Films clearly show a tendency away from $L1_0$ lattice values, and the different elastic properties of the phases are relevant only at the early stages of growth when films experience large strains.

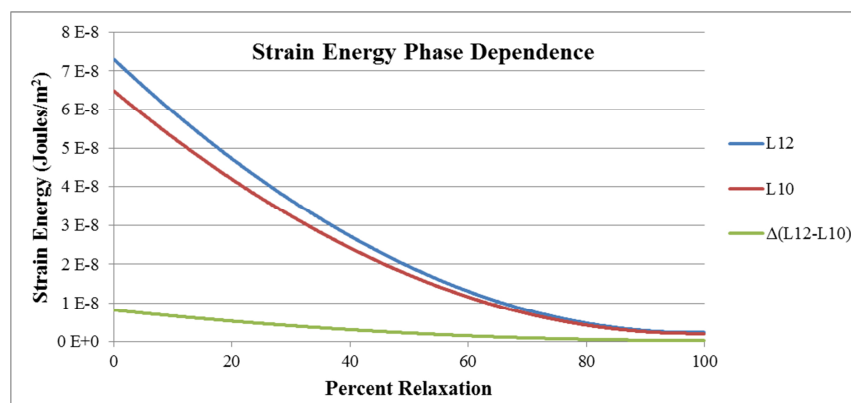


Fig. 16 – Total strain energies from elastic and misfit contributions for 50 nm thick films.

3.6 – Ordering Behavior

At sufficiently low deposition temperatures, films will be kinetically limited from transforming completely into the equilibrium ordered phases during the finite length of the deposition process. $\text{Fe}_{38.5}\text{Pd}_{61.5}$ material arriving at the surface during PLD is expected to be a mixture of ions, atomic clusters, and nanoparticles in the disordered FCC phase of the material [32]. This was confirmed by depositing $\text{Fe}_{38.5}\text{Pd}_{61.5}$ via PLD at 3.0 J/cm^2 in 100 mTorr (13.3 Pa) He onto Type A carbon support grids (Ted Pella) at room temperature for HRTEM. After 150 pulses it can be seen that a coalescing network of 2 nm nanoparticles has begun to form on the TEM grid (Fig. 17). With no superlattice planes present in the FFT pattern it is confirmed that material is deposited in the disordered FCC phase.

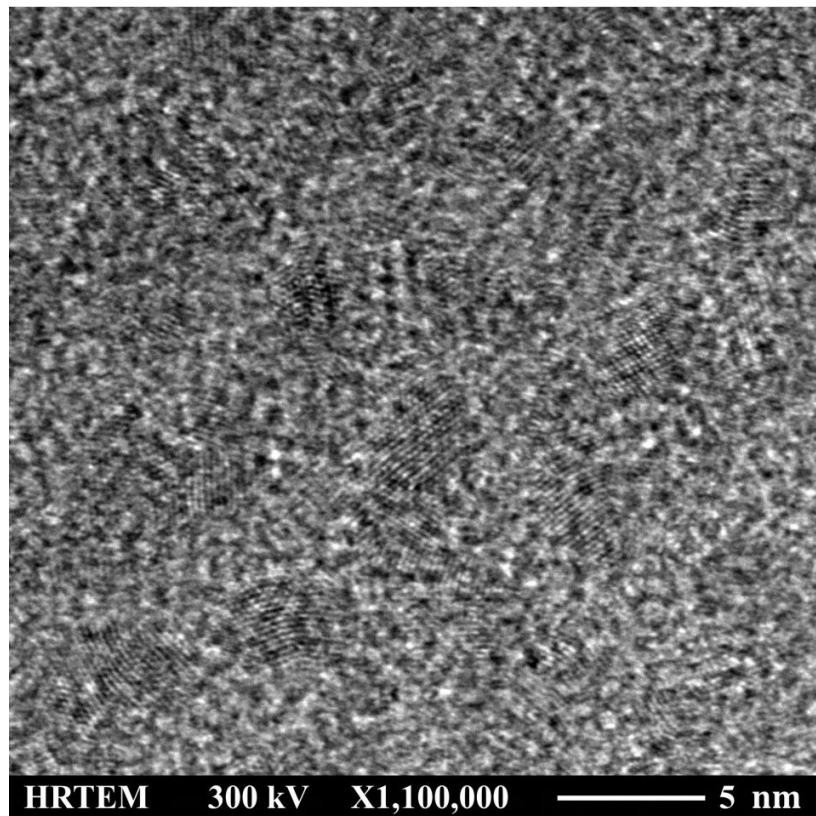


Fig. 17 – HRTEM micrograph of $\text{Fe}_{38.5}\text{Pd}_{61.5}$ material deposited by PLD, forming a coalesced network of disordered, FCC nanoparticles.

After arrival onto the heated substrate this FCC material will begin to increase in long range order. Transformations between the disordered FCC, $L1_0$, and $L1_2$ phases of the Fe-Pd system are first-order phase transitions [33], experiencing nucleation and growth of ordered phases as opposed to a continuous increase in ordering at the atomic scale. However, as illustrated in Landau's free energy vs. generalized order parameter plots, there is an instability temperature below which the transformation can occur as a higher-order phase transition [34]. Concentration or strain fluctuations, both of which are present in the thin films studied, also can increase the likelihood of a higher-order phase transition [35].

The long-range ordering parameter S as defined for $L1_2$, which is different than S as defined for $L1_0$, may be determined from the XRD data by careful comparison of the superlattice and fundamental peak intensities. For quantitative analysis this is complex but well-established, and covered in depth in the experimental procedures. As classically defined, the ordering parameter will take the value of zero when the Fe and Pd atoms are randomly distributed over the entire FCC lattice, and approaches unity as the $L1_2$ Fe sites are filled exclusively by Fe atoms and the Pd sites exclusively by Pd atoms. For the non-stoichiometric $Fe_{38.5}Pd_{61.5}$ the $L1_2$ ordering parameter can achieve a maximum value of $S = 0.82$, as there will always be Fe remaining on the Pd sites of the $L1_2$ lattice. As a result, the ratio of superlattice to fundamental peaks, I_{001}/I_{002} , has a theoretical maximum of 0.0886 for the epitaxial $L1_2$ - $Fe_{38.5}Pd_{61.5}$ films. This is problematic given the higher values found for the single phase films in this study at 600°C and 650°C (Table 1). Closer study shows that the anomaly in superlattice peak intensities arises from an elevation in peaks shared by c-axis oriented $L1_0$ relative to other superlattice peak variants. This discrepancy has been found to result from Fe atoms in the 600°C and 650°C films sitting in unequal concentrations across the three Pd sites of the $FePd_3$ superlattice, forming a

slightly perturbed version of the $L1_2$ phase that gives special preference to the c-axis oriented $(1/2, 1/2, 0)$ sites and will be discussed later at length (Chapter 4).

Comparing the degree of ordering found in these films to other publications, nanocrystalline powders of $Fe_{40}Pd_{60}$, just outside of the projected two phase region of the equilibrium phase diagram, have long range order parameters that increase from disordered FCC to $L1_0$ in a linear manner with increasing temperature, starting at approximately 30% ordered by volume at $375^\circ C$ and fully ordered by $625^\circ C$ [36]. Putting aside the complications of any perturbation and treating the films as conventional $L1_2$, films in this study show good general agreement with the published $Fe_{40}Pd_{60}$ nanocrystalline ordering behavior. Films grown at $500^\circ C$ are found to be in the territory of 60 to 70 % ordered. The $600^\circ C$ and $650^\circ C$ films are 97% and 100% ordered, respectively. Consequently, the degree of ordering in the films is similar to other nanoscale studies, occurring significantly below the bulk order-disorder transition temperature.

3.7 – Major Findings

Thin films of $\text{Fe}_{38.5}\text{Pd}_{61.5}$ were grown by PLD onto MgO (001) substrates between 500°C and 650°C. Films grown at 550°C exhibit different behaviors than those grown at other temperatures, experiencing a two-phase decomposition and meriting further discussion. All films grow with cube-on-cube epitaxy with the substrate and show a preference for a tetragonally distorted $L1_2$ phase due to epitaxial strain, with the degree of order rising steadily across the temperature range. No signs of the $L1_0$ phase were observed for any films in the study. Thermal mismatch with the substrate is negligible and film strain declines with increasing deposition temperature. The difference in elastic strain energies between the $L1_0$ and $L1_2$ phases is shown to be small once full coherency is lost, explaining why the lower lattice mismatch of the $L1_0$ phase does not dominate behavior; this allows another contribution, possibly magnetism, to preference the $L1_2$ phase. An anomaly from the predicted values for superlattice intensities of the $L1_2$ phase has also been noted.

In the following chapter the anomalous superlattice behavior of the films will be shown to arise from the existence of a metastable hybrid of the $L1_0$ and $L1_2$ structures, $L1'$, once theorized to exist in the prototypical Au-Cu ordered system based on statistical thermodynamics [37]. The unique two-phase films grown at 550°C will then be examined closer in Chapter 5, with the phases identified and the origination and behavior of the decomposition discussed.

References

- [1] B. Movchan and A. Demchishin, *Fiz. Met. Metalloved* **28**, 83 (1969)
- [2] M. Ohtake, S. Ouchi, F. Kirino, and M. Futamoto, *J. Appl. Phys.* **111**, 07A708 (2012)
- [3] D. Wei and Y. Yao: *Appl. Phys. Lett.* **95**, 172503 (2009)
- [4] R. Honig, *RCA Rev.* **23**, 567 (1962) & **30**, 285 (1969)
- [5] B. Cullity, *Introduction to Magnetic Materials* (Addison-Wesley, Reading, MA, 1972)
- [6] E. Burzo and P. Vlaic, *J. Optoelectron. Adv. M.* **12**, 1869 (2010)
- [7] X. Sun, X. Xu, G. Dong, and X. Jin, *Phys. Lett. A* **372**, 1687 (2008)
- [8] H. Lu, W. Zheng, and Q. Jiang, *J. Phys. D: Appl. Phys.* **40**, 320 (2007)
- [9] K.Sato, B. Bian, and Y. Hirotsu, *J. Appl. Phys.* **91**, 8516 (2002)
- [10] O. Madelung, U. Rossler, and M. Schulz, *Landolt-Börnstein: Numerical Data and Functional Relationships in Science and Technology* (Springer-Verlag, 1999) Vol. 41B
- [11] E. Raub, H. Beeskow, and O. Loebich, *Z. Metallkd.* **54**, 549 (1963)
- [12] T. Ichitsubo and K. Tanaka, *J. Appl. Phys.* **96**, 6220 (2004)
- [13] M. Rao and W.A. Soffa, *Scripta Mater.* **36**, 735 (1997)
- [14] J. Matthews and A Blakeslee, *J. Cryst. Growth*, **27**, 118 (1974)
- [15] J. Matthews and A Blakeslee, *J. Cryst. Growth*, **29**, 273 (1975)
- [16] J. Matthews and A Blakeslee, *J. Vac. Sci. Tech.*, **12**, 126 (1975)
- [17] Y. Sumino, O. Anderson, and I. Suzuki, *Phys. Chem. Miner.* **9**, 38 (1983)
- [18] M. Durand, *J. Appl. Phys.* **7**, 297 (1936)
- [19] I. Suzuki, *J. Phys. Earth* **23**, 145 (1975)
- [20] A. Kußmann and K. Jessen, *Z. Metallkd.* **54**, 504 (1963)
- [21] T. Mehaddene, E. Kentzinger, B. Hennion, K. Tanaka, H. Numakura, A. Marty, V. Parasote, M. Cadeville, M. Zemirli, and V. Pierron-Bohnes, *Phys. Rev. B* **69**, 024304 (2004)
- [22] J. Toonder, J. Dommelen, and F. Baaijens, *Mod. Simul. Mater. Sci. Eng.* **7**, 909 (1999)
- [23] T. Ichitsubo and K. Tanaka, *J. Appl. Phys.* **96**, 6220 (2004)
- [24] B. Dutta and S. Ghosh, *J. Phys., Condens. Matter* **21**, 395401 (2009)
- [25] A. Al-Ghaferi, P. Müllner, H. Heinrich, G. Kostorz, J. Wiezorek, *Acta Mater.* **54**, 881 (2006)
- [26] T. Mehaddene, E. Kentzinger, B. Hennion, K. Tanaka, H. Numakura, A. Marty, V. Parasote, M. Cadeville, M. Zemirli, and V. Pierron-Bohnes, *Phys. Rev. B* **69**, 024304 (2004)
- [27] G. Wang, E. Delczeg-Czirjak, Q. Hu, K. Kokko, B. Johansson, and L. Vitos, *J. Phys.: Condens. Matter* **25**, 085401 (2013)
- [28] P. Flinn, G. McManus, and J. Rayne, *J. Phys. Chem. Solids* **15**, 189 (1960)
- [29] B. Dutta, S. Bhandary, S. Ghosh, B. Sanyal, *Phys. Rev. B* **86**, 024419 (2012)
- [30] T. Uesugi, Y. Takigawa and K. Higashi, *Mater. Trans.*, **46**, 1117 (2005)
- [31] S. M. Lang, *Properties of High-Temperature Ceramics and Cermets* (National Bureau of Standards, Washington, D.C. 1960).
- [32] R. Eason, *Pulsed Laser Deposition of Thin Films* (John Wiley & Sons, 2007)
- [33] B. Zhang, M. Lelovic, and W. Soffa, *Scripta Metall. Mater.* **25**, 1577 (1991)
- [34] L. Landau, and E. Lifshitz, *Statistical Physics. 3rd edn.* (Pergamon Press, London, 1980)
- [35] K. Binder, *Rep. Prog. Phys.* **50**, 783 (1987)
- [36] J. Lyubina, O. Gutfleisch, and O. Isnard, *J. Appl. Phys.* **105**, 07A717 (2009)
- [37] W. Shockley, *J. Chem. Phys.* **6**, 130 (1938)

4 – L1' Ordering : Evidence of L1₀-L1₂ Hybridization

4.1 - Introduction

A unique finding of the growth temperature study of Fe_{38.5}Pd_{61.5} deposited onto MgO (001) substrates in Chapter 3 was that L1₂ natured films grown at 600°C and 650°C possessed anomalous superlattice peak intensities, where reflections also allowed by c-axis oriented L1₀ are elevated slightly in relation to other variants. These films were confirmed to be of a single, uniform composition by backscattered electron microscopy. VSM hysteresis loops (Ch.3, Fig 7) do not suggest the presence of two separate phases, especially one with the coercivity expected for L1₀ ordering. MFM shows no discernible indication of two-phase magnetic behavior or the nanoscale presence of magnetically hard precipitates. XRD peaks of the films are sharp, singular and Gauss-Lorentzian in profile, indicating the film has only one set of lattice parameters. It was concluded from this evidence that no significant L1₀ precipitates were present to contribute to the superlattice peak anomaly. Intensity variations are instead suggested to arise from tetragonality in Fe_{38.5}Pd_{61.5} films induced by tensile epitaxial strain, breaking symmetry in the three face-centered L1₂ Pd superlattice sites into two variants which no longer share the same composition. This perturbation gives special preference to the c-axis oriented (1/2, 1/2, 0) sites, and will be shown to be the result of L1₀-L1₂ hybridization into a metastable L1' phase. This chapter expands markedly on initial observations of the anomaly with the growth of additional films of varying thickness and rigorous quantitative XRD analysis of multiple peaks, confirming the presence of an L1' phase. It also addresses the proper handling of ordering in the complex L1' system by expanding conventional notation for the L1₀ and L1₂ phases and offers speculation concerning formation.

4.2 - History of L1' Ordering

Existence of L1' ordering was first proposed by William Shockley in 1938 for Au-Cu alloys, based on Mean Field Theory (MFT) and Bethe's nearest-neighbor assumption statistical thermodynamics [1]. Au-Cu is considered the prototypical ordered FCC material system, exhibiting not only the tetragonal L1₀ phase but both cubic L1₂ variants, and consequentially serves as the model for most theoretical work on FCC ordering phenomena. In this treatment the FCC lattice can be viewed as a compilation of four interlocking simple cubic sublattices; each occupied by some statistical composition and designated L₁, L₂, L₃ and L₄ (Fig. 1). For the disordered case (L₁ = L₂ = L₃ = L₄) the entire system can be represented by one parameter, alloy composition. L1₂ (L₁ ≠ L₂ = L₃ = L₄) and L1₀ (L₁ = L₂ ≠ L₃ = L₄) structures are fully described by the alloy composition in combination with an ordering parameter relating the relative compositions of the two sublattices. Tetragonal L1' (L₁ ≠ L₂ ≠ L₃ = L₄) and orthorhombic (L₁ ≠ L₂ ≠ L₃ ≠ L₄) symmetries are also possible, requiring two and three ordering parameters respectively due to their lower symmetries and increased number of variant sublattices.

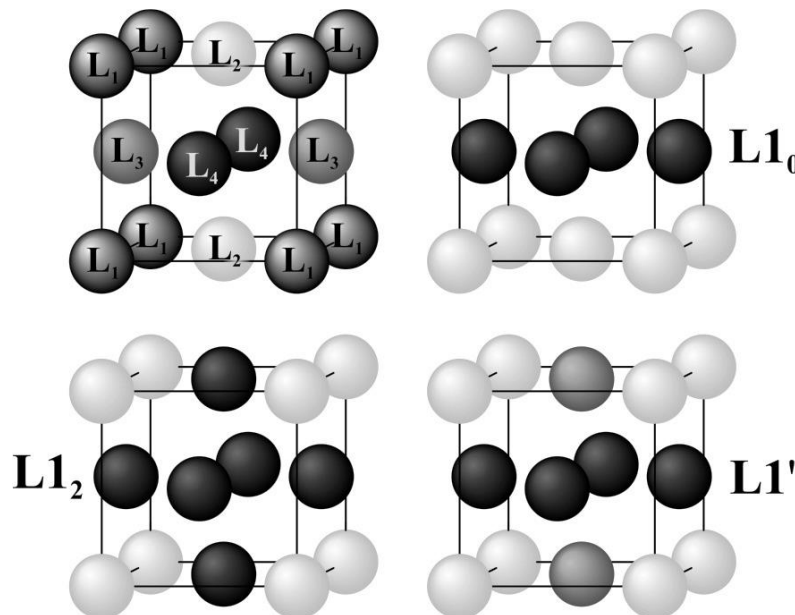


Fig. 1 - Illustration of the four simple cubic FCC sublattices and how different variations of equivalent sites create the three ordered phases discussed for the Fe-Pd system.

Shockley proceeded to break these sublattice variations into three distinct types based on the manner free energy responded to compositional changes in his first-order calculations; the cubic disordered phase (FCC), the cubic ordered phase ($L1_2$), and the tetragonal ordered phase ($L1_0$). In doing so, Shockley combines the $L1_0$ and $L1'$ symmetries which, “for most purposes can be lumped into a single phase.” The $L1'$ portion of this “ $L1_0$ ” phase, however, dominates the calculated phase diagram (Fig. 2) at low temperatures and non-stoichiometric compositions. Created from a first nearest-neighbor approximation, the Shockley diagram only qualitatively matches the experimental phase diagram, and the addition of second nearest neighbors has been shown to dramatically improve agreement by changing the $FCC \rightarrow L1_0$ transition from higher order to first order nucleation and growth [2]. The $L1'$ phase in the MFT model accommodates the non-stoichiometry of an alloy by placing the over-abundant constituent on the L_2 site, leaving the remaining three sublattice sites to fully order to their preferred singular element. For example, an alloy of type $Au_{50-x}Cu_{50+x}$ would result in an $L1'$ phase consisting of site occupancies $L_1 = Au$, $L_2 = ((1 - 4x) Au + (4x) Cu) \%$, and $L_3 = L_4 = Cu$.

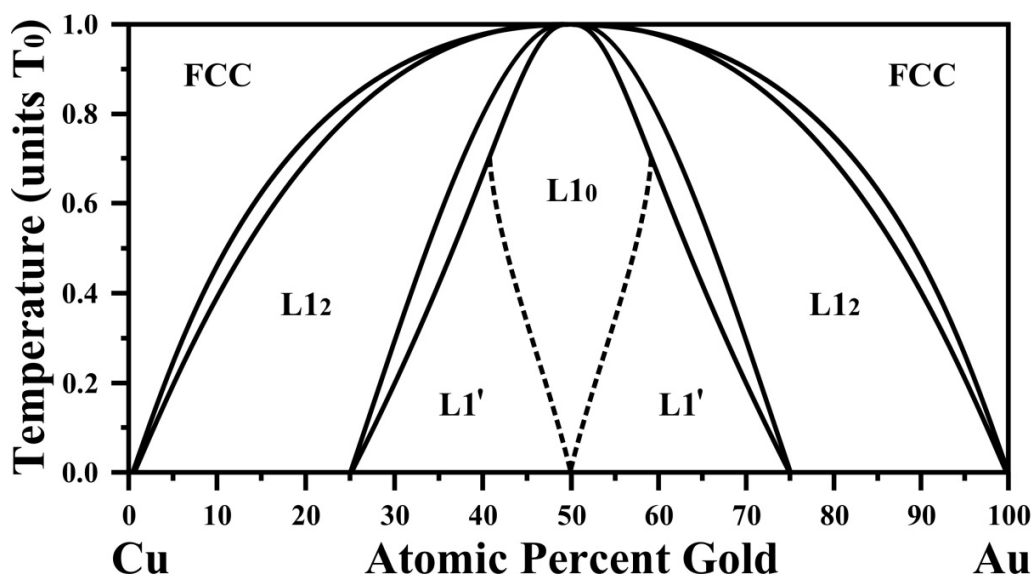


Fig. 2 – An illustration of Shockley’s calculated phase diagram [1] for the Cu-Au system. The dotted lines represent a transition between the tetragonal $L1_0$ and $L1'$ phases.

Having no experimental confirmation, and originally predicted to be unstable by Ising spin models [3], quasi-chemical theory [4], Cluster Variation Method (CVM) calculations [5], and Monte Carlo (MC) simulations [5], the L1' phase was long considered an artifact of Shockley's first-order approach. In 1986, through the refinement of some minor approximations present in earlier CVM work, Ducastelle et al. [6] again predicted the presence of the L1' phase using both tetrahedron and tetrahedron-octahedron clusters; the latter spanning a region of similar size and shape to Shockley's (Fig. 3). This was followed by targeted MC simulations exhibiting a stable, low-temperature L1' ordered phase sharing a higher-order transition with L1₀, and first-order transition with L1₂ (Fig. 4) [7].

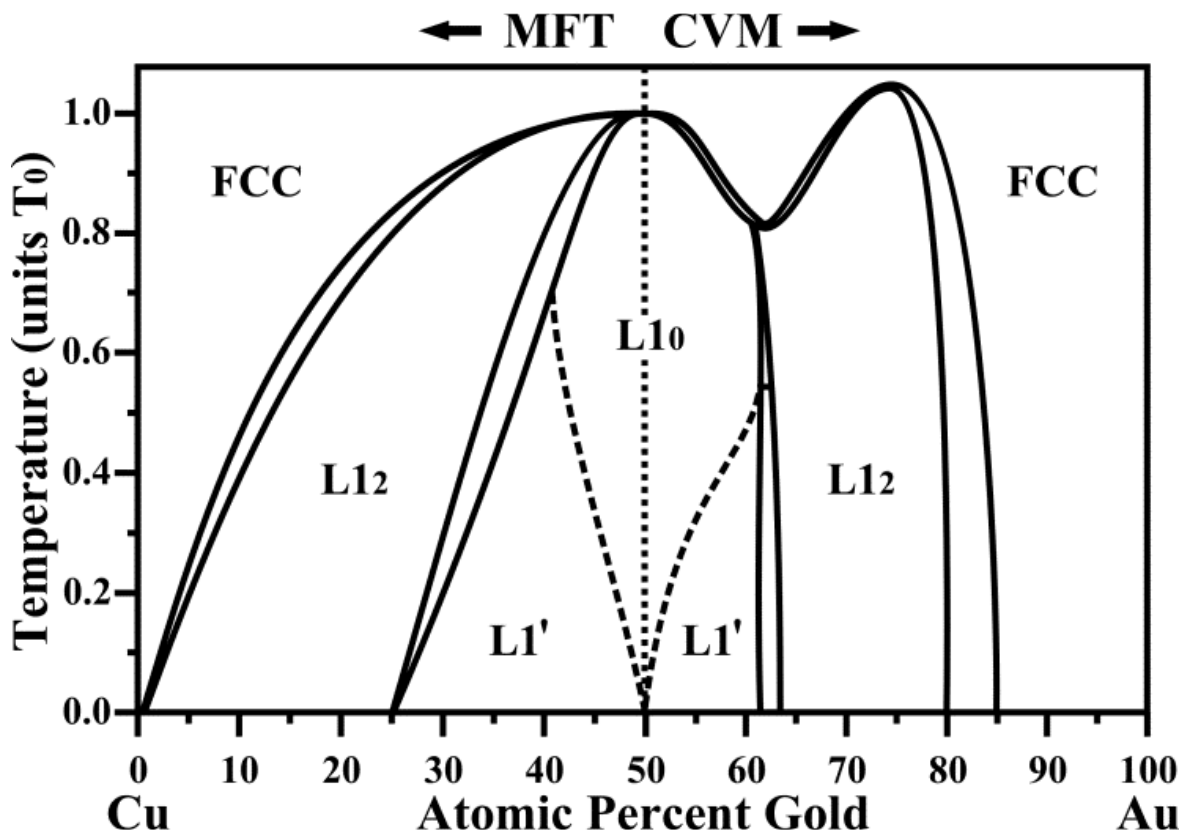


Fig. 3 – Combined theoretical phase diagrams for an ordered FCC system derived from MFT [1] and CVM [6], both predicting similar L1' stability regions.

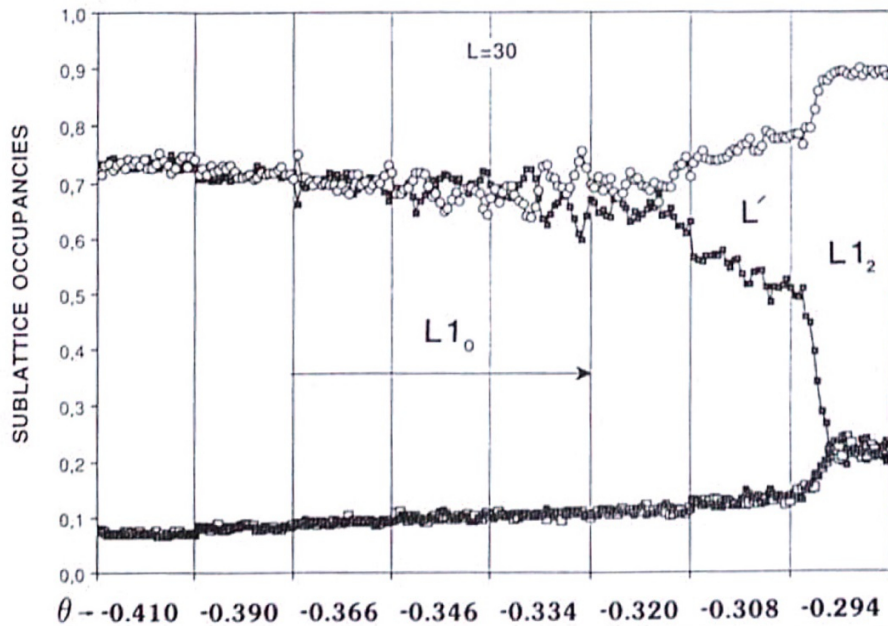


Fig. 4 – Monte Carlo calculation of the concentration of the FCC sub-lattice sites near the $L1_0$ - $L1_2$ superdegenerate point approached at different slopes (θ), supporting the CVM prediction of a stable $L1'$ phase region [7].

The higher-order transition likely originates from the $L1'$ primitive cell (Pearson symbol tP4) sharing the conventional cell and P4/mmm space group symmetry of the $L1_0$ phase. The inability of $L1'$ to reduce to the $L1_0$ primitive cell (tP2) represents a loss of translational symmetry within the space group, increasing periodicity along the $\langle 110 \rangle$ directions of the cube from $a\sqrt{2}/2 \langle 110 \rangle$ to $a\sqrt{2} \langle 110 \rangle$ (Fig. 5).

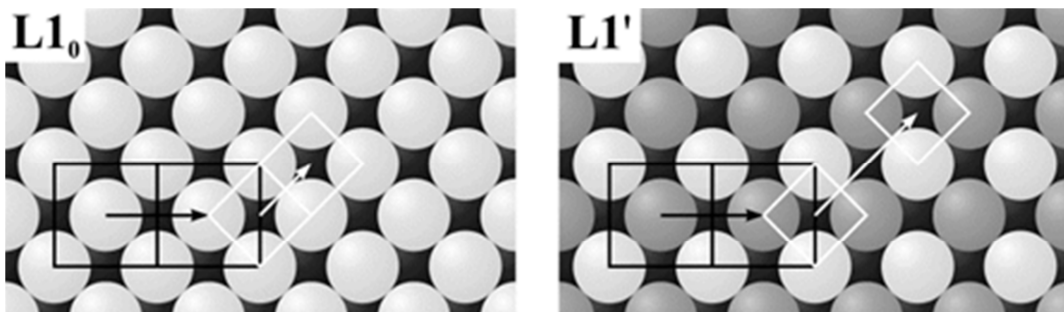


Fig. 5 - View of the (001) crystal facet of $L1_0$ and $L1'$, illustrating how $L1'$ breaks the translational symmetry of $L1_0$ despite sharing the same space group symmetry.

4.3 - Formal Treatment of the Ordered Phases

4.3.1 – Structure Factor and Allowed Reflections

The crystal structure factor, F_{hkl} , accounts for the constructive and destructive interference of lattice planes (h, k, l) resulting in crystal diffraction (Chapter 2). Summed over the N atoms of position (x, y, z) in the crystal structure, this term determines the classification of extinct, fundamental, and superlattice peaks and is given by

$$F_{hkl} = \sum_{n=1}^N f_n \exp[2\pi i(hx_n + ky_n + lz_n)]. \quad (1)$$

For the disordered FCC phase all atomic sites in the conventional unit cell are equivalent. Stoichiometric $L1_0$ and $L1_2$ at perfect long-range order can be viewed as possessing α -sites occupied preferentially by A-atoms, and β -sites occupied by B-atoms. For $L1_0$ there are an equal number of α -sites (L_1, L_2) and β -sites (L_3, L_4). $L1_2$ in contrast only possesses one α -site (L_1) but three β -sites (L_2, L_3, L_4). The sites and scattering factors f_n for these phases are listed in Table 1.

| Site Position | Atomic Scattering Factor | | |
|-----------------------------------|--------------------------|------------|------------|
| | FCC | $L1_0$ | $L1_2$ |
| $(0 \ 0 \ 0)$ | f_α | f_α | f_α |
| $(\frac{1}{2} \ \frac{1}{2} \ 0)$ | f_α | f_α | f_β |
| $(\frac{1}{2} \ 0 \ \frac{1}{2})$ | f_α | f_β | f_β |
| $(0 \ \frac{1}{2} \ \frac{1}{2})$ | f_α | f_β | f_β |

Table 1 – Atomic sites and scattering factors for the conventional cell of the disordered FCC, as well as ordered $L1_0$ and $L1_2$ phases.

For the disordered FCC phase this reduces the structure factor to the single expression

$$F(FCC)_{hkl} = f_{\alpha}(1 + e^{i\pi(h+k)} + e^{i\pi(h+l)} + e^{i\pi(l+k)}) \quad (2)$$

Invoking Euler's formula, $e^{i\pi n} = (-1)^n$, the last three terms reduce to 1 when n is even and -1 when n is odd. When reflection indices h, k and l are all even or all odd, the four terms in the structure factor add constructively and result in a fundamental reflection. In all other scenarios two of the terms become negative and lead to perfect destructive interference.

In the ordered $L1_2$ phase it can be observed that, as $f_{\alpha} \neq f_{\beta}$, no peaks can be completely extinct from destructive interference. $L1_2$ peaks are broken into a fundamental variant that coincides with the allowed reflections for FCC, and superlattice reflections that are extinct for FCC but have a scattering factor of $f_{\alpha} - f_{\beta}$ for the $L1_2$ phase. $L1_0$ exhibits the same fundamental peaks as FCC but has a more complicated superlattice than $L1_2$. Some superlattice reflections, where $(h + k)$ is odd, experience destructive interference and become extinct, while superlattice reflections where $(h + k)$ is even have a structure factor of $2(f_{\alpha} - f_{\beta})$.

$$F(L1_2)_{hkl} = f_{\alpha} + f_{\beta}(e^{i\pi(h+k)} + e^{i\pi(h+l)} + e^{i\pi(l+k)}) \quad (3)$$

$$F(L1_0)_{hkl} = f_{\alpha}(1 + e^{i\pi(h+k)}) + f_{\beta}(e^{i\pi(h+l)} + e^{i\pi(l+k)}) \quad (4)$$

This trend is best exhibited by viewing the conventional cells of the phases in reciprocal space

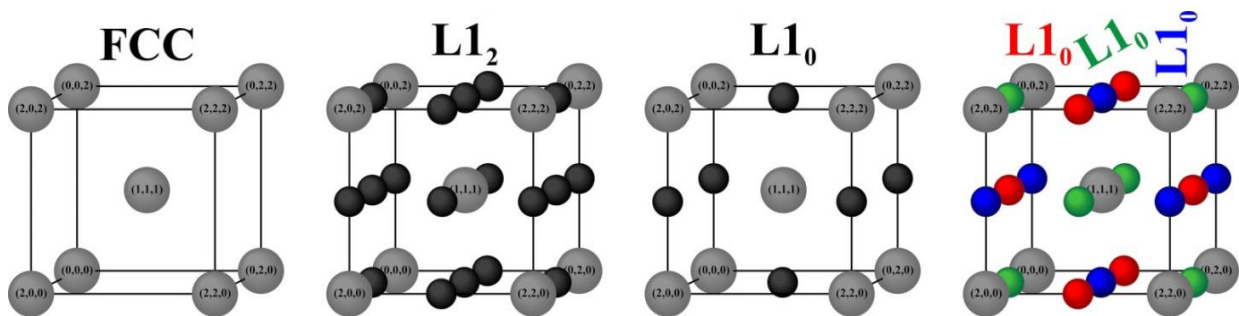


Fig. 6 – Reciprocal space representations of the FCC, $L1_2$, and $L1_0$ phases, as well as a superposition of three orthogonal variants of the tetragonal $L1_0$ phase mimicking the $L1_2$ phase.

In reciprocal space (Fig. 6) each point represents a reflection from a set of planes with a normal vector starting from the origin, and a planar spacing inverse to the magnitude of the vector. As the FCC conventional cell is not a primitive lattice, certain reflections will not exist if planes are labeled according to the conventional cell. In juxtaposition, the L1₂ conventional cell is also a simple cubic primitive cell making all reflections possible, though the intensities of the superlattice peaks are modified. The L1₀ conventional cell (tP4) can be broken into a smaller primitive cell (tP2), once again necessitating some extinct reflections in the conventional labeling. The L1₀ reciprocal space is dependent on orientation, though three L1₀ crystals aligned across different orthogonal axes will produce all of the superlattice peaks of the L1₂ structure when superimposed.

4.3.2 – L1₀ and L1₂ Formal Notations

It is important when discussing the L1' phase to expand upon the rigorous formalism established for the existing ordered phases of the system [8]. As established, binary ordered structures L1₀ and L1₂ have two types of atoms and two atomic site variants: α-sites occupied preferentially by A-atoms, and β-sites occupied by B-atoms. Imperfect ordering and non-stoichiometric compositions introduce the necessity to view each site as having its own concentration of species rather than remaining occupied by a single element. The concentrations of A-atoms and B-atoms in the alloy, X_A and X_B respectively, follow the conservation relation:

$$X_A + X_B = 1 \quad (5)$$

Similarly, the concentrations of A and B on each lattice site must be conserved, so that

$$A_\alpha + B_\alpha = 1 \quad (6)$$

$$A_\beta + B_\beta = 1 \quad (7)$$

The atomic scattering factors can now be written for the α -sites and β -sites as

$$f_{\alpha} = A_{\alpha}f_A + B_{\alpha}f_B \quad (8)$$

$$f_{\beta} = A_{\beta}f_A + B_{\beta}f_B \quad (9)$$

Lastly, so that both L1₀ and L1₂ can be talked about in the same general terms, quantities y_{α} and y_{β} are defined to be the fraction of each site type in the lattice (for L1₀ $y_{\alpha} = y_{\beta} = 0.5$, while for L1₂ $y_{\alpha} = 0.25$ and $y_{\beta} = 0.75$). Conservation once more dictates that

$$y_{\alpha} + y_{\beta} = 1 \quad (10)$$

and two more relations can be reached

$$X_A = y_{\alpha}A_{\alpha} + y_{\beta}A_{\beta} \quad (11)$$

$$X_B = y_{\alpha}B_{\alpha} + y_{\beta}B_{\beta} \quad (12)$$

A long-range order parameter S for both L1₀ and L1₂ ordering is defined so that it is linearly proportional to $(A_{\alpha} + B_{\beta})$, with $S = 1$ for a stoichiometric fully-ordered material and $S = 0$ representing complete disorder, so that

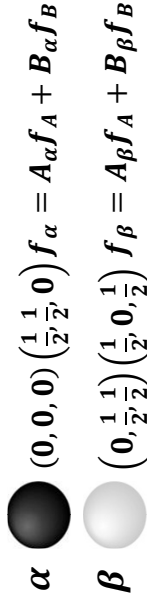
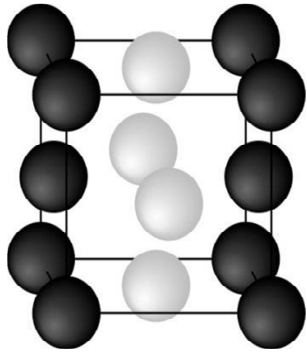
$$S = A_{\alpha} + B_{\beta} - 1 = A_{\alpha} - A_{\beta} = B_{\beta} - B_{\alpha} \quad (13)$$

which, utilizing Eq. 10, 11, 12, and some algebra, is classically expressed as

$$S = \frac{A_{\alpha} - X_A}{1 - y_{\alpha}} = \frac{B_{\beta} - X_B}{1 - y_{\beta}}. \quad (14)$$

The parameter S can reach unity only for a stoichiometric compound. This definition guarantees that the structure factors for both L1₀ and L1₂ superlattice reflections are proportional to S for non-stoichiometric compositions. In order to condense mathematical derivations, Fig. 7 and Fig. 8 on the following pages provide a summary of superlattice structure factor calculations, as well as the limitations placed on the ordering parameter by non-stoichiometry for both phases.

$L1_0$ Ordering Parameter



Identities

$$\begin{aligned}
 X_A + X_B &= 1 \\
 Y_\alpha + Y_\beta &= 1 \\
 A_\alpha + B_\alpha &= 1 \\
 A_\beta + B_\beta &= 1
 \end{aligned}$$

$$\begin{aligned}
 Y_\alpha A_\alpha + Y_\beta A_\beta &= X_A \\
 Y_\alpha B_\alpha + Y_\beta B_\beta &= X_B \\
 Y_\alpha &= 0.5; Y_\beta = 0.5 \\
 A_\alpha + A_\beta &= 2X_A \\
 B_\alpha + B_\beta &= 2X_B
 \end{aligned}$$

X_Z = fraction Z in alloy
 Z_χ = fraction Z on χ site
 Y_χ = fraction χ sites in alloy
 f_Z = scattering factor for Z

Structure Factor Calculations

Fundamental ($2f_\alpha + 2f_\beta$) $2(A_\alpha f_A + B_\alpha f_B) + 2(A_\beta f_A + B_\beta f_B)$
 $4(X_A f_A + X_B f_B)$

L1₀ Superlattice ($2f_\alpha - 2f_\beta$) $2(A_\alpha f_A + B_\alpha f_B) - 2(A_\beta f_A + B_\beta f_B)$
 $2(A_\alpha - A_\beta)f_A + 2(B_\alpha - B_\beta)f_B$
 $2(A_\alpha - A_\beta)(f_A - f_B)$

$2S(f_A - f_B)$ where $S = (A_\alpha - A_\beta)$

Ordering Parameter

$$S = (A_\alpha - A_\beta) = A_\alpha - \frac{X_A - Y_\alpha A_\alpha}{Y_\beta} = \frac{(Y_\alpha + Y_\beta)A_\alpha - X_A}{Y_\beta}$$

$$S = (B_\beta - B_\alpha) = B_\beta - \frac{X_B - Y_\beta B_\beta}{Y_\alpha} = \frac{(Y_\alpha + Y_\beta)B_\beta - X_B}{Y_\alpha}$$

$$S = \frac{A_\alpha - X_A}{1 - Y_\alpha} = \frac{B_\beta - X_B}{1 - Y_\beta}$$

Ordering Limits

$$1 \geq A_\alpha \geq A_\beta \geq 0$$

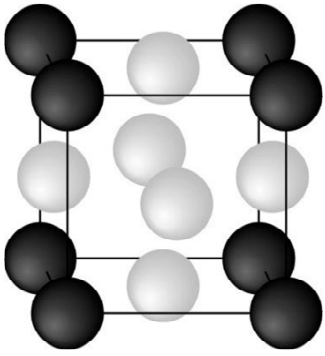
$$1 \geq X_A + \frac{S}{2} \geq X_A - \frac{S}{2} \geq 0$$

$$S \leq 1 - 2|0.5 - X_\alpha|$$

$$S \leq 2X_A \text{ for } X_A \leq 0.5 \text{ \& } S \leq 2(1 - X_A) \text{ for } X_A \geq 0.5$$

Fig. 7 – Calculations for the structure factor and ordering limits of the $L1_0$ phase.

L1₂ Ordering Parameter



α $(0, 0, 0)$ $f_\alpha = A_\alpha f_A + B_\alpha f_B$
 β $(0, \frac{1}{2}, \frac{1}{2})$ $(\frac{1}{2}, 0, \frac{1}{2})$ $(\frac{1}{2}, \frac{1}{2}, 0)$ $f_\beta = A_\beta f_A + B_\beta f_B$

Identities

$$\begin{aligned}
 X_A + X_B &= 1 \\
 Y_\alpha + Y_\beta &= 1 \\
 A_\alpha + B_\alpha &= 1 \\
 A_\beta + B_\beta &= 1 \\
 Y_\alpha A_\alpha + Y_\beta A_\beta &= X_A \\
 Y_\alpha B_\alpha + Y_\beta B_\beta &= X_B \\
 Y_\alpha &= .25; Y_\beta = .75 \\
 A_\alpha + 3A_\beta &= 4X_A \\
 B_\alpha + 3B_\beta &= 4X_B
 \end{aligned}$$

X_Z = fraction Z in alloy
 Z_χ = fraction Z on χ site
 Y_χ = fraction χ sites in alloy
 f_Z = scattering factor for Z

Structure Factor Calculations

Fundamental ($f_\alpha + 3f_\beta$) $A_\alpha f_A + B_\alpha f_B + 3(A_\beta f_A + B_\beta f_B)$
 $4(X_A f_A + X_B f_B)$

L1₂ Superlattice ($f_\alpha - 2f_\beta + f_\beta$) $A_\alpha f_A + B_\alpha f_B - (A_\beta f_A + B_\beta f_B)$
 $(A_\alpha - A_\beta)f_A + (B_\alpha - B_\beta)f_B$
 $(A_\alpha - A_\beta)(f_A - f_B)$

$S(f_A - f_B)$ where $S = (A_\alpha - A_\beta)$

Ordering

$$\begin{aligned}
 S &= (A_\alpha - A_\beta) = A_\alpha - \frac{X_A - Y_\alpha A_\alpha}{Y_\beta} = \frac{X_A - Y_\alpha A_\alpha}{Y_\beta} = \frac{(Y_\alpha + Y_\beta)A_\alpha - X_A}{Y_\beta} \\
 S &= (B_\beta - B_\alpha) = B_\beta - \frac{X_B - Y_\beta B_\beta}{Y_\alpha} = \frac{X_B - Y_\beta B_\beta}{Y_\alpha} = \frac{(Y_\alpha + Y_\beta)B_\beta - X_B}{Y_\alpha}
 \end{aligned}$$

Ordering Limits

$$\begin{aligned}
 1 &\geq A_\alpha \geq A_\beta \geq 0 \\
 1 &\geq X_A + \frac{3}{4}S \geq X_A - \frac{1}{4}S \geq 0 \\
 S &\leq 1 - 4|0.25 - X_A| \text{ when } X_A \leq 0.25, \text{ i.e. } S \leq 4X_A \\
 S &\leq 1 - \frac{4}{3}|0.25 - X_A| \text{ when } X_A \geq 0.25, \text{ i.e. } S \leq \frac{4}{3}(1 - X_A)
 \end{aligned}$$

Fig. 8 - Calculations for the structure factor and ordering limits of the L1₂ phase.

It can be seen from structure factor calculations that $L1_0$ fundamental reflections ($2f_\alpha + 2f_\beta$) are of intensity $4(X_A f_A + X_B f_B)$, while superlattice reflections ($2f_\alpha - 2f_\beta$) have intensity $2S(f_A - f_B)$. Similarly, $L1_2$ fundamentals ($f_\alpha + 3f_\beta$) are of intensity $4(X_A f_A + X_B f_B)$, with superlattice ($f_\alpha - f_\beta$) intensities of $S(f_A - f_B)$.

4.3.3 – Expansion to the $L1'$ phase

$L1'$ ordering introduces a third site to the binary A-B system at the L_2 position. This γ -site can be viewed to be preferentially occupied by A-atoms, but orders separately of the α -site so that $A_\alpha \geq A_\gamma \geq A_\beta$. The atomic scattering factor of the γ -site will be $f_\gamma = A_\gamma f_A + B_\gamma f_B$, and as on other sites: $A_\gamma + B_\gamma = 1$. Conservation dictates that former identities be expanded so that

$$y_\alpha + y_\beta + y_\gamma = 1 \quad (15)$$

$$X_A = y_\alpha A_\alpha + y_\beta A_\beta + y_\gamma A_\gamma \quad (16)$$

$$X_B = y_\alpha B_\alpha + y_\beta B_\beta + y_\gamma B_\gamma \quad (17)$$

The structure factor of the $L1'$ phase can be written as

$$F(L1')_{hkl} = f_\alpha(1) + f_\gamma(e^{i\pi(h+k)}) + f_\beta(e^{i\pi(h+l)} + e^{i\pi(l+k)}) \quad (18)$$

This preserves much of the $L1_0$ phase behavior and results in three variants: fundamental, superlattice reflections where $(h + k)$ is odd, and superlattice reflections where $(h + k)$ is even. The primary difference from $L1_0$ is that when $(h + k)$ is odd the first two terms do not perfectly destructively interfere ($L1_2$ behavior), and this results in a second type of superlattice reflection.

Another way to view the superlattice behavior of the $L1'$ structure is as a superposition of $L1_0$ and $L1_2$ type ordering. When this is done graphically using reciprocal space it is easy to see that three variants exist (Fig. 9). One set of superlattice peaks are contributed solely from the $L1_2$ nature of the hybrid phase, and therefore can be called “ $L1_2$ superlattice ordering”.

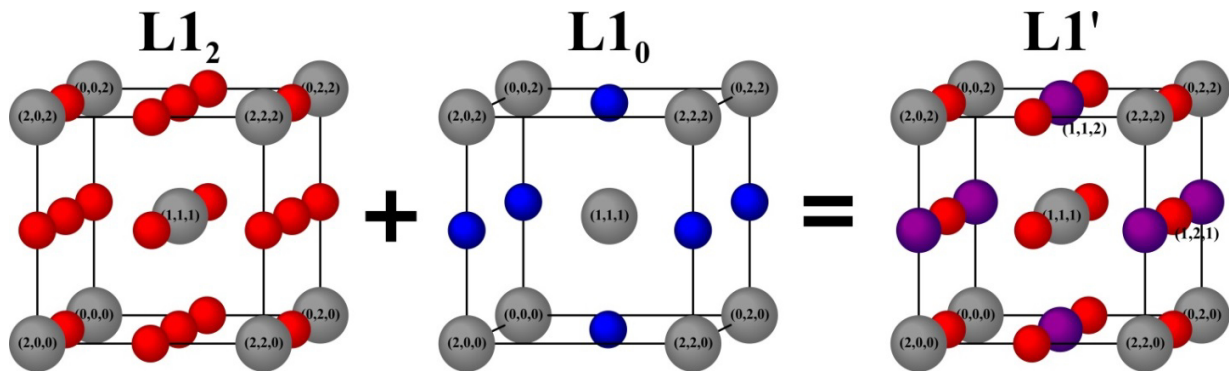


Fig. 9 – Reciprocal space of the $L1_0$ and $L1_2$ phases with their superposition into the $L1'$ phase.

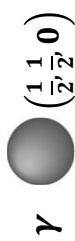
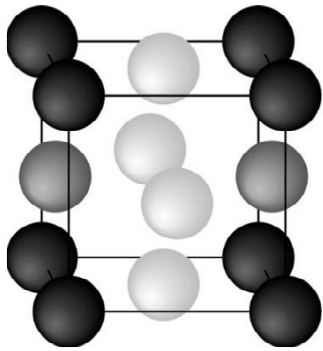
The $L1_2$ superlattice ordering of the $L1'$ phase has a structure factor $(f_\alpha - f_\gamma)$ as the two f_β terms cancel. The other superlattice peak is a combination of reflections from both $L1_0$ and $L1_2$ types of ordering, and can be called “mixed superlattice ordering”. This mixed superlattice variant has a structure factor of $(f_\alpha + f_\gamma - 2f_\beta)$. Fundamental peaks, as for all cases before, have a structure factor that is a summation of all the atomic sites $(f_\alpha + f_\gamma + 2f_\beta)$.

As for the $L1_0$ and $L1_2$ phases, it is convenient to condense the relevant calculations for the structure factor of $L1'$ onto one page (Fig. 10). The addition of a γ -site requires that two ordering parameters now be defined to describe the system. The choice of one these ordering parameters is straightforward, collecting the leading term of the $L1_2$ type superlattice ordering we can define the first ordering parameter so that

$$S_{\alpha\gamma} = A_\alpha - A_\gamma \quad (19)$$

This choice for the first ordering parameter closely follows the definition of the order parameter for $L1_0$ and $L1_2$ ordering, $S = A_\alpha - A_\beta$, and cannot exceed the value of one. In fact, $S_{\alpha\gamma}$ is actually a conventionally defined ordering parameter across a 2D monolayer sublattice of α and γ sites. In this 2D layer $S_{\alpha\gamma} = 1$ will form a perfect chessboard pattern, and $S_{\alpha\gamma} = 0$ represents complete disorder in the monolayer and a uniform composition across the two sites.

L1' Ordering Parameters



Identities

$$X_A + X_B = 1$$

$$y_\alpha + y_\beta + y_\gamma = 1$$

$$A_\alpha + B_\alpha = 1$$

$$A_\beta + B_\beta = 1$$

$$A_\gamma + B_\gamma = 1$$

$$y_\alpha A_\alpha + y_\beta A_\beta + y_\gamma A_\gamma = X_A$$

$$y_\alpha B_\alpha + y_\beta B_\beta + y_\gamma B_\gamma = X_B$$

$$y_\alpha = .25; y_\beta = .5; y_\gamma = .25$$

$$A_\alpha + 2A_\beta + A_\gamma = 4X_A$$

$$B_\alpha + 2B_\beta + B_\gamma = 4X_B$$

Fundamental $A_\alpha f_A + B_\alpha f_B + 2(A_\beta f_A + B_\beta f_B) + (A_\gamma f_A + B_\gamma f_B)$
 $(f_\alpha + 2f_\beta + f_\gamma)$
 $4(X_A f_A + X_B f_B)$

L1₂ Superlattice
 $(f_\alpha - f_\beta + f_\beta - f_\gamma)$
 $A_\alpha f_A + B_\alpha f_B - (A_\gamma f_A + B_\gamma f_B)$
 $(A_\alpha - A_\gamma) f_A + (B_\alpha - B_\gamma) f_B$
 $(A_\alpha - A_\gamma)(f_A - f_B)$

$S_{\alpha\gamma}(f_A - f_B)$ where $S_{\alpha\gamma} = (A_\alpha - A_\gamma)$

Mixed Superlattice
 $(f_\alpha - 2f_\beta + f_\gamma)$
 $A_\alpha f_A + B_\alpha f_B - 2(A_\beta f_A + B_\beta f_B) + (A_\gamma f_A + B_\gamma f_B)$
 $(A_\alpha - 2A_\beta + A_\gamma) f_A + (B_\alpha - 2B_\beta + B_\gamma) f_B$
 $(A_\alpha - 2A_\beta + A_\gamma)(f_A - f_B)$

$2 S_{mixed}(f_A - f_B)$ where $S_{mixed} = (A_\alpha - 2A_\beta + A_\gamma)/2$

X_Z = fraction Z in alloy
 Z_X = fraction Z on χ site
 y_χ = fraction χ sites in alloy
 f_Z = scattering factor for Z

or

$(S_{\alpha\gamma} + 2S_{\gamma\beta})(f_A - f_B)$ where
 $S_{\alpha\gamma} = (A_\alpha - A_\gamma)$
 $S_{\gamma\beta} = (A_\gamma - A_\beta)$

and $S_{\alpha\gamma} + S_{\gamma\beta} = (A_\alpha - A_\beta)$

Fig. 10 - Calculations for the structure factor and ordering limits of the L1' phase.

The choice of the second ordering parameter is not as clearly determined and there are several justifiable possibilities. The leading term for mixed superlattice ordering is $(A_\alpha + A_\gamma - 2A_\beta)$, and can take values as high as 2 when approaching L1₀ stoichiometric ordering ($A_\alpha = A_\gamma = 1, A_\beta = 0$). This problem can be resolved by emulating the L1₀ ordering calculations with the inclusion of a leading value of 2, i.e. $2S_{mixed}(f_A - f_B)$, making the new ordering parameter

$$S_{mixed} = \frac{A_\alpha + A_\gamma - 2A_\beta}{2} = \frac{A_\alpha + A_\gamma}{2} - A_\beta \quad (20)$$

This is a valid choice for the second ordering parameter, being linearly independent with the first ordering parameter and the compositional constraint in Eq. 16. Physically speaking, S_{mixed} represents the degree of ordering between alternating monolayers, which is the same as L1₀ ordering while treating A_α and A_γ as an averaged statistical site.

Another possibility for picking the second ordering parameter is to note that $A_\alpha - A_\beta$, used to define the L1₀ and L1₂ order parameters, is the sum of the independent contributions $A_\alpha - A_\gamma$ and $A_\gamma - A_\beta$. The first term has already been utilized as the ordering parameter $S_{\alpha\gamma}$, the second

$$S_{\gamma\beta} = A_\gamma - A_\beta \quad (21)$$

can be defined as a second ordering parameter for the L1' phase. $S_{\gamma\beta}$ appears in the structure factor calculations for the mixed ordering superlattice in the form of $(S_{\alpha\gamma} + 2S_{\gamma\beta})(f_A - f_B)$. Similar to the $S_{\alpha\gamma}$ parameter, $S_{\gamma\beta}$ is a conventionally defined ordering parameter across a sublattice of the γ and β sites.

The choice of $S_{\alpha\gamma}$ and $S_{\gamma\beta}$ as L1' ordering parameters can be shown to be a more elegant representation than that of $S_{\alpha\gamma}$ and S_{mixed} . Across all compositions the L1₀ and L1₂ phases can be viewed as constrained subsets of L1' ordering, regardless of which set of ordering parameters is used. For the $S_{\alpha\gamma}$ - $S_{\gamma\beta}$ notation, when $S_{\alpha\gamma} = 0$ ($A_\alpha = A_\gamma$) then $S_{\gamma\beta} = A_\alpha - A_\beta$ becomes the conventional L1₀ ordering parameter. Similarly, when $S_{\gamma\beta} = 0$, $S_{\alpha\gamma}$ is identical to the conventional

L1₂ ordering parameter. Both the L1₀ and L1₂ phases are therefore special cases of L1' ordering where one of the structure factors is zero, regardless of stoichiometry. The choice of S_{αγ}-S_{γβ} notation adds additional insight into the nature of L1' ordering, emphasizing hybridization of the L1₀ and L1₂ phases, and the contribution of both sublattices to the structure factor (S_{αγ} + 2S_{γβ}) of the mixed superlattice reflection. For the alternate S_{αγ}-S_{mixed} notation, as with the S_{αγ}-S_{γβ} notation, the L1₀ phase will still have S_{αγ} = 0 regardless of composition. In this notation, however, L1₂ type ordering always will have S_{αγ} = 2S_{mixed}. For example, fully L1₂ ordered Fe_{38.5}Pd_{61.5} would be represented as S_{αγ} = 0.82 and S_{mixed} = 0.41; opposed to S_{αγ} = 0.82 and S_{γβ} = 0. This choice of notation is not incorrect, but it ceases to provide the more intuitive understanding of the L1' ordering process that S_{αγ}-S_{γβ} notation offers.

Defining the ordering limitations based on composition is complicated from the calculations seen for L1₀ (Fig. 7) and L1₂ (Fig. 8) phases by the addition of a second ordering parameter. We start with the defined L1' phase behavior

$$1 \geq A_\alpha \geq A_\gamma \geq A_\beta \geq 0 \quad (22)$$

Treating Eq. 16, 19 and 21 as a system of linear equations and diagonalizing the matrix

$$\begin{bmatrix} 1 & 0 & -1 \\ 0 & -1 & 1 \\ 1 & 2 & 1 \end{bmatrix} \begin{bmatrix} A_\alpha \\ A_\beta \\ A_\gamma \end{bmatrix} = \begin{bmatrix} S_{\alpha\gamma} \\ S_{\gamma\beta} \\ 4X_A \end{bmatrix} \quad (23)$$

$$\begin{bmatrix} 1 & 0 & -1 \\ 0 & -1 & 1 \\ 0 & 0 & 4 \end{bmatrix} \begin{bmatrix} A_\alpha \\ A_\beta \\ A_\gamma \end{bmatrix} = \begin{bmatrix} S_{\alpha\gamma} \\ S_{\gamma\beta} \\ 4X_A - S_{\alpha\gamma} + 2S_{\gamma\beta} \end{bmatrix} \quad (24)$$

$$\begin{bmatrix} 1 & 0 & 0 \\ 0 & 1 & 0 \\ 0 & 0 & 1 \end{bmatrix} \begin{bmatrix} A_\alpha \\ A_\beta \\ A_\gamma \end{bmatrix} = \begin{bmatrix} X_A + \frac{3}{4}S_{\alpha\gamma} + \frac{1}{2}S_{\gamma\beta} \\ X_A - \frac{1}{4}S_{\alpha\gamma} - \frac{1}{2}S_{\gamma\beta} \\ X_A - \frac{1}{4}S_{\alpha\gamma} + \frac{1}{2}S_{\gamma\beta} \end{bmatrix} \quad (25)$$

Combining these equations yields

$$1 \geq X_A + \frac{3}{4}S_{\alpha\gamma} + \frac{1}{2}S_{\gamma\beta} \geq X_A - \frac{1}{4}S_{\alpha\gamma} + \frac{1}{2}S_{\gamma\beta} \geq X_A - \frac{1}{4}S_{\alpha\gamma} - \frac{1}{2}S_{\gamma\beta} \geq 0 \quad (26)$$

The central inequalities reduce to trivial statements ($S_{\gamma\beta} \geq -S_{\gamma\beta}$) so the outer inequalities determine the limits on ordering for the L1' phase

$$3S_{\alpha\gamma} + 2S_{\gamma\beta} \leq 4(1 - X_A) \quad (27)$$

$$S_{\alpha\gamma} + 2S_{\gamma\beta} \leq 4X_A \quad (28)$$

These limits reduce to the same as for L1₀ or L1₂ ordering when either $S_{\alpha\gamma}$ or $S_{\gamma\beta}$ becomes zero.

4.4 – Observation of the L1' Phase

In the growth temperature series (Chapter 3) it was observed that films grown at 600°C and 650°C possessed anomalous superlattice peak intensities which, combined with evidence excluding L1₀ ordering, first suggested the possibility of a c-axis oriented L1' phase. In particular the ratio of superlattice to fundamental peaks, I_{001}/I_{002} , is capped at 0.0886 for epitaxial L1₂-Fe_{38.5}Pd_{61.5} but ratios as high as 0.128 were being measured. To an observer familiar with the substantially larger superlattice intensities in the related CoPt and FePt L1₀ systems, where I_{001}/I_{002} can approach 2, both of these values may appear spuriously low [9]. The change in magnitude originates from the switch of L1₀ to L1₂ ordering and the difference in the atomic form factors of Pt and Pd, both of which result in roughly four-fold drops in the superlattice intensities. As discussed in Chapter 2, quantitative XRD is able to accurately predict the relative peak intensities of bulk Fe-Pd phases within 2 to 3 % error. The epitaxial films in this study likely narrow this error due to simpler geometry, elimination of indeterminate texture, less disorder at grain boundaries, and familiarization with the diffractometer being used. Consequently, the 10 to 35% variations from the expected intensity ratios measured represent a significant deviation. Additional films grown at 600°C for this study confirm both the reproducibility of the L1' phase and provide a larger body of data points to support its presence.

4.4.1 – XRD Methodology and Analysis of Error

To verify the presence of L1' type ordering, a quantitative comparison of peaks intensities belonging to each of the structure factor variants must be made. As calculations rarely perfectly predict results, it is absolutely critical to perform analysis in such a way that possible errors from the numerous correction terms are systematically minimized. One simple way to do this is by analyzing pairs of relative peak intensities that occur under similar diffraction conditions.

The first peak pairs are taken from θ - 2θ scans with scattering vectors perpendicular to the film, providing the (001) mixed L1₀/L1₂ superlattice and (002) fundamental peaks. The simple normal geometry ($\chi = 0$) of these scans reduces error by removing the defocusing correction, as well as simplifying the absorption correction term. The Lorentz correction remains influential for these peaks but is not subject to significant errors as it is determined strictly from the θ - 2θ geometry. One major source of possible error is the polarization correction, which reasonably could lead to a 1 to 2 % error in the predicted relative intensities (Chapter 2), and in the worst case scenario no more than 6 %. Any correction for an under-accounted polarization factor, however, would serve to lower the predicted I_{001}/I_{002} intensity ratio. The model would therefore be under-predicting the amount of ordering present and polarization error would strengthen the argument for L1'. The Debye-Waller temperature correction is very small to begin with at room temperature (~2% for I_{001}/I_{002}) so any error from the term can be assumed to be vanishingly small; though orientation corrections have been determined for L1₀ FePd [10]. The absorption correction can serve as an error to the I_{001}/I_{002} intensity ratio due to some uncertainty in film thicknesses. Doubling film thickness results in an approximately 3 % loss in the ratio and thickness errors can be viewed as a negligible contribution for actual deviations, which will be much smaller. Surface topology of films may also lead to some error in the absorption term, notably for the island forming 650°C films. The integrals needed to discretely solve for this error

are specific to the 3D surface and unapproachably complicated without the aid of extensive computer modeling. As a first-order approximation, the film can be viewed as having a lower average density but remaining smooth. Such an approximation suggests an error on the scale of 1-2% for the island forming films. For the majority of films, grown at 600°C, their smooth nature on long length scales will make any topological effects less consequential.

The second pair of peaks utilized for analysis are the (121) L_{12} exclusive and (112) mixed L_{10}/L_{12} superlattice peaks, the lowest order pair of accessible peaks with similar indices, i.e. both containing c-axis components lifting diffraction out of the film plane. These peaks share nearly identical Bragg angles as the degree of tetragonality in the films is still relatively close to cubic, but the peaks are found at different χ tilts for epitaxial films. The similar Bragg angle of these peaks nearly eliminates the impact of the Lorentz, Debye-Waller and polarization correction factors. This leaves the absorption factor, which is simplified by the removal of θ -dependence and consequentially behaves much like I_{001}/I_{002} ratio in terms of error, and the defocusing correction. The defocusing correction is determined empirically for the diffractometer geometry being used and should not be a significant source of error.

The relative errors expected for both the I_{001}/I_{002} and I_{112}/I_{121} ratios are expected to be small and, due to polarization, I_{001}/I_{002} may actually be conservative. The ratio I_{001}/I_{002} is sensitive to the degree of ordering in the films as (002) is a fundamental reflection. If the two ordering parameters follow the same general behavior ($S_{\gamma\beta} \propto S_{\alpha\gamma}$), errors in I_{001}/I_{002} will affect the holistic state of order in the system but have little role in providing information on $L_{1'}$ nature. The I_{112}/I_{121} ratio of the films, which is more insensitive to errors, is independent of the fundamental peak intensity. Deviations to this I_{112}/I_{121} ratio are a more direct representation of the L_{12} vs. $L_{1'}$ nature of a film. All film peaks were measured after removing background signal from the θ -2 θ scans.

4.4.2 – L1' Confirmation through XRD Results

Comparing the measured intensity ratios against those expected for perfect L1₂ ordering (Table 2), it can be seen that the films have large deviations from the expected values. This is particularly clear in the I₁₁₂/I₁₂₁ ratios, which are invariant to changes in the holistic degree of ordering compared to the fundamental reflections. These I₁₁₂/I₁₂₁ values fall well outside the expected margin of error discussed earlier, in many cases by an order of magnitude or greater. The I₀₀₁/I₀₀₂ values are subject to a greater level of deviation, in some cases resulting in decreased values from those calculated for fully ordered L1₂. This arises as some films have not maximally ordered, which is equivalent to saying the α-sites, which are able to fully order, have A_α < 1. Complete data for two of the earliest films is missing, due to their unfortunate destruction or damage during or between characterization methods, much of which was performed before the L1' phenomenon was realized to have occurred.

| Substrate | Temp. | Thickness | L1 ₂ Values @ S _{max} | | Experimental | | Deviation | |
|---------------|--------|-----------|---|------------------------------------|------------------------------------|------------------------------------|------------------------------------|------------------------------------|
| | | | I ₀₀₁ /I ₀₀₂ | I ₁₁₂ /I ₁₂₁ | I ₀₀₁ /I ₀₀₂ | I ₁₁₂ /I ₁₂₁ | I ₀₀₁ /I ₀₀₂ | I ₁₁₂ /I ₁₂₁ |
| Crystec GmbH | 600 °C | 45 nm | 0.0889 | 0.5022 | 0.0959 | - | 7.87 % | - |
| Crystec GmbH | 600 °C | 45 nm | 0.0889 | 0.5011 | 0.0982 | 0.6357 | 10.40 % | 26.87 % |
| Crystec GmbH | 650 °C | 45 nm | 0.0889 | 0.5076 | - | 0.6572 | - | 29.47 % |
| Crystec GmbH | 650 °C | 45 nm | 0.0887 | 0.5084 | 0.0984 | 0.5777 | 10.99 % | 13.62 % |
| Sigma Aldrich | 600 °C | 80 nm | 0.0868 | 0.5200 | 0.0735 | 0.8042 | -15.37 % | 54.65 % |
| Sigma Aldrich | 600 °C | 115nm | 0.0850 | 0.5304 | 0.0774 | 0.7507 | -8.94 % | 41.55 % |
| Sigma Aldrich | 600 °C | 85 nm | 0.0866 | 0.5198 | 0.0871 | 0.7893 | 0.61 % | 51.85 % |
| Sigma Aldrich | 600 °C | 70 nm | 0.0876 | 0.5136 | 0.1183 | 0.7786 | 35.01 % | 51.59 % |

Table 2 – A comparison of eight films found to be in the L1' phase, examining their expected values at full L1₂ ordering juxtaposed to their experimental values. The deviations for I₁₁₂/I₁₂₁ are shown to be well above the calculated margin of error, while I₀₀₁/I₀₀₂ ratios vary more as they depend on the holistic degree of ordering, which is not always maximal.

| Substrate | Temp. | Thickness | $S_{\alpha\gamma}$ | $S_{\gamma\beta}$ | A_α | A_γ | A_β | C-axis | A-axis | C/A Ratio |
|---------------|--------|-----------|--------------------|-------------------|------------|------------|-----------|--------|--------|-----------|
| Crystec GmbH | 600 °C | 45 nm | 0.76* | 0.05* | 0.98* | 0.22* | 0.17* | 3.81 Å | 3.85 Å | 0.9880 |
| Crystec GmbH | 600 °C | 45 nm | 0.77 | 0.05 | 0.98 | 0.22 | 0.17 | 3.80 Å | 3.85 Å | 0.9876 |
| Crystec GmbH | 650 °C | 45 nm | 0.79* | 0.04* | 1.00* | 0.21* | 0.17* | 3.82 Å | 3.85 Å | 0.9941 |
| Crystec GmbH | 650 °C | 45 nm | 0.80 | 0.03 | 1.00 | 0.20 | 0.17 | 3.82 Å | 3.85 Å | 0.9923 |
| Sigma Aldrich | 600 °C | 80 nm | 0.60 | 0.07 | 0.88 | 0.27 | 0.20 | 3.83 Å | 3.85 Å | 0.9946 |
| Sigma Aldrich | 600 °C | 115nm | 0.65 | 0.07 | 0.91 | 0.25 | 0.19 | 3.83 Å | 3.85 Å | 0.9939 |
| Sigma Aldrich | 600 °C | 85 nm | 0.68 | 0.08 | 0.93 | 0.25 | 0.18 | 3.82 Å | 3.85 Å | 0.9937 |
| Sigma Aldrich | 600 °C | 70 nm | 0.76 | 0.09 | 1.00 | 0.24 | 0.15 | 3.81 Å | 3.86 Å | 0.9890 |

*Sample destroyed during prior testing, numbers interpolated from partial data

Table 3 – The ordering parameters, Fe compositions at the three atomic sites, and lattice parameters of eight $L1'$ $Fe_{38.5}Pd_{61.5}$ films. Many of the films approach nearly full ordering $A_\alpha \approx 1$, and have non-zero components to both $S_{\alpha\gamma}$ and $S_{\gamma\beta}$, representing an $L1'$ nature. Of particular note is the correlation between $S_{\gamma\beta}$ and the tetragonality of the films.

Once the relative intensities of these peak pairs are known $S_{\alpha\gamma}$ and $S_{\gamma\beta}$ can be determined (Table 3). The ordering parameter $S_{\alpha\gamma}$ remains significantly larger than $S_{\gamma\beta}$ under all film conditions, showing a general predominance of $L1_2$ nature. The Fe occupancy of α -sites (A_α) approaches but does not exceed 100%. This was not constrained during fitting, meaning measurement errors could easily have placed it above unity. While circumstantial evidence, this is a strong positive indicator of analytical accuracy. As the two values I_{001}/I_{002} and I_{112}/I_{121} are fitted by two variables, $S_{\alpha\gamma}$ and $S_{\gamma\beta}$, they are able to produce “exact” order parameters. A change of 0.01 to the value of $S_{\alpha\gamma}$ or $S_{\gamma\beta}$ equates to an error in the intensity ratios on the order of 3 to 5 %, consequently the order parameters calculated can be taken to be accurate to the hundredths place.

There are some notable differences to the ordering parameters based on the substrates used. Films from the original temperature series on Crystec GmbH brand substrates, considered to be of high quality, produce relatively consistent values for A_α , A_γ , and A_β . Films grown on substrates from alternate suppliers were found, both for these particular films and many others

discussed in Chapter 5, to produce a range of growth behaviors due to impurities and hydrophilic surface pitting. A good example can be found in Fig. 11, which displays micrographs of two films taken from the tables above with markedly different surfaces.

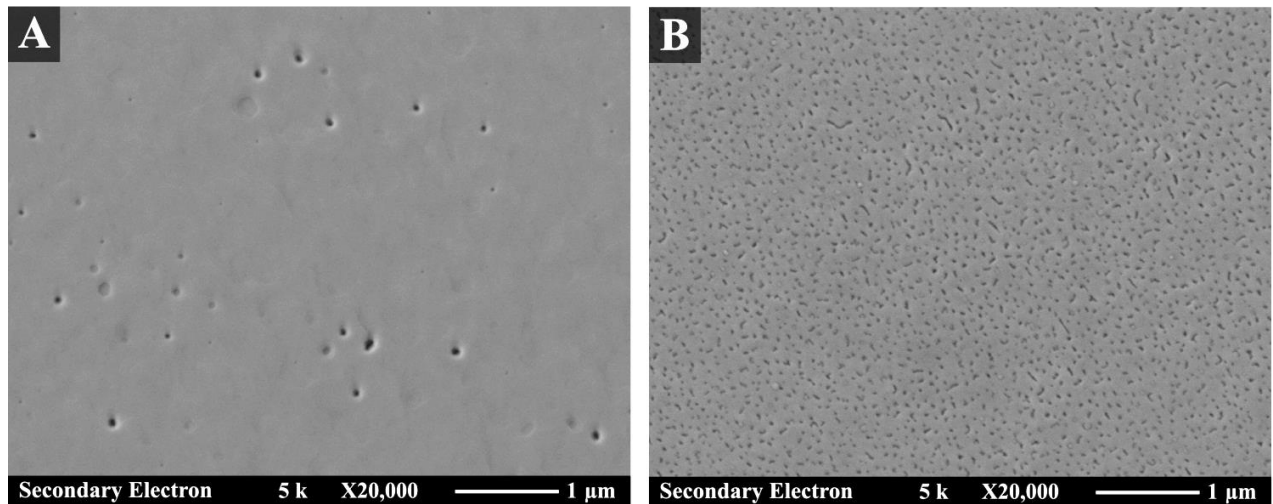


Fig. 11 – Secondary electron micrographs of a 70 nm thick (A) and 115 nm thick (B) films from the XRD study in Table 2 and 3. Hydrophilic surface pitting of the MgO substrates can lead to unpredictable number and size of voids as the film coalesces.

Tetragonality within each sub-set of films can be seen to correlate with increasing $S_{\gamma\beta}$, the ordering term which breaks cubic symmetry. This suggests that heightened tetragonality due to epitaxial strain encourages the formation of the L1' phase in an effort to relieve energy in the system. The bulk lattice constants for the L1₂ phase at Fe_{38.5}Pd_{61.5} ($S_{\alpha\gamma} = .82$, $S_{\gamma\beta} = 0$) are approximately 3.83 Å. L1₀ at this composition ($S_{\alpha\gamma} = 0$, $S_{\gamma\beta} = .77$) has $a = 3.88$ Å and $c = 3.73$ Å ($\{2a+c\}/3 = 3.83$ Å), and a tetragonality of $C/A = 0.961$ [11]. The L1' phase should exist between these bounds and its natural tetragonality may serve to relieve strain energy compared to L1₂. This still leaves the absence of the more tetragonal L1₀ as an unanswered question, which likely results from the unaccounted magnetic energy contribution to the system.

4.4.3 – Feasibility of an L1₀-L1₂ Microstructure

In order to fully embrace the existence of L1' in the system it is important to show that possible alternatives are not tenable. Direct confirmation through HRTEM is difficult as the L1' phase found in these films represents a small compositional shift which impacts the intensity and not location of possible reflections. This ~5 % compositional shift also tests the current boundaries of atomic resolution High Angle Annular Dark Field Scanning Transmission Electron Microscopy (HAADF-STEM) as only one atom on average would be expected to be perturbed in an atomic column for every ~8 nm of material thickness along the optimal (001) or (100) zone axes. Natural variations in thickness or interfacial disorder from sample preparation could be expected to negate or overwhelm the small contrast from L1' ordering for samples thin enough for atomic resolution STEM.

It is possible to reproduce the intensity ratios for the L1' films with a two-phase microstructure of L1₂ and c-oriented L1₀ phases, both of Fe_{38.5}Pd_{61.5} composition. If the alloy does form in a two-phase field its constituents should have separate compositions in equilibrium. Fig. 12 demonstrates that no distinct compositional variance has been observed even for the most

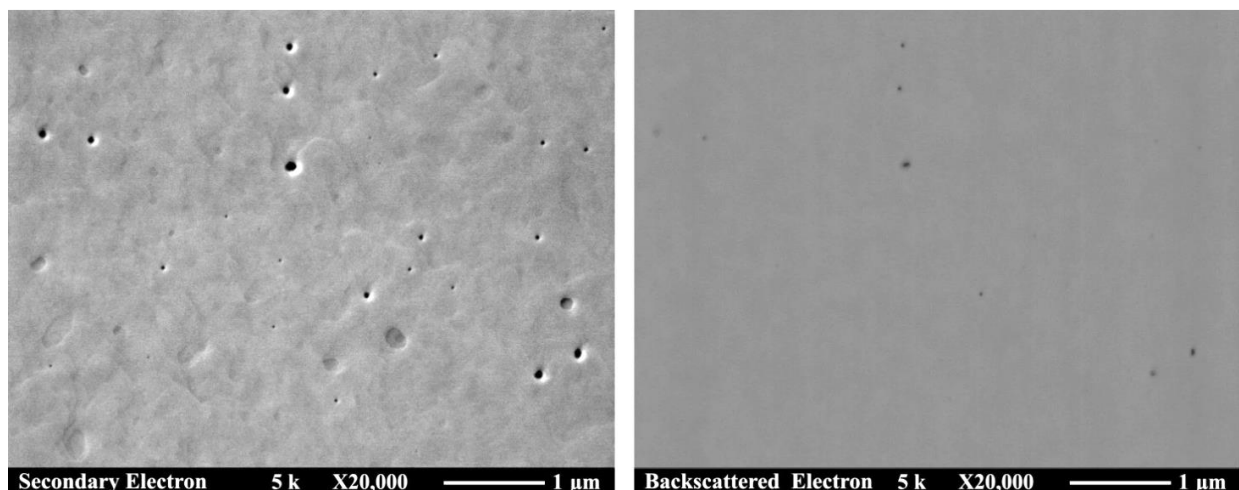


Fig. 12 – Secondary and backscattered electron micrographs of the 70 nm thick L1' film showing no discernible differences in composition, the few features present in backscatter being voids.

distinctly L1' of the films, though the degree of compositional separation could be below the Z-contrast or spatial resolution of backscattered microscopy.

If a two-phase microstructure is present it will need to have formed through nucleation in a first-order phase transition to exclude the possibility of the L1' phase, as continuous ordering from the L1₂ to L1₀ phases necessitates the presence of L1' as an intermediary state. For the four thicker films a two-phase L1₀-L1₂ microstructure can be calculated to require approximately 13 % L1₀ by volume, with ordering scaling as $S/(S_{\max}) = A_{\alpha}$ for both phases. A c-axis oriented L1₀ precipitate with a high degree of ordering can be expected to manifest in magnetic behavior at 13 % volume. VSM hysteresis loops of the thicker films, in addition to those already covered in Chapter 3, possess coercivities in the range of 330 to 430 Oersted (Fig. 13). As L1₀ ordered Fe₄₂Pd₅₈ 10 nm particles grown on MgO substrates still exhibit coercivities above 3000 Oersted [12], and are still above the values observed down to 3 nm [13], this strongly suggests the absence of L1₀. The form of the hysteresis loops closely follows those for the 600°C films from the original temperature study (Ch.3, Fig 7).

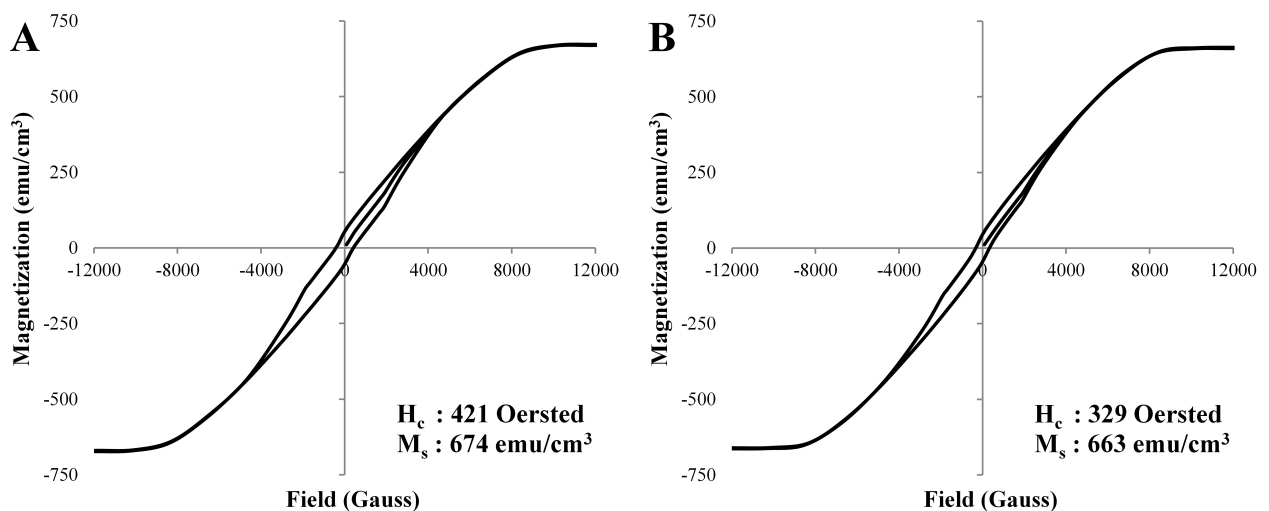


Fig. 13 – Hysteresis loops corresponding to the 70 nm thick (A) and 115 nm thick (B) films in Fig. 11. The low coercivities (H_c) of these films compared to L1₀ suggest absence of the phase.

As domain pinning is expected to play a large role in these films, speculation concerning the effect of L1' ordering on coercivity is prone to a degree of error, as film morphology will exert a sizable influence. A general trend between larger $S_{\gamma\beta}$ values and higher coercivity is expected to exist as tetragonality should increase the magnetocrystalline anisotropy of the film. Finely dispersed L1₀ particles would also be expected to increase pinning, which is not observed.

The absence of c-axis oriented L1₀ precipitates is strengthened by the addition of MFM analysis (Fig. 14). Magnetically hard L1₀ regions of a film should have a stark contrast against

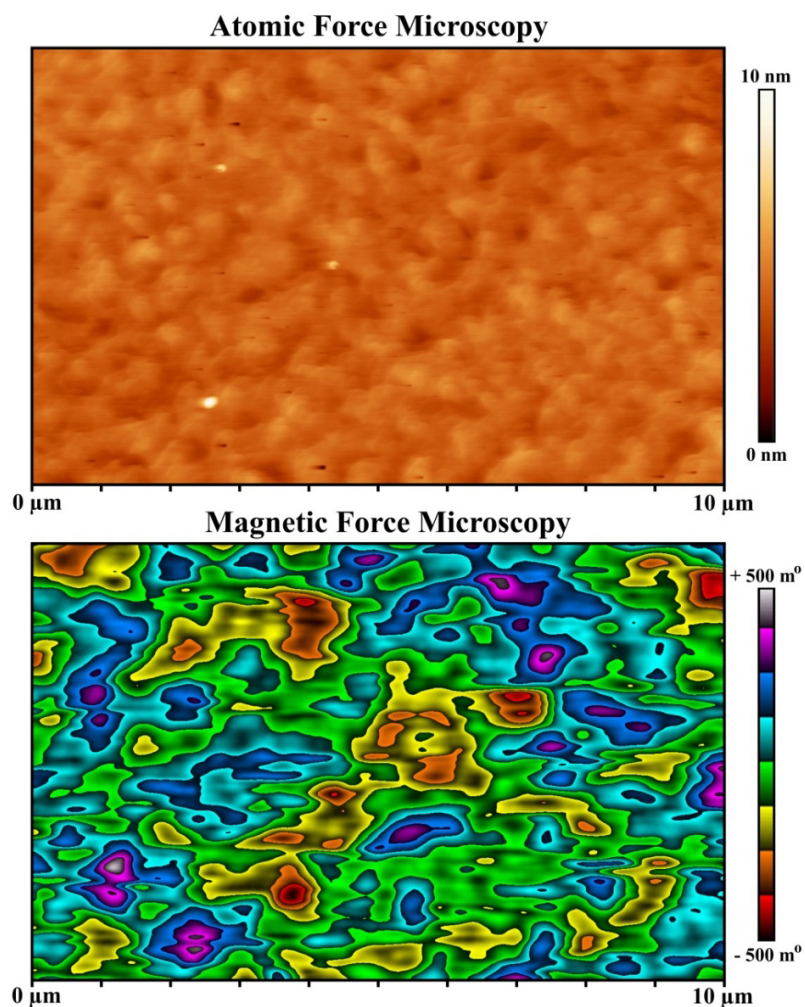


Fig. 14 – Paired atomic and magnetic force micrographs of the film with the strongest L1' ordering (70 nm thick). Magnetic force microscopy shows random magnetic structure and no regions of strong contrast, suggesting a single phase film without magnetically hard precipitates.

the magnetically soft $L1_2$ matrix, which lacks a strong magnetic easy axis and will rotate more freely. Instead, MFM shows a random deviation about the average force on the tip, seen clearly in the contour map with an equal number of high and low points that has no correlation to surface topology. Fe-Pd films are expected to exhibit a striped domain structure with 30 to 50 nm spacing when the magnetic easy axis is aligned out-of-plane [14, 15]. The MFM pattern found in Fig. 14 is instead consistent with the film having a general in-plane orientation for its magnetic easy axis, which is more congruous with a weak $L1_2$ easy axis along the $\langle 111 \rangle$ directions than the strong $L1_0$ easy axis along $[001]$ for films thicker than 30 nm [15-18].

The absence of any $L1_0$ signature in the magnetic behavior at 13% volume fraction is suggestive but not definitive. This volume, however, is well above the detection limit of XRD and would be recognized if convoluted with an $L1_2$ peak. Any $L1_0$ precipitate must consequently share identical lattice parameters with the $L1_2$ matrix. For all the films in Table 3, the $L1_0$ precipitates would be placed under considerable compression for large ordering parameters ($S > 0.8$) $a \rightarrow 3.88 \text{ \AA}$, despite the $L1_2$ matrix ($a = 3.83 \text{ \AA}$) remaining under tensile strain. It would be highly unusual, and energetically unfavorable, for a film to form compressed regions when growing epitaxial to a substrate that is placing it under tensile strain. In juxtaposition, $L1'$ provides a clear account for the strain energy and behavior of the films. Heightened tetragonality for films on each substrate brand is accompanied by a corresponding increase in $S_{\gamma\beta}$, which is related to the strength of $L1_0$ type ordering in $L1'$. As $S_{\gamma\beta}$ increases, the a-axis lattice parameter of $L1'$ will transition away from the $L1_2$ value of 3.83 \AA , toward the $L1_0$ 3.88 \AA . Tetragonality in the films accompanied by $S_{\gamma\beta}$ ordering can therefore lower strain and elastic energy. Developing strain energy during growth is hypothesized to drive the $L1'$ perturbation, and explains the sensitivity of the phase to film thickness, temperature, and the starting substrate surface.

4.5 – Origination of L1' Behavior

Having established the likelihood of the L1' phase forming for epitaxial films of Fe_{38.5}Pd_{61.5}, discussion can transition to the manner that L1' comes to constitute the film: either as a perturbation away from a primordial conventional ordered phase, or as the primary phase arising from the very onset of ordering in the film.

4.5.1 – The Case for L1₂ Perturbation : Snoek/Zener Type Effects

As the Fe_{38.5}Pd_{61.5} films remain predominantly L1₂ in overall nature it is possible that they originate as conventional L1₂ and are subsequently perturbed from this equilibrium by strain conditions in the film. Tensile strain breaks symmetry in the three face-centered L1₂ Pd superlattice sites, creating two variants. Fe atoms are smaller than those of Pd and will be affected differently by the induced strain. In particular they may come to preference the c-axis Pd site of the material to better accommodate epitaxial strain and this perturbation would create the L1' phase from an originally L1₂ film.

This proposed phenomenon is similar to several well-known observations: The Snoek effect concerning the behavior of interstitials in steel [19], and the Zener effect in alloys of α -Brass [20, 21]. In the Snoek effect, strain breaks symmetry of the BCC Fe lattice of α -steel, therefore carbon or nitrogen atoms come to preferentially occupy one of the interstitial sites over others; though the term Snoek effect, “is [nowadays] used in a wider sense, implying the relaxation phenomenon associated with reorientation of isolated solute atoms in any crystal lattice or even in amorphous structures.” [22] For the related Zener effect, stress is found to induce a preferential orientation of Zn-Zn atom pairs in brass, which is a substitutional alloy of Cu and Zn atoms in an FCC lattice structure. The L1' phase may be considered a subset of either

the Snoek or Zener effects, and if a bulk sample of L1' could be produced, experiments involving a Snoek pendulum to measure the diffusion dampening of the alloy may be insightful.

As the difference between L1₂ and L1' behavior is fairly complicated to establish *ex situ*, *in situ* identification to monitor any change of behavior during deposition is prohibitive. If a film could be safely removed from its MgO substrate, which in theory can be done without harming the film with a solution of sodium bicarbonate in water at the rate of 80 nm/hr over the better portion of a year [23], the behavior of the unstrained film may be insightful to the nature of L1' ordering. A more productive path may be to determine if L1' Fe_{38.5}Pd_{61.5} films can be grown on more hydrophilic NaCl (001) substrates, which Fe_{38.5}Pd_{61.5} could be expected to deposit on with the same epitaxial orientation [24]. This would increase the level of experimental difficulty as NaCl must be cleaved under vacuum, but is expected to be a viable way to produce free-standing Fe_{38.5}Pd_{61.5} films for study.

4.5.2 – The Case for Native L1': Simultaneous Continuous Ordering

Transitions between the FCC, L1₀, and L1₂ phases are generally first-order and require nucleation and growth with distinct phase boundaries. As illustrated in Landau's free energy vs. generalized order parameter plots (Fig. 15), there is an instability temperature (T_i) below which the transformation can occur as a continuous higher-order phase transition [25]. The vertical axis of the plot is the change in free energy from the disordered to ordered state, with a long-range order parameter η (as S will be used shortly to represent entropy). Above T_i an energy barrier exists between the disordered and ordered state of the material, preventing it from ordering without nucleation. Below T_i the system is able to move incrementally to states of higher order through a continuous transformation.

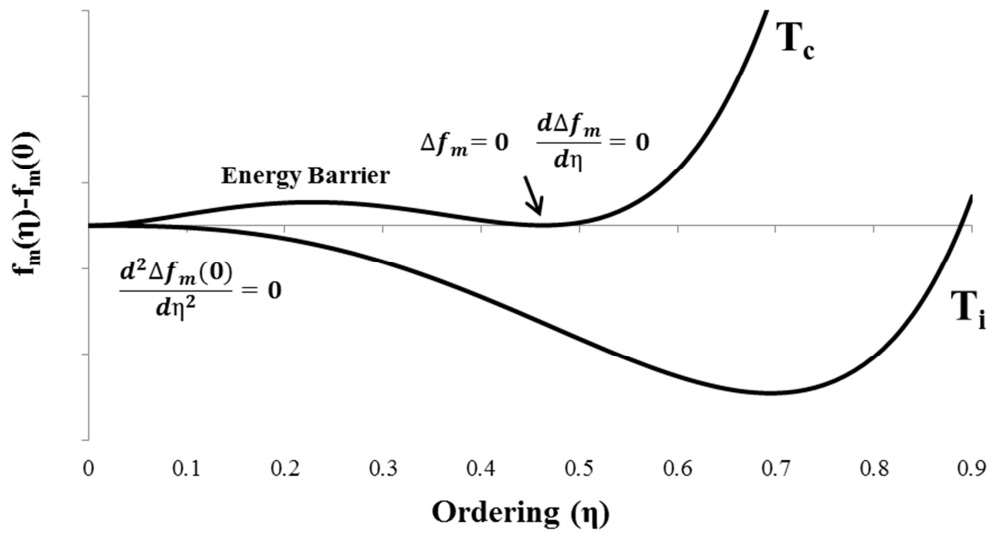


Fig. 15 – Landau free energy plot illustrating the effect of temperature on the nature of ordering. T_c represents the critical temperature and the onset of order. T_i is the instability temperature, marking the transition away from first-order nucleation to continuous ordering.

It is possible that films were grown beneath the instability temperatures for both $L1_0$ and $L1_2$ type ordering, and experience simultaneous continuous ordering. This would imply that the films form in the $L1'$ phase directly during the ordering process of a strained $Fe_{38.5}Pd_{61.5}$ film. Interpolation from cluster variation method modeling for the Au-Cu and Fe-Pt systems [26, 27] suggests that instability temperatures are high for Fe-Pd, on the order of 90 % the ordering temperature. Carrying this ratio over to the experimental diagram of the Fe-Pd system (Fig. 16), it can be seen that the deposition temperatures may fall below the instability temperatures for both ordered phases. This line of reasoning suggests that instead of the complete absence of $L1_0$ from the expected two-phase region of the phase diagram, the system resides in a mixture of local ordering moving the system toward both $L1_0$ and $L1_2$ on the atomic scale simultaneously, in an effort to balance energy contributions from both strain and magnetism.

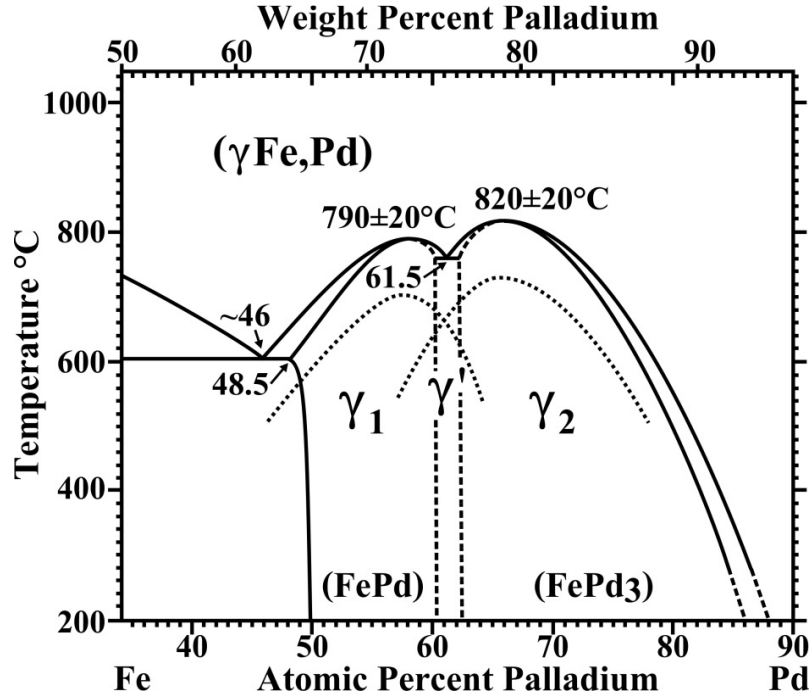


Fig. 16 – Partial phase diagram of the Fe-Pd material system centered about the $Fe_{38.5}Pd_{61.5}$ eutectoid composition. Dashed lines in the diagram represent uncertain boundaries in the experimental phase diagram. Dotted lines represent the approximate instability temperatures of the $L1_0$ and $L1_2$ phases, underneath which $L1'$ may be expected to form from simultaneous continuous ordering.

4.5.3 - First Principles Calculation of Instability Temperatures

In this section a first-order assessment of the instability temperature for both the $L1_0$ and $L1_2$ phases of Fe-Pd is made to compare against the cluster variation method, expanding upon the generalized Bragg-Williams approach and Khachatryan's Static Wave Concentration (SCW) methods [28-30]. The derivation for the instability temperature starts with the interchange energies (V_n) from first and second nearest-neighbors in the FCC crystal.

$$V_{1st} = \frac{1}{2}(E_{AA}^{(1st)} + E_{BB}^{(1st)} - 2E_{AB}^{(1st)}) \quad (29)$$

$$V_{2nd} = \frac{1}{2}(E_{AA}^{(2nd)} + E_{BB}^{(2nd)} - 2E_{AB}^{(2nd)}) \quad (30)$$

The terms of type $E_{AA}^{(2nd)}$ are pairwise interaction energies between atoms, in the case of $E_{AA}^{(2nd)}$ the interaction between two A type atoms between second nearest-neighbor sites. In general the Hemholtz free energy of mixing in solution of A & B atoms can be written as

$$F_m = E_m - TS_m \quad (31)$$

The heat of mixing term E_m can be broken down into either 1st and 2nd neighbor interactions E_1 and E_2 , or components based on the disordered state E_d and the addition of ordering E_o .

$$E_m = E_1 + E_2 = E_d + E_o \quad (32)$$

Introducing the alloy composition C , and the long-range order parameter η , for the $L1_0$ and $L1_2$ phases it follows that

$$C_\alpha^{L1_0} = C - \frac{1}{2}\eta \quad C_\alpha^{L1_2} = C - \frac{1}{4}\eta \quad (33)$$

$$C_\beta^{L1_0} = C + \frac{1}{2}\eta \quad C_\beta^{L1_2} = C + \frac{3}{4}\eta \quad (34)$$

From here, with an extensive use of algebra and analysis of nearest-neighbor relations in the $L1_0$ and $L1_2$ crystals [31], the heat of mixing contributions are found to be

$$E_1^{L1_0} = NV_{1st}\{12C(1 - C) + \eta^2\} \quad E_1^{L1_2} = NV_{1st}\{12C(1 - C) + \frac{6}{8}\eta^2\} \quad (35)$$

$$E_2^{L1_0} = NV_{2nd}\{6C(1 - C) - \frac{6}{4}\eta^2\} \quad E_2^{L1_2} = NV_{2nd}\{6C(1 - C) - \frac{9}{8}\eta^2\} \quad (36)$$

$$E_d^{L1_0} = NC(1 - C)\{12V_{1st} + 6V_{2nd}\} \quad E_d^{L1_2} = NC(1 - C)\{12V_{1st} + 6V_{2nd}\} \quad (37)$$

$$E_o^{L1_0} = \frac{1}{4}N\eta^2\{4V_{1st} - 6V_{2nd}\} \quad E_o^{L1_2} = \frac{3}{16}N\eta^2\{4V_{1st} - 6V_{2nd}\} \quad (38)$$

The entropy of mixing term of Eq. 31 in the mean field approximation for ideal mixing is given by Boltzmann's entropy formula

$$S_m = k_B \ln \Omega \quad (39)$$

Assuming random mixing on the sublattices, the configuration entropy depends on the total number of possible arrangements of microstates for the system:

$$S_m^{L1_0} = k_B \ln \frac{\left\{\frac{1}{2}N\right\}!}{\{N_A^\alpha\}!\{N_B^\alpha\}!} \frac{\left\{\frac{1}{2}N\right\}!}{\{N_A^\beta\}!\{N_B^\beta\}!} \quad (40)$$

$$S_m^{L1_2} = k_B \ln \frac{\left\{\frac{3}{4}N\right\}!}{\{N_A^\alpha\}!\{N_B^\alpha\}!} \frac{\left\{\frac{1}{4}N\right\}!}{\{N_A^\beta\}!\{N_B^\beta\}!} \quad (41)$$

These expressions can be expanded in terms of C and η using Sterling's approximation so that

$$S_m^{L1_0} = \frac{-k_B N}{4} \left\{ \begin{aligned} &2\left(C - \frac{1}{2}\eta\right) \ln \left(C - \frac{1}{2}\eta\right) + 2\left(1 - C + \frac{1}{2}\eta\right) \ln \left(1 - C + \frac{1}{2}\eta\right) \\ &+ 2\left(C + \frac{1}{2}\eta\right) \ln \left(C + \frac{1}{2}\eta\right) + 2\left(1 - C - \frac{1}{2}\eta\right) \ln \left(1 - C - \frac{1}{2}\eta\right) \end{aligned} \right\} \quad (42)$$

$$S_m^{L1_2} = \frac{-k_B N}{4} \left\{ \begin{aligned} &3\left(C - \frac{1}{4}\eta\right) \ln \left(C - \frac{1}{4}\eta\right) + 3\left(1 - C + \frac{1}{4}\eta\right) \ln \left(1 - C + \frac{1}{4}\eta\right) \\ &+ \left(C + \frac{3}{4}\eta\right) \ln \left(C + \frac{3}{4}\eta\right) + \left(1 - C - \frac{3}{4}\eta\right) \ln \left(1 - C - \frac{3}{4}\eta\right) \end{aligned} \right\} \quad (43)$$

Khachatryan's SCW method approaches site occupancies and interchange energies as formulated in reciprocal k-space, with the use of discrete Fourier transforms. The real space site occupation $n(r)$ can be described this way as

$$n(r) = C + \sum_k Q(k) \exp(ik \cdot r) \quad (44)$$

Here the average composition C is modified by a superposition of concentration waves with wave vectors k and magnitude Q(k), localized in the first Brillouin zone.

This allows the interchange energies to be expressed by a Fourier transform with the summation occurring over the first and second neighbors.

$$V(k_0) = \sum_r V(r) \exp(ik_0 \cdot r) \quad (45)$$

For the first and second nearest-neighbor interactions of an FCC structure this yields

$$V(0) = 12V_{1st} + 6V_{2nd} \quad (46)$$

$$V(k_0) = -4V_{1st} + 6V_{2nd} \quad (47)$$

Which allows for Eqs. 37 and 38 to be rewritten as

$$E_d^{L1_0} = NC(1 - C)V(0) \quad E_d^{L1_2} = NC(1 - C)V(0) \quad (48)$$

$$E_o^{L1_0} = -\frac{1}{4}N\eta^2V(k_0) \quad E_o^{L1_2} = -\frac{3}{16}N\eta^2V(k_0) \quad (49)$$

If the heats of formation for the disordered and ordered phases are known, it is now possible to solve for $V(0)$ and $V(k_0)$. For Fe-Pd there are predicted heats of formation available that are calculated from the cluster variation method [32].

$$E_d^{FePd} = N(4 \times 10^{-3})Ry \quad E_d^{FePd_3} = -N(1 \times 10^{-3})Ry \quad (50)$$

$$E_o^{FePd} = -N(6 \times 10^{-3})Ry \quad E_o^{FePd_3} = -N(3 \times 10^{-3})Ry \quad (51)$$

Combined with Eq. 48 and 49, the known concentrations, and $\eta = 1$ of the stoichiometric ordered phases, this results in the interaction energies

$$V(0)^{FePd} = 12 \times 10^{-3} Ry \quad V(0)^{FePd_3} = -5.33 \times 10^{-3} Ry \quad (52)$$

$$V(k_0)^{FePd} = 24 \times 10^{-3} Ry \quad V(k_0)^{FePd_3} = 16 \times 10^{-3} Ry \quad (53)$$

To find the critical temperatures, T_c , the free energy related to ordering for the two ordered phases can now be approached as in Fig. 15. The form of F_m is conveniently compressed by the use of stoichiometric compositions ($C = 0.5$ for $L1_0$ and $C = 0.25$ for $L1_2$) and subtraction of the disordered $F_m(0)$, resulting in the more manageable

$$F_m(\eta)^{FePd} - F_m(0)^{FePd} = -\frac{1}{4}N\eta^2V(k_0)^{FePd} + \frac{k_BNT}{4}\left\{2(1-1\eta)\ln\left(\frac{1}{2}-\frac{1}{2}\eta\right) + 2(1+1\eta)\ln\left(\frac{1}{2}+\frac{1}{2}\eta\right) - 4\ln\left(\frac{1}{2}\right)\right\} \quad (54)$$

$$F_m(\eta)^{FePd_3} - F_m(0)^{FePd_3} = -\frac{3}{16}N\eta^2V(k_0)^{FePd_3} + \frac{k_BNT}{4}\left\{3\left(\frac{1}{4}-\frac{1}{4}\eta\right)\ln\left(\frac{1}{4}-\frac{1}{4}\eta\right) + 3\left(\frac{3}{4}+\frac{1}{4}\eta\right)\ln\left(\frac{3}{4}+\frac{1}{4}\eta\right) - 3\ln\left(\frac{3}{4}\right)\right. \\ \left.+ \left(\frac{1}{4}+\frac{3}{4}\eta\right)\ln\left(\frac{1}{4}+\frac{3}{4}\eta\right) + \left(\frac{3}{4}-\frac{3}{4}\eta\right)\ln\left(\frac{3}{4}-\frac{3}{4}\eta\right) - \ln\left(\frac{1}{4}\right)\right\} \quad (55)$$

These equations can now be graphed as Landau free energy plots. For FePd this results in Fig 17, which shows a critical temperature of approximately 1895 K. The vanishingly small energy barrier formed at T_c suggests that the instability temperature will be very similar to T_c for FePd.

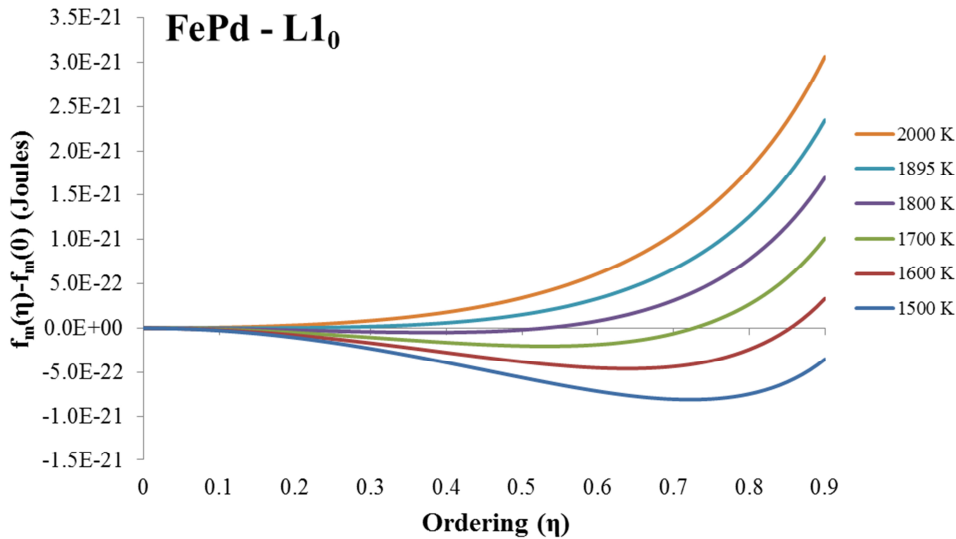


Fig. 17 – Landau free energy plot of Eq. 54 for FePd, normalized per atom. The critical temperature $T_c = 1895$ K, and the lack of a significant energy barrier implies T_i is nearly T_c .

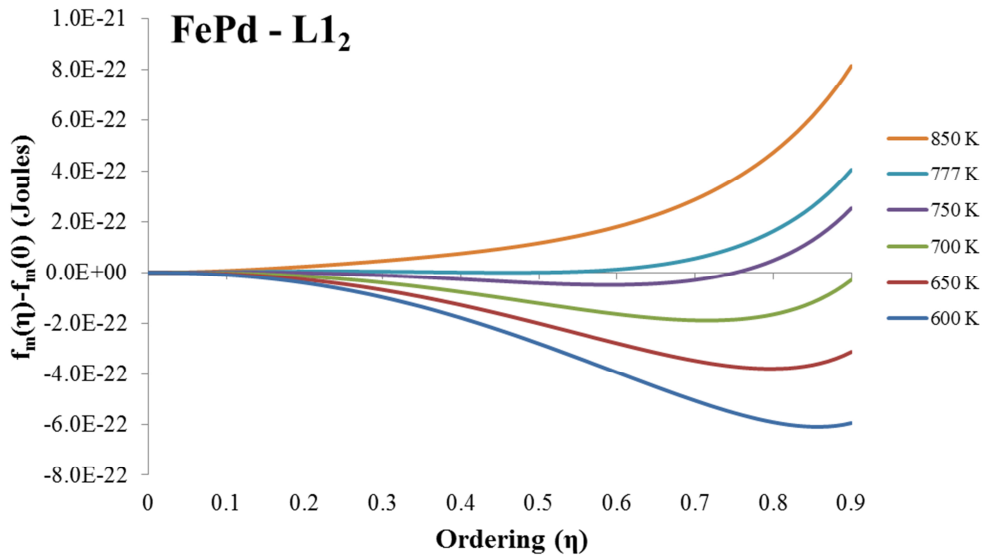


Fig. 18 – Landau free energy plot of Eq. 55 for FePd₃, normalized per atom. The critical temperature $T_c = 777$ K, and unlike FePd a small energy barrier is present at T_c .

The Landau plot of FePd₃ (Fig. 18) shows a critical temperature of approximately 777 K and a clear energy barrier at T_c that is better visualized on a different vertical scale (Fig. 19). The presence of this barrier suggests there will be more separation between T_i and T_c for FePd₃.

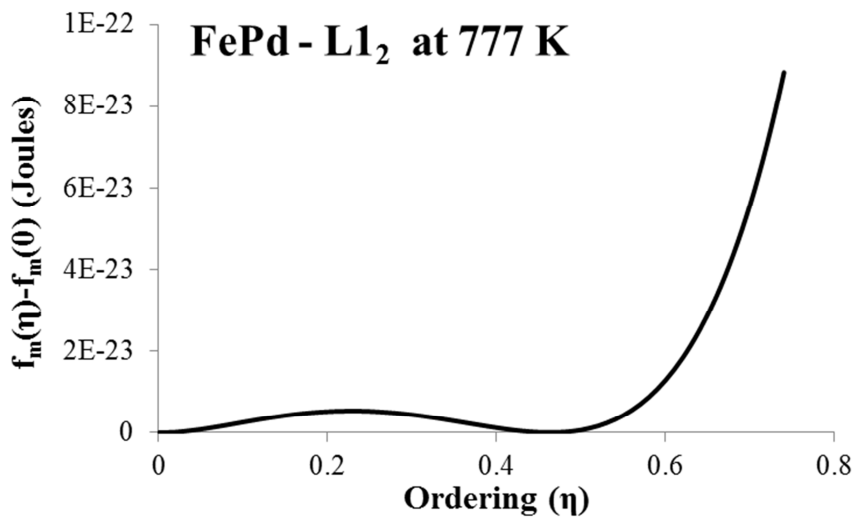


Fig. 19 – Landau free energy plot of Eq. 55 for FePd₃ at 770 K, normalized per atom. The larger energy barrier for ordering than FePd suggests more separation between T_c and T_i .

The instability temperatures T_i for both phases can now be calculated by taking the second derivative of the free energy of ordering, Eqs. 54 and 55. Setting $\eta = 0$ and solving for the inflection point, representing the removal of an energy barrier to ordering, the temperature for continuous ordering can be found.

$$\frac{d^2}{d\eta^2} \Delta F_m(\eta)^{FePd} = -\frac{1}{2}NV(k_0)^{FePd} + \frac{k_BNT}{4} \left\{ \frac{4}{\eta^2-1} \right\} \quad (56)$$

$$\frac{d^2}{d\eta^2} \Delta F_m(\eta)^{FePd_3} = -\frac{3}{8}NV(k_0)^{FePd_3} + \frac{k_BNT}{4} \left\{ \frac{3}{4-4\eta} + \frac{3}{12+4\eta} + \frac{9}{4+12\eta} + \frac{9}{12-12\eta} \right\} \quad (57)$$

$$\frac{d^2}{d\eta^2} \Delta F_m(0)^{FePd} = 0 \quad T_i^{FePd} = \frac{V(k_0)^{FePd}}{2k_B} \quad (58)$$

$$\frac{d^2}{d\eta^2} \Delta F_m(0)^{FePd_3} = 0 \quad T_i^{FePd_3} = \frac{3V(k_0)^{FePd_3}}{8k_B} \quad (59)$$

The instability temperatures are thusly $T_i^{FePd} = 1894.6$ K and $T_i^{FePd_3} = 710.5$ K. Eqs. 58 and 59 here conform to the formula given for the instability temperature as a function of concentration, which can be used to assess changes to T_i with composition. [33, 34]

$$k_B T_i = 2C(1 - C)V(k_0) \quad (60)$$

The ordering temperatures found using this first-order approximation are significantly different than those of the experimental diagram. Like the shift of the congruent compositions away from the stoichiometric compounds, much of this is attributed to the large but unaddressed magnetic contribution to the free energy. However, this model agrees well qualitatively with the cluster variation approach and predicts the instability temperatures for both the phases to be very close to their critical temperatures, in the range of 91 to 100% of their value. Consequentially, continuous ordering is considered a viable pathway even at the elevated depositions temperatures used for the films in this study.

4.6 – Major Findings

Through epitaxial deposition of $L1_0$ - $L1_2$ eutectoid $Fe_{38.5}Pd_{61.5}$ films PLD onto MgO (001) substrates, experimental verification of the long-theorized $L1'$ hybrid ordered structure has been reached. The quantitative methodology needed to assess films of this nature by XRD is presented along with thorough analysis of possible errors. New formalisms have been established for the discussion of ordering in this type of structure, with the definition of two ordering parameters highlighting the hybridized nature of the phase. The possibility of a two-phase $L1_0$ - $L1_2$ microstructure is ruled out as unlikely through magnetic and crystallographic analysis. $L1'$ type ordering is theorized to arise either as a Snoek effect type perturbation of the $L1_2$ phase due to strain, or as the result of simultaneous ordering toward both the $L1_0$ and $L1_2$ phases on the atomic scale.

References

- [1] W. Shockley, J. Chem. Phys. **6**, 130 (1938)
- [2] W. Soffa, D. Laughlin, N. Singh, Phil. Mag., **90**, 287 (2010)
- [3] S. Wei, A. Mbaye, L. Ferreira and A. Zunger, Phys. Rev. B **36**, 4163 (1987)
- [4] Y. Li, J. Chem. Phys. **17**, 447 (1949)
- [5] R. Kikuchi, Prog. Theor. Phys. Supplement **87**, 69 (1986)
- [6] A. Finel and F. Ducastelle, Europhysics Letters **3**, 135 (1986)
- [7] R. Tetot, A. Finel and F. Ducastelle, J. Stat. Phys **61**, 121 (1990)
- [8] B. Warren, *X-Ray Diffraction* (Addison-Wesley, Reading, MA, 1969)
- [9] E. Yang, D. Laughlin, and J. Zhu, IEEE Trans. on Magnetics **48**, 7 (2012)
- [10] X. Sang, A. Kulovits and J. Wieszorek, Acta Cryst. A **67**, 229 (2011)
- [11] E. Raub, H. Beeskow, and O. Loebich, Z. Metallkd. **54**, 549 (1963)
- [12] K. Sato, B. Bian, and Y. Hirotsu, J. Appl. Phys. **91**, 8516 (2002)
- [13] T. Schied, a. Lotnyk, C. Zamponi, L. Kienle, J. Buschbeck, M. Weisheit, B. Holzapfel, L. Schultz, and S. Fähler, J. Appl. Phys. **108**, 033902 (2010)
- [14] P. Tiberto, F. Celegato, M. Coisson and F. Vinai, IEEE Trans. Magn., **44**, 3921 (2008)
- [15] V. Gehanno, R. Hoffman, Y. Samson, A. Marty and S. Auffret, Eur. Phys J. B **10**, 457, (1999)
- [16] N. Miyata, H. Asami, and T. Mizushima, J. Phys. Soc. Jpn. **55**, 946 (1986)
- [17] L. Magat, A. Yermolenko, G. Ivanova, G. Makarova, and Y. Shur, Phys. Met. Metall. **26**, 132 (1968)
- [18] V. Myagkov, V. Zhigalov, B. Belyaev, L. Bykova, L. Solovyov, and B. Bondarenko, J. Magn. Magn. Mater. **324**, 1571 (2012)
- [19] J. Snoek, Physica **8**, 711 (1941)
- [20] C. Zener, Trans. AIME **152**, 122 (1943)
- [21] C. Zener, Phys. Rev. **71**, 34 (1947)
- [22] M Koiwa, Materials Science and Engineering A, **370**, 9 (2004)
- [23] T. Edler and S. Mayr, Adv. Mater. **22**, 4969 (2010)
- [24] F. Liscio, D. Makarov, M. Maret, B. Doisneau-Cottignies, H. Roussel and M. Albrecht. Nanotechnology, **21**, 065602 (2010)
- [25] L. Landau, and E. Lifshitz, *Statistical Physics. 3rd edn.* (Pergamon Press, London, 1980)
- [26] T. Mohri, J. Phase Equilib. Diff. **32**, 537 (2011)
- [27] Y. Tanaka, K. Udoh, K. Hisatsune, and K. Yasuda, Philos. Mag. **69**, 925 (1994)
- [28] W. Bragg and E. Williams, Proc. Roy. Soc. London, A **145**, 699 (1934)
- [29] A. Khachaturyan, T. Lindsey and J. Morris, J. Metall. Trans, **A19**, 249 (1988)
- [30] A. Khachaturyan, *Theory of Structural Transformations in Solids* (Wiley and Sons, New York, 1983)
- [31] A. Cottrell, *Theoretical Structural Metallurgy* (Edward Arnold, London, 1960)
- [32] Y. Chen, T. Atago and T. Mohri, J. Phys. Condens. Matter, **14**, 1903 (2002)
- [33] W. Soffa and D. Laughlin, Acta Metall. **37**, 3019 (1989)
- [34] W. Soffa and D. Laughlin, *Proceedings of an International Conference on Solid → Solid Phase Transformations* (Metallurgical Society of AIME, Warrendale, PA, 1982)

5 – Two-Phase Films Grown at 550°C

5.1 - Introduction

From the growth temperature study of $\text{Fe}_{38.5}\text{Pd}_{61.5}$ films deposited onto on MgO (001) substrates at 500°C, 550°C, 600°C and 650°C (Chapter 3), it became apparent that $\text{Fe}_{38.5}\text{Pd}_{61.5}$ films grown at 550°C exhibit dramatically different behaviors from those grown at 500°C, 600°C or 650°C. This will be shown to be result of an unexpected two-phase decomposition between the disordered FCC and ordered $L1_2$ phases, despite the system residing in what is thought to be an $L1_0$ - $L1_2$ two-phase region. This microstructure consists of disordered $\text{Fe}_{60}\text{Pd}_{40}$ FCC secondary phases with 10 to 100 nm facets oriented along the $\langle 110 \rangle$ substrate directions, embedded within a nearly stoichiometric ordered $\text{Fe}_{27}\text{Pd}_{73}$ $L1_2$ Pd-rich matrix. These secondary phase, magnetically soft precipitates exhibit single domain magnetic axis rotation, while the ordered $L1_2$ matrix has a magnetic easy axis aligned in-plane.

This unique two-phase microstructure is postulated to be induced by the degree of epitaxial strain present in the films growing at 550°C, as the deposition temperature is sufficient for coalescence and larger grain sizes than the columnar films grown at 500°C, but low enough that the misfit dislocations needed for relaxation at the interface are considerably less mobile than those at higher deposition temperatures. In this chapter the unique two-phase microstructure of the films grown at 550°C will then be examined closely in terms of crystallographic, compositional and magnetic properties. The origination and behavior of the two-phase decomposition will then be discussed in relation to the experimental phase diagram, highlighting a possible pathway to arrive at the observed microstructural state.

5.2 - Characterization of the Two-Phase Microstructure

From the initial characterization of the 550°C films in Chapter 3 (Fig. 1) it became clear that their behavior was inconsistent with the general trends of the temperature study. This ranged from the increased surface topography compared to films grown at temperatures above and below them, to the marked decreases in the size and shape of their VSM hysteresis loops. Consequently, further characterization was required to assess their microstructural nature.

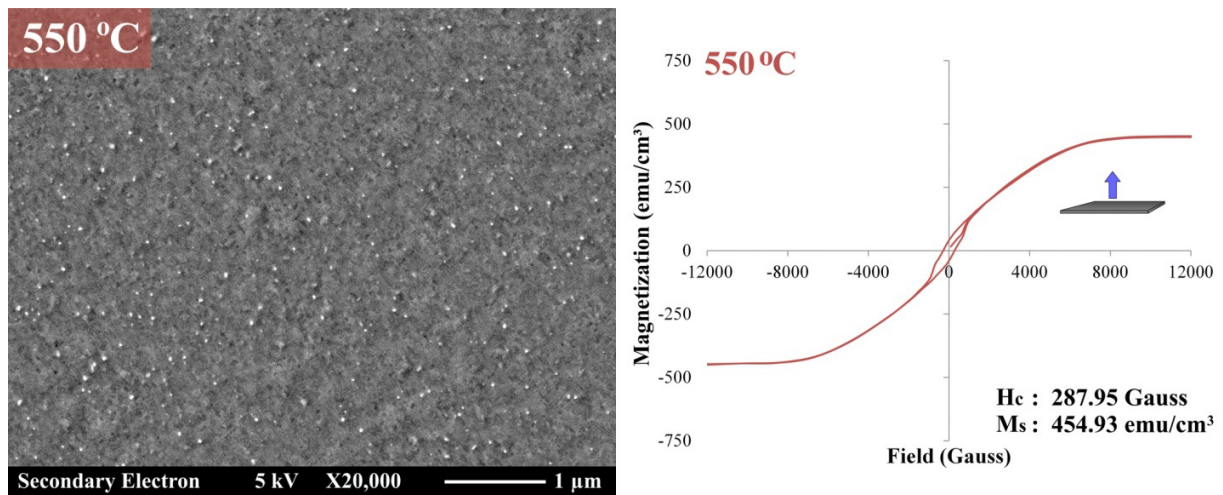


Fig. 1 - SEM secondary electron micrograph of a 550°C Fe_{38.5}Pd_{61.5} film with distinctive features which rise from the surface and corresponding VSM hysteresis loop with low coercivity and saturation magnetization, originally presented as results in Chapter 3.

5.2.1. Backscattered Electron Microscopy

The compositional contrast provided by backscattered electron microscopy in an SEM is often a critical tool for the imaging of multi-phase microstructures. Utilizing a relatively low working voltage of 5 nm, the interaction volume can be limited within the depth of the Fe-Pd film (Chapter 2, Section 2.3.1), yielding the necessary resolution to image the nanostructured film, as well as lowering background signal from the substrate and increasing contrast from

atomic number changes. This analysis shows that the 550°C films are definitively two-phase in nature (Fig. 2). Rectangular surface features in secondary electron imaging can be seen to correlate with the presence of an Fe-rich secondary phase within a denser, Pd-rich surrounding matrix. These {110} faceted, Fe-rich secondary phases are oriented along the <110> substrate directions and have sides ranging from 10 to 100 nm in length.

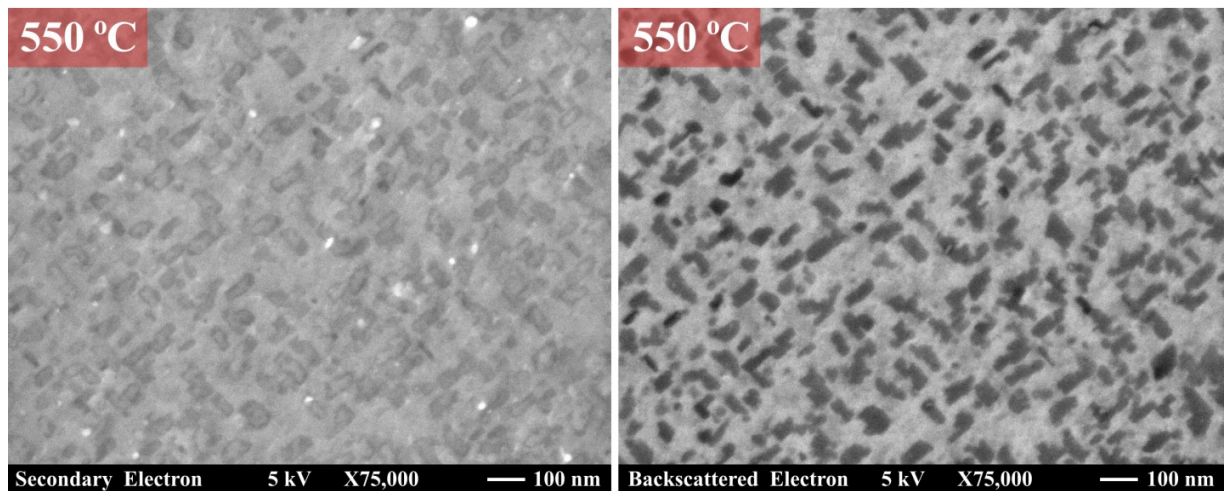


Fig. 2 - SEM secondary electron and atomic z-contrast backscattered electron micrographs of a two-phase $Fe_{38.5}Pd_{61.5}$ film grown at 550°C, showing rectangular features which correlate to Fe-rich FCC phases with preferential facets along the <110> family of directions, embedded in a Pd-rich continuous matrix phase.

Image analysis, utilizing open-source ImageJ software [1-3], establishes that the Fe-rich secondary phase constitutes approximately 32 % of the film surface by areal fraction. It is expected that the depth of these secondary phases approach or reach the substrate interface, as the areal phase fraction and volume phase fraction, as determined later by Auger analysis, are in close agreement. Contrast threshold filtering allows for an approximate particle (in this case precipitate) size distribution to be constructed from backscattered micrographs. The general process for this is illustrated for a 550°C film in Fig. 3.

ImageJ Micrograph Analysis Example

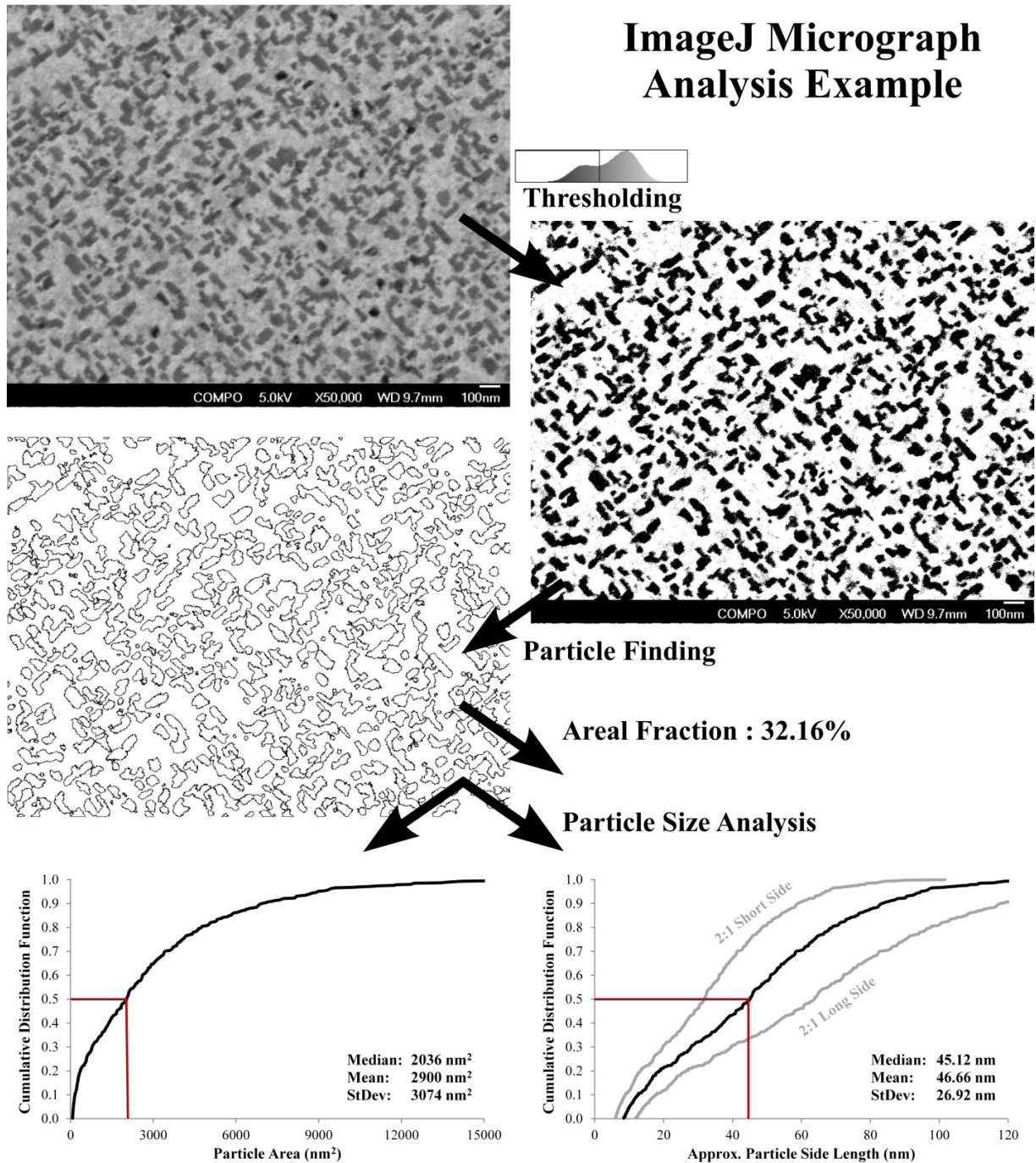


Fig. 3 – A detailed illustration of the image analysis process used for the two-phase films. A backscattered electron micrograph is broken down into a black and white image using a contrast threshold, splitting two convoluted Gaussian signal peaks. The black and white image is then used to compute phase fractions, as well as to outline and measure particle distributions. The median particle area is $\sim 2000 \text{ nm}^2$, approximately a $45 \times 45 \text{ nm}$ square or $32 \times 64 \text{ nm}$ rectangle.

This analysis method will tend to overestimate the average size of precipitates by connecting some in close proximity that do not actually appear to touch, as interpreted by the human eye, and will also include some small points of contrast in the matrix that may not be particles. The analysis for most measured precipitates is reliable and, as the median is resistant to both these types of outliers, it can be said with high confidence to be about 2000 nm². The precipitates can be approximated as rectangles with an aspect ratio somewhere between 1:1 and 2:1, with larger precipitates tending to be more rectangular. This places the median precipitate in the range between a square of 45 x 45 nm and 32 x 64 nm rectangle, which appears to be an accurate assessment of the distribution. Considerably more of the secondary phase will reside in precipitates larger than the median size, with precipitates either larger or smaller than ~5300 nm² representing half of the secondary phase by area. This explains why a cross-hatched pattern of 50 x 100 nm rectangular precipitates appears to be the dominant feature of the backscattered micrographs, even though they are not strictly “average” in size.

5.2.2 - X-Ray Diffraction

Through the use of XRD ϕ -scans (Fig. 4), it can be confirmed that the two-phase films maintain cube-on-cube epitaxy with the MgO (001) substrates. Similar to the films grown at other temperatures, the presence of all four {101} Fe-Pd superlattice peaks can only be formed by the L1₂ ordered phase or by two coexisting, perpendicular in-plane variants of L1₀ with axes along the [010] and [100] directions. Reciprocal Space Mapping (RSM) [4] about the (204) fundamental peaks of the Fe_{38.5}Pd_{61.5} films and MgO substrate (Fig. 5) allows for both lattice parameters of the film to be determined. A tetragonal distortion is observed, with $a = 3.850 \text{ \AA}$ and $c = 3.805 \text{ \AA}$, consistent with all the films studied in this thesis and attributed to epitaxial strain. Using a high-order reflection, such as (204), yields an increased accuracy for

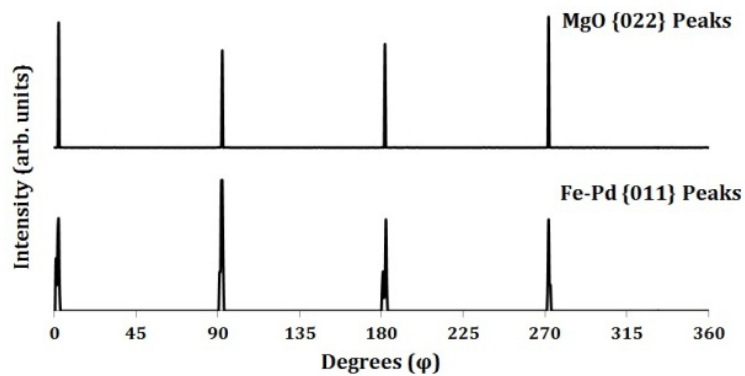


Fig. 4 – XRD ϕ -scans about the Fe-Pd {011} and MgO {022} peaks of an $Fe_{38.5}Pd_{61.5}$ film grown at 550°C confirm cube-on-cube epitaxy and are consistent with an $L1_2$ matrix phase.

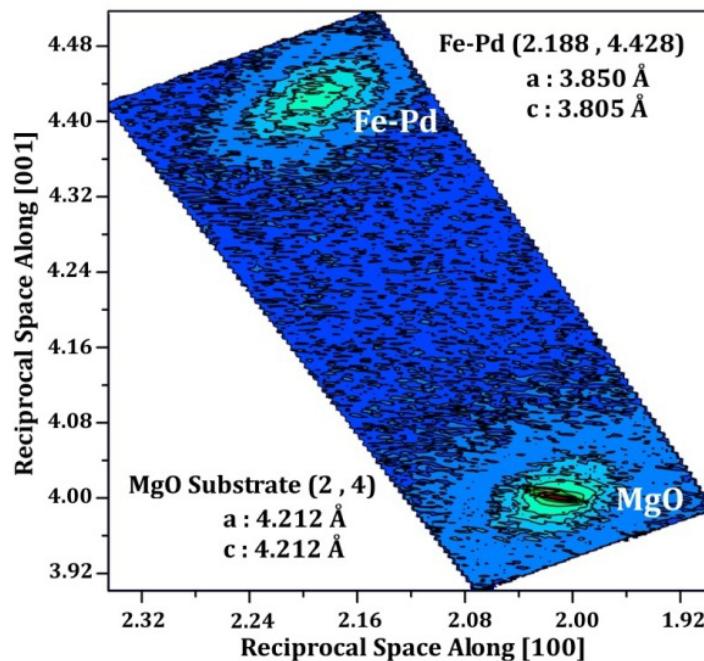


Fig. 5 – Reciprocal space map about the (204) peaks of the MgO substrate and an $Fe_{38.5}Pd_{61.5}$ film grown at 550°C, confirming that the $Fe_{38.5}Pd_{61.5}$ film is tetragonally distorted under tensile strain from epitaxial conformance to the substrate. The singular and symmetric nature of the $Fe_{38.5}Pd_{61.5}$ film peak implies that both film phases have identical lattice parameters.

determination of the film’s lattice parameters. From the single-peak nature of the Fe-Pd (204) intensity map, with no asymmetric spread and a reasonably tight distribution, it can be inferred that both phases of the system will share identical lattice parameters. Utilizing the known

superlattice intensities and peak locations of the films, the dominant Pd-rich matrix can be assigned as a tetragonally distorted $L1_2$ phase. The single set of lattice parameters for both the phases suggests that the Fe-rich secondary phase will be one of four possibilities: amorphous, disordered FCC, the c-axis oriented variant of the $L1_0$, or an implausible variant of the $L1_2$ phase with an Fe concentration considerably higher than the eutectoid composition.

5.2.3 – Magnetic Properties

With knowledge that the Pd-rich matrix is $L1_2$ in nature, the perpendicular hysteresis loop of the 550°C film can be broken speculatively into two separate parts, each contributed by one of the phases present (Fig. 6). If the magnetic easy axis of the $L1_2$ matrix rests in-plane, the perpendicular loop will exhibit a linear magnetic relation until saturation. Removing this contribution from the hysteresis loop, the remainder of the magnetic behavior may be attributed to the Fe-rich secondary phase.

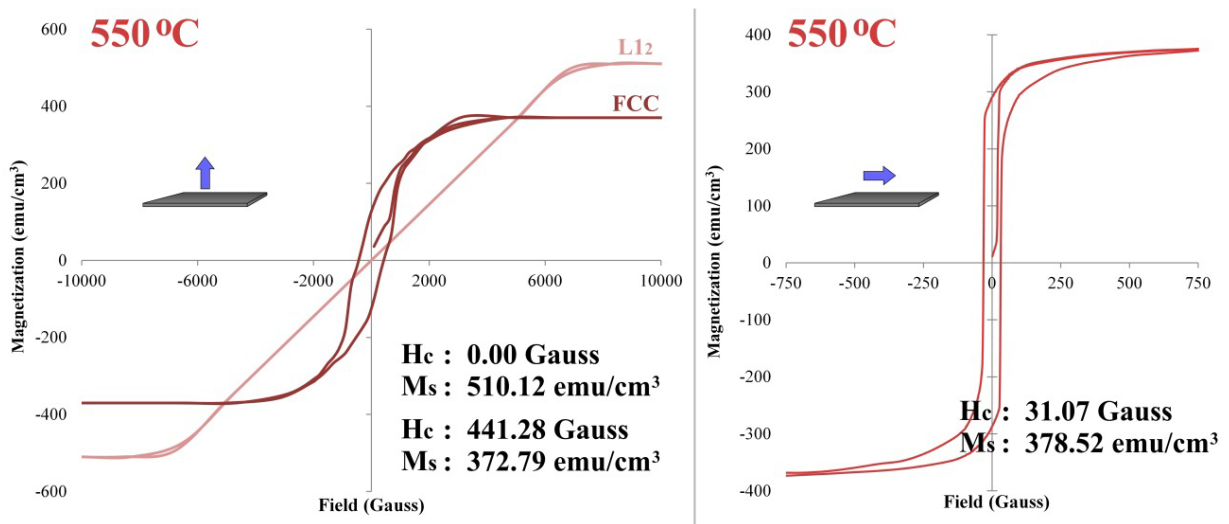


Fig. 6 – VSM hysteresis loops of a 550°C $\text{Fe}_{38.5}\text{Pd}_{61.5}$ film, showing the out-of-plane hysteresis loop broken into two components: one from the Pd-rich $L1_2$ matrix which has its magnetic easy axis in-plane, the second from the Fe-rich FCC secondary phases exhibiting single domain magnetic axis rotation. The in-plane hysteresis loop confirms the $L1_2$ matrix phase has a magnetic axis resting in-plane.

This second contribution, especially in its initial magnetization behavior, is a close match to that predicted by the Stoner–Wohlfarth model for an array of single-domain particles with randomly oriented magnetic axes experiencing magnetic rotation (Fig. 7) [5, 6].

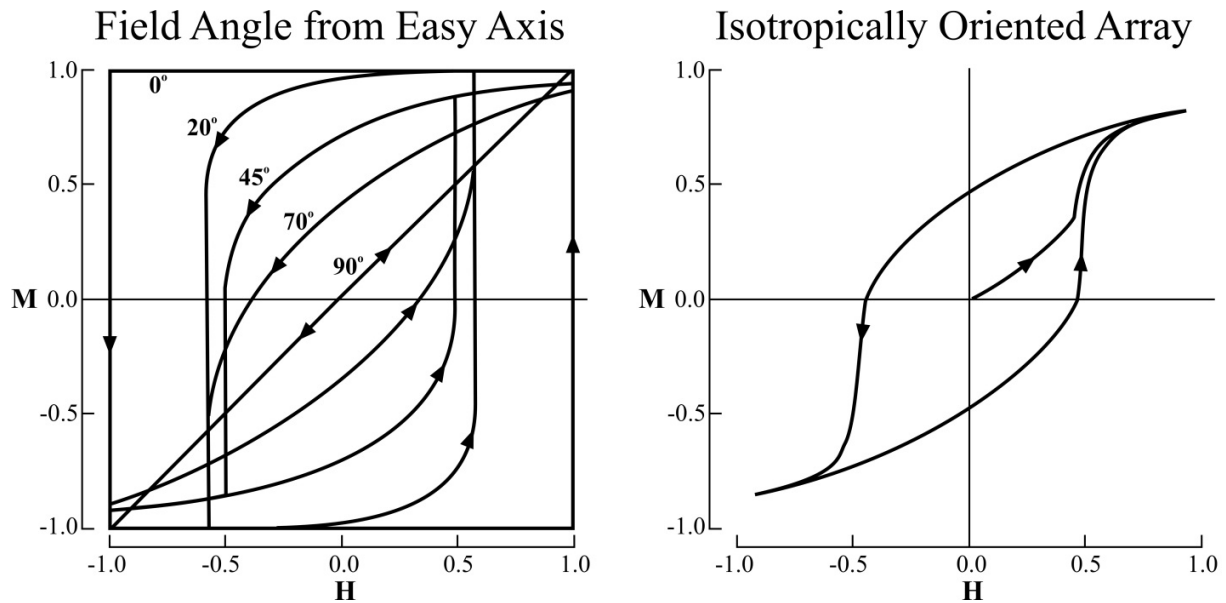


Fig. 7 – Hysteresis loops derived from the Stoner-Wohlfarth model, where magnetic particles with an easy axis of magnetization are placed in a magnetic field oriented at some fixed angle to the preferential axis. A 90° difference between the easy axes of the particles and the field results in a linear hysteresis loop, which will be the general form of a film with an easy axis laying in-plane. A random orientation of particle easy axes will result in the hysteresis curve on the right.

The isotropic distribution of magnetic axes and low coercivity in the Fe-rich phase suggests that it is composed of disordered FCC or amorphous material; thereby excluding the c-axis variant of the ordered $L1_0$ phase. Both FCC and $L1_2$ have comparable magnetocrystalline anisotropies of $K \sim -2 \times 10^4$ ergs/cm³, where the easy axis of magnetization is much weaker than that of $L1_0$ and rests along the $\langle 111 \rangle$ directions or their $\langle 110 \rangle$ projections onto the film [7-9]. The geometry of the Fe-rich precipitates also varies considerably, with some precipitates elongating along the $\langle 110 \rangle$ directions, and many being thicker along the c-axis than they are

wide. The multiplicity of shape and magnetocrystalline anisotropies supports the random distribution of magnetic easy-axes in the precipitate phase.

The in-plane hysteresis loop of the film confirms that the $L1_2$ matrix has a magnetic easy axis oriented parallel to the film. FePd films with weak anisotropy and small film thicknesses prefer to align in-plane magnetically, transitioning out of the plane as the balance between the magnetostatic energy and the energy contributed from the uniaxial anisotropy changes with film thickness [10]. The tetragonally-distorted $L1_2$ ordered phase has a relatively weak anisotropy component out of the plane of the film, compared to the alternating monolayers of the $L1_0$ phase, so an in-plane magnetization can be expected for films 50 nm thick. MFM (Fig. 8) was performed after applying a 1 Tesla field out-of-plane to saturate the film. The measurement was made at remanence, with the MFM tip magnetized out-of-plane, to confirm the expected magnetic properties of the two-phase microstructure.

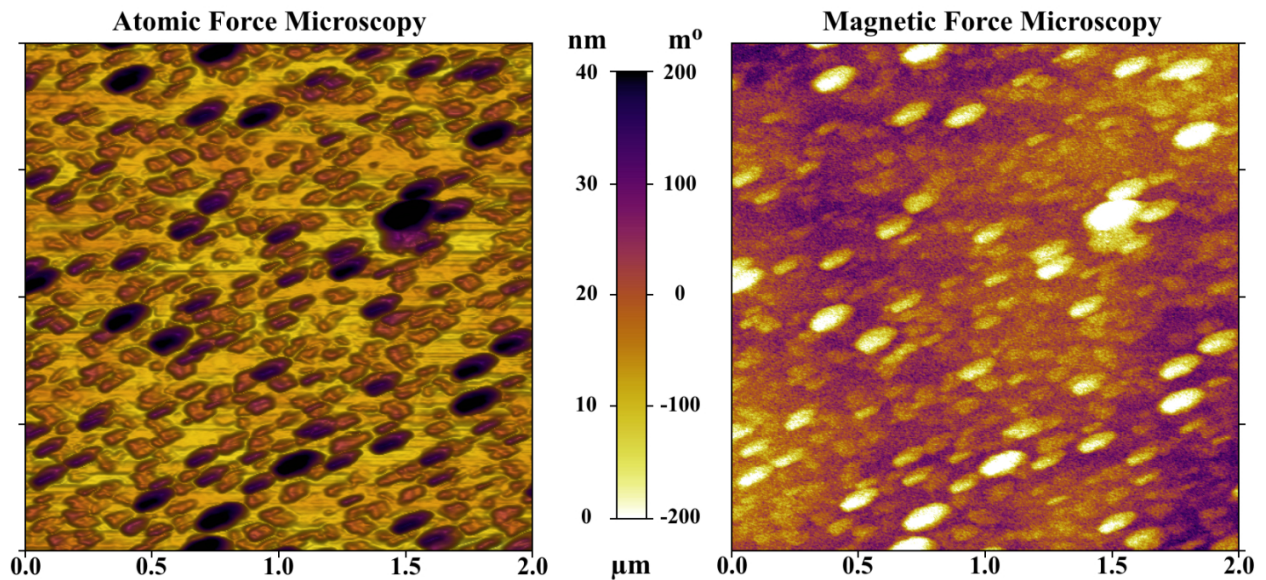


Fig. 8 – Paired atomic force and out-of-plane magnetic force micrographs of an $Fe_{38.5}Pd_{61.5}$ film grown at 550°C showing a nanoscale topography on the 10 to 20 nm scale. The Fe-rich secondary phases are magnetized more readily out of plane than the surrounding $L1_2$ matrix, which has a magnetic easy axis that resides in-plane.

It is observed that the Fe-rich secondary phase, which has clear topography, magnetizes more freely out-of-plane than the surrounding $L1_2$ matrix; confirming that it consists of rotatable single domains and that the surrounding matrix has an in-plane magnetic easy axis.

Both the $L1_2$ and Fe-rich secondary phases of the 550°C film experience a significant decrease in their saturation magnetizations, measured as 0.785 and 0.573 μ_B per statistical atom, respectively, compared to the single phase $Fe_{38.5}Pd_{61.5}$ films in the study ($\sim 1 \mu_B$). The decrease of magnetization in the dominant $L1_2$ matrix phase can be attributed directly to the loss of Fe from the eutectoid composition, which is the constituent that accounts for most of the magnetic moment in the alloy [11]. If the composition of the Pd-rich $L1_2$ matrix is interpolated linearly from the loss in magnetic moment compared to other films in the study, it results in a prediction that the matrix is between 72 % and 73 % palladium, nearly the stoichiometric $FePd_3 L1_2$ phase. The secondary phase precipitates, with approximate stoichiometry of $Fe_{60}Pd_{40}$ scaling from the areal fraction, exhibit a very low magnetization despite their Fe-rich composition. One possible explanation for this loss is that the precipitates have large interfacial areas relative to their volume, which has been shown to significantly decrease the expected saturation magnetization in several other nanoscale films and particles, and is attributed to a number of competing theories [12]. The Fe-rich nature of the secondary phase may also result in a loss of chemical ennoblement originating from the Pd, making precipitates more vulnerable to oxidation. Combined with the uncertain degree of crystallinity, all of these effects further complicate the magnetic state of the material.

5.2.4 – Composition: Auger Electron Microscopy

Due to its micron-scale interaction volumes, EDXS could not be utilized to determine the compositions of the two-phase microstructure. As the sampling depth of Auger microscopy is

only a few nanometers, and the incident electron beam can be focused to less than 10 nm laterally, high resolution AES was used to determine the quantitative composition of the two phases present in a 550°C film [13]. The surface of the film was analyzed as received, and subsequently after 0.5 nm, 2 nm, and 7 nm of material was removed from the sample surface by Ar sputter etching to reduce ambient carbon contamination. The relative ratio of Fe to Pd remained constant through each sputtering step and the carbon signature was completely eliminated past 2 nm of material removal, as well as most of the oxygen by 7 nm. As seen in Fig. 9, sputtering to remove contaminants from the surface greatly improves on the ability to assess the Pd Auger peaks in the spectrum, which overlap with carbon.

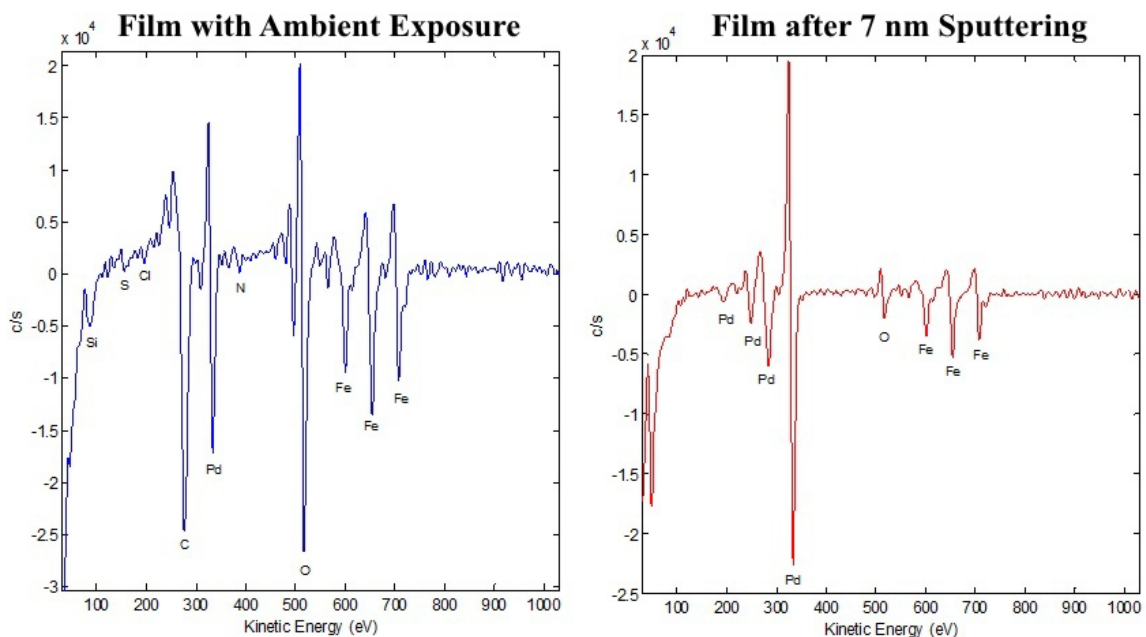


Fig. 9 – Auger spectrums of a 550°C $Fe_{38.5}Pd_{61.5}$ film showing the native film after ambient exposure, and after 7 nm of ion sputter etching to remove surface contamination.

Auger compositional analysis shows that the matrix phase of the material is 72.66 at % Pd with a standard deviation of 1.07 at %, while the Fe-rich secondary phase is 40.56 at % Pd with 5.53 at % standard deviation, both sampled over $n = 8$ regions (Table 1) (Fig. 10) .

| | Matrix | | Precipitates | |
|----------------|--------|-------|--------------|-------|
| | Fe at% | Pdat% | Fe at% | Pdat% |
| n = 1 | 25.32 | 74.68 | 66.11 | 33.89 |
| n = 2 | 27.85 | 72.15 | 63.35 | 36.65 |
| n = 3 | 28.75 | 71.25 | 63.21 | 36.79 |
| n = 4 | 27.69 | 72.31 | 58.97 | 41.03 |
| n = 5 | 28.06 | 71.94 | 61.66 | 38.34 |
| n = 6 | 26.65 | 73.35 | 58.77 | 41.23 |
| n = 7 | 26.67 | 73.33 | 48.97 | 51.03 |
| n = 8 | 27.72 | 72.28 | 54.47 | 45.53 |
| Average | 27.34 | 72.66 | 59.44 | 40.56 |
| StDev | 1.07 | 1.07 | 5.53 | 5.53 |

Table 1 – Compositional analysis of selected points in both the matrix and secondary phase precipitates of a 550°C Fe_{38.5}Pd_{61.5} film. These values indicate an overall L1₂-Fe₂₇Pd₇₃/FCC-Fe₆₀Pd₄₀ microstructure for the two-phase films. Greater variation is found in the secondary phase, which is consistent with its non-contiguous nature.

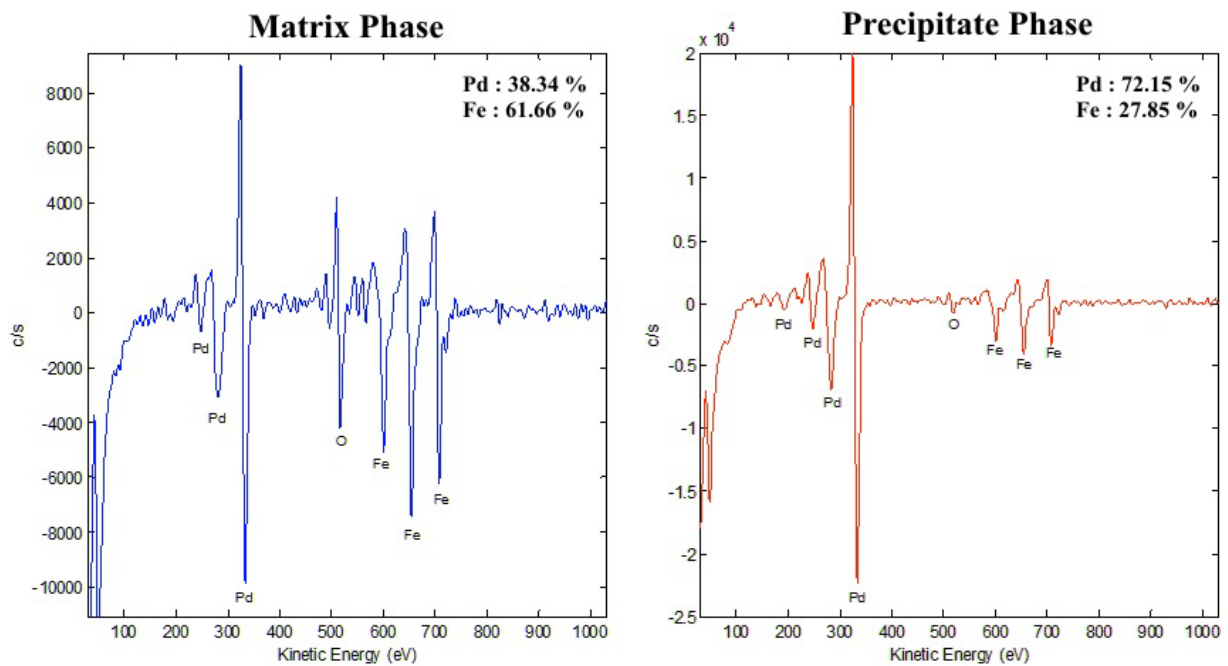


Fig. 10 – Auger spectrums of a 550°C Fe_{38.5}Pd_{61.5} film taken on a secondary-phase precipitate (Left) and on the contiguous Pd-rich matrix (Right) after 7 nm of material removal. The compositional differences between the two spectrums are observed in the changing height of the peaks attributed to each element. The Fe-rich secondary phase exhibits a stronger oxygen peak.

These phase compositions are nearly identical to those deduced independently from the interpolation of magnetic properties, and necessitate that the volumetric and areal phase fractions are nearly equal. The dispersed Fe-rich secondary phase microconstituents have a larger compositional variation than the contiguous Pd-rich matrix phase. This is consistent with the belief that they precipitated out of the matrix, which has given up excess Fe to reach its near stoichiometric composition.

Auger analysis of the film shows that the $\text{Fe}_{27}\text{Pd}_{73}$ matrix and $\text{Fe}_{60}\text{Pd}_{40}$ secondary phases have 6 to 7 at % and 20 to 30 at % oxygen concentrations, respectively, after 7 nm of material had been removed. The preferential oxidation of the Fe-rich secondary phase is highlighted by Auger compositional mapping (Fig. 11).

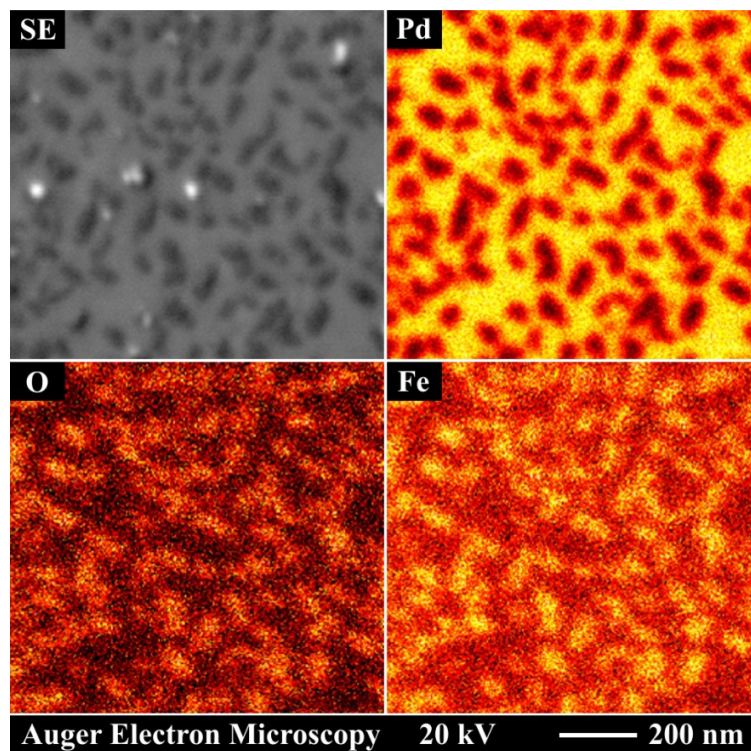


Fig. 11 – Secondary electron micrograph and corresponding composition maps of Pd, Fe & O from AES at 20kV on a 550°C $\text{Fe}_{38.5}\text{Pd}_{61.5}$ two-phase film, after 2 nm of material was removed by ion sputtering to reduce the carbon contaminant signature. The compositional maps show $\text{Fe}_{40}\text{Pd}_{60}$ secondary phases with a high oxygen signature embedded in an $\text{Fe}_{27}\text{Pd}_{73}$ matrix.

The oxygen content in the film decreases markedly between 2 nm and 7 nm of material removal, suggesting that the oxygen arises from environmental exposure and not from diffusion from the MgO substrate during deposition. Pure FCC Fe has a low solubility for oxygen as the oxygen/metal radii ratio is 0.63, well above the 0.59 structural limitation for the octahedral interstitial sites [14]. For the Fe-rich binary secondary phases, with an established lattice parameter in the territory of 3.836 Å, the radii ratio is just below 0.59 and solubilities on the order of 20% could theoretically be accommodated [15]. It is likely, however, that over time with environmental exposure, the near surface region of the Fe₆₀Pd₄₀ secondary phases may have formed a thin oxide layer which transitions to an interstitial solution away from the free surface. The film as a whole was confirmed to be deposited stoichiometrically from the Fe_{38.5}Pd_{61.5} target, and no other elements were detected with a concentration level above 0.1%. Oxidation is not expected to significantly impact film topography, as raised Fe₆₀Pd₄₀ features are found directly post-deposition with minimal exposure to ambient conditions before characterization.

Having both confirmed the L1₂-Fe₂₇Pd₇₃ composition, and eliminated the possibility that the Fe-rich Fe₆₀Pd₄₀ phase is L1₀ ordered, it can be determined that the latter is at least partially crystalline. In order to account for the intensity of the fundamental (002) film peak, which cannot be fully contributed from the L1₂ matrix (given the superlattice intensity, the maximum fundamental L1₂ reflection intensity can be determined), the Fe-rich phase must be at least 52 % FCC in nature. If the extra 2 at % Fe deviation from FePd₃ in the matrix sits on the c-axis oriented Pd sites, similar to the strain-induced L1' perturbation found at higher temperatures (Chapter 4), the Fe-rich phase could be up to 100% crystalline. Given the strong {110} faceting nature of the Fe₆₀Pd₄₀, an assumption will be made that the phase is dominantly FCC in behavior.

5.3 - Origins of the Two-Phase Decomposition

The origination of this unique two-phase microstructure of films deposited at 550°C still needs to be addressed. Long-range ordering, whether type L1' or L1₂, of the Fe_{38.5}Pd_{61.5} films has been found to rise with increasing deposition temperature. A two-phase microstructure of the disordered and ordered phases should exist at some transitional temperature; with the ordered phase nucleating from, and growing through, a disordered matrix phase *of the same composition*. In contrast, the Pd-rich nature of the ordered Fe₂₇Pd₇₃ matrix phase implies that this did not occur, and instead the Fe-rich Fe₆₀Pd₄₀ disordered regions have precipitated out. The films deposited at 550°C are likely, therefore, to have started growth in a single ordered phase, and at some point underwent a two-phase decomposition resulting in the microstructure described in this chapter. Films grown at 500°C, 600°C, and 650°C have not experienced this two-phase decomposition, suggesting that the two-phase decomposition is not driven by equilibrium conditions in the film.

5.3.1 - Argument for a Strain-Induced Transition

One of the largest disparities experienced during growth is in the strain conditions of depositing films. The decrease of film strain with rising deposition temperature is consistent with the thermally activated formation and glide of misfit dislocations, possibly 60° mixed edge/screw dislocations that are well known to be glissile in cubic heteroepitaxial thin films. It is proposed that films at 550°C start growth in a single ordered phase, likely the perturbed L1' as found in the 600°C films. In the early stages of growth it is expected to be energetically favorable for the film to nucleate in a single phase that is distorted tetragonally by strain. With increasing film thickness and the start of coalescence, it is possible for the elastic strain energy of the film to grow faster than the kinetics of the film are able to relieve it through misfit

dislocations. Under these conditions, the strain energy could become large enough to induce a phase transformation that lowers the energy of the system. The decomposition of $L1' \rightarrow FCC + L1_2$ could therefore be an alternative path to relieve strain energy within the film when other modes of relaxation are insufficient.

Additional films, not included in the temperature series, were grown at 550°C on alternative MTI Corp. and Sigma Aldrich brand MgO (001) substrates under similar processing conditions to those used earlier in this study, with some variations in deposition rate and deposition time. Many of these alternate films were kept from fully coalescing due to the presence of hydrophilic surface pitting and substrate impurities, demonstrating the need of high quality MgO for epitaxial Fe-Pd film growth. Depending on the brand of substrate, these defects can be readily observed by SEM (Fig. 12) or AFM (Fig. 13 and 14). The unpredictable surface conditions of these substrates may have inadvertently provided some insight into the two-phase behavior, as the films produced exhibit a wide range of local strain conditions compared to the much smoother films presented in Chapter 3.

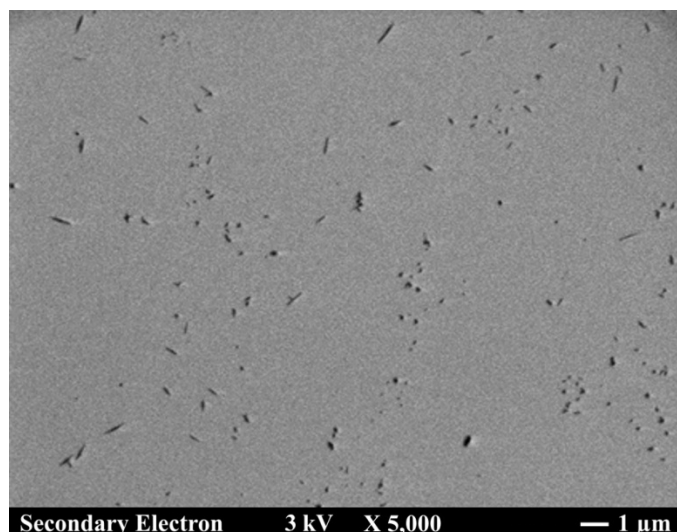


Fig. 12 – Secondary electron micrograph of an as received MTI brand MgO (001) substrate directly after removal from packaging, showing hydrophilic pitting and a micro-rough surface.

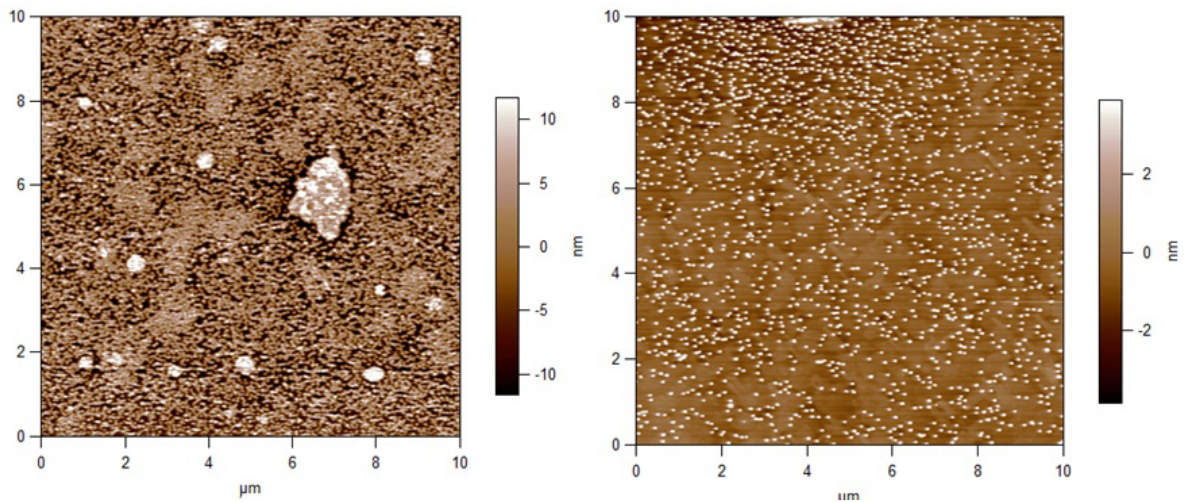


Fig. 13 – AFM micrographs of two MTI brand MgO (001) substrates removed from the same shipment and annealed simultaneously at 1000°C in an oxidizing tube furnace to expose impurities (white spots). Variations in the impurity levels and surface topography of the supposedly identical substrates highlight the difficulty of growing truly reproducible films on anything but the highest quality MgO surfaces.

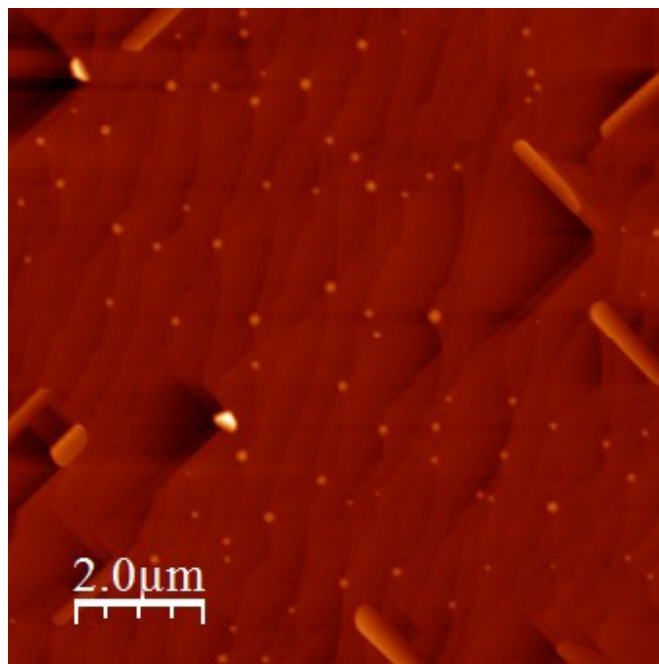


Fig. 14 – AFM micrograph of a Crystec MgO (001) substrate, of the type used in Chapter 3, annealed at 1000°C in an oxidizing tube furnace. In direct comparison to Fig. 13, the level and distribution of substrate impurities is markedly different and the surface is much smoother.

The microstructure of these films provides further evidence for a strain-induced phase transition, as the disordered phase can often be seen nucleating in a fine structure preferentially along the film edges as well as along steps in film thickness, believed to be a result of the inhomogeneous strain concentrations in these regions. This is particularly clear in one film which adopted the pattern of a continuous network (Fig. 15). The Fe-rich precipitates are topographically raised and exist within the body of the film, but they are especially prevalent at steps where film thickness changes and in a fine pattern along the film boundary.

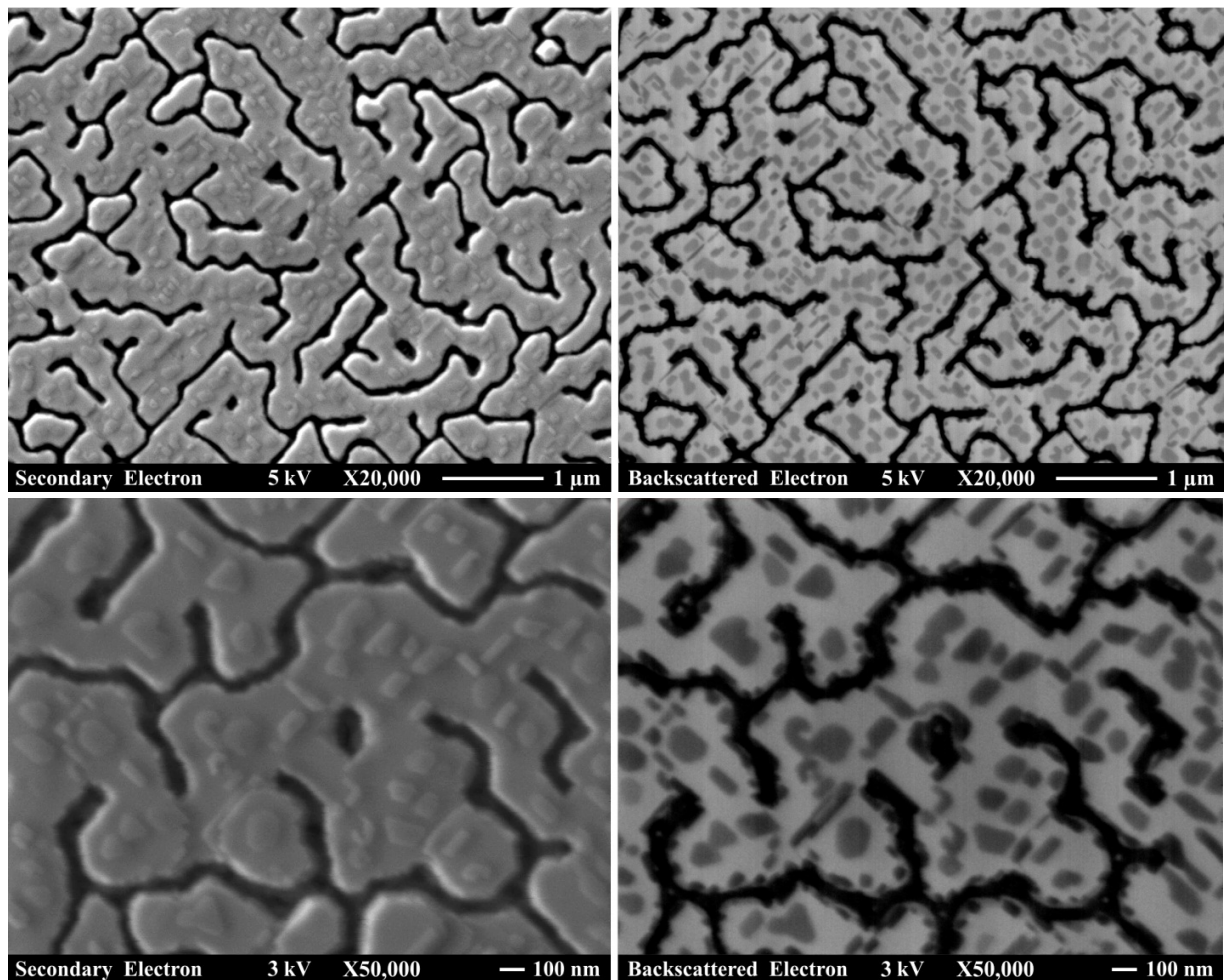


Fig. 15 – SEM secondary electron and backscattered electron micrographs of a two-phase $Fe_{38.5}Pd_{61.5}$ film grown at $550^{\circ}C$, highlighting the preference of precipitates to be found at areas of inhomogeneous strain such as thickness steps and along the film edge.

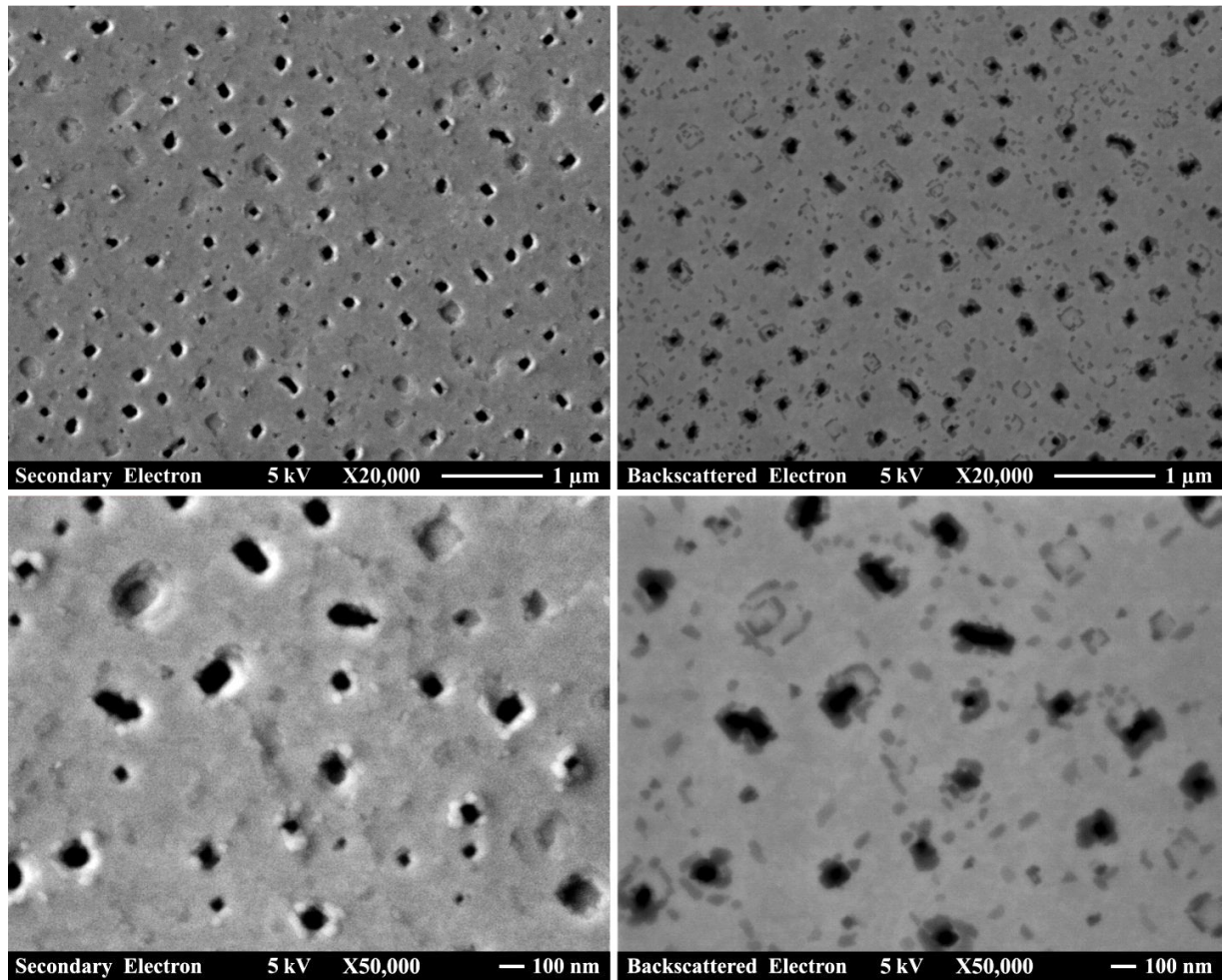


Fig. 16 – SEM secondary electron and backscattered electron micrographs of a two-phase $Fe_{38.5}Pd_{61.5}$ film grown at $550^{\circ}C$, highlighting the preference of precipitates to be found at areas of inhomogeneous strain such as coalescing voids.

Another film (Fig. 16) that grew more continuously over the MgO substrate demonstrates a mix of precipitates, some of the size and orientations found in the temperature series films and located within generally smooth regions. There are also clusters of the secondary phase clearly ringing all coalescing, or already coalesced, voids in the film which will have highly inhomogeneous strain conditions. The different areal fraction of precipitates in this film suggests that the exact composition of the two phases will be subject to strain and growth conditions in the film and are not the result of decomposition in an equilibrium two-phase field.

5.3.2 - Metastable Phase Diagram

The phase diagram surrounding the eutectoid composition of the Fe-Pd system is not well understood from a theoretical standpoint. Attempts to model the system using Lennard-Jones type potentials and cluster variation methods have resulted in a close reproduction of the order-disorder transition temperatures of the Fe-Pd system, but cannot explain the shift of the congruent composition from equiatomic, which is attributed to multibody or magnetic interactions [16]. Phase diagrams that have been calculated from thermodynamic modeling parameters, and refined to experimental data, do not agree fully with the empirical phase diagram but do offer some insight into the behavior of the Fe-Pd system. Models from at least two different groups [17, 18] predict an inflection of the $L1_0 + L1_2 \rightarrow L1_2$ phase boundary back to 70 to 71 at % Pd at room temperature. This inflection is a known feature of all phase diagrams with ordered constituents, as thermodynamics at 0 K dictate that all ordered phases must be present as stoichiometric line compounds to minimize entropy; however this inflection in the phase boundary will generally occur at cryogenic temperatures for most material systems.

Using known behaviors of the system, the outline of a metastable phase diagram for Fe-Pd on MgO may be constructed accounting for the absence of $L1_0$; where an FCC + $L1_2$ two-phase region extends down to room temperature. The lines used in this diagram will be subject to conditions in the film such as strain, interfacial energy, and nanoscale size effects, so they are strictly qualitative in nature. To begin bounding such a diagram, metastable extensions of the $L1_0$ and $L1_2$ equilibrium curves can be made, under the umbrella of which each of the two phases can be considered to be energetically favorable compared to FCC, if not the lowest energy phase, due to the balance of structural and magnetic energies in the un-strained system. The hybrid-nature $L1'$ phase could be expected to generally form near the eutectoid, in the region

encompassed by both the $L1_0$ and $L1_2$ phases; or by their instability temperatures, which are similar enough the difference can be ignored. Removing the $L1_0$ phase from the diagram due to strain in the system, ostensibly due to an unfavorable magnetic energy contribution compared to $L1_2$ ordering, but maintaining the general order-disorder transition temperature across the Fe-rich region; a rough metastable diagram can be drawn (Fig. 17). $L1'$ is a loose designation, as it encompasses the entire spectrum of ordering between $L1_0$ and $L1_2$. With increasing strain the $L1'$ region will subsequently shift or disappear as its $L1_0$ component appears to be unfavorable, leading the Pd-rich boundary of the FCC + $L1'$ region to approach stoichiometric $FePd_3$. As a result, at the $Fe_{38.5}Pd_{61.5}$ composition the alloy can rest, depending on strain, in an $L1'$ or variable FCC + $L1'$ region with an extreme value approaching FCC + $L1_2$. It is hypothesized that the two-phase $L1_2-Fe_{27}Pd_{73}/FCC-Fe_{60}Pd_{40}$ microstructure found in this study is produced by the decomposition of $L1'-Fe_{38.5}Pd_{61.5}$ in this type of a two-phase field.

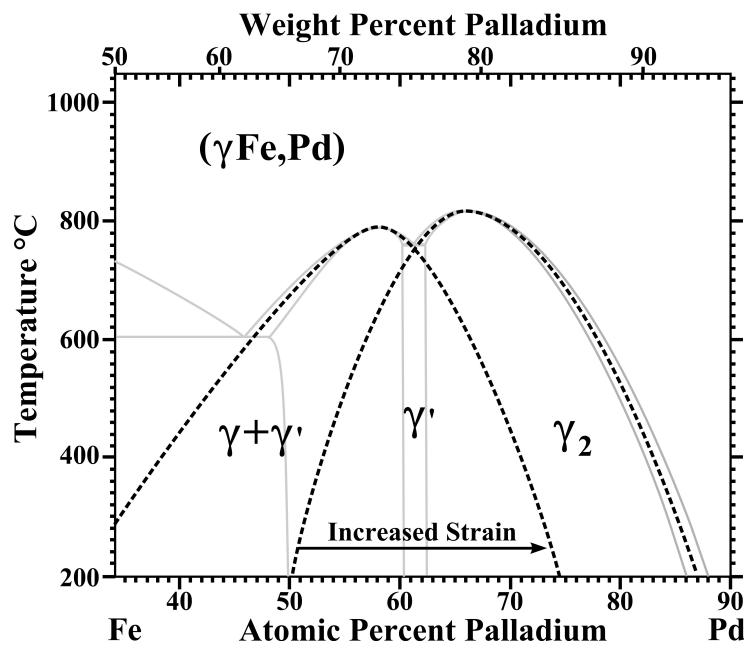


Fig. 17 – Possible behavior for a metastable phase diagram of strained Fe-Pd on MgO (001). The hybrid $L1'$ phase is proposed to disappear or shift to Pd-rich compositions with sufficient strain, yielding an FCC + $L1_2$ two-phase region stretching across the $Fe_{38.5}Pd_{61.5}$ composition.

As $L1_0$ is known to grow on MgO (001) substrates across much of the excluded region, it is important to note the *ad hoc* nature of the metastable diagram. The diagram presented assumes that the films undergoing decomposition have begun to grow as $L1'$ and have already partly relaxed before the phase change. If this relaxation has moved the film past the in-plane lattice parameter of the $L1_0$, the phase may continue to be excluded as it is unlikely to form as a compressed precipitate.

5.3.3 – Formation and Diffusion

The presence of Fe-rich, disordered $Fe_{62}Pd_{38}$ – $Fe_{75}Pd_{25}$ FCC columns on the 10 nm scale have been observed to form within ordered equiatomic FePd films in another study [19]. The presence of these disordered structures was suggested to correspond to the presence of anti-phase boundaries or other defects, which become a preferential site for diffusion and aggregation of Fe atoms during growth [20]. As the disordered FCC phase shares less symmetry with the parent $L1_2$, and Fe may experience preferential aggregation to defects in the Fe-Pd system, the Fe-rich FCC phase can be expected to precipitate during the phase transition rather than the ordered $L1_2$.

The diffusion behavior of Fe and Pd remains relatively constant across all binary alloy compositions and both species have comparable values, with Fe being about twice as mobile at 550°C. At $Fe_{40}Pd_{60}$, near the $Fe_{38.5}Pd_{61.5}$ eutectoid composition, the Fe atoms have a self-diffusion coefficient $D_{o\ Fe}^* = 0.69\text{ cm}^2\text{s}^{-1}$ and activation energy $Q_{Fe}^* = 61.8\text{ kcal/mol}$; while $D_{o\ Pd}^* = 0.79\text{ cm}^2\text{s}^{-1}$ and $Q_{Pd}^* = 63.6\text{ kcal/mol}$ [21]. The dominant diffusion term for the thin film, however, will be surface diffusion from the interfaces. For an FCC metal, surface diffusion has a lower activation energy than the bulk, roughly $Q_S \sim 0.6 Q_B$ [22], or can be approximated from the melting temperature [23], with both methods yielding surface diffusion coefficients on the order of $5.0 \times 10^{-11}\text{ cm}^2\text{s}^{-1}$ for the $Fe_{38.5}Pd_{61.5}$ depositions. This term is expected to contribute to

the diffusion flux only over a 0.5 nm surface thickness at any instance during deposition [24], but is much larger than the $\sim 1 \times 10^{-17} \text{ cm}^2\text{s}^{-1}$ supplied in the bulk. The mean free diffusion path length can be taken as $\bar{x} = \sqrt{2Dt}$, where D is the diffusion coefficient (which is temperature dependent) and t is time. The mean diffusion length in the lateral film directions due to surface diffusion is on the order of 200 nm, as opposed to the 2 nm available during the deposition time for bulk diffusion. The microstructure of the two-phase films is on the scale of hundreds of nanometers, consequently the formation of the observed two-phase decomposition is likely to occur early in the growth process as surface diffusion is necessary. Strain will be high in the early stages of film growth due to the level of epitaxial coherence to the substrate, so this is consistent with the hypothesis of a strain-induced two-phase decomposition.

The prominence of surface diffusion in the two-phase film may also explain some of the film topography, as Fe and Pd adatoms deposited on the surface will experience different diffusion gradients. During PLD material arrives at the surface in discrete bursts. The 50 nm films have approximately 260 atomic monolayers, deposited 0.4 monolayers per second over 7200 individual 10 Hz pulses. Fe has a higher diffusion rate than Pd, so Fe adatoms from new material landing on the more prominent L1₂ matrix will diffuse along the surface to the precipitate phase, leaving behind a new Pd-enriched Fe₂₇Pd₇₃ layer. As Fe_{38.5}Pd_{61.5} is deposited on the Fe₆₀Pd₄₀ precipitates, however, the less mobile excess of Pd is offset partly by the incoming Fe flux from the surrounding matrix, which could result in some degree of mass accumulation in the Fe-rich precipitates and their rise above the surface of the matrix phase.

5.4 – Major Findings

$\text{Fe}_{38.5}\text{Pd}_{61.5}$ films grown at 550°C on MgO (001) substrates have been found in a unique two-phase microstructure of prismatic, $\text{Fe}_{60}\text{Pd}_{40}$ disordered FCC secondary phases with 10 to 100 nm facets oriented along the $\langle 110 \rangle$ substrate directions, embedded within a nearly stoichiometric ordered $\text{L1}_2\text{-Fe}_{27}\text{Pd}_{73}$ matrix. These secondary phase precipitates exhibit single domain magnetic axis rotation, while the ordered L1_2 matrix has a magnetic easy axis aligned in-plane. This unique two-phase microstructure is postulated to be induced by the degree of epitaxial strain in the coalescing film, which throughout this thesis has also been proposed to drive the absence of L1_0 in the films at this composition. A hypothesis has been put forward to explain the two-phase decomposition, involving a metastable extension of the FCC + L1_2 region of the phase diagram through the eutectoid composition due to epitaxial strain. The effect of MgO surface quality on the ability to reproduce strain conditions in Fe-Pd films is also highlighted in this chapter.

References

- [1] W. Rasband, *ImageJ* (U. S. National Institutes of Health, Bethesda, Maryland, USA, 2012) <http://imagej.nih.gov/ij/>
- [2] C. Schneider, W. Rasband, and K. Eliceiri, *Nature Methods* **9**, 671, (2012)
- [3] M. Abramoff, P. Magalhaes, and S. Ram, *Biophotonics International* **11**, 36 (2004)
- [4] P. Fewster, *Crit. Rev. Solid State* **22**, 69 (1997)
- [5] E. Stoner and E. Wohlfarth, *Philos. T. Roy. Soc. A* **240**, 59A (1948)
- [6] B. Cullity, *Introduction to Magnetic Materials* (Addison-Wesley, Reading, MA, 1972)
- [7] N. Miyata, H. Asami, and T. Mizushima, *J. Phys. Soc. Jpn.* **55**, 946 (1986)
- [8] L. Magat, A. Yermolenko, G. Ivanova, G. Makarova, and Y. Shur, *Phys. Met. Metall.* **26**, 132 (1968)
- [9] V. Myagkov, V. Zhigalov, B. Belyaev, L. Bykova, L. Solovyov, and B. Bondarenko, *J. Magn. Magn. Mater.* **324**, 1571 (2012)
- [10] V. Gehanno, R. Hoffmann, Y. Samson, A. Marty, and S. Auffret, *Eur. Phys. J. B* **10**, 457 (1999)
- [11] E. Burzo and P. Vlaic, *J. Optoelectron. Adv. M.* **12**, 1869 (2010)
- [12] H. Lu, W. Zheng, and Q. Jiang, *J. Phys. D: Appl. Phys.* **40**, 320 (2007)
- [13] C. Powell and M. Seah, *J. Vac. Sci. Technol. A* **8**, 735 (1990)
- [14] R. Barrer, *Discuss. Faraday Soc.* **4**, 68 (1948)
- [15] J. Kitchener, J. Bockris, M. Gleiser, and J. Evans, *Trans. Faraday Soc.* **48**, 995 (1952)
- [16] T. Horiuchi, M. Igarashi, F. Abe, and T. Mohri, *Calphad* **26**, 3 (2002)
- [17] R. Davies, R. Dinsdale, A. Gisby, J. Robinson, and J. Martin, *Calphad* **26**, 229 (2002)
- [18] G. Ghosh, C. Kantner, and G.B. Olson, *J. Phase Equilib.* **20**, 295 (1999)
- [19] D. Halley, B. Gilles, and D. Jalabert, *J. Appl. Phys.* **91**, 9757 (2002)
- [20] X. Zhang, S. Godfrey, M. Weaver, M. Strangwood, P. Threadgill, M. Kaufman, and M. Loretto, *Acta Mater.* **9**, 3723 (1996)
- [21] J. Fillon and D. Calais, *J. Phys. Chem. Solids* **38**, 81 (1977)
- [22] N. Gjostein, *Diffusion, Papers Presented at a Seminar of the American Society for Metals* (ASM International, Gaithersburg, 1973) p. 241
- [23] Y. Mishin and W. Gust, *Ionics* **7**, 247 (2001)
- [24] J. Fisher, *J. Appl. Phys.* **22**, 74 (1951)

6 – Contributions and Suggested Work

Having presented a number of related studies, this chapter will address the collective impact of the included work and outline a number of suggested additional experiments for those wishing to expand upon the previous findings.

6.1 – Contributions to the Field

One significant contribution to the field presented in this dissertation is the discovery and experimental verification of the L1' hybrid phase presented in Chapter 4. While introduced periodically as a possibility for ideal magnetic FCC systems between 1938 and 1986, such a phase existing is not commonly addressed in modern literature and could be considered a largely unknown prospect at the time of its first experimental appearance in the Fe-Pd system. During the calculation of long-range ordering parameters for Fe_{38.5}Pd_{61.5} films, initially thought to reside in the L1₂ phase, it was noted that the ordering parameters exceeded not only the maximum values for non-stoichiometric L1₂, but unity as well. In the absence of indicative L1₀ behavior, it was the author's own original proposal that the non-stoichiometric Fe in the alloy may be accommodated differently across Pd sites of the lattice, explaining the anomalously high (001) superlattice peaks. The procedure for determining and quantifying such a perturbation from quantitative XRD was developed, and the presence of the L1' phase was confirmed. Notation for discussing such a hybrid structure and the assignment of two ordering parameters is presented for the first time, having not been discussed or developed during the brief Au-Cu theoretical proposals. The approximation of instability temperatures for FePd and FePd₃ from first and second nearest-neighbor interactions is also currently absent from the publication history of the alloy and is presented as original work in this thesis.

This thesis presents the first comprehensive study of epitaxial film growth at the $\text{Fe}_{38.5}\text{Pd}_{61.5}$ eutectoid composition, and more generally for the entire Pd-rich region of the Fe-Pd alloy. While an L1_0 - L1_2 microstructure, chessboard or otherwise, did not manifest, the behavior of the alloy to trend to L1_2 single-phase dominated behavior shows that the two-phase region of the Fe-Pd diagram is very responsive to processing conditions such as strain, explaining the high degree of experimental uncertainty concerning the equilibrium phases of the eutectoid region. The work presented is also the first expansive study of Fe-Pd alloy film growth and morphology on MgO (001) substrates at any composition by PLD. In particular, it highlights the role of MgO (001) surfaces in controlling film morphology for PLD at temperatures $\geq 600^\circ\text{C}$.

The two-phase decomposition of $\text{Fe}_{38.5}\text{Pd}_{61.5}$ films grown by PLD at 550°C presents a new type of behavior for films of ordered systems, where strain in the film induces a disordered phase precipitate from an ordered matrix. In some situations this could be detrimental to the desired properties of the film and the findings in this thesis outline how to avoid such unwanted phenomena if identified by others in the future. However, with some enterprise, this behavior may be adopted to other ordered systems in an attempt to create desirable two-phase microstructures induced by strain during film growth. For example, in the two-phase $\text{Fe}_{38.5}\text{Pd}_{61.5}$ films presented in Chapter 5, the Fe-rich precipitates might be coerced back into an ordered L1_0 phase with altered processing conditions such as post-deposition annealing.

In conclusion, two types of ordering phenomena new to the field are presented and developed within the work of this thesis, in addition to filling gaps in the experimental record concerning both the specific $\text{Fe}_{38.5}\text{Pd}_{61.5}$ composition and the growth of epitaxial Fe-Pd thin films via PLD. Both of these new ordering phenomena are not necessarily specific to Fe-Pd and may manifest themselves, for better or worse, in other technically relevant material systems.

6.2 – Suggested Future Work

The work presented in this thesis, as per cliché, raises more questions than it definitively answers and could have been continued for many more years. This section will outline some of the most obvious experimental expansions, as well as providing some insights from the point of experience. Foremost, given the number of closely related material systems, attempts to reproduce the ordering phenomena presented in this thesis by growing eutectoid Fe-Pt, Co-Pt, or Au-Cu thin films would be of distinct interest in an effort to determine the generality of the new behaviors. Suggested experiments will focus more narrowly on Fe-Pd alloys.

Within the Fe-Pd system, a number of readily controllable parameters can be expected to alter the microstructure and phases of epitaxial films. Strain conditions within the films have been attributed to result in much of the $\text{Fe}_{38.5}\text{Pd}_{61.5}$ alloy's unique behavior on MgO (001). A study concerning the effect of deposition rates on both the L1' and two-phase phenomena is a logical expansion on the original temperature study, as the same $\text{Fe}_{38.5}\text{Pd}_{61.5}$ target and setup can be used. Slower deposition rates should result in slower accumulation of strain energy in the films, as more time at higher kinetic rates allow for misfit dislocations to better relieve mismatch with the substrate. Another expansion, i.e. requiring little experimental change, is studying the effect of post-deposition annealing on $\text{Fe}_{38.5}\text{Pd}_{61.5}$ films. The two-phase films grown at 550°C could be expected to evolve with further exposure to elevated temperatures, with the Fe-rich FCC precipitates either growing or expanding, and possibly even ordering into the L1₀ phase. Post-deposition annealing may also help determine whether the L1' phase arises from the Snoek effect or simultaneous L1₀/L1₂ ordering. If driven by simultaneous ordering, the L1' phase may be held together at room temperature by a low driving force for phase separation. Long anneals could then result in the formation of two ordered phases due to increased diffusion. If instead

L1' is driven by the Snoek effect, further relaxation of strain in the film during a long anneal could bring the system to an equilibrium L1₂ structure.

With more effort and cost, additional targets can be made at neighboring compositions. With increasing Fe concentrations the degree of L1' type ordering is likely to increase. It would be of great interest to observe the transition from L1₂ dominant to L1₀ dominant behavior and whether it is smooth or discontinuous. If post-deposition annealing of Fe_{38.5}Pd_{61.5} provides fruitful data, a possible low-cost alternative would be the subsequent deposition of Fe or Pd thin films after the deposition of Fe_{38.5}Pd_{61.5}, which after a sufficiently long anneal could achieve films of a non-eutectoid stoichiometry. This introduces a number of new variables and may yield more new phenomena rather than addressing a shift in stoichiometry.

Substrate effects also play a large role in strain conditions and provide another parameter to explore. The quality of MgO surfaces from different suppliers, and sometimes within suppliers, varies considerably. As the highest quality substrates are not always available commercially, studies into MgO surface preparation may help to provide better control of Fe-Pd thin film morphology and consequentially local strain conditions. This may involve trying to anneal out surface pitting and defects using high temperature furnaces, or holding the substrate at temperature under vacuum longer before deposition. It is also possible to condition the MgO substrate under a low pressure oxidizing atmosphere directly prior to deposition, as opposed to an inert gas vacuum, to test the difference in the surface state on film growth. The introduction of Pt, Pd, Cr, or Au seed layers, as reviewed in Chapter 1, provide other options for study.

Alternate substrates are available, for which Fe-Pd may be expected to deposit with cube-on-cube epitaxy. Strontium titanate has a perovskite crystal structure with a cubic lattice parameter of $a = 3.905 \text{ \AA}$ [1], which is a far better match than MgO at $a = 4.212 \text{ \AA}$ [1] but costs

about six times as much. The close lattice match to $\text{Fe}_{38.5}\text{Pd}_{61.5}$ does make it intriguing for small scale study, however, as strain will be much lower and should dramatically impact the ordering phenomena in the films if they are strain-induced. Alternatively, lanthanum aluminate has a perovskite structure with $a = 3.790 \text{ \AA}$ [1], so films could be grown for comparison in compressive strain; opening a whole realm of possibilities. Thermal mismatch reintroduces itself with the move away from MgO substrates but, as linear expansion coefficients of both alternate substrates are not dramatically smaller, should still play a limited role [1]. Oxidized Si substrates provide another avenue for study, moving away from epitaxial growth altogether.

NaCl has a rock salt structure with $a = 5.640 \text{ \AA}$ [2] but FePd is known to grow with cube-on-cube epitaxy on NaCl substrates, at least in the form of nanoparticles [3]. Using NaCl introduces experimental complications as it is extremely hydrophilic and needs to be cleaved under vacuum to produce reliable surfaces [4]. If films can be successfully grown, this same behavior turns into an asset as NaCl substrates can be dissolved to create free standing films. There is some possibility that MgO substrates could be dissolved as well with the aid of chemical solutions [5]. The creation of freestanding films is of particular interest as they can be observed readily via HRTEM to confirm their crystallographic behavior at the atomic scale, in the direction perpendicular to the surface.

While HRTEM cannot be used to directly confirm the presence of an L1' phase, the preparation of TEM samples would be able to provide additional pertinent information. Notable areas of interest include the Fe-Pd/MgO interface and the type and location of dislocations within the film. Cross sections of the two-phase films grown at 550°C would also answer a number of questions, including direct verification of the FCC Fe-rich phase and observation of the interface along the $\{110\}$ facets between the FCC and L1_2 phases in the film. Preparing TEM samples of

these films is non-trivial, and it is possible that techniques such as focused ion beam milling may still introduce defects into cross-sectional samples that alter the state of ordering. With sufficient time and finances it would be one of the higher priority pursuits initiated by the findings in this thesis.

Moving away from thin film growth, entire theses could be written engaging in a detailed study of the $\text{Fe}_{38.5}\text{Pd}_{61.5}$ target used for deposition, exposing the bulk to different processing conditions and annealing. Melting part of the target and spinning the material as a ribbon would allow for the detailed TEM study of the bulk using conventional electro-polishing, dimpling and ion milling preparation techniques. Understanding of the bulk alloy behavior at $\text{Fe}_{38.5}\text{Pd}_{61.5}$ would allow for better insight into the material at the nanoscale. Alternatively the $\text{Fe}_{38.5}\text{Pd}_{61.5}$ target could be deposited at room temperature onto Mo TEM grids with thin amorphous carbon scaffolds. The resulting nanoparticles or films could be annealed in furnaces at different temperatures and observed readily by HRTEM.

References

- [1] L. Peng, X. Xi, B. Moeckly and A. Alpay. *Appl. Phys. Let.* **83**, 4592 (2003)
- [2] T. Pearsall, *Strained-Layer Superlattice: Materials Science and Technology* (Academic Press, New York, 1991)
- [3] K. Sato, K. Aoyagi, and T. Konno, *J. Appl.Phys.* **107**, 024304 (2010)
- [4] C. Thompson, J. Floro and H. Smith, *J. Appl. Phys.* **67**, 4099 (1990)
- [5] T. Edler and S. Mayr, *Adv. Mater.* **22**, 4969 (2010)